

**FUNDAMENTAL STUDY OF ENGINEERED NANOCRYSTALLINE AND
AMORPHOUS SILICON BASED HIGH CAPACITY, REVERSIBLE AND STABLE
ANODES FOR LITHIUM-ION BATTERIES**

by

Rigved Epur

B.Tech in Metallurgical Engineering and Materials Science, Indian Institute of Technology

Roorkee, Roorkee, India, 2006

M.S in Materials Engineering, Auburn University, Auburn, 2009

Submitted to the Graduate Faculty of
Swanson School of Engineering in partial fulfillment
of the requirements for the degree of
Doctor of Philosophy

University of Pittsburgh

2014

UNIVERSITY OF PITTSBURGH
SWANSON SCHOOL OF ENGINEERING

This dissertation was presented

by

Rigved Epur

It was defended on

July 8, 2014

and approved by

Jung-Kun Lee, PhD, Associate Professor, Department of Mechanical Engineering and
Materials Science

Ian Nettleship, PhD, Associate Professor, Department of Mechanical Engineering and
Materials Science

John A. Barnard, PhD, Professor, Department of Mechanical Engineering and Materials
Science

Spandan Maiti, PhD, Assistant Professor, Department of Bioengineering

Dissertation Director: Prashant N. Kumta, PhD, Edward R. Weidlein Chair Professor,
Department of Mechanical Engineering and Materials Science, Department of
Bioengineering, Department of Chemical and Petroleum Engineering

Copyright © by Rigved Epur

2014

**FUNDAMENTAL STUDY OF ENGINEERED NANOCRYSTALLINE AND
AMORPHOUS SILICON BASED HIGH CAPACITY, REVERSIBLE AND STABLE
ANODES FOR LITHIUM-ION BATTERIES**

Rigved Epur, PhD

University of Pittsburgh, 2014

Commercial lithium-ion battery (LIB) systems at present employ graphite as the anode having a theoretical capacity of 372 mAh/g. However, for hybrid electric vehicles and electrical grid energy storage, batteries with much higher capacity and cycle life are needed. There is hence a critical need to explore alternative higher capacity alternative systems. Silicon, with a theoretical capacity of 4200 mAh/g is widely considered a promising alternative candidate anode to graphite. However, Si undergoes colossal volume expansion (>300%) during lithium alloying and de-alloying. This leads to pulverization resulting in loss of electrical contact of Si with the current collector thereby causing rapid decrease in capacity and consequent failure. It has been demonstrated that nanostructured (*nc*-Si) and amorphous (*a*-Si) forms of Si and Si based nanocomposites provide mechanical integrity preventing pulverization due to the reduced number density of atoms within a nano-sized grain and the ‘free volume’ effects in amorphous Si resulting in better capacity retention and cycle life.

In this dissertation, the following simple and cost effective approaches for generating nanostructured composites of silicon are discussed: (1) Si nanoparticles of high specific surface area by high energy mechanical milling (HEMM), (2) Amorphous silicon (*a*-Si) films by electrodeposition, (3) Heterostructures of vertically aligned carbon nanotubes (VACNTs) and Si

by chemical vapor deposition (CVD), and (4) low cost template based high throughput synthesis of hollow silicon nanotubes (h-SiNTs).

All of the above amorphous and nanocrystalline Si based composites were thoroughly investigated using material and electrochemical characterizations and accordingly, a structure-property relationship was established. Among the aforementioned structures, the electrodeposited *a-Si* films exhibited excellent cyclability (0.016% loss per cycle), while CNT/Si heterostructures showed a very low first cycle irreversible loss of only 10%. The hollow silicon nanotubes exhibited a reasonable first cycle irreversible loss (25%) but exhibited extraordinary cycling stability with a low capacity fade rate of $\sim 0.06\%$ loss/cycle at the end of 400 cycles. These amorphous and nanocrystalline based silicon anodes prepared by cost effective methods, due to their superior electrochemical properties, show considerable potential to replace the current graphite based anodes for the next generation of high energy density Li-ion batteries.

TABLE OF CONTENTS

TABLE OF CONTENTS	VI
LIST OF TABLES	X
LIST OF FIGURES	XI
ACKNOWLEDGEMENTS	XVII
1.0 INTRODUCTION.....	1
1.1 MOTIVATION	1
1.2 BACKGROUND	8
1.2.1 Lithium-ion Battery.....	8
1.2.2 Rechargeable Lithium-ion batteries	9
1.2.3 Rocking Chair cells.....	11
1.2.4 Theoretical Capacity, Energy density and Differential capacity	13
1.2.5 Design considerations for battery materials	16
1.2.6 Lithium-Ion battery configurations	20
1.2.7 Cathode materials.....	24
1.2.8 Electrolytes	32
1.2.9 Anodes.....	43
1.2.10 Silicon anodes.....	54
1.2.11 Electrochemical lithiation reactions in Silicon.....	57
1.2.12 Failure mechanism in silicon anodes	60

1.2.13	Approaches to address the problem.....	64
1.2.14	Impact of Synthesis Methods.....	77
2.0	OBJECTIVES	83
2.1	LIMITATION OF CURRENT SILICON BASED ANODES	83
2.2	HYPOTHESIS AND APPROACH	84
3.0	EXPERIMENTAL TECHNIQUES	89
3.1	SYNTHESIS OF NANOCRYSTALLINE AND AMORPHOUS SILICON STRUCTURES	89
3.1.1	High Energy Mechanical Milling (HEMM)	89
3.1.2	Electrodeposition	91
3.1.3	Chemical Vapor Deposition	93
3.1.4	Hydrothermal Synthesis	94
3.2	CHARACTERIZATION OF THE GENERATED SILICON NANOCOMPOSITES	95
3.2.1	X-ray Diffraction Analysis	95
3.2.2	Scanning Electron Microscopy (SEM)	96
3.2.3	Raman Spectroscopy	97
3.2.4	Transmission Electron Microscopy (TEM)	97
3.2.5	Electrochemical Characterization	98
4.0	SILICON NANOPARTICLE ANODE GENERATED BY HIGH ENERGY MECHANICAL MILLING (HEMM)	102
4.1	INTRODUCTION	102
4.2	EXPERIMENTAL	105
4.2.1	Materials synthesis	105

4.2.2	Materials characterization	106
4.2.3	Electrochemical characterization.....	107
4.3	RESULTS AND DISCUSSION	108
4.4	CONCLUSIONS	122
5.0	AMORPHOUS SILICON FILM ANODE BY ELECTRODEPOSITION FROM ORGANIC SOLVENTS	124
5.1	INTRODUCTION	124
5.2	EXPERIMENTAL.....	126
5.2.1	Amorphous silicon film deposition.....	126
5.2.2	Film characterization	127
5.2.3	Electrochemical characterization.....	127
5.3	RESULTS AND DISCUSSION	128
5.4	CONCLUSION	142
6.0	CHEMICAL VAPOR DEPOSITION DERIVED SILICON COATED VERTICALLY ALIGNED CARBON NANOTUBE ANODES.....	143
6.1	INTRODUCTION	143
6.2	EXPERIMENTAL.....	145
6.2.1	SiCNT nanocomposite preparation.....	145
6.2.2	Materials and electrochemical characterization	146
6.2.3	Binder-less CNT/Si electrode preparation using scribable technique	147
6.3	RESULTS AND DISCUSSION	148
6.4	BINDER-LESS, SCRIBABLE CNT/SI HETEROSTRUCTURE ANODES	157

6.5	CONCLUSIONS	170
7.0	HOLLOW SILICON NANOTUBE ANODE PREPARED USING SACRIFICIAL <i>MGO</i> NANOROD TEMPLATE	172
7.1	INTRODUCTION	172
7.2	EXPERIMENTAL.....	175
7.2.1	Synthesis of MgO nanorods	175
7.2.2	Synthesis of h-SiNTs.....	176
7.2.3	MgO template regeneration.....	176
7.2.4	Materials Characterization.....	177
7.2.5	Electrochemical testing	177
7.3	RESULTS AND DISCUSSION	178
7.3.1	Silicon nanotube synthesis	178
7.3.2	Materials characterization.....	181
7.3.3	Electrochemical characterization.....	186
7.3.4	Template regeneration	204
7.4	CONCLUSION	208
8.0	SUMMARY	209
	PERMISSIONS.....	213
	BIBLIOGRAPHY.....	214

LIST OF TABLES

Table 1: Various rechargeable lithium batteries developed during the 1970's and 1980's [32] ..	11
Table 2: Lithium salts as electrolyte solutes [89].....	35
Table 3: Electrochemical stability of electrolyte systems: Non active electrodes.....	37
Table 4: List of ionic conductivities of Li_2O based glasses at given temperatures.....	40
Table 5: Specific capacities and molar volume changes exhibited by the different candidate elements during cycling	51
Table 6: Crystal structure, unit cell volume, formula units per unit cell, crystal volume per Si atom and theoretical density of the Li-Si system [115]	58
Table 7: Values of the circuit elements obtained after modeling the equivalent circuit using a complex non-linear least square (CNLS) method for EIS spectra obtained at the end of de-lithiation step after 1st, 100th, 200th, 300th and 400 cycles	199
Table 8: Percentage of conversion of various reactions during the MgO nanorod template synthesis and regeneration processes.....	207

LIST OF FIGURES

Figure 1: A simplified Ragone plot or diagram showing the energy domains of different electrochemical storage systems compared with the conventional internal combustion gas engine [1]	2
Figure 2: Sketch of a rocking-chair type lithium-ion electrochemical cell with graphite anode and LiMO_2 (M=Metal) cathode and reactions at anode and cathode during charge-discharge processes	13
Figure 3: Schematic illustration of relative energies of electrolyte energy gap and the electrodes	18
Figure 4: Typical polarization curve of a battery	19
Figure 5: Schematic illustration of a cylindrical Li-ion cell [38]	21
Figure 6: Schematic illustration of a Li-ion coin/button cell [38]	22
Figure 7: Schematic illustration of a Li-ion prismatic cell [38]	23
Figure 8: Schematic illustration of a Li-ion pouch cell	23
Figure 9: Unit cell constants, cell volume along with the phase diagram obtained from electrochemical results obtained on Li_xCoO_2 [42]	27
Figure 10: The electrochemical profile of $\text{Li}/\text{LiMn}_2\text{O}_4$ over the voltage range ($0 < x < 2$) [61]	30
Figure 11: Structures of orthorhombic LiFePO_4 and trigonal quartz-like FePO_4 [77]	32
Figure 12: Crystal structure of hexagonal graphite showing the AB layer stacking sequence, the unit cell, and the subdivision in basal plane and prismatic surfaces [37]	46
Figure 13: Schematic illustration of lithium intercalation into graphite structure and view perpendicular to basal plane of LiC_6 [71]	47
Figure 14: Stage formation during electrochemical intercalation of lithium into graphite [71]..	48
Figure 15: Exfoliation of graphite structure due to solvent co-intercalation [85]	49

Figure 16: Influence of dilation strain parameter upon critical size below which fracture will not occur for materials with different values of fracture toughness, expressed in MPa(sqrt m) [131].	53
Figure 17: Total capacity of Li-ion battery presented as a function of anode capacity for two cathodes having capacities of 140 mAh/g and 200 mAh/g [133].	56
Figure 18: Li-Si phase diagram [135].	58
Figure 19: Galvanostatic charge-discharge profiles for micro-Si (10 μ m) cycling at a current density of 100 mA/g in the voltage window of 0.0-2.0V (vs. Li/Li+) [136].	60
Figure 20: Variation of internal resistance in silicon anode [118].	62
Figure 21: Specific capacity vs. potential of the first 10 cycles of Si electrode. (a) and (a-1) As-received Si, (b) and (b-1) Si after 10 min of etching, (c) and (c-1) Si after 30 min of etching [66].	64
Figure 22: Schematic of SiNWs grown directly on current collector do not pulverize due to facile strain relaxation and SEM image of SiNWs [2].	72
Figure 23: Left- SEM & HRTEM images of vertically aligned carbon nanotubes (VACNTs) coated with silicon droplets; Right-Capacity plot of the heterostructures cycled at 100 mA/g between voltage range-0.02 to 1.2 V vs. Li ⁺ /Li [5].	73
Figure 24: SEM & HRTEM (top) images of the double walled SiNTs; long term stability plot of these nanotubes cycled at 12C rate [30].	76
Figure 25: High energy mechanical mill from SPEX CertiPrep.	90
Figure 26: Electrochemical cell used for electrodeposition of silicon from organic solvents.	92
Figure 27: Autoclave used for hydrothermal reactions.	95
Figure 28: Schematic of the components of a prototype coin cell configuration.	100
Figure 29: X-ray diffraction patterns of showing the phase evolution with increased milling time and progress of the mechanochemical reaction - Mg ₂ Si + SiO with different milling times [197].	109
Figure 30: X-ray diffraction patterns of the product derived following mechanochemical reduction [197].	111
Figure 31: X-ray diffraction patterns of the product derived following mechanochemical reduction followed by HCl and HF wash [197].	112
Figure 32: Raman spectra obtained on the sample obtained after 15 hours of milling followed by HCl (6N) and HF (2%) wash [197].	113

Figure 33: (a) – (c) SEM images obtained on the final product and (d) Bright field TEM image of the agglomerated final product [197].	115
Figure 34: Schematic of silicon particle size reduction obtained by chemical etching induced by the 2%HF acid wash [197].	116
Figure 35: BET surface area (m ² /g) of the powder obtained at the end of 15 h of mechanochemical reaction, after HCl (6N) wash and after HF (2%) wash steps [197].	117
Figure 36: (a) Nitrogen adsorption isotherms and (b) and pore diameter distribution obtained by BJH method on the silicon nanoparticles [197].	119
Figure 37: (a) Voltage vs. capacity plot and (b) dQ/dV plot of the high surface area (HSA) silicon particles cycled at 100 mA/g between 0.02 to 1.2 V vs. Li ⁺ /Li [197].	120
Figure 38: Capacity vs. cycle number plot of the HSA-Si particles cycled at 100 mA/g between 0.02 V to 1.2 V vs. Li ⁺ /Li [197].	121
Figure 39: Cyclic voltammogram of 0.5M SiCl ₄ in propylene carbonate with 0.1M TBACL as supporting electrolyte (scan rate: 10 mV s ⁻¹).	129
Figure 40: Chronopotentiogram for SiCl ₄ electrochemical reduction on copper at -1mA cm ⁻² for one hour	130
Figure 41: GAXRD plots of electrodeposited silicon at incidence angles of 0.1°, 0.5° & 1.5°	131
Figure 42: Raman spectra of the electrodeposited silicon using 633 nm red laser.	132
Figure 43: (a) SEM image of the electrodeposited film after 1 hour of galvanostatic reduction at -1mA cm ⁻² & EDAX spectra of the electrodeposited film after 1 hour of galvanostatic reduction at -1mA cm ⁻² .	133
Figure 44: Charge/discharge profile of electrodeposited silicon cycled at 400 mA g ⁻¹ for cycles: 1, 2, 50 and 100.	135
Figure 45: Differential capacity plot vs. voltage for the electrodeposited films at the end of 1st and 2nd cycles.	136
Figure 46: Capacity and columbic efficiency plots cycled at 400 mA g ⁻¹ between 1.2 to 0.02 V for 100 cycles.	137
Figure 47: Rate capability tests performed on the deposited films at C/4, C/2, 1C, 2C and 4C rates	138
Figure 48: SEM image of the electrodeposited film at the end of the 100th cycle showing the presence of surface pits.	139

Figure 49: Impedance spectra of the electrodeposited amorphous silicon at the end of charged state for the 1st, 2nd, 5th, 10th, 50th and 100th cycle	141
Figure 50: (a) and (b): SEM images of the vertically aligned carbon nanotubes	148
Figure 51: SEM images of Si deposited on CNTs with (a) thin film type and (b) droplet type morphologies.....	149
Figure 52: X-ray diffraction pattern of the pure CNTs and CNT/Si heterostructures with both film and droplet type morphologies.....	150
Figure 53: Raman spectra of (a) vertically aligned CNTs and (b) Si with film and droplet morphologies.....	151
Figure 54: dQ/dV plot of lithiation and delithiation of silicon for 1st, 2nd and 20th cycles.....	153
Figure 55: Cycling performance and coulombic efficiencies of CNT/Si heterostructure for thin film (open circle) and droplet (filled circle) morphologies	155
Figure 56: Voltage vs Capacity plots of CNT/Si heterostructure for thin film (solid line) and droplet (dash-dot line) morphologies.....	156
Figure 57: Schematic showing the fabrication of scribable SiCNT electrode on copper foil ...	157
Figure 58: SEM images of (a) vertically aligned carbon nanotubes grown on quartz (VACNTs), (b) VACNTs coated with silicon (SiCNT), (c) SiCNTs after being pelletized by isostatic pressing, (d) SiCNTs after being scribed and rolled and (e) HRTEM image of the silicon coated CNTs.....	159
Figure 59: Voltage vs. capacity plot of the scribed CNT/Si composite on copper foil cycled at 300 mA/g between 0.01 to 1 V vs. Li^+/Li	161
Figure 60: TGA plot of CNT/Si heterostructures performed in air from 25°C to 1000°C at a heating rate of 10°C/min.....	162
Figure 61: dQ/dV plot of the scribed CNT/Si electrodes	163
Figure 62: Long term electrochemical cycling plot of the scribed CNT/Si composite on copper foil cycled at 300 mA/g between 0.01 to 1 V vs. Li^+/Li	165
Figure 63: Rate capability plot of the scribed CNT/Si composite on copper foil cycled at 300 mA/g between 0.01 to 1 V vs. Li^+/Li	167
Figure 64: Impedance spectra of the SiCNT scribed electrodes after the de-lithiation step at the end of 1st and 50th cycles.....	169
Figure 65: (a) MgO nanorod cake obtained after calcining $Mg(OH)_2$ and (b) Hollow silicon nanotube (h-SiNT) cake obtained after leaching the MgO nanorod template using HCl.....	181

Figure 66: (a) XRD patterns of calcined MgO, core-shell MgO/Si and h-SiNTs formed after leaching MgO nanorods and (b) Raman spectra obtained on the h-SiNTs after leaching MgO nanorods.....	182
Figure 67: SEM images of (a) MgO nanorods obtained after calcination at 500C, taken 1000X (b) silicon coated MgO nanorods taken at 10,000X and (c) hollow silicon nanotubes at 10,000X (h-SiNTs) after etching MgO template using HCl (inset shows open end of the nanotube taken at 80,000X).....	184
Figure 68: (a) HRTEM image of an open ended h-SiNT; (b) High magnification of h-SiNT showing amorphous structure and (c) SAED pattern of h-SiNTs.....	186
Figure 69: Voltage vs. specific capacity plot of h-SiNTs cycled at 300 mA/g between the voltage ranges: 0.01 to 1 V vs. Li+/Li	188
Figure 70: Differential capacity plot of h-SiNTs cycled at 300 mA/g between the voltage range: 0.01 to 1 V vs. Li+/Li	189
Figure 71: Long term cycling plot of h-SiNTs cycled at 300 mA/g for 1st cycle and 2A/g for the rest of the cycles between the voltage range: 0.01 to 1 V vs. Li+/Li.....	190
Figure 72: Voltage vs capacity plots of h-SiNTs cycled at 300 mA/g for 1st cycle and 2A/g for the rest of the cycles between the voltage range: 0.01 to 1 V vs. Li+/Li.....	191
Figure 73: Rate characteristics of h-SiNTs cycled at 0.5 A/g, 1 A/g, 2 A/g, 4 A/g between the voltage range: 0.01 to 1 V vs. Li+/Li.....	192
Figure 74: SEM images of as cast (top row), after lithiation (middle row) and after de-lithiation (bottom row) of h-SiNT electrodes along with binder and Super-P at different magnifications.....	194
Figure 75: SEM images of h-SiNT electrodes along with binder and Super-P (a) before cycling and (b) after 500 charge-discharge cycles, cycled at 2 A/g between the voltage range 0.01 to 1 V vs. Li+/Li.....	196
Figure 76: Impedance spectra of the h-SiNTs obtained at the end of de-lithiation step after 1st, 100th 200th, 300th and 400th cycles. Current density applied: 2A/g, Voltage: 0.01 to 1 V vs. Li+/Li	198
Figure 77: Equivalent circuit for the interpretation of h-SiNTs (Rs: solution resistance; Ro and Ri: charge transfer resistance of inner and outer molecular layers; CPEi and CPEo: constant phase elements of the inner and outer molecular layers	199
Figure 78: FTIR spectra obtained on the cycled h-SiNTs at different stages (1st, 50th and 500 cycles). The electrodes were cycled at 2A/g between the voltage range 0.01 to 1 V vs. Li+/Li . Spectra were obtained at the end of the de-lithiation step	201

- Figure 79:** Discharge capacities of h-SiNTs using VC and FEC as additives to the LiPF₆ electrolyte cycled at 300 mA/g for 1st cycle and 5A/g for the rest of the cycles between the voltage range: 0.01 to 1 V vs. Li+/Li..... 203
- Figure 80:** XRD pattern of Mg(OH)₂ and Magnesium acetate obtained during the template regeneration process. NaOH reacted with the MgCl₂ formed during the etching reaction to precipitate out Mg(OH)₂ that is further reacted with acetic acid to form magnesium acetate 206

ACKNOWLEDGEMENTS

I would like to express my heartfelt gratitude to my advisor, Prof. Kumta, for his continuous support, encouragement and valuable suggestions that played a vital role during my research studies and it has been an honor being his student. His knowledge, insights and enthusiasm in doing research is something that I always look up to and hope to follow in my life. I am very thankful for all the opportunities that he has given me such as allowing me to present my research at various conferences, introducing me to other experts in the field and encouraging me to engage in other activities, which have in turn helped me grow both personally and professionally.

I would like to thank my committee members, Drs. Jung-Kun Lee, John Barnard, Ian Nettleship and Spandan Maiti for their discussions and feedback. Also, I would like to thank Dr. Ayyakkannu Manivannan for helping me conduct material characterization studies at NETL. Special thanks to Drs. Moni K. Datta, Abhijit Roy and Oleg Velikokhatnyi for their constant support and guidance throughout my PhD. I would further like to extend my thanks to all the post-docs, graduate students, technicians and administrative assistants in Prof. Kumta's group for their support, camaraderie and making the lab a great place to work. I am grateful to all my friends who have made my life cheerful and memorable at Pittsburgh.

I am indebted to my parents, sister and in-laws for their unconditional love, emotional support and encouragement throughout my graduate studies. I would like to express my deep

sense of appreciation to my wife, friend and partner, Madhumati, who has always been there and stood by me as I went through the vicissitudes of life. Thank you for your patience, support and for providing me with everything that I needed to focus on my research, without which I couldn't have accomplished my dissertation work. I feel fortunate and blessed for having my son, Dhruv, enter my life and fill it with love, happiness and joy. He has been a great source of inspiration to me that life needs to happen in an exuberant manner.

Words fail to express my gratitude to my Guru, Sadhguru Jaggi Vasudev, for being the guiding light at every stage and giving me the inner support whenever I needed.

1.0 INTRODUCTION

1.1 MOTIVATION

Energy, in multiple forms has not only been an essential resource for the survival of mankind, but, has also played a critical role in the advancement of human civilization for centuries. In order to cater to the needs of the growing global population and the burgeoning industrialization of the developing nations combined with the continuing growth of the developed countries, it is imperative to avail the energy sources in an efficient, environmentally friendly, affordable and sustainable manner. More than four fifths of the total energy consumed in the United States is obtained from fossil fuels such as petroleum, natural gas and coal. In addition to depleting the planet of its resources, continued fossil fuel dependence is associated with increased carbon footprint leading to eventual climate change and consequent global warming due to excessive CO_2 generation, an outcome that is dire but also rife with adverse environmental and energy consequences in nature. Consequently, harnessing energy from renewable sources such as wind, solar, oceanogenic and geothermal heat are in great demand. While being continually replenished and hence indefinite and ethereal in nature, these sources are in general, non-mobile and geographically constrained in their availability, thereby, severely limiting their wide range of applicability. On the other hand, electrochemical energy storage devices such as batteries and capacitors, wherein, stored chemical energy is used to generate electricity and fuel cells which convert electrochemical energy to electricity, all offer pragmatic solution to meet the needs of a wide range of applications such as portable electronics, electric vehicles, grid energy storage

including space exploration. A Ragone plot (**Figure 1**) can be used to compare the energy and power capabilities of these energy storage systems. While capacitors are used for high power applications, fuel cells are mainly employed as large energy generation devices. On the other hand, batteries fall in the intermediate range, thereby enabling them to be used for a broader market comprising of portable electronics including the transportation sector largely dominated by electric vehicles.

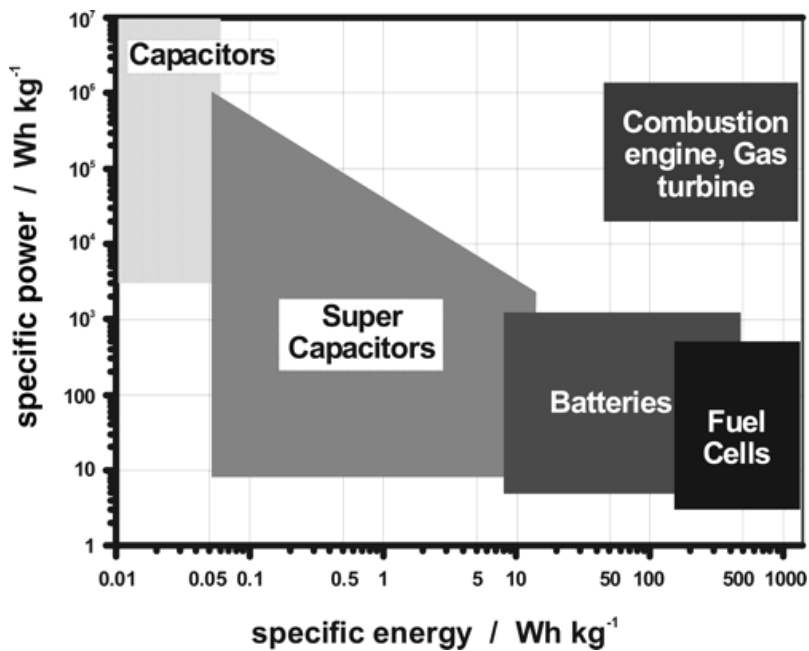


Figure 1: A simplified Ragone plot or diagram showing the energy domains of different electrochemical storage systems compared with the conventional internal combustion gas engine [1]

Among the various battery systems, lithium-ion batteries (LIBs) have become the leading choice for portable energy storage applications due to their compact design and high energy density. Sony Corporation commercialized the first LIB in 1990 and since then, they have been the flagship energy storage devices for consumer electronics such as cell phones, camcorders, laptops and portable digital assistants (PDAs), digital cameras and their recording and communication media. Over the past decade, many improvements have been made in terms of storage capacity, long term stability, and shelf life and safety, which has led the LIBs to enter into the power tools and electric vehicle market in the form of EVs (Electric Vehicles) and PHEVs (Plug in Hybrid Electric Vehicles). Despite these improvements, the ever-growing demands of the automobile market and the burgeoning economies in Asia continues to propel the impetus for the cost effective development of materials with improved cyclability, rate capabilities and especially high energy densities with the concomitant hope of also meeting the power densities. Current LIBs employ graphite with a theoretical capacity of 372 mAh/g, as the anode and $LiCoO_2$ or $LiMn_2O_4$ as the standard cathode, having energy densities in the range of 100 to 250 Wh/kg.

Analogous to graphite, the silicon element alloys with lithium at low electrode potentials (vs. Li^+/Li) to form a sequence of alloys ultimately leading to the highly lithiated phase of $Li_{22}Si_5$, rendering it as a viable anode candidate. The theoretical charge storage capacity obtained for this phase above is approximately 4200 mAh/g, which is more than ten times the theoretical capacity of graphite. However, the formation of this phase with high molar content of lithium per formula weight results in a large volume expansion (>300%) of the crystal lattice, which eventually leads to the pulverization of the material upon de-alloying. This mechanical failure upon repeated charging and discharging (alloying and de-alloying) results in loss of electrical

contact with the current collector, ultimately leading to an undesirable capacity fade and cell failure.

Several approaches have been developed to address the problem of mechanical failure due to the ensuing colossal volume changes occurring during lithium cycling. These include the use of nanosized silicon particles, active-inactive matrices, amorphous silicon composites and strain engineered 1-D dimensional nanostructures [2-12]. It is demonstrated that the nanostructured and amorphous forms provide mechanical integrity without pulverization due to the reduced number density of atoms within a nano-sized grain and the ‘free volume’ effects in amorphous silicon, which, results in better capacity retention and cycle life. The confinement of higher atom density along grain boundaries leading to grain boundary sliding prevents failure and subsequent fracture. Furthermore, it is envisaged that due to the presence of defects and absence of long range order in amorphous silicon, the volume expansion upon lithium alloying is distributed homogenously and the net effect of crack formation and propagation is thus conceived to be less catastrophic compared to crystalline silicon [8, 13, 14]. Hence, the amount of pulverization of the active material is conceived to be significantly reduced, giving rise to enhanced capacity retention and cyclability.

The work described in this dissertation is thus aimed at capitalizing on these aspects leading to the development of nanostructures of silicon such as silicon nanoparticles, amorphous silicon thin films, carbon nanotube (CNT)/Si heterostructures, and hollow silicon nanotubes (h-SiNTs) by simple, facile, high throughput and cost effective methods. These nanostructures thus exhibit high specific capacity, good cyclability, coulombic efficiency and also good rate capability. Accordingly, four distinctly unique but at the same complementary and synergistic

strategies and approaches were developed which are described in the following that essentially forms the main specific aims of this dissertation work.

Approach-1: Silicon nanoparticulate electrodes exhibit high capacity retention and cyclability compared to bulk silicon anodes [6]. The smaller particle size offers strain relaxation [15] and is mechanically more stable during lithiation and de-lithiation processes. The current methods reported for producing silicon nanoparticles include laser pyrolysis [16], laser ablation [17], gas evaporation [18, 19] and high temperature solid state reduction [20]. Although some of these methods claim to be scalable for producing silicon nanoparticles, they require expensive starting materials, complicated equipment and highly skilled labor, which ultimately increases the cost associated with their production. High energy mechanical milling (HEMM) is a relatively simple and inexpensive technique that is used to generate scalable quantities of powders in a short period of time [21]. In this approach, *SiO* and magnesium silicide (Mg_2Si) were used as the starting materials in a high energy mechanical mill to generate nano-particles of silicon via the direct mechanochemical reduction process involving the two reactants. An etching step using hydrofluoric acid (*HF*) was then employed to decrease the particle size by continuous oxidation and dissolution of the surface oxide layers formed on the silicon surface. These silicon nanoparticles (Si NPs) showed good first discharge capacity but are still limited by large first cycle irreversible losses (FIR) and high capacity fade requiring further improvements to the approaches and electrode fabrication techniques.

Approach-2: Previous work on thin films of amorphous silicon (*a-Si*) on copper substrates developed by RF magnetron sputtering showed excellent capacity retention and high specific capacity [22-24]. However, sputtering is an expensive technique and is more suitable for wafer scale production of thin films of *a-Si*. In this approach, electrodeposition has been utilized

as a simple and inexpensive technique to form thin films of *a-Si* on copper substrates [25]. The electrodeposition process was carried out in an electrolytic bath comprising of silicon halide salt dissolved in an organic solvent. A negative current was applied to a copper foil immersed in the electrolyte for 1 h to produce thin uniform films of *a-Si*. These *a-Si* films exhibited a stable reversible capacity of 1300 mAh/g for 100 cycles, which is nearly threefold greater than those of graphite based anodes.

Approach-3: Carbon nanotubes (CNTs) have attracted considerable attention due to their superior mechanical and electrical properties [26, 27]. Heterostructures containing multiwall carbon nanotubes (MWCNTs) and amorphous silicon are developed using a chemical vapor deposition (CVD) approach wherein, the CNTs act as mechanically robust supports to accommodate the mechanical stresses arising from silicon and also serve as one dimensional electronic pathway to provide for improved charge transport. To generate these heterostructures, vertically aligned carbon nanotubes (VACNTs) were first synthesized in a CVD reactor onto which, silane (SiH_4) gas was decomposed to form CNT/Si composites [28]. During the CVD process, conditions such as partial pressure of silane gas was varied to produce droplets as well as thin film morphologies of *Si* on the CNTs. Although the thin film morphology showed greater specific capacity upon electrochemical cycling, the capacity retention of the films was found to be inferior to those of droplets. This was possibly due to the free volume arising from the finite spacing between the droplets into which the silicon droplets could expand on freely, without any mechanical failure [28]. To overcome these shortcomings and generate architectures that would be able to endure the catastrophic volume expansion stresses due to alloying of *Si* with *Li* as well as sustain long cycling response, other nanoscale architectures of *Si* were also studied which led to the following approach.

Approach-4: Silicon nanotubes (Si-NTs) have attracted significant interest as a stable anode system for lithium ion batteries [12, 29, 30]. The hollow nanotube structure of silicon (h-SiNTs) accommodates the large mechanical strain generated during the charge-discharge mechanism, thereby making it less susceptible to decrepitation and pulverization [12]. However, the methods reported to synthesize the hollow silicon nanotubes involve chemical infiltration and electro-spinning [12, 30] which require expensive precursors and are also characterized by low yields. In this work, inexpensive precursors are used to produce large quantities (1g of *MgO* nanorods synthesized in a 120 ml reactor) of magnesium oxide (*MgO*) nanorods. These nanorods are used as a template onto which amorphous silicon was deposited using CVD by thermal cracking of silane gas to form *MgO/Si* composite. This core-shell structure was later dissolved in acid to leach off the *MgO* template to produce a high yield (up to 0.5 g of h-SiNTs produced with a deposition time of 15 minutes) of hollow silicon nanotubes (h-SiNTs). These h-SiNTs exhibited capacities greater than 2500 mAh/g and showed excellent capacity retention for over hundreds of cycles with a very low fade rate (~0.068 % loss/cycle).

In this dissertation, synthesis methods involving HEMM, CVD, electrodeposition and hydrothermal synthesis were studied to generate different nanostructured composites of nanocrystalline and amorphous silicon, as well as an intrinsic mixture of both crystalline modifications. These composites exhibit a strain-engineered structure to overcome the colossal volumetric changes, which usually occur in bulk crystalline silicon based anodes. Consequently, these engineered structures demonstrated high specific capacity, low first cycle irreversible (FIR) loss, good coulombic efficiency, as well as good capacity retention, and may thus serve as a viable alternative to graphite based anodes that are currently used in commercial Li-ion batteries. These approaches are all described and discussed in detail in the subsequent sections.

1.2 BACKGROUND

1.2.1 Lithium-ion Battery

A lithium-ion battery is defined as a single or multiple electrochemical cells connected either in series or in parallel where lithium (Li^+) ions shuttle between the negative and positive electrodes during charging or discharging processes, respectively. Because of their high specific capacity and overall cell voltage, lithium-ion batteries currently lead the battery market along with other competitive systems being lead acid and primary alkaline ($Zn-MnO_2$) batteries. Before their utilization and commercialization of rechargeable Li-ion systems, lithium was primarily used in the battery industry in the form of primary non-rechargeable batteries. Primary *Li* batteries consisted of lithium metal as the anode and lithium perchlorate ($LiClO_4$) salt dissolved in propylene carbonate (PC) solvent as the electrolyte. These lithium batteries were first developed in the 1970's by Matsushita (*Li-CFx*, 1973) and Sanyo (*Li-MnO₂*, 1975), and were mainly used in artificial pacemakers, LED-fishing boats, cameras and in portable memory back-up applications. *Li* metal-based battery systems used in these applications were eventually discarded following the complete conversion of chemical to electrical energy stemming from the electrochemical reactions. Considerable attention was hence directed towards developing materials and chemistries for batteries with recharging capabilities to extend their life and meet the growing needs for energy storage in a variety of applications. Attempts to develop *Li* metal based rechargeable batteries however, faced several hurdles in terms of their safe operation as the cycling caused issues with the thermal stability causing the *Li* to melt which in turn resulted in violent reactions. Li-ion based batteries, wherein, lithium (Li^+) ions shuttle between the negative and positive electrodes during charging or discharging processes, respectively, were

found to be much safer in terms of their operation. Lithium-ion batteries currently lead the battery market as they have high specific capacity and overall cell voltage. Other competitive systems include lead acid and primary alkaline ($Zn-MnO_2$) batteries. The primary alkaline batteries are popularly used in household electronics such as torch lights, radios, music players, portable electronic devices, etc. They contain zinc (Zn) metal and manganese oxide (MnO_2) as the negative and positive electrodes, respectively. As electricity (or electrons) is drawn from the electrochemical cell, zinc oxidizes to form zinc oxide (ZnO) and MnO_2 reduces to form Mn_2O_3 . The electrolyte used in these cells is primarily made of potassium hydroxide and hence the name, alkaline batteries. In lead acid batteries, the negative and positive electrodes are made of lead (Pb) and lead oxide (PbO_2), respectively. As the energy is drawn from the battery, redox reactions occur on the electrodes resulting in the formation of lead sulfate ($PbSO_4$) at both the electrodes. During the recharge process, electrons are driven externally to the negative electrode, wherein, the $PbSO_4$ is reduced to form elemental lead (Pb) and accordingly at the positive electrode, $PbSO_4$ is oxidized to form PbO_2 .

1.2.2 Rechargeable Lithium-ion batteries

The first generation of rechargeable lithium-ion batteries consisted of Li metal anode and titanium disulfide (TiS_2) as cathode delivering an energy density of 480 Wh/kg [31]. Following this, several other chemistries were developed which mainly involved lithium metal as the anode and cathodes containing conducting polymers, MoS_2 , $NbSe_3$ and vanadium oxide [32]. **Table 1** shows the various rechargeable lithium metal battery systems that were developed during 1970's and 1980's [32]. The use of pure Li metal as anode however, posed problems with dendrite

formation upon repeated cycling as this could result in a short circuit causing fire hazards, thereby bringing safety issues in the battery assembly [33]. Efforts to resolve this involved the development of an alloy for anode that was made of *Li* and *Al* instead of pure lithium metal. While this alloy improved the safety feature of the battery, its poor mechanical properties prevented it from being wound for use in cylindrical type cells. Another approach involved dioxolane based electrolytes developed by Tadiran Batteries, wherein, as a safety measure, the battery would shut down during the event of an increase in cell temperature [34]. In this case, when the cell temperatures rose to 110°C due to short circuit resulting from the dendrite formation, the dioxolane electrolyte polymerized to form a high resistance-insulating barrier. The battery therefore ceased to operate as this barrier prevented further ionic and electronic transport. Considerable research conducted to replace the *Li* metal anode and identify a material that could store *Li* as ionic Li^+ gave birth to the concept of lithium-ion (Li-ion) battery with the identification of carbon as an anode host in 1980's.

Table 1: Various rechargeable lithium batteries developed during the 1970's and 1980's [32]

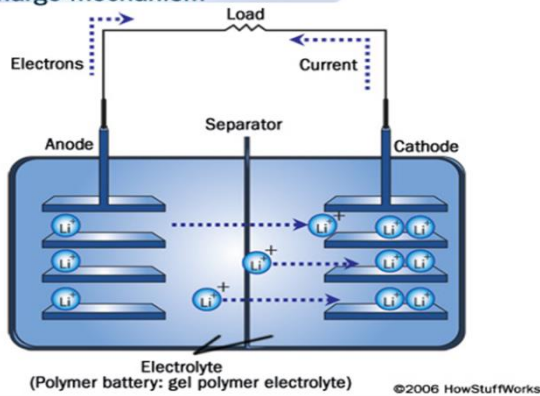
System	Voltage	Wh/kg	Wh/L	Company
<i>Li/TiS₂</i>	2.1	130	280	'78 Exxon
<i>LiAl/TiS₂</i>				'79 Hitachi
<i>Al/LiAlCl₄-SO₂/C</i>	3.2	63	208	'81-85 Duracell
<i>Li/V₂O₅</i>	1.5	10	40	'89 Tohsiba
<i>Li/NbSe₃</i>	2.0	95	250	'83-'86 Bell Lab
<i>LiAl/Polyaniline</i>	3.0	-	180	'87 Bridgestone
<i>LiAl/Polypyrrolle</i>	3.0	-	180	'89 Kanebo
<i>LiAl/Polyacene</i>	3.0	-	-	'91 Kanebo/Seiko
<i>Li/MoS₂</i>	1.8	52	140	'97 MoLi
<i>Li/CDMO(Li_xMnO₂)</i>	3.0	-	-	'89 Sanyo
<i>Li/Li_{0.3}MnO₂</i>	3.0	50	140	'89 Tadiran
<i>Li/VO_x</i>	3.2	200	300	'90 HydroQuebec

1.2.3 Rocking Chair cells

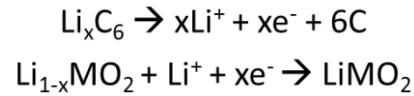
Graphite based anodes were developed in the early 1980's wherein graphene layers were used to intercalate Li^+ ions at low electrode potentials to address the undesirable Li dendrite formation that occurs during the recharging process [35]. At the same time, lithium transition metal oxides ($LiMO_2$, $M=Co, Ni, Mn$), particularly, $LiCoO_2$, were developed wherein Li^+ ions are extracted reversibly at high electrode potentials giving rise to a higher overall cell voltage [36]. **Figure 2**

shows the schematic of a typical lithium-ion battery with graphite anode and a transition metal oxide cathode along with their reactions during the charging and discharging processes. During the discharge process, *Li* spontaneously oxidizes from the intercalated graphene layers (LiC_6) to form Li^+ ions and the electrons generated travel through the external circuit providing electrical energy to the load applied. On the other electrode, the cathode ($Li_{1-x}MO_2$) takes up the electrons and the accompanying Li^+ ions through the electrolyte, to form a lithium rich transitional metal oxide ($LiMO_2$). During the charging process, the electrons are driven by an external source from the cathode where Li^+ ions de-intercalate from $LiMO_2$ and insert into the graphite layers on the anode. The movement of Li^+ ions between the electrode hosts results in an intercalation phenomenon thus giving birth to the ‘rocking chair’ type lithium-ion batteries. The overall voltage of these cells is the difference between the electrochemical potentials of the component anode and cathode materials. Also, in a typical ‘rocking chair’ cell, the transfer of the Li^+ is facilitated by an electronically non-conducting electrolyte acting as an ionic transport medium between the anode and cathode. Sony Corporation commercialized the first rocking chair battery using graphite as the anode and $LiCoO_2$ as cathode. Ever since, there has been significant interest in the development of low cost and high energy density anode and cathode materials for lithium-ion battery applications.

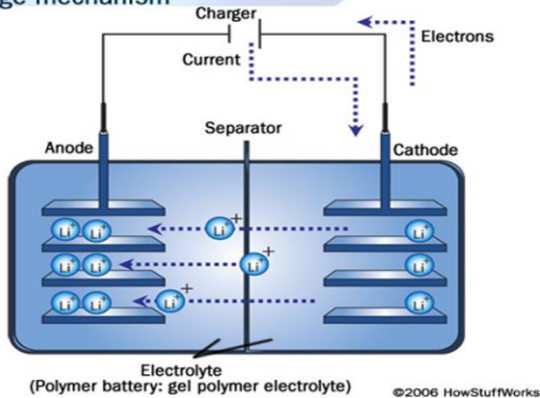
**Lithium-ion rechargeable battery
Discharge mechanism**



Discharge Process



**Lithium-ion rechargeable battery
Charge mechanism**



Charge Process

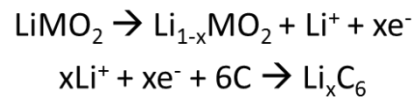


Figure 2: Sketch of a rocking-chair type lithium-ion electrochemical cell with graphite anode and LiMO_2 (M=Metal) cathode and reactions at anode and cathode during charge-discharge processes

1.2.4 Theoretical Capacity, Energy density and Differential capacity

There are several parameters that need complete understanding in order to fully characterize and compare the different electrochemical energy storage systems. Amongst them, theoretical capacity, energy density and differential capacity are widely used for practical applications where design considerations are important for selecting the anode or cathode materials.

Theoretical Capacity: As outlined in the earlier sections, in a lithium-ion battery, charge in the form of Li^+ ions is stored in an electrode and moved across the electrode/electrolyte

interface during the charge and discharge processes. Specific capacity is the total amount of charge (in coulombs or A.h) that can be stored in the form of transportable Li^+ ions per unit weight (grams) of the material. Theoretical capacity of a material (either anode or cathode) is a quantity (usually expressed in mAh/g or mAh/cm³) that defines a material's maximum ability equated to the molar equivalent of the compound to store Li^+ ions during the charge/discharge process.

$$\begin{aligned} \text{Gravimetric Capacity} &= \frac{N \times F}{M} \left(\frac{\text{Coulomb}}{g} \right) \\ &= \frac{N \times F}{3.6M} \left(\frac{\text{mAh}}{g} \right) \end{aligned}$$

$$\text{Volumetric Capacity} = \text{Gravimetric Capacity} \times \text{density}$$

$$= \frac{N \times F}{3.6M} \times \delta \left(\frac{\text{mAh}}{\text{cm}^3} \right)$$

N = moles of transportable Li^+ ions (= no. of electrons) per each mole of material

F = Faraday's constant (= 96487 Coulomb or 26.8 Ah)

M = Formula weight of the material (g/mol)

δ = Density of the material (g/cm³)

Energy density: It is defined as the total energy that can be stored during the charging process or the energy that can be utilized during the discharging process. In other words, it is the work done to move a charge (specific capacity, Q) across the voltage difference (V_{avg}) between

the two terminals of the battery. The average voltage (V_{avg}) usually depends on the degree of intercalation (x_m) of Li^+ ions or the amount of Li alloyed with the compound comprising the electrode. Therefore, the energy density of a battery is estimated using the formula below:

$$\text{Energy Density } \varepsilon = \frac{N \times F}{M} \int_0^{x_m} V dx \left(\frac{Wh}{kg} \right)$$

x_m = the maximum degree of insertion of lithium ions or the amount of Li alloyed with the compound.

Differential capacity ((dQ/dV)): Differential capacity (dQ) is an important electrochemical characterization parameter, as it provides vital information on the several reactions that occur during the discharging and charging of a battery. Diffusion controls the electrochemical reactions that occur at the electrodes during the charge/discharge process. Two main testing methods namely, galvanostatic and potentiostatic are typically used to characterize the electrochemical properties of the assembled half-cells or full-cells.

In a potentiostatic testing method, a constant voltage is applied across the cell and the resulting current is measured. In a galvanostatic testing method, a constant current is applied to the electrode and the resulting change in voltage across the cell due to various faradaic and non-faradaic processes is measured. A voltage plateau is usually observed at electrode potentials wherein two phases co-exist as a result of lithium intercalation or alloying reaction. There is an insignificant change in the potential with time during this reaction following the Gibbs phase rule ($F=C-P+2$) and the voltage profile appears flat in the two phase region. Using the equation below, a very high value for a change in charge with respect to voltage or dQ/dV can be obtained

especially when there is a phase change indicative of the onset potential and the potential of completion of the phase transformation reaction. Accordingly, the peaks obtained from the (dQ/dV) vs. voltage provide valuable information on the various electrochemical reactions that occur during the testing methods.

$$I = \left(\frac{dQ}{dt} \right) = \left(\frac{dQ}{dV} \right) \times \left(\frac{dV}{dt} \right)$$

1.2.5 Design considerations for battery materials

The basic principle of a rechargeable battery is the conversion of chemical energy to electrical energy during the discharge process and vice versa during the charge process. The pertinent electrochemical reactions responsible for the energy conversion occur at the site of the electrode-electrolyte interface. The electrolyte acts as a filter for the passage of Li^+ ions between the electrodes, but does not allow the flow of electrons. During the discharge process, *i.e* when the electrical energy is utilized by connecting the battery terminals to an external load, oxidation reaction occurs at the anode wherein electrons are generated. These electrons travel through the external circuit, pass through the load and arrive at the cathode where they are consumed for the reduction reaction. Hence, the anode is termed as the negative electrode and cathode is termed as the positive electrode. The Li^+ ions also travel from anode to cathode inside the battery to balance the charge. During the charging process, the load in the external circuit is replaced with a power supply where the electrons are drawn from the cathode and driven across the external

circuit to the anode. The anode takes the electrons where the reduction reaction converts the electrical energy to chemical energy, which is again available during the next discharge process.

When the external circuit is open or when no current is drawn from the cell, the electrostatic driving force in the opposite direction balances the chemical driving force on the mobile Li^+ species in one direction. The chemical driving force, which is the difference in the chemical potentials of the anode and cathode, is expressed using the standard Gibbs free energy change per mole of reaction represented as ΔG_r° .

$$\Delta G_r^\circ = \mu_a - \mu_c$$

The equivalent available electrostatic free energy per mole is given by $-nFE^\circ$, where n represents the number of electrons of charged species transferred by per mole of reactants and E° represents the standard electrical potential difference between the two electrodes in equilibrium.

$$\Delta G_r^\circ = -nFE^\circ$$

$$-nFE^\circ = \mu_a - \mu_c$$

$$E^\circ = \frac{\mu_a - \mu_c}{-nF}$$

Hence, it is apparent to increase the battery's overall capacity and cell voltage in order to obtain higher energy densities. As mentioned in the previous section, the overall cell voltage depends on the intrinsic material properties (chemical potential, μ^{Li}) of the anode and cathode. However, it is also essential that the materials chosen be such that difference in the chemical potentials does not adversely affect the electrochemical stability of the electrolyte. **Figure 3** shows the Fermi energy levels of the anode, cathode and electrolyte, respectively [37]. The Fermi energy level of the cathode (E_c) should be above the highest occupied molecular orbitals (HOMO) of the electrolyte to avoid any oxidation by the cathode. Similarly, the Fermi energy

level of the anode should be below the lowest unoccupied molecular orbitals (LUMO) of the electrolyte to prevent any reduction reaction due to anode. In summary, it is extremely important that the anode and cathode materials be selected or designed such that the difference in redox energies ($E_a - E_c$ or eV_{oc}) lie within the band gap (E_g) of the electrolyte thereby indicative of a stable electrochemical system.

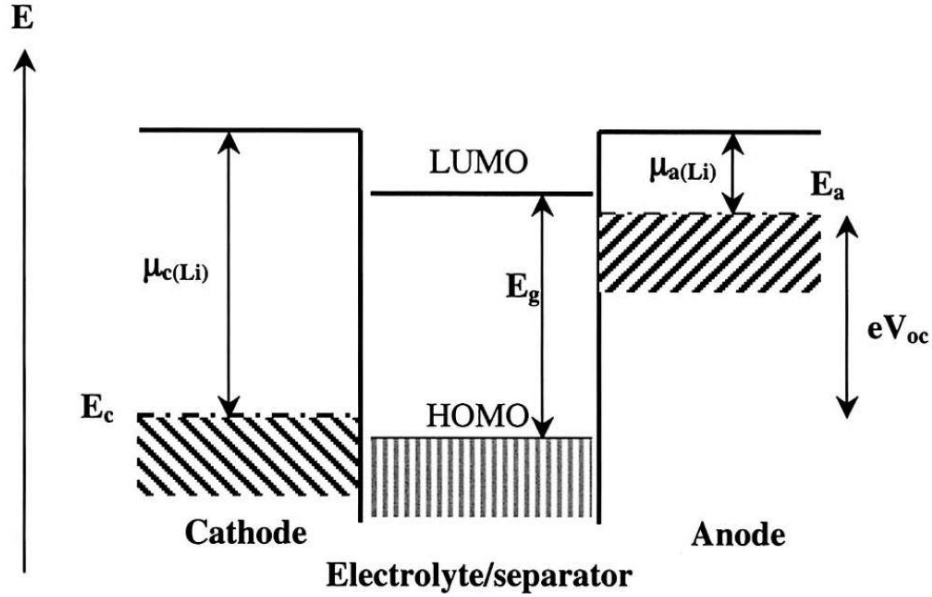


Figure 3: Schematic illustration of relative energies of electrolyte energy gap and the electrodes

E° is also expressed as the open circuit voltage E_{oc} at thermodynamic equilibrium when no current passes through the electrochemical cell. However, during practical operations, the resistance of the electrolyte to ionic transport at the electrode-electrolyte interfaces and electrical resistance between the individual cell components give rise to cell impedance. The internal resistance of the electrochemical cell is given by the following equation:

$$R = R_{el} + R_{int} + R_e$$

$$R_{el} = \left(\frac{L}{\sigma_i A} \right)$$

Where R_{el} represents the electrolyte resistance, R_{int} is the interfacial resistance at the electrode-electrolyte interface for the charge transfer reactions and R_e represents the sum of internal contact resistances arising from all the individual cell components. This resistance arising from the electrolyte (R_{el}) is governed by the thickness of the separator (L) or the effective distance between the anode and cathode, the ionic conductivity of the electrolyte (σ_i) and the effective area between the electrodes (A). Therefore, when a load is applied or current is drawn from a battery, there is a drop in the open circuit potential due to the internal impedances/resistance, which is given by the following equation:

$$E = E_{oc} - IR$$

The difference in the thermodynamic equilibrium voltage and the output voltage as a function of current is also known as polarization and the voltage-current characteristic curve is termed as polarization curve. **Figure 4** shows a typical polarization curve during the discharge process. The shape of the curve is determined by the kinetic limitations of the reactions and other processes that occur during the battery operation. The slope of the curve varies according to the current applied and can be divided into three distinct regions as shown in the **Figure 4**.

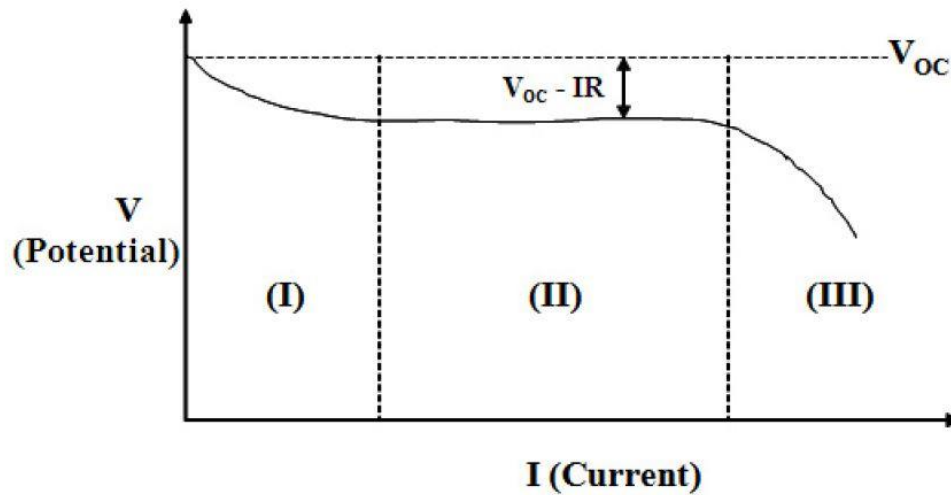


Figure 4: Typical polarization curve of a battery

In region-I, there is a rapid decrease in voltage with current and is referred to as activation polarization wherein, the impedances are due to the kinetics involved with the charge-transfer reactions that occur at the electrode-electrolyte interface of the cathode and anode. Following region-I, there is a slight change in voltage in region-II which is known as ohmic polarization. This region encompasses all the resistances: electrolyte resistance, resistance due to current collectors and other cell components, resistance between the active materials present in the electrode, and the resistance between the current collector foil and the electrode coating. Following this region, there is a rapid decrease in voltage known as concentration polarization as shown in the region-III. The electroactive species at the electrode-electrolyte interface is continuously consumed by the discharge reaction process and needs to be replenished from the bulk. At higher current densities, the limitations due to diffusion of species become more prominent and hence require an electrolyte with high ionic conductivity to transport the ions to the interface more rapidly in order to sustain the charge-transfer reactions. Electrode materials with improved electronic conductivity could also aid this process thereby facilitating the transport of electrons and ions thus leading to lower charge transfer resistances.

1.2.6 Lithium-Ion battery configurations

Different applications require the energy storage device or the battery pack to be designed according to a certain dimensions and geometry. The commercially available Li-ion batteries are usually available in the following formats:

1.2.6.1 Cylindrical cell

The cylindrical cell is easy to manufacture and exhibits good mechanical stability. It is currently the widely used format for Li-ion batteries. The dimensions can vary but the most common cylindrical Li-ion cell is the 18650, wherein, the first two digits ‘18’ represent the diameter of the cell in millimeters and the rest of the digits, ‘650’ denote the length of the cell, in tenths of a millimeter (**Figure 5**). The cylindrical cells are commonly used in power tools, communication devices, laptops and other wireless communication devices.

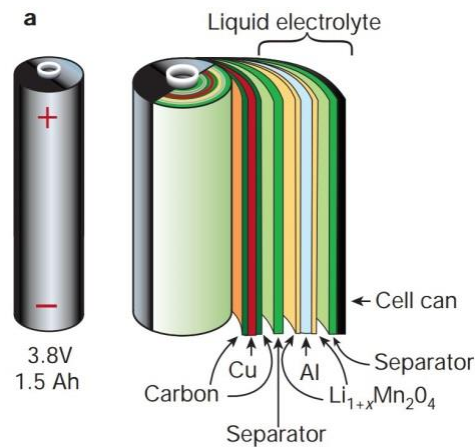


Figure 5: Schematic illustration of a cylindrical Li-ion cell [38]

1.2.6.2 Button cell/Coin cell

These cells have a relatively flat geometry and are very compact. They may be stacked to obtain higher voltages. The most commonly used button/coin cell is the CR 2032, wherein, the first letter C represents lithium based chemistry, the second letter R indicates the geometry is round. The first two numbers ‘20’ refers to the diameter of the cell in millimeter and the height of the cell is given by the latter two numbers, ‘32’; expressed in tenths of a millimeter (**Figure 6**). The

button cells are widely used in applications such as wristwatches, biomedical devices, industrial instruments, and for all research study purposes.

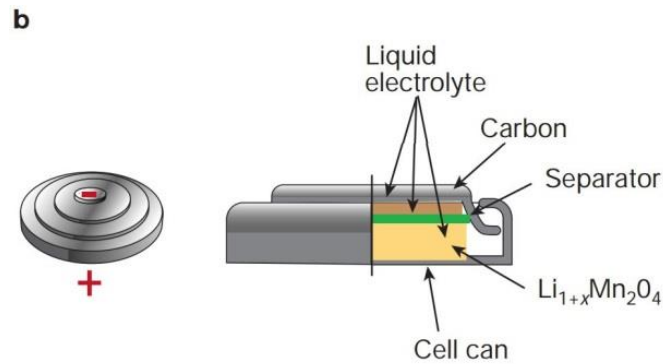


Figure 6: Schematic illustration of a Li-ion coin/button cell [38]

1.2.6.3 Prismatic Cell

The prismatic cell mainly has a flat geometry with very thin pack sizes. They are predominantly used in cell phones and PDAs. The dimensions of the prismatic cell vary according to the product specifications and the manufacturer (**Figure 7**). Despite their elegant design and efficient packaging, these batteries have lower energy densities and mechanical stability compared to the cylindrical cells.

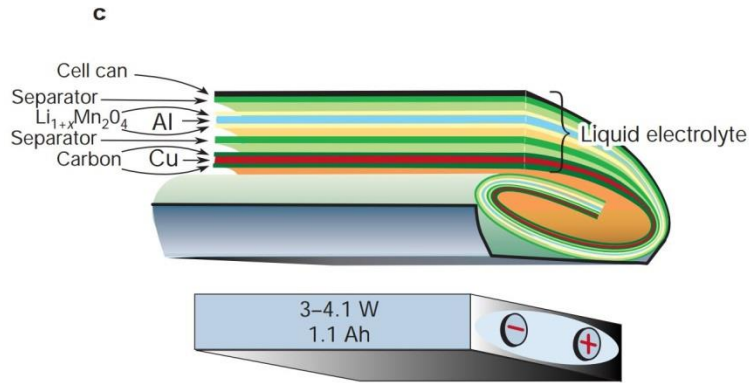


Figure 7: Schematic illustration of a Li-ion prismatic cell [38]

1.2.6.4 Pouch cell

In the pouch cells, both the electrodes are enclosed in a pliable and heat sealable foils; and the electrical contacts are usually welded and sealed inside a pouch (**Figure 8**). These cells are used in mobile phones, military devices and manufacturing larger battery modules for electric vehicles in auto industry.

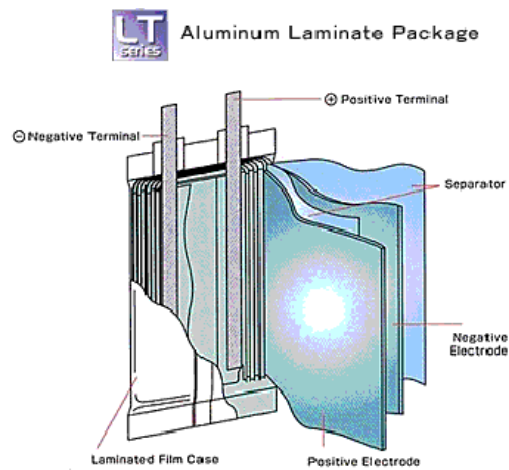


Figure 8: Schematic illustration of a Li-ion pouch cell

The complete battery pack or module employed for practical applications contains several components such as the electrode materials, separators, electrolyte, current collectors, battery management system (BMS) and packaging material. In this dissertation, only the components responsible for electrochemical charge transfer processes such as the anode, the cathode and the electrolyte will be discussed.

1.2.7 Cathode materials

Cathode materials used in commercial Li-ion batteries are usually either layered compounds such as $LiCoO_2$, $LiNiO_2$; or manganese based spinels – $LiMn_2O_4$; or olivine based $LiFePO_4$ compounds. The principal function of a cathode material is to serve as a host to accommodate charge in the form of intercalated Li^+ ion species. However, for commercial applications that require high energy density and safety, there are several other requirements that a material must meet in order to be employed as cathode and they are listed below:

- i. Have high Gibbs free energy for the discharge/lithiation reaction resulting in a high overall cell voltage for increased energy density.
- ii. Show good reversibility of the reactions with Li^+ and transition metal (M^{n+}) ion and is capable of oxidizing and reducing effectively during the charge and discharge processes, respectively.
- iii. Able to reversibly intercalate maximum number of Li^+ with the host structure, giving rise to high specific capacity.
- iv. Exhibit faster coupled diffusion of Li^+ ions and good electronic conductivity of the host material for high rate capability.

- v. Demonstrate good structural stability in the voltage range and also beyond, in the event of an under-charge or over-charge phenomena.
- vi. Exhibit good chemical stability in different electrolytes that are used in Li-ion batteries.
- vii. Incur lower production cost.
- viii. Incur lower toxicity, be environmentally benign and exhibit good recyclability.

The first class of cathode materials developed for rechargeable Li-batteries comprised of dichalcogenides and trichalcogenides such as titanium disulfide (TiS_2), vanadium diselenide (VSe_2), niobium triselenide ($NbSe_3$) and molybdenum disulfide (MoS_2). In the case of TiS_2 , the lattice consists of a hexagonal closed pack structure with Ti ions located in the octahedral sites along with alternating sulfur sheets, resulting in an ABAB stacking sequence. The individual TiS_2 sheets are held together by weak van der Waals forces and are separated by a *gallery space*, where guest species can reside. The Li^+ species can occupy this space between the alternating sulfur sheets enabling them to reversibly intercalate to form a single phase Li_xTiS_2 structure ($0 \leq x \leq 1$), resulting in good cyclability. During the 1977-79 period, Exxon capitalized on this technology to commercialize their button cells made of TiS_2 cathode coupled with $LiAl$ anodes for use in watches and other small electronic devices. Other chalcogenides such as VSe_2 has also been found to be electrochemically active cathode material, but undergoes a two-phase behavior to form Li_2VSe_2 [39]. The initial two-phase region is between VSe_2 and Li_xVSe_2 followed by another two-phase region between Li_xVSe_2 and $LiVSe_2$; and the final two-phase region is between $LiVSe_2$ and Li_2VSe_2 . Despite the two phase formation, the octahedra of the newly formed phases undergo minimum deformation, thus enabling VSe_2 cathodes to undergo reversible cycling.

Group VI sulfides such as MoS_2 are not expected to be electrochemically active, but when the molybdenum coordination is converted from trigonal prismatic to octahedral through the insertion of one Li per mole of MoS_2 , it can be used as an effective cathode material, and was commercialized by MoliEnergy in 1980. Another class of materials, trichalcogenides such as $NbSe_3$ were identified as cathode materials at The Bell Laboratories[40]. It was found that $NbSe_3$ reversibly reacted with lithium to form electrochemically active Li_3NbSe_3 , but however exhibited low operating voltages, low rates and suffered from severe degradation problems[41].

1.2.7.1 $LiCoO_2$

The current widely used $LiCoO_2$ in Li-ion battery applications was first reported by Goodenough in 1980 as a potential cathode material, bearing a similar layered structure to the earlier developed chalcogenide based cathodes. [36]. $LiCoO_2$ belongs to the $R\bar{3}m$ structure where only 0.5 Li per Co could reversibly be cycled in $Li_{1-x}CoO_2$, giving rise to a theoretical capacity of ~130 mAh/g [36]. Additionally, it also exhibits a high operating voltage (3.1-4.2V) and a smaller change in the discharge voltage during the lithium extraction/insertion [36], making an attractive candidate for high energy density cathodes. The high cell voltage in $LiCoO_2$ arises from the high chemical potential of lithium μ^{Li+} that is associated with the $Co^{3+/4+}$ redox couple. However, it also suffers from certain drawbacks. Upon extracting more lithium ($x>0.5$) when charged beyond 4.2 V, the layered structure present in $LiCoO_2$ undergoes structural distortion from hexagonal to monoclinic as shown in **Figure 9** [42]. Additionally, cobalt dissolution also occurs when charged beyond 4.2 V [43].

This structural degradation and chemical instability results in a capacity fade, thus limiting only half of Li ions to be extracted per mole of $LiCoO_2$. However, several approaches

have been developed to overcome these challenges that include coating the $LiCoO_2$ surface with oxides such as Al_2O_3 , ZrO_2 and TiO_2 [44-47]. These coatings served as a protective layer that prevented the dissolution of Co, arising from its interaction with acidic species such as HF present in the electrolyte. Furthermore, the higher cost and toxic nature of cobalt has encouraged the research community to explore other alternative cathode materials that exhibit higher capacity, have lower cost; and are more environmentally friendly.

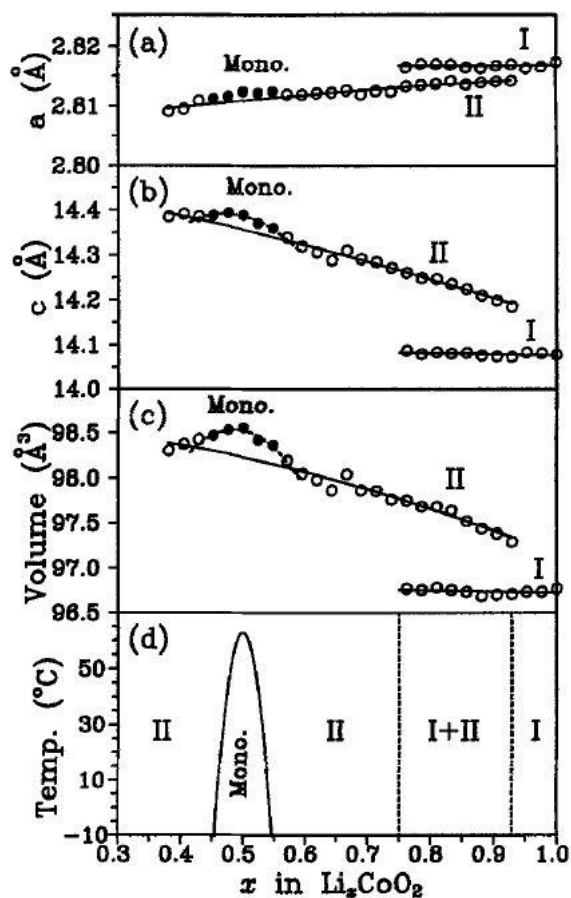


Figure 9: Unit cell constants, cell volume along with the phase diagram obtained from electrochemical results obtained on Li_xCoO_2 [42]

1.2.7.2 LiNiO₂

Since the introduction of *LiCoO₂*, several other transition metal oxides have been extensively studied as potential cathode systems. *LiNiO₂*, which is another layered compound belonging to the same family of *LiCoO₂*, generated great interest due to its higher reversible capacity and lower cost and toxicity compared to *Co* [48, 49]. However, synthesizing defect free *LiNiO₂* poses a great challenge as the Ni^{3+} ions tend to migrate from the *Ni* plane to *Li* plane [50]. This migration in the defective *LiNiO₂* causes non-stoichiometry and promotes the pinning of *NiO₂* layers together. This leads to a reduction in the lithium diffusion coefficient, large polarization leading to large capacity fade and poor rate capability. Additionally, *LiNiO₂* is found to undergo Jahn-Teller distortion or tetragonal structural distortion due to the low spin of $Ni^{3+} : d^7 (t_{2g}^6 e_g^1)$ ion and irreversible phase transformations occurring during electrochemical cycling [51-53]. Doping through substitution of *Ni* with other cations such as *Co* and *Mg* addresses some of these challenges. For example, while substituting some of the *Ni* sites with *Co*, results in the suppression of Jahn-Teller distortion [53], substituting *Ni* with *Mg* ion in the rhombohedral site results in a $Li_{1+x}NiMg_xO_{2(1+x)}$ phase that exhibits no phase transformations and good thermal stability, and brings about significant improvement in capacity retention [54].

1.2.7.3 Spinel based cathodes

Lithiated manganese spinel compound, *LiMn₂O₄* was first developed by Thackeray *et al.* and showed great promise as a cathode material due to its advantages such as lower cost, environmentally benign in nature and potentially greater safety in handling in comparison to *LiCoO₂* [55, 56]. *LiMn₂O₄* belongs to the $Fd\bar{3}m$ structure wherein *Mn* and *Li* occupy the 16d

octahedral and 8a tetrahedral sites, respectively. As a result, the Li^+ ion diffusion occurs in a three dimensional fashion as opposed to a two dimensional path, typically observed in the case of the layered compounds. This attribute has made it an attractive candidate for making high power Li-ion batteries used in electric vehicles. Despite its advantages in terms of cost, high power and safety, spinel compounds suffer from problems such as high capacity fade associated with non-stoichiometry, chemical and structural instability [57]. The discharge/charge reaction proceeds in two steps in the case of $LiMn_2O_4$ as shown in the **Figure 10** [58-61]. During the charging process, the lithium extraction first occurs at 4V from the 8a tetrahedral sites to form the λ - MnO_2 structure where the initial cubic symmetry is maintained, but with a decrease in lattice parameter due to the oxidation of Mn^{3+} to Mn^{4+} . The second step of lithiation occurs at 3V, wherein, during charging, the additional Li occupy the empty 16c octahedral sites. The second step causes the Li , which is already present in the 8a tetrahedral sites to occupy the octahedral $16c$ sites to minimize the electrostatic repulsion. This results in the formation of a tetragonally distorted structure from the original cubic phase, and this phenomenon is attributed to the Jahn-Teller distortion due to the high spin of Mn^{3+} . This structural transformation causes strain in the particles, leading to rapid capacity fade. Some of these problems have been overcome by doping elements such as Co , Ni , Fe , Mg , Cr to improve its cyclability [62-64]. Metal oxide coatings such as V_2O_5 and Al_2O_3 have also been explored to prevent the dissolution of Mn ions from the spinel cathode into the electrolyte resulting in improved electrochemical performance [37, 63, 65].

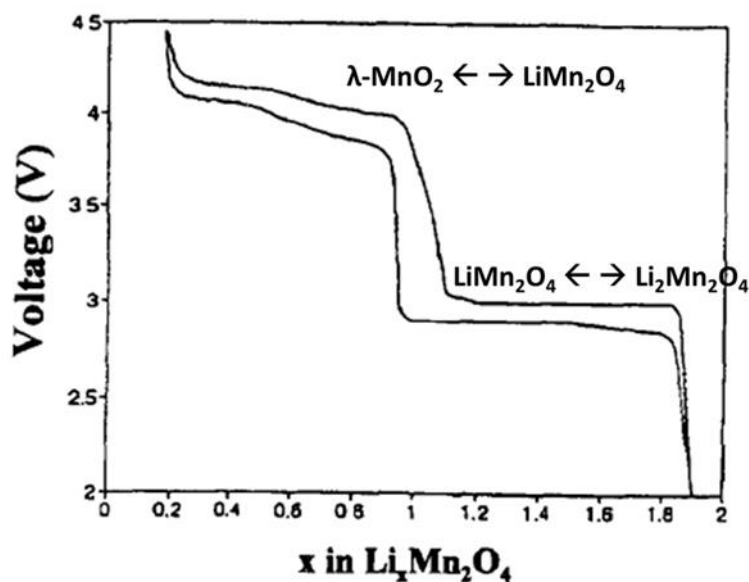


Figure 10: The electrochemical profile of $Li/LiMn_2O_4$ over the voltage range ($0 < x < 2$) [61]

1.2.7.4 Other layered oxide cathodes

Mn based layered oxides have attracted great interest as cathode materials due to their advantages of manganese chemistry as well as the high capacity from the layered structures. $LiMnO_2$ is an example of such manganese based oxides that is formed in the layered structure similar to $LiCoO_2$ and $LiNiO_2$ and has a theoretical capacity of ~ 285 mAh/g. However, the structure of the $LiMnO_2$ compound depends upon the preparation method. While the thermodynamically stable orthorhombic structure of $LiMnO_2$ is prepared by high temperature synthesis, the metastable layered $LiMnO_2$ is usually obtained by soft chemical routes such as ion exchange and hydrothermal processes. For example, Bruce *et al.*, prepared layered $LiMnO_2$ from $NaMnO_2$ by ion exchange process with $LiBr$ [66]. Despite its high capacity, it undergoes a large capacity fade due to the irreversible phase transformation of the layered to the spinel structure

during the charging process [67, 68]. Here, upon reaching the stoichiometry of $Li_{0.5}Mn$, the Mn and Li ions move rapidly to the tetrahedral sites surrounded by Li vacancies due to the stabilization gained by charge disproportionation of Mn^{3+} to Mn^{2+} (tetrahedral) and Mn^{4+} (octahedral) [69, 70]. Accordingly many studies have been done to stabilize the layered structure of $LiMnO_2$ and these mainly involve doping with elements such as Co , Ni , Cr etc [70-73]. Recently equal amounts of the three transition metals (Ni , Mn and Co) used to form $Li(Ni_{1/3}Mn_{1/3}Co_{1/3})$, commonly referred to as NMC has exhibited a high capacity of 200 mAh/g [72] and good rate capability [74, 75].

1.2.7.5 Olivine based cathodes

More recently, cathodes containing olivine compounds comprising of $LiFePO_4$ have become very popular because of their excellent attributes such as high capacity, excellent reversible extraction of Li^+ ions to form $FePO_4$, lower cost and environmentally benign [76]. The olivine structure consists of 1-D channels, which enables the Li^+ ions to diffuse easily during the intercalation/de-intercalation processes. Upon charging, the orthorhombic $LiFePO_4$ transforms into $FePO_4$ which has a trigonal quartz like structure (**Figure 11**) [77]. This occurs through the formation of a two phase region ($LiFePO_4$ - $FePO_4$) and thus exhibits a flat discharge curve at 3.4 V. When compared to Li-ion batteries made of $LiCoO_2$ as cathodes, $LiFePO_4$ exhibits much higher capacities of approximately 170 mAh/g at a discharge voltage around 3.4 V. Also, the minimal structural change involving the $FePO_4/LiFePO_4$ transition provides excellent stability for hundreds of cycles. However, due to small polaron hopping, $LiFePO_4$ exhibits lower electronic conductivity (10^{-8} to 10^{-10} Scm^{-1}) and Li diffusivity (1.8×10^{-14} cm^2s^{-1}), which limits its use in high power applications [78]. Several methods were developed to address the challenge of electronic conductivity and diffusivity by reducing the particle size [71, 79, 80], use

of metal doping [81-83] and carbon coatings [84-86]. Conductive coatings of carbon and doping with aliovalent metal ions have shown to improve its conductivity and as result, have been successfully used to intercalate and de-intercalate Li^+ ions at ultra-high rates [81, 84, 87, 88].

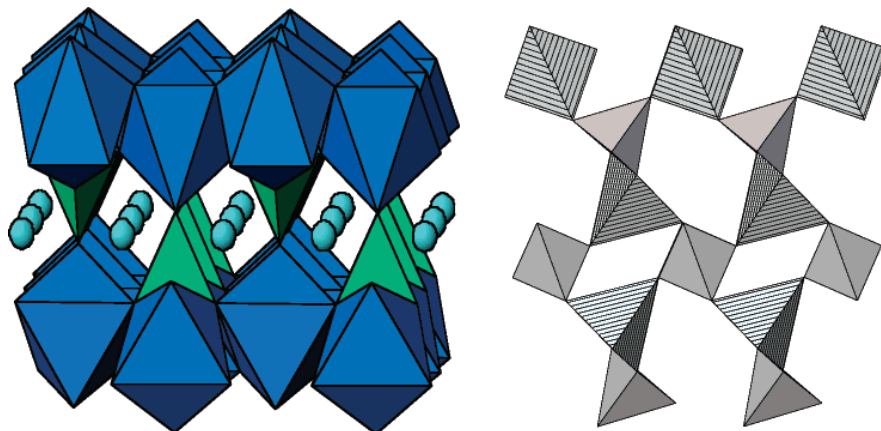


Figure 11: Structures of orthorhombic $LiFePO_4$ and trigonal quartz-like $FePO_4$ [77]

1.2.8 Electrolytes

An electrolyte is an important component of a lithium-ion battery as it serves as the medium for the transfer of Li^+ ions during the charge-discharge process. It typically contains one or more salts of lithium, which serves as the source for the mobile Li^+ ion species; and two or more mixtures of solvent. The electrolyte is present between the anode and cathode of the electrochemical cell and is in constant contact with the electrode materials. Therefore, it is important to select the electrolyte that is compatible with the electrode materials, working conditions and power requirements for the intended application. Ideally, the electrolyte used in lithium-ion batteries should:

- i. Have high Li^+ ion conduction to lower the internal cell resistance and be electrically insulating to prevent self-discharge and/or cell short circuiting.

- ii. Exhibit wide electrochemical window to that prevent the decomposition of electrolyte at very high voltages (>4 V).
- iii. Exhibit good electrochemical stability to prevent undesirable reactions on cathode or anode surface.
- iv. Be inert to other components of the battery such as separators, current collectors and other packaging materials.
- v. Have low melting and high boiling points.
- vi. Exhibit low toxicity for industrial handling, production and recycling.
- vii. Have lower production costs to compete.

The different kinds of electrolytes categorized as non-aqueous liquid electrolytes, solid electrolytes and polymer/gel based electrolytes will be discussed in this section.

1.2.8.1 Non-aqueous liquid electrolytes

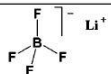
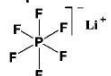
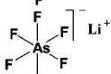
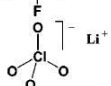
Because of their high ionic conductivity, the non-aqueous liquid electrolytes are widely used in current commercial applications such as portable electronics and electric vehicles, where high current densities are typically used. These electrolytes are usually composed of a lithium salt dissolved in an appropriate solvent mixture. The lithium salt should however have (a) good solubility in a wide temperature range (usually between -20°C and 50°C), (b) chemical inertness, *i.e.*, both the ions in the salt should not react with other components of the battery and solvent; and (d) stability, *i.e.*, they should not decompose at high voltages, especially on the cathode during charging to voltages greater than 4V. **Table 2** shows the various lithium salts used in commercial Li-ion batteries, along with their physical properties and conductivities [89]. Simple

lithium salts such as $LiCl$ and LiF cannot be used as Li salts in the electrolyte because of their poor solubility due to the small ionic radius of Li^+ ion. Instead, complex anion based salts such as in the case of $LiPF_6$, where an anion core and a stabilizing Lewis acid are usually employed. The formal negative charge of F^- is well distributed by the Lewis acid complex - PF_5 , resulting in good solubility and lower melting point [89].

During the charging or discharging process, the electrolyte decomposes to form an electronically insulating but ionically conducting layer called solid electrolyte interphase (SEI) on the electrode surface. Though this phenomenon is undesirable, as it results in the irreversible consumption of Li , it also serves as a protective layer on the electrode surface thus serving such that further electrolyte decomposition is prevented. $LiPF_6$ is currently the most widely used lithium salt in Li-ion batteries because of its ability to form stable SEI layers on the electrodes and current collectors. Other commonly used electrolytes contain lithium salts such as $LiBF_4$, $LiClO_4$ and $LiAsF_6$, dissolved in various organic solvents [90]. Perchlorate salts such as $LiClO_4$ has attracted a lot of attention due to its high conductivity (9 mScm^{-1} in EC/DMC at 20°C) [91] and ability to form a stable SEI layer compared to that of $LiPF_6$ and $LiBF_4$ [92-94]. Additionally, they are less hygroscopic and easy to handle. However, due to the high oxidation state of chlorine (+7), the perchlorate ion reacts violently with organic species at high temperatures and high voltages, making it unfavorable for practical applications [95, 96]. $LiBF_4$ is another lithium salt, which exhibits good performance for a wide range of temperatures ($< -10^\circ\text{C}$ and $> 50^\circ\text{C}$). Here, the BF_4^- ion has a very high mobility but has a low dissociation constant and results in moderate ionic conductivity [97, 98]. Although $LiPF_6$ is currently the most widely used electrolyte for commercial applications, another lithium salt of chelated borate ion [bis(oxalate) borate], $LiBOB$, is gaining importance due its higher electrochemical stability [99].

For example, *LIBOB* added to the electrolyte mixtures shows the formation of stable SEI layer in the case of graphite anodes [100] and also seem to stabilize the high voltage spinels such as $LiNi_{0.5}Mn_{1.5}O_4$ [101].

Table 2: Lithium salts as electrolyte solutes [89]

Salt	Structure	M. Wt	$T_m/^\circ\text{C}$	$T_{\text{decomp.}}/^\circ\text{C}$ in solution	Al-corrosion	$\sigma/\text{mS}\text{cm}^{-1}$ (1.0 M, 25 °C)	
						in PC	in EC/DMC
LiBF₄		93.9	293 (d)	> 100	N	3.4 ^a	4.9 ^c
LiPF₆		151.9	200 (d)	~ 80 (EC/DMC)	N	5.8 ^a	10.7 ^d
LiAsF₆		195.9	340	> 100	N	5.7 ^a	11.1 ^c
LiClO₄		106.4	236	>100	N	5.6 ^a	8.4 ^d
Li Triflate	$Li^+ CF_3SO_3^-$	155.9	>300	>100	Y	1.7 ^a	
Li Imide	$Li^+ [N(SO_2CF_3)_2]^-$	286.9	234 ^b	>100	Y	5.1 ^a	9.0 ^e
Li Beti	$Li^+ [N(SO_2CF_2CF_3)_2]^-$				N		

In addition to the ions in the salt, the solvent also plays an important role in the battery performance. Some of the important electrolyte properties such as electrolyte decomposition, formation of SEI layer on the electrode surface, viscosity and dielectric constant are greatly affected by the composition of the solvent used. It is usually impossible to find a single solvent that satisfies all the requirements for an electrolyte in a practical Li-ion cell and hence, solvent mixtures composed of a combination of two or more solvents are used. **Table 3** gives the list of solvents and their electrochemical stability window in various lithium salts. The most commonly used solvents for battery applications belong to the family of organic polar aprotic solvents such as ethers, esters and alkyl carbonates because of their chemical stability, low melting point and

rapid ionic transport [102]. Cyclic ester based solvents such as ethylene carbonate (EC) and propylene carbonate (PC) are used because of their high permittivity, which enables the good dissolution of the salts at high concentrations. Although PC has overall good solvent properties, it is known to intercalate into the graphene layers in graphite, resulting in the collapse of the graphitic structure [103-105]. But in the case of EC, the solvent does not intercalate into the graphite structures but decomposes to form a solid interphase layer (SEI) which is stable and prevents further decomposition [106-108]. Additionally, the high permittivity of these cyclic esters results in strong interaction with the dipole molecules, giving rise to high viscosity of the final electrolyte. Electrolytes used in practical battery applications are required to have high fluidity or low viscosity for faster mobility and ionic conductivity. Hence, linear carbonates such diethyl carbonate (DEC), dimethyl carbonate (DMC) are often added in specific ratios to the electrolyte to obtain desirable values of fluid viscosity and permittivity for better performance [109].

Table 3: Electrochemical stability of electrolyte systems: Non active electrodes

Solvent	Salt/Conc (M)	Working Electrode	E_a^a	E_c^b
PC	Et ₄ NBF ₄ /0.65	GC	6.6	0.5 1.0-1.2
	Bu ₄ NPF ₆	Ni		
	LiClO ₄ /0.1	Au, Pt		
	LiClO ₄ /0.5	Porous Pt	4.0	
	LiClO ₄	Pt	4.7	
	LiClO ₄	Au	5.5	
	LiAsF ₆	Pt	4.8	
EC	Et ₄ NBF ₄ /0.65	GC	6.2	0.9 1.36
	Bu ₄ NPF ₆	Ni		
	LiClO ₄ /0.1	Au, Pt		
DMC	Et ₄ NBF ₄ /0.65	GC	6.7	1.32
	LiClO ₄ /0.1	Au, Pt		
	LiPF ₆ /1.0	GC	6.3	
	LiF	GC	5.0	
	LiClO ₄ /0.1	Au, Pt	6.7	
DEC	Et ₄ NBF ₄ /0.65	GC	6.7	1.32
	LiClO ₄ /0.1	Au, Pt		
EMC	Et ₄ NBF ₄ /0.65	GC	6.7	1.25
	LiPF ₆ /1.0	GC	6.7	
γBL	LiAsF ₆ /0.5	Au, Ag		
THF	Et ₄ NBF ₄ /0.65	GC	5.2	1.25
	LiClO ₄	Pt	4.2	
	LiAsF ₆ /1.0	GC	4.25(0.1)	
	LiAsF ₆	Pt	4.2	
	LiClO ₄	Pt	4.1	
2-Me-THF	LiAsF ₆ /1.0	GC	4.15(0.1)	1.25
	LiAsF ₆ /1.0	GC	4.2	
	LiAsF ₆	Pt	4.1	
	Et ₄ NBF ₄ /0.65	GC	5.1	
DME	LiClO ₄	Pt	4.5	1.25
	LiAsF ₆	Pt	4.5	

^{a,b} Anodic and cathodic limits, potential referred to Li⁺/Li. ^cThe salt-free condition was realized via and ultramicroelectrode technique

1.2.8.2 Solid electrolytes

Another class of electrolytes, known as solid electrolytes is widely being explored for their use in Li-ion batteries because of its several attractive features over the liquid electrolytes such as better mechanical, chemical and thermal stability. These electrolytes are basically inorganic solid Li-ion conductors, where only the Li^+ ions have mobility as the remaining cations and anions are immobilized in a rigid framework resulting in a high Li^+ transference number. Additionally, due to their very low electronic conductivity, no separators are required when using the solid electrolytes, thereby decreasing the overall cost of the battery. Furthermore, due to the immobile anions in the rigid framework, the electrolyte decomposition on the electrodes and current collectors is greatly minimized.

Based on their structure, the solid electrolytes are mainly classified into two major classes: glassy/amorphous electrolytes and crystalline/ceramic electrolytes.

Glassy electrolytes have attracted interest as solid electrolytes because of their advantages such as isotropic ionic conductivity, ease of production and lack of grain boundaries (**Table 4**). Absence of grain boundaries in a solid electrolyte is essential for the safe operation of the battery. This because they resist Li^+ ion mobility while enhancing the movement of other ions, which may contribute to undesirable dendrite formation and short circuiting of the battery. Oxide glasses were first used as the glassy electrolytes and later mixed with *Selenium* and *Boron* to improve their conductivity [110]. Another class of compounds containing phosphorus oxynitride glasses, also known as LIPON, were developed at Oak Ridge National Laboratory (ORNL) and have gained much attention in practical applications, especially in thin film Li-ion

batteries [111]. The LIPON films are usually made by RF sputtering using Li_3PO_4 target in nitrogen plasma or by thermal evaporation using nitrogen ion beam [112, 113]. LIPON shows excellent chemical stability and allows for negligible self-discharge in both fully charged and fully discharged state for extended periods of time [114].

Crystalline solid electrolytes are usually ceramic electrolytes of oxides, sulfides, nitrides, halides and other polyanions. Perovskite structures with the general formula ABO_3 have become attractive candidates as crystalline solid ion conductors, because of their significant tolerance to ionic substitution, resulting in open lattice structures for Li^+ ion conduction. For example, single crystals of $Li_{3x}La_{2/3-x}TiO_3$ with $x=0.11$ show high conductivity in the range of 10^{-3} S/cm, due to presence of large number of vacancies on the Li site [115]. However contact with metallic lithium or negative anode containing lithium results in the reduction of Ti^{4+} ion [104], due to which there is an increase in the electronic conductivity of the structure, thereby preventing it to be used in commercial Li-ion batteries. Lithium analogues of NASICON (Na Super Ion Conductors) having the general formula $Li_{1+x}M_2(PO_4)_3$ ($M=Ti, Ge, Zr$) have also been explored as Li^+ ion electrolytes, wherein, the PO_4 and MO_6 polyhedra are connected at the corners to form 3D channels for lithium ion conduction [44]. The M cation is usually the Ti^{4+} and also suffers from similar problems as that of perovskite structure wherein, the reduction of Ti by lithium intercalation increases the electronic conductivity. To overcome this challenge, doping with trivalent ions such as Al has shown to improve the ionic conductivity by three orders of magnitude [44, 45].

Table 4: List of ionic conductivities of Li_2O based glasses at given temperatures

Materials (Composition)	Conductivity (S/cm)	Measurement Temperature ($^{\circ}C$)
$Li_2B_4O_7$	1.0×10^{-4}	300
$LiBO_2$	4.0×10^{-3}	300
$Li_2O-B_2O_3$ (42.5-57.5)	6.1×10^{-3}	350
$Li_2O-B_2O_3$ (63-37)	6.3×10^{-11}	25
$Li_4B_7O_{12}Cl$	2.5×10^{-4}	200
$Li_4B_7O_{12}Cl$	8.0×10^{-3}	300
$Li_2O-Li_2Cl_2-Li_2SO_4-SiO_2-B_2O_3$ (35-10-30-12.5-12.5)	9.7×10^{-2}	350
$Li_2O-Li_2Cl_2-B_2O_3$ (31.8-12.3-55.9)	1.7×10^{-2}	300
$Li_2O-Li_2Cl_2-B_2O_3-Al_2O_3$ (29-24-3-44)	1.5×10^{-2}	350
$Li_2O-LiF-B_2O_3$ (20-36-44)	3.1×10^{-4}	200
$Li_2O-Li_3PO_4-B_2O_3$ (25-10-65)	1.0×10^{-3}	330
$Li_2O-Li_2SO_4-B_2O_3$ (0.5-0.15-1)	2.4×10^{-3}	350
$Li_2O-Li_2SO_4-B_2O_3$ (0.71-1.1-1)	2.1×10^{-2}	300
$Li_2Si_2O_5$	1.9×10^{-3}	350
Li_2O-SiO_2 (40-60)	1.0×10^{-6}	100
$Li_2Al_2Si_4$	4.0×10^{-4}	300
$Li_2O-Nb_2O_3$	6.1×10^{-4}	200
$Li_2O-B_2O_3-LiNbO_3$ (40-35-25)	8.0×10^{-4}	350
$Li_2O-Al_2O_3-SiO_2$ (25-25-50)	6.1×10^{-4}	250
$Li_2O-B_2O_3-SiO_2$ (39-13-48)	1.5×10^{-4}	350
$Li_2Si_2O_5-Li_2SO_4$ (71.5-28.5)	8.7×10^{-4}	350
$LiNbO_2-SiO_2$	1.0×10^{-4}	200
$Li_2O-Y_2O_3-SiO_2$ (40-6-54)	1.4×10^{-3}	300
$LiPO_3-LiF$ (60-40)	6.7×10^{-9}	25
$LiPO_3-LiCl$ (70-30)	1.0×10^{-3}	220
$LiPO_3-LiI$ (67-33)	1.0×10^{-3}	194
$LiPO_3-LiBr$ (67-33)	1.3×10^{-3}	220
$LiPO_3-Li_2SO_4$ (67-33)	3.5×10^{-3}	250
$B_2O_3-0.56Li_2-0.08LiF$	6.3×10^{-4}	300
$B_2O_3-0.56Li_2-0.08LiI$	3.2×10^{-3}	300
$Li_2O-LiF-Al(PO_3)_3$ (30-50-20)	1.0×10^{-2}	300
$Li_2O-LiF-Al(PO_3)_3$ (15-70-15)	1.3×10^{-3}	220
$Nb_2O_5-Li_2O_2$ (50-50)	5.3×10^{-3}	350
$Ta_2O_5-Li_2O_2$ (50-50)	6.4×10^{-3}	350

1.2.8.3 Polymer electrolytes

Liquid electrolytes often suffer from problems of chemical and mechanical instability [46]. For example, the commonly used liquid electrolyte, *i.e.* $LiPF_6$ dissolved in EC/DEC often contains transesterification products such as HF and PF_5 which are very corrosive and affects the battery performance [47]. On the other hand, solid polymer electrolytes are not limited by such problems and are non-volatile, easy to handle and mechanically durable. The concept of polymer electrolytes was first proposed with the discovery of ionic conductivity in poly ethylene oxide (PEO) [42]. Since then, tremendous interest has been shown in this area and is currently widely used in commercial applications under the trade name, LiPo or Li-Poly batteries. These solid polymer electrolytes can either be solvent free ion coupled systems or solvent containing gel polymer systems.

PEO based electrolyte is the most common solvent-free polymer electrolyte. The dissolution of the lithium salt in these electrolytes occurs through the complex formation between the Li^+ ion and the ether oxygen of the PEO chain. However, when the size of anions in the salt is large, as in the case of bis (trifluoromethylsulfonyl) imide ($(CF_3SO_2)_2N$), charge delocalization occurs and results in undesirable properties such as poor binding strength and dissociation of Li^+ ions [43]. The high ionic conduction exhibited by PEO based electrolytes is due to the segmental motion of the chains, which is usually found in the amorphous phase and hence, it is important to minimize the crystallinity in the polymer chain. Therefore, the crystalline conducting phase is often avoided by using plasticizers, cross-linked and branched polymers [51-53]. Also, when the temperature of the polymer is decreased, the chain tends to become less mobile and the segmental motion of the polymer is greatly minimized, resulting in

significant reduction in the conductivity of the electrolyte. Hence it is very critical to select the polymer with a very low glass transition temperature (T_g).

Another class of polymer electrolytes is the gel electrolytes, wherein, an organic liquid electrolyte is incorporated into a polymer matrix. The lithium salt in this case is either dissolved in the solvent or attached to the polymer matrix. The polymers usually used as the matrices are polyvinylidene fluoride (PVDF), polyacrylonitrile (PAN), poly (methyl methacrylate) poly vinyl alcohol (PVA), etc. The ionic conductivity of the PVDF matrix based electrolytes can be improved by adding secondary particles such as $BaTiO_3$ [54], TiO_2 , cross-linked dipoxy polyethylene glycol (DIEPEG) to modify the pore structure; and HFP (hexafluoro propylene) to decrease the crystallinity.

Another class of polymer electrolytes is known as single ion electrolytes, wherein, the anions are fixed rigidly in the polymer network and only the cations are mobile. While this results in high transference number for the Li^+ ions, the ionic conductivities are very low due to poor dissociation of the ions, and hence, make them impractical for commercial applications.

1.2.8.4 Additives

Additives are a special class of compounds that are often added to the electrolyte (especially liquid based non-aqueous) for advanced functionality such as flame retardation, formation of a stable SEI layer, enhanced ionic conduction etc. In a recent development, electrolyte additives comprising of vinylene carbonate (VC) and fluoroethylene carbonate (FEC) was shown to improve performance in terms of cycling stability, solid electrolyte interface (SEI) and first cycle irreversible loss [72, 116].

1.2.9 Anodes

Anode in a Li-ion battery is also referred to as negative electrode since it undergoes oxidation to produce electrons during the discharge process. As discussed earlier, the anode used in the first generation of lithium batteries was made of elemental *Li* because of its attractive features such as low molecular weight and high electropositivity. But these batteries suffered from severe safety problems such as explosion hazard due to the short circuiting of the cell arising from the lithium dendritic growth upon recharging the battery. This drawback prompted the researchers to explore an alternative material to *Li* metal; an anode with a host structure, wherein, the Li^+ ions can be inserted reversibly during the charge-discharge processes, thus preventing the formation of dendrites. Following this approach, Sony® commercialized the first Li-ion battery with graphite (*C*) and $LiCoO_2$ acting as the anode and cathode hosts, respectively, with a working voltage of 3.6 V and gravimetric energy densities between 120 and 150 Wh/kg. While this *C/LiCoO₂* system is currently the most widely used Li-ion battery in portable applications such as cell phones, laptops, PDAs and cameras etc, considerable efforts are being directed to develop new anode materials. The materials selected as anode hosts for Li-ion batteries should exhibit the following criteria:

- i. Alloy at low electrode potentials with Li^+ ions, comparable to metallic Li to maximize the overall cell voltage.
- ii. Exhibit good cyclability and capacity retention for a long cycle life.
- iii. Show good chemical stability to electrolyte and solvent within a large potential window.
- iv. Be inexpensive and safe to handle for commercialization.

1.2.9.1 Carbonaceous materials

The existence of lithium intercalated compounds with graphite was known for several decades before they found application as anode hosts in Li-ion battery [117, 118]. Attempts to electrochemically intercalate Li^+ into graphite from Li salt electrolytes (dissolved in DME and DMSO) was first done by Besenhard *et al* [119, 120]. Their first use in Li-ion batteries was reported by Basu *et al* in 1980 wherein, lithium-graphite intercalated compounds (GIC) were used as anodes in a $LiCl-KCl$ molten salt electrolyte [121]. Consequently patents were applied by Basu and Ikeda for the GIC based anodes in 1981 [122] and 1982 [123], respectively, for their use in room temperature Li-ion batteries. Since then, extensive research was done in developing carbon based anode hosts and eventually resulted in the commercialization of the first Li-ion battery with a carbon anode by Sony® in 1990 [124].

The carbonaceous materials used as anodes in Li-ion batteries are made of sp^2 hybridized C-atoms arranged in a hexagonal network forming the graphene layers, known as honeycomb structure. These graphene sheets are stacked upon one another by weak van der Waals forces to form ordered structures, commonly referred as crystallites. The stacking of these graphene layers in the carbonaceous materials can be of two types: the ABAB stacking (2H or α -phase) sequence possessing a hexagonal symmetry, and the ABCABC type stacking, exhibiting a rhombohedral (3R or β -phase) symmetry. Carbons that are readily available often contain up to 30% of β -phase carbons, which are formed due to certain mechanical treatments such as shearing, milling and ultrasonic treatment [58, 59]. This phase can easily be converted to the thermodynamically stable α -phase by heating to high temperatures. The graphitic structure results in two different surfaces, known as the basal plane and the prismatic (edge) surfaces as shown in the **Figure 12** [71]. The basal planes are smooth and homogenous containing only carbon atoms, whereas, the prismatic

surfaces are rough, heterogeneous and may also contain other atoms such as oxygen in the form of surface functional groups. Lithium intercalation into graphite occurs mainly through the prismatic planes and the basal planes are inert to any intercalation [60, 79]. Therefore, it is critical to understand and control the relative amounts of the prismatic and basal planes in the carbonaceous materials used for making anodes.

The weak van der Waals forces enable the graphene layers to glide over one another by translational and rotational modes introducing stacking faults in the carbon matrix [125, 126]. This results in the loss of periodic arrangement of the layers, forming a structure known as turbostratic structure. The inter-planar distances in these disordered carbon structures are diffused and on an average, larger than that of graphite. The disordered carbons are generally of two types: soft and hard carbons. In soft carbons, the turbostratic disorder can be removed easily by heating them to very high temperatures ($>3000^{\circ}\text{C}$) in an inert atmosphere. However, in the case of hard carbons, it is very difficult to remove the turbostratic order by thermal annealing and hence remain disordered. Ordered and disordered carbons differ greatly in their electrochemical properties such as intercalation potential with lithium, gravimetric capacity, first cycle irreversible loss, quality of the SEI layer and rate capability.

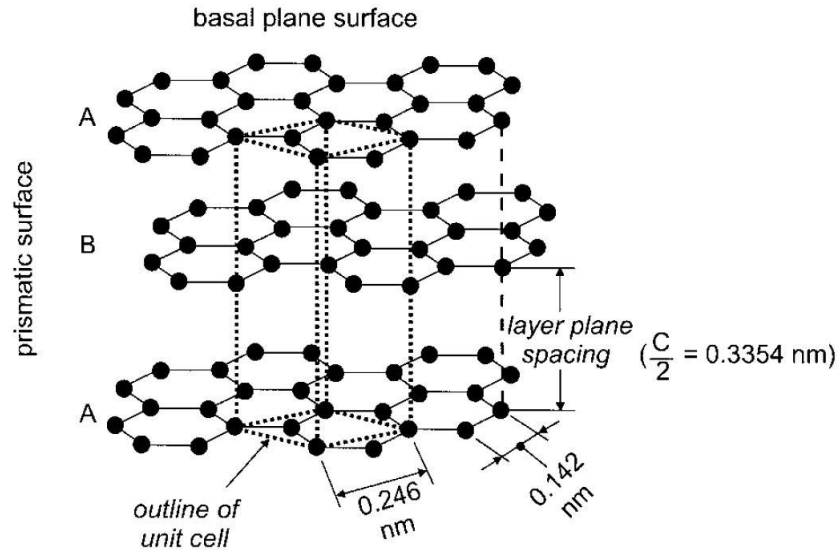


Figure 12: Crystal structure of hexagonal graphite showing the AB layer stacking sequence, the unit cell, and the subdivision in basal plane and prismatic surfaces [37]

The lithium intercalation into the graphite layers (prismatic) occurs by a periodic sequence (stages) involving the formation of intercalant layers and this phenomenon is called the staging mechanism [127]. An n th stage compound is defined as the structure containing ‘ n ’ number of graphene layers between two intercalated layers (layers containing Li^+ ion). In a well-ordered graphitic structure, a maximum of one Li can be accommodated for 6 carbon atoms. Therefore, a stage-I compound has the stoichiometric formula LiC_6 wherein, the intercalant layer containing Li^+ ions are separated by one graphene layer as shown in the **Figure 13**. The adjacent in-plane neighboring sites for Li intercalation are usually avoided, resulting in an in-plane lithium density of LiC_6 . After intercalation, the ABAB sequence of the graphene layers is shifted to an energetically favorable AA type stacking order. Due to intercalation of an external ion (Li^+), there is an average increase in distance (10.3%) between the graphene layers [80]. This staging mechanism can be observed easily from the voltage vs. time plot obtained by intercalating graphite with lithium in a galvanostatic mode (**Figure 14**). The voltage plateaus in

Figure 14 indicate the presence of two phases or two different stage compounds. For example from the **Figure 14**, the two phases, namely the stage-I and stage-II compounds are observed to co-exist wherein, the voltage remains constant at 0.1 V during the regime where the two phases are present [83].

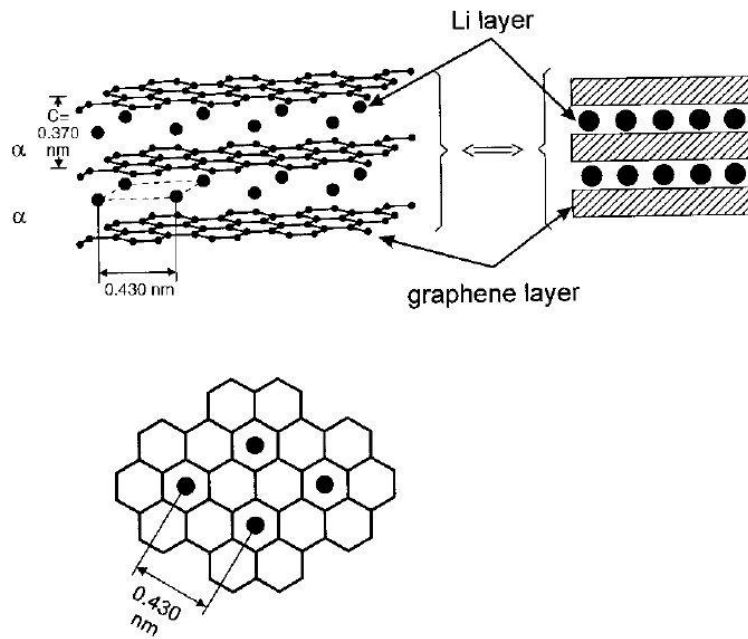


Figure 13: Schematic illustration of lithium intercalation into graphite structure and view perpendicular to basal plane of LiC_6 [71]

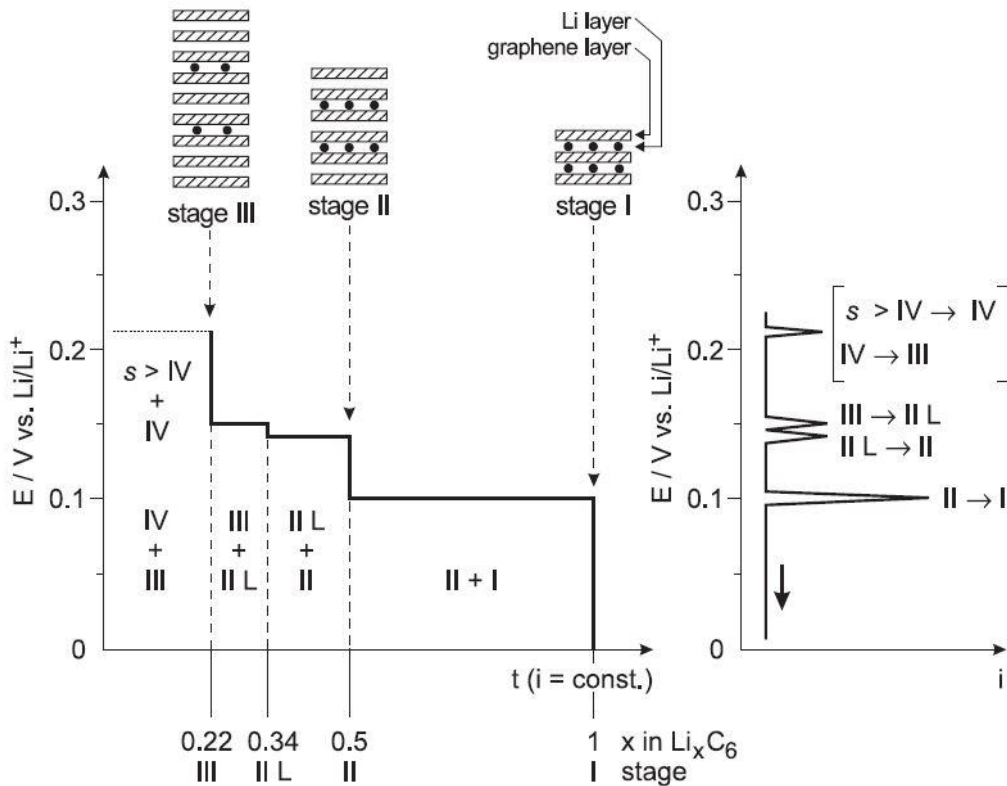


Figure 14: Stage formation during electrochemical intercalation of lithium into graphite [71]

Another important feature of the carbonaceous compounds is the irreversible capacity that arises due to the formation of solid electrolyte interphase layer (SEI) on graphitic surfaces [82, 86, 128]. This is due to the solvent decomposition that occurs at around 0.8 V and is parallel to the lithium intercalation reaction. This phenomenon can be very damaging, especially when using propylene carbonate (PC) as the solvent in the electrolyte. In PC based electrolytes, the solvent molecules co-intercalate along with the Li^+ ions in the form of $Li^+(solv)_y$ into graphite layers to form $Li^+(solv)_yC_n$ [85]. This solvated intercalation results in the large expansion in the graphitic structure (~150%) leading to exfoliation of graphene planes and loss in capacity (**Figure 15**). To address this problem, ethylene carbonate (EC) based solvents are used as they do not participate in the solvated intercalation reaction [129]. Instead, they form a protective SEI

layer on the graphite surface. Since the viscosity of EC is very high due to its high permittivity, it is often mixed with linear carbonates such as diethyl carbonate (DEC) or dimethyl carbonate (DMC) to enhance its fluidity and is thus widely used in commercial Li-ion batteries [129].

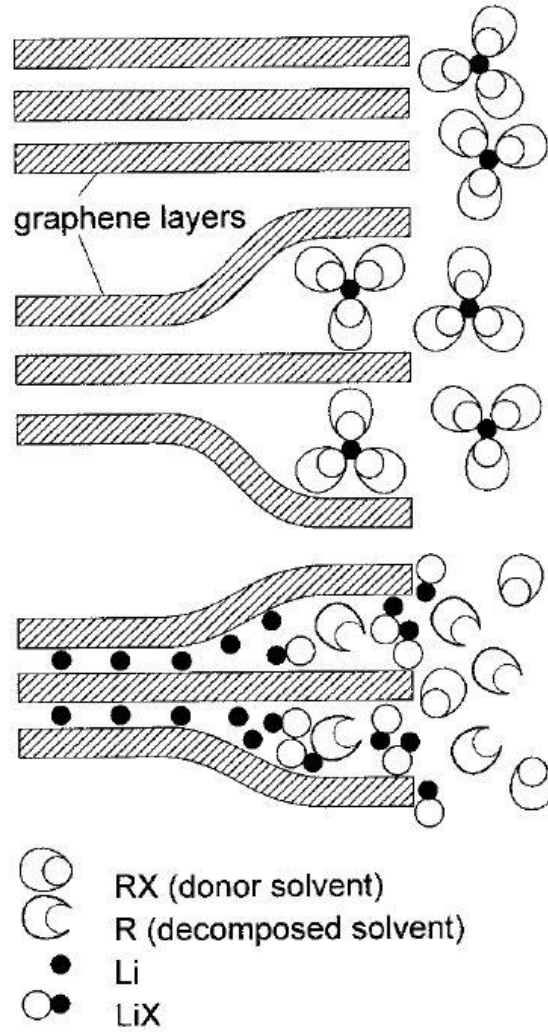
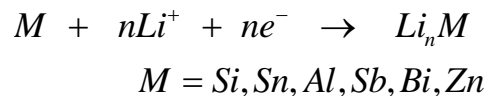


Figure 15: Exfoliation of graphite structure due to solvent co-intercalation [85]

1.2.9.2 Intermetallic and alloy anodes

The low cost and good cycle life of graphite-based anodes have enabled them to be widely used in commercial portable applications. Due to the increasing demand for energy storage for emerging applications such as automotive industry and grid storage, batteries with higher energy densities are gravely needed. Metallic alloy based anodes have attracted a lot of attention as a promising alternative to carbonaceous electrodes due to their high gravimetric and volumetric densities. Pure elements such as *Si*, *Sn*, *Al* and *Bi* are capable of alloying with substantial amounts of lithium at low electrode potentials according to the following reaction, resulting in higher energy densities:



The theoretical capacity of these elements can be calculated from the molar amount of *Li* that can be alloyed via an electrochemical lithiation reaction and these values are presented in

Table 5.

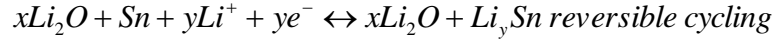
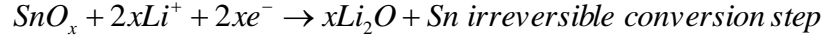
Table 5: Specific capacities and molar volume changes exhibited by the different candidate elements during cycling

Element	C	Si	Sn	Al	Bi
Maximum Lithiated phase	LiC ₆	Li _{4.4} Si	Li _{4.4} Sn	Li ₉ Al ₄	Li ₃ Bi
Gravimetric capacity (mAh/g)	372	4200	992	2235	385
Volumetric Capacity (mAh/cm³)	833	9784	7247	6035	3773
Volume change (%)	12	297	257	238	115

Initial work on lithium alloys and intermetallics was conducted on the systems: *Li-Al* [91, 92, 98], *Li-Sn* [93-95], *Li-Mg*[96], *Li-Sb*[100, 101] and *Li-Si* [103-105] using molten salt electrolytes at high temperatures (~400°C). The metal alloy anodes undergo large volume changes during the alloying and de-alloying processes. These colossal changes cause large mechanical stresses, eventually leading to fracture of the active material, which is commonly referred to as ‘pulverization’ or ‘crumbling’ of the electrode. The resulting secondary fine particles from pulverization are often not well connected and remain electrically insulated from the current collector, resulting in a loss of active material or capacity. Several approaches were explored to solve the mechanical failure problem in these alloy anode systems which include:

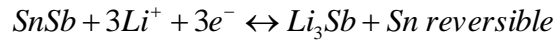
- Use of nanostructured and amorphous materials.
- Use of mixed conductor matrices: active-inactive and active-active matrix systems.

In 1995, Fuji® commercialized a metal alloy anode based Li-ion battery under the trade name - Stallion® lithium-ion cell [130] that exhibited much higher capacities compared to its counterparts that use graphite anode. The Stallion® cell used an amorphous tin oxide composite anode, SnO_x dispersed in a glassy matrix of B_2O_3 , Al_2O_3 and tin phosphate. The electrochemically active tin that undergoes lithiation and de-lithiation during the cycling processes was formed by the following reactions:



The electrochemically inactive matrix containing borate-alumina-phosphate glass acts as a supporting media for the tin nanodomains that are formed in the first in-situ reduction of SnO_x . There is an irreversible loss in capacity in the first cycle due to loss of lithium as a result of the reduction of the parent SnO_x phase to form Sn and Li_2O .

Another system known as the active-active concept was proposed by Besenhard wherein $SnSb$ was used as the starting material [106]. The alloying reactions for this system are shown below:



The lithium alloying reaction occurs in a sequential fashion, wherein, lithium first alloys at higher potentials with antimony to form Li_3Sb and Sn domains [107, 108]. The remaining Sn domains further alloy with Li to form Li_ySn phases. During the de-lithiation process, after all the Li is de-alloyed from Sb and Sn , the original phase $SnSb$ is restored. This phase separation and restoration phenomenon during the charge-discharge process results in a morphology that prevents the aggregation of the finely dispersed Sn to form large Sn grains which is responsible for the mechanical failure arising from large volume changes. Intermetallic phases between and Sn and Fe such as $SnFe$, Sn_2Fe , Sn_2Fe_3 and Sn_3Fe_5 were studied by Dahn *et al* wherein Sn alloys with Li to form Li_xSn alloys and Fe domains [110-114]. The electrochemically inactive Fe is very fine (~10 nm) and surrounds the alloyed Sn particles as a conductive matrix, thus improving the inter-particle conductivity.

Several studies found that reducing the particle size of the active materials alleviated the mechanical stresses [15, 131]. Huggins *et al* calculated using a theoretical model, the conditions under which fracture can occur in a two-phase structure due to specific volume mismatch [131]. Accordingly, a terminal particle size can be calculated from this model, (**Figure 16**) below which, further fracture does not occur; and this value is dependent on the material, magnitude of the volume mismatch and fracture toughness of the lower specific volume phase.

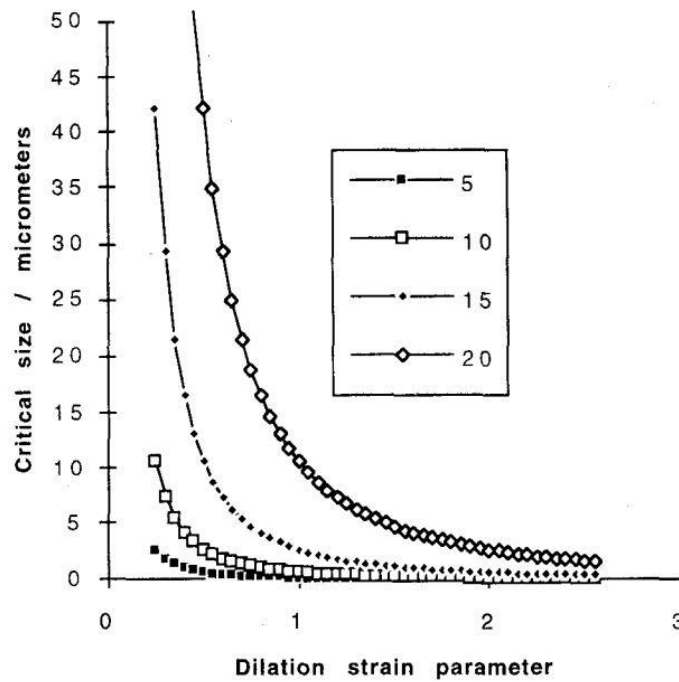


Figure 16: Influence of dilation strain parameter upon critical size below which fracture will not occur for materials with different values of fracture toughness, expressed in MPa(sqrt m) [131]

Also, the materials with particle sizes in the nanometer range have the ability to undergo superplastic deformation during the alloying and de-alloying processes to accommodate the large volume changes. The relationship between the strain rate ($\dot{\varepsilon}$), applied stress (σ) and grain size (d) is given by the following equation [132]:

$$\dot{\varepsilon} = A\sigma^n d^{-p} D_0 \exp(-Q/RT)$$

Where A is a constant, n is the stress exponent ($n \approx 2$), p is the grain size exponent ($p \approx 2-3$), Q is the activation energy and R is the gas constant. The strain rates obtained from the above equation are very slow for conventional grain sizes ($\sim 10 \mu\text{m}$) and superplasticity can be obtained only at high temperatures. However, decreasing the particle size enables the superplastic behavior at room temperature. Additionally, nanostructured materials have large fraction of atoms located at the grain boundaries which results in improved mechanical properties such as mechanical hardness, fracture toughness and ductility [97].

1.2.10 Silicon anodes

The advancement in portable electronics and demand for longer driving range electric vehicles has necessitated the battery manufacturers and research community to develop Li-ion batteries with higher amounts of stored energy without increasing the overall weight of the battery pack. Batteries with higher energy densities can be obtained by increasing the specific capacity and/or output voltage of the individual constituent electrochemical cells. The total specific capacity of an individual electrochemical cell is calculated by the following equation:

$$C = \frac{C_a \times C_b}{C_a + C_b}$$

where C_a and C_c are the specific capacities of anode and cathode, respectively.

Figure 17 shows the total capacity of the battery that can be attained, plotted against anode capacity for two different cathodes: *LiCoO₂* and *LiMnO₂* (140 mAh/g, *LiCoO₂* and 200 mAh/g, *LiMnO₂* derivative) [133]. It is obvious that a higher cathode capacity is essential for an overall high specific capacity of the battery. But even with a cathode having a large capacity of 200 mAh/g, while there is an initial rapid increase in overall capacity with the anode capacity approaching values of ~1200 mAh/g, there is only a modest improvement in total capacity with further increase in anode capacity. Therefore, while selecting materials for anode to develop next generation of high energy density batteries, it is important that their theoretical capacity is greater than 1200 mAh/g in order to attain the maximum attainable capacity for a given cathode.

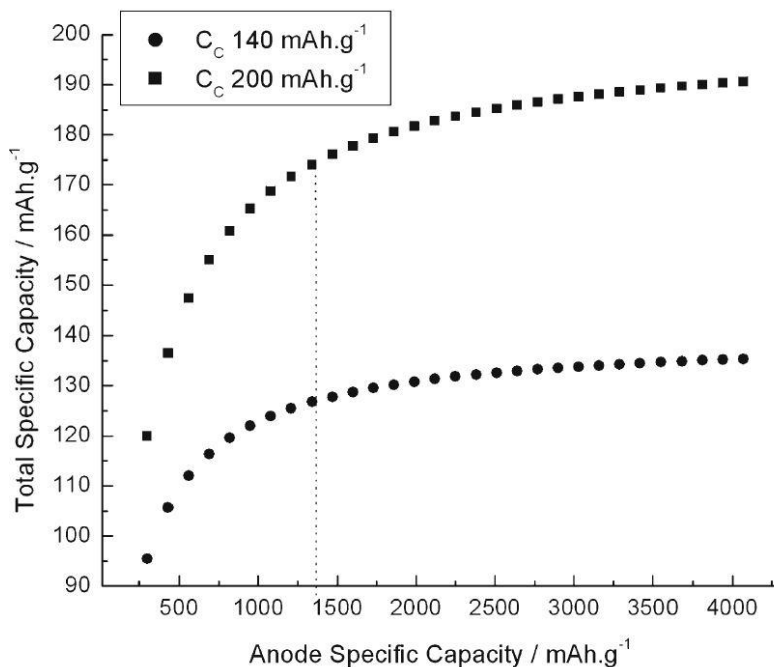


Figure 17: Total capacity of Li-ion battery presented as a function of anode capacity for two cathodes having capacities of 140 mAh/g and 200 mAh/g [133]

Graphite, which is currently used as anode in all commercial Li-ion batteries has a theoretical capacity of only 372 mAh/g and thus, is certainly not an ideal candidate for developing high energy density batteries. As discussed earlier, metal alloy anode systems are suitable alternatives in terms of achieving higher gravimetric capacities and among them, silicon is very attractive because of its elemental abundance in earth's crust, low cost and high theoretical capacity of 4200 mAh/g, which is attributed to its ability to form the highest lithiated phase, $Li_{22}Si_5$. These promising characteristics make it possible for silicon to potentially replace graphite as a high specific capacity anode.

1.2.11 Electrochemical lithiation reactions in Silicon

The electrochemical formation of *Li-Si* alloys was first demonstrated in high temperature cells operating between 400°C to 500°C by Sharma and Seefurth in 1976 [104] and then by Huggins *et al* in 1981 [115]. The *Li-Si* phase diagram (**Figure 18**) indicates the formation of the following *Li-Si* phases: $Li_{12}Si_7$ ($Li_{1.71}Si$), $Li_{14}Si_6$ ($Li_{2.33}Si$), $Li_{13}Si_4$ ($Li_{3.25}Si$) and $Li_{22}Si_5$ ($Li_{4.4}Si$) [134]. The possible formation of the highest lithiated phase, $Li_{22}Si_5$, therefore determined the theoretical capacity of *Si* to be 4200 mAh/g.

As described in the previous section, during the discharging process, bulk crystalline silicon, alloys with lithium to form different *Li-Si* phases as listed in **Table 6** [115]. The formation of these phases is associated with a large change in volume upon lithiation. The complete lithiation of silicon, forming the $Li_{22}Si_5$ phase results in a four-fold increase or 400% change in volume. This large volume expansion is catastrophic resulting in the formation of large amount of mechanical stresses in the active material, which in turn leads to cracking or pulverization of the electrode.

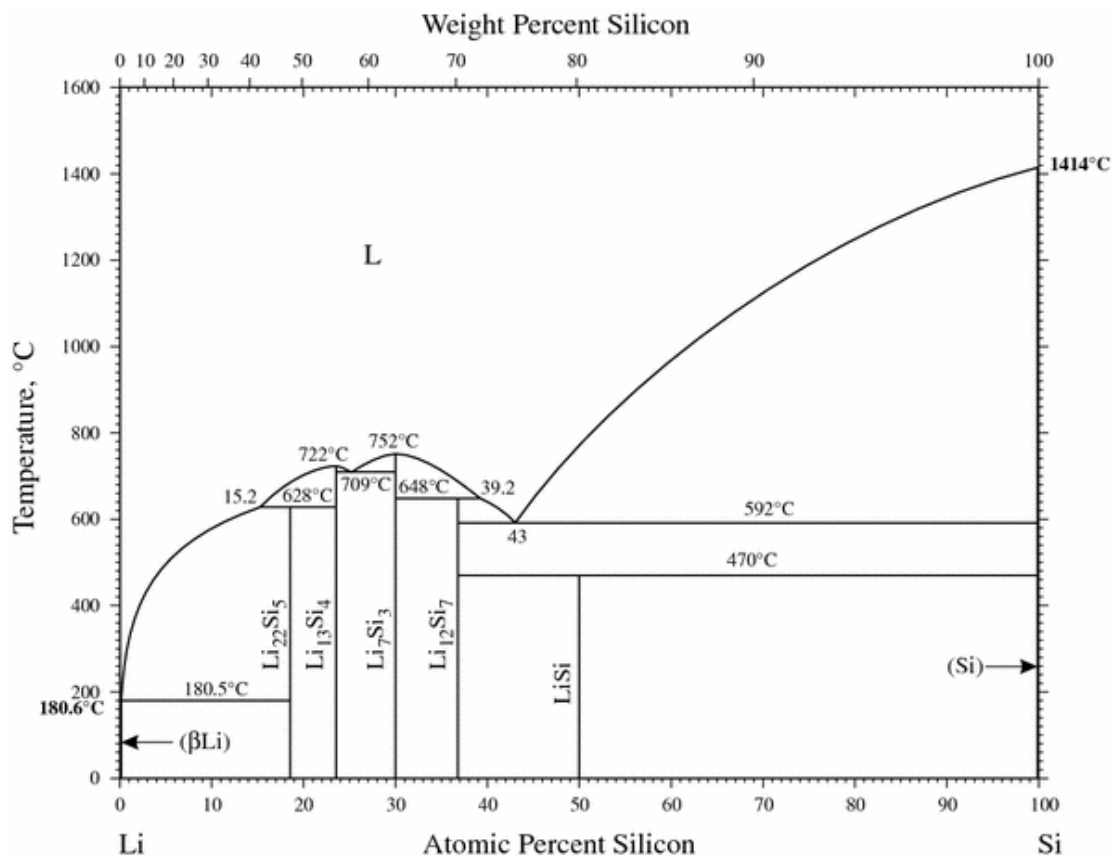


Figure 18: Li-Si phase diagram [135]

Table 6: Crystal structure, unit cell volume, formula units per unit cell, crystal volume per Si atom and theoretical density of the Li-Si system [115]

Compound and crystal structure	Unit cell volume (\AA^3)	Volume per silicon atom (\AA^3)
Silicon cubic	160.2	20.0
$\text{Li}_{12}\text{Si}_7$, ($\text{Li}_{1.71}\text{Si}$) orthorhombic	243.6	58.0
$\text{Li}_{14}\text{Si}_6$, ($\text{Li}_{1.71}\text{Si}$) rhombohedral	308.9	51.5
$\text{Li}_{13}\text{Si}_4$, ($\text{Li}_{3.25}\text{Si}$) orthorhombic	538.4	67.3
$\text{Li}_{22}\text{Si}_5$, ($\text{Li}_{4.4}\text{Si}$) cubic	659.2	82.4

However, Dahn *et al* observed through in-situ X-ray diffraction measurements that the electrochemical alloying of crystalline *Si* with *Li* at very low current rates first resulted in the amorphization of *Si* to form Li_xSi alloys followed by crystallization to form a maximum lithiated phase of $Li_{15}Si_4$ having a theoretical capacity of 3579 mAh/g [117]. During the first cycle, *Li* alloys with *Si* to form a new amorphous Li_xSi phase along with the unreacted *Si* phase. The presence of these two phases results in a flat voltage profile during the discharge reaction, where the free energy available is consumed in the nucleation of the new amorphous phase. **Figure 19** shows a typical voltage profile of crystalline silicon cycled at a current density of 100 mA/g [136]. The presence of flat voltage profile at ~0.2 V during the lithiation reaction in first cycle indicates the presence of the Li_xSi and crystalline silicon phases. A very high first discharge capacity of 3700 mAh/g was obtained followed by a huge irreversible loss of 75%, resulting in a charge capacity of only 880 mAh/g. Furthermore, the capacity drops to less than 500 mAh/g by the end of 5th cycle. The poor electrochemical performance of crystalline *Si*, thus ruled out its potential to replace graphite as a high capacity anode.

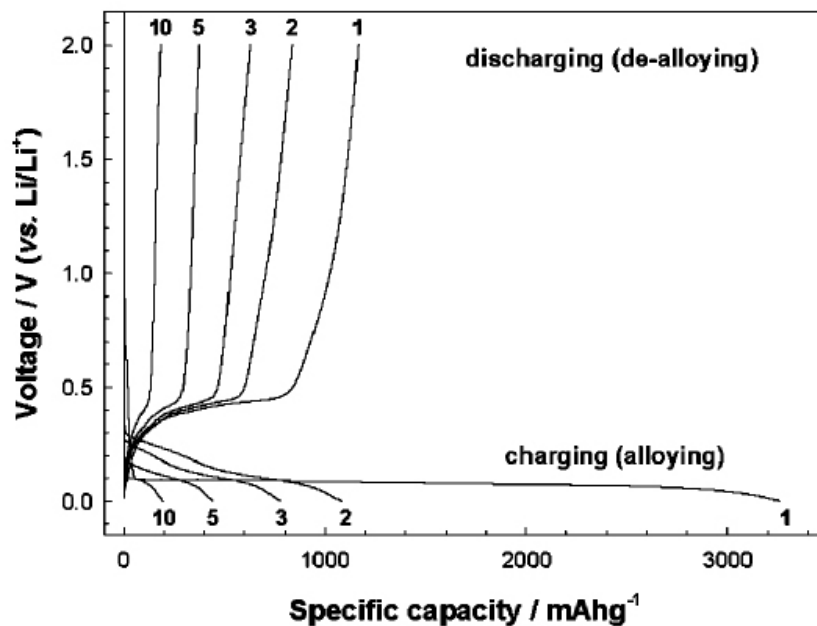


Figure 19: Galvanostatic charge-discharge profiles for micro-Si (10µm) cycling at a current density of 100 mA/g in the voltage window of 0.0-2.0V (vs. Li/Li⁺) [136]

1.2.12 Failure mechanism in silicon anodes

As described in the previous section, bulk crystalline silicon exhibits a large first cycle irreversible (FIR) loss and rapid capacity fade, thus greatly limiting its use in commercial applications. Initial studies performed to understand the failure mechanism attributed the large first cycle irreversible loss only to the material pulverization and loss of material conductivity [136]. However, other factors such as solid electrolyte interphase (SEI) films [137] and presence of surface oxides [66, 138] were also found to be responsible for the poor electrochemical performance of the bulk crystalline silicon anodes and are described below:

1.2.12.1 Loss of active material

The large volumetric changes during the alloying and de-alloying reactions results in building up of mechanical stresses that leads to pulverization and loss of inter-particle contact/conductivity. This loss in electronic conductivity can easily be illustrated by measuring the internal resistance of the electrochemical cell. Ryu *et al* conducted a galvanostatic intermittent titration technique (GITT) experiment, wherein, a current density of 100 mA/g was applied for 10 minutes to allow the lithiation/de-lithiation reactions to occur and then the current was turned off for the next 20 minutes [118]. Closed circuit voltage (CCV) and quasi open circuit voltage (QOCV) were measured when the current was applied and turned off, respectively, and their difference was used to calculate the internal resistance. Variations in internal resistance as shown in **Figure 20** indicates a decrease in the internal resistance which is due to improvement of inter-particle contact caused by the volume expansion of the silicon particles. This decrease may also be attributed to the electronically conducting Li_xSi alloys that are usually formed during the lithiation process [118]. However, during the de-alloying cycle, the internal resistance increased rapidly beyond 0.4 V. This is because, extraction of Li from the Li_xSi alloys that is almost complete during the de-lithiation process subjects the active material to large tensile forces due to volume contraction. Given the ease of micro-crack propagation under tensile force fields, the Si particle undergoes cracking, resulting in a loss of conductivity or capacity. The formation of cracks and pulverization of the active material during the electrochemical cycling has been observed and confirmed by in situ AFM and SEM methods [15, 119, 120].

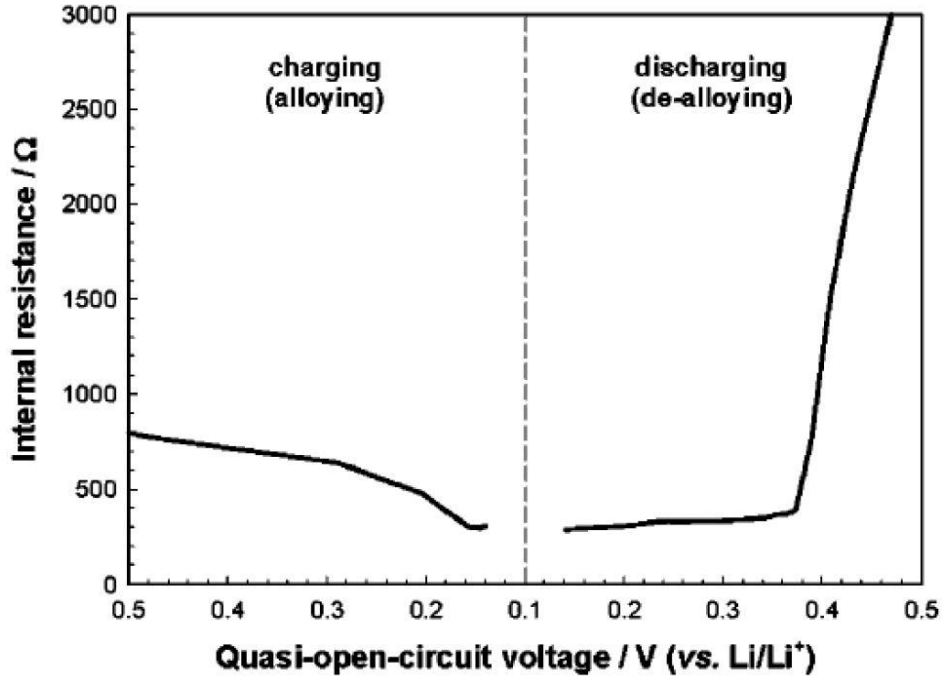


Figure 20: Variation of internal resistance in silicon anode [118]

1.2.12.2 Formation of Solid Electrolyte Interphase (SEI) films

Solid electrolyte interphase layer, commonly referred to as SEI layer is a protective film that forms on the surface of the negative electrode during the first cycle as a result of electrolyte decomposition. In the case of Si, the components of the SEI layer are mainly composed of lithium alkyl carbonates such as LiF , $Li_xPO_yF_z$, Li_2CO_3 , SiF_x , Li_2O etc [68-70]. SEI is often a dynamic process and continues to progress, especially in the case of alloy-based anodes, wherein, new surfaces formed continuously as a result of material cracking and pulverization act as fresh surfaces for further electrolyte decomposition or SEI formation. The lithium lost in forming the SEI products is irreversible, and hence constitutes the first cycle irreversible (FIR) loss, lower coulombic efficiency and capacity fade [69]. To suppress the formation of SEI, additives such as vinylene carbonate (VC) [73, 139] and fluoroethylene carbonate (FEC) [72, 73]

are usually added to the electrolyte. This has shown to lower the first cycle irreversible loss and improve the cyclability of the electrode.

1.2.12.3 Presence of surface oxide layer

Bare silicon surface usually has a surface oxide layer (SiO_2 or SiO_x) and the thickness of this layer usually depends on the particle size. As the particle size is reduced, there is an increase in specific surface area (SSA), resulting in an increase in surface oxide layer coverage. Commercial nanosized silicon can contain upto 26 wt% of SiO_2 and is electrochemically inactive, resulting in decreased overall specific capacity of electrode [66]. Etching with hydrofluoric acid for about 30 minutes can dissolve the surface oxide. The resulting oxide-free silicon particles have shown a significant improvement in capacity (shown in **Figure 21**) [66]. Unlike SiO_2 , silicon sub oxides such as SiO_x are electrochemically active and when present on the surface of the active Si , can contribute to irreversible capacity loss due to its reduction to form Si and Li_2O during the lithiation process [66, 67].

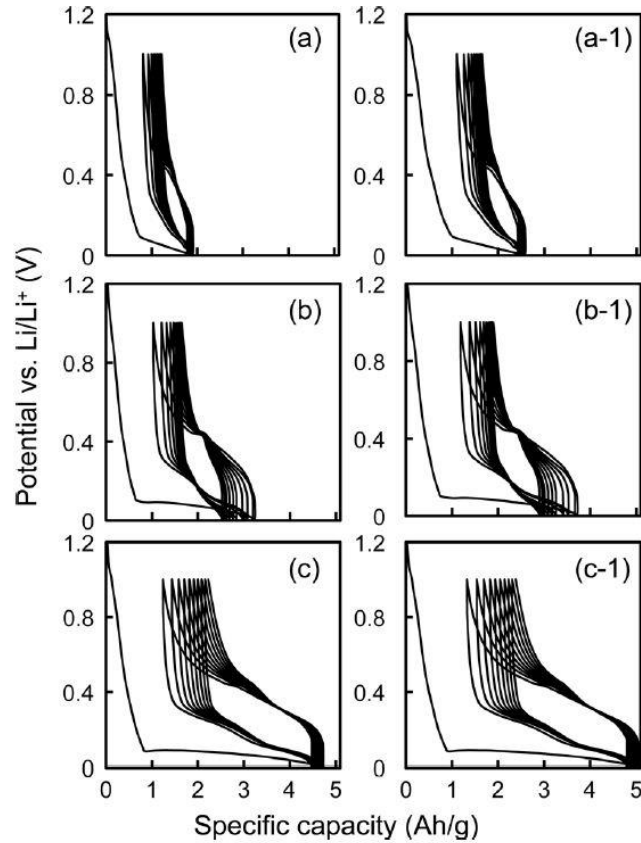


Figure 21: Specific capacity vs. potential of the first 10 cycles of Si electrode. (a) and (a-1) As-received Si, (b) and (b-1) Si after 10 min of etching, (c) and (c-1) Si after 30 min of etching [66].

1.2.13 Approaches to address the problem

To address the large first cycle irreversible loss and rapid capacity fade in silicon based anodes, several approaches have been developed which are discussed below:

1.2.13.1 Nano sized and nanocrystalline silicon

There have been several reports indicating that reduction in the crystallite or particle size of the active material significantly improves the capacity retention [15, 131, 140-142]. Huggins *et al*

suggested that a critical radius could be determined below which, the fracture of the particle would not occur and this value depended on the extent of lithiation and the fracture toughness of the lower specific volume phase [131]. Consequently, the percent volume expansion or the strain generated in the material was found to be directly proportional to the extent of lithiation in the material. Liang *et al* first reported the use of silicon nanoparticles as anode and obtained a reversible capacity of 1700 mAh/g at the end of the 10th cycle [143]. Although inferior to the cyclability of graphite based anodes, it was a significant improvement compared to bulk crystalline *Si* electrodes. Since then, several attempts have been made to synthesize nanosized silicon by different synthesis routes and all the results have demonstrated better capacity retention [75, 136, 144, 145]. A recent study in fact, reports a strong particle size dependence on the cyclability, wherein, silicon particles below 150 nm in diameter did not fracture while those of larger sizes developed surface cracks resulting in the fracture of material upon lithiation demonstrating the influence of reduced particle size on the electrochemical response minimizing or even eliminating the adverse catastrophic effects of the colossal volume expansion related stresses [15].

1.2.13.2 Active-inactive matrices

The generation of the inactive phase via *in situ* electrochemical reaction of Li^+ , for example in the case of SnO_2 , results in the irreversible consumption of Li^+ generating Li_2O , which nevertheless, serves as a glassy Li-ion conductor as well as a binding matrix serving as a spectator 'glue' phase holding the active material accommodating the large volume expansion of Sn [130]. Similarly, the sub-oxides of silicon (SiO_x) were also studied wherein the lower suboxides of silicon ($SiO_{0.8}$) exhibited higher capacity (~1600 mAh/g) but poor cyclability.

Higher suboxides- $SiO_{1.1}$ however exhibited lower capacity (~800 mAh/g) but expectedly better capacity retention [146]. These silicon suboxide materials still had a large first cycle irreversible loss of ~50%, arising from the formation of Li_2O by the irreversible reduction of SiO_x by Li during the first cycle [144].

However, the generation of ‘active-inactive’ component phases directly via *ex situ* approaches that are not electrochemical in nature thus obviating the extraneous consumption of Li to form inactive species that serve to bind and hold the lithiated phase. The *ex situ* generation of electrochemically active and inactive thermodynamically stable phases serve to directly expose the active phase for lithium reaction thus serving to significantly reduce the first cycle irreversible losses to values considerably lower than 50% seen in the Fuji® tin oxide systems wherein the oxide is electrochemically reduced to form electrochemically active-inactive phases thus consuming a large amount of Li that is irreversibly lost. In the *ex situ* approach, the thermodynamic Li-inactive phase is homogeneously distributed within the thermodynamic Li-active phase. This eliminates the irreversible consumption of Li leading to the first cycle irreversible (FIR) loss of Li . Accordingly, TiN , TiB_2 , SiC and C have been studied as potential inactive matrices for silicon based anodes by the Kumta group [9-11, 22, 147]. Here, bulk crystalline Si was mechanically milled with the above-mentioned matrices to form a homogeneous phase, wherein, Si is dispersed uniformly in the electrochemically inactive matrix. These electronically conducting matrices are electronically conducting and help in the charge transfer reactions associated with the lithium alloying and de-alloying with silicon. Silicon obtained from these approaches was either nanocrystalline or amorphous. Although very low capacities of 300-400 mAh/g were obtained, the cyclability was better in comparison to commercial microcrystalline silicon.

1.2.13.3 Active-active matrices

The active-inactive matrix approach, while improving the cyclability of the anode compared to the bulk crystalline silicon, attained reversible capacities that were significantly lower compared to the theoretical capacity of silicon. This is because the inactive material selected was heavier which decreased the overall capacity of the electrode. To overcome this problem, a matrix that is soft, ductile and lightweight is needed to alleviate the stresses generated during the lithiation of the active material, thereby improving the cyclability of the electrode while not compromising on the overall capacity. Carbon appears to be an obvious choice, since it is much lighter than previously explored nitrides or borides; and mechanically soft, thus serving as a good secondary matrix.

Si/C composites were first developed by Dahn *et al* in the 1990s by decomposing polymers of silicon and carbon such as polymethylphenylsiloxane (PMPS) and polyphenylsesquisiloxane (PPSSO) in the temperature range of 900°C - 1300°C [143]. The *Si/C* composites obtained at 1000°C showed a reversible capacity of 550 mAh/g but the capacity dropped to 200 mAh/g when higher decomposition temperatures (1300°C) were used. The formation of electrochemically inactive *SiC* at very higher temperatures (1300°C) resulted in lower capacity and additionally, composites with a desired *Si/C* composition was difficult to achieve using these *Si* and *C* polymers. Other precursors such as epoxy silanes [148] and pitch polysilanes [149-152] were also used at high decomposition temperatures to synthesize the *Si/C* composite. The capacities obtained from these materials, however were low (<500 mAh/g) and exhibited large first cycle irreversible loss, possibly due to the presence of oxygen and formation of *SiC* at very high temperatures. Therefore, research was focused towards using silane gas

(SiH_4) as the silicon precursor (instead of polysilane polymers) that could be decomposed at low temperatures of 500°C and below. Nanosized silicon in the range of 10-20 nm deposited on KS6 graphite by decomposing silane gas in a thermal vapor deposition (TVD) showed a reversible capacity around 1000 mAh/g, low first cycle irreversible loss of 26% and a fade rate of only 2% [153]. The good cyclability of this Si/C composite was attributed to the good adhesion of the nanosized silicon (50 nm) particles to the graphite surface of KS6. Although Si/C composites with high capacity and capacity retention were obtained by the TVD of Si precursor gases, it was still difficult to control the particle size, structure and composition. This could be achieved using ball milling, which is a simple and high throughput approach, wherein, Si is milled with graphite and a polymer serving as a diffusion barrier preventing the milling induced diffusive reaction between Si and C forming the electrochemically inactive SiC , resulting in a homogenous Si/C composite. Wang *et al* and Datta *et al* have developed Si/C nanocomposites by mechanical milling of commercial microcrystalline Si and graphite along with polyacrylonitrile (PAN) followed by heated treatment in argon [147, 154, 155]. Silicon, in these nanocomposites was observed to be uniformly dispersed in the carbon matrix and PAN served as the appropriate diffusion barrier between Si and C , to prevent the formation of silicon carbide, SiC during mechanical milling. These first generation Si/C nanocomposites accordingly exhibited stable capacities in the range 550 to 700 mAh/g with a low first cycle irreversible loss of 26-30%.

1.2.13.4 Amorphous silicon

Unlike crystalline silicon, amorphous silicon ($\alpha\text{-Si}$) does not exhibit any long-range order, and contains large number of defects and free volume. Due to the presence of this disordered structure, the volume expansion upon lithium insertion is distributed homogeneously, and the net

effect of crack formation and propagation is less catastrophic compared to crystalline silicon [13, 14, 156]. Hence, the amount of pulverization of the active material is significantly reduced, which gives rise to enhanced capacity retention and cyclability. For Li-ion battery applications, thin films of *a-Si* are usually grown on metal substrates such as *Ni* and *Cu* using physical vapor deposition (PVD) techniques and are directly assembled in coin cells without additives such as binders and other conductive additives [14, 23, 24, 157]. For example, a 100 nm *a-Si* film deposited on *Ni* foil by vacuum evaporation exhibited a very high first discharge capacity of 2500 mAh/g and a stable reversible capacity of 2000 mAh/g for 50 cycles [157].

Additionally, Maranchi *et al* studied *a-Si* films (250 nm thick) deposited on *Cu* foil by RF magnetron sputtering that exhibited high first and second discharge capacities of 4100 mAh/g and 3800 mAh/g, respectively [24]. These films had excellent capacity retention until 29 cycles, beyond which there was a rapid capacity fade, resulting in a capacity of only 1800 mAh/g at the end of 40 cycles. Although stable for few cycles, the good cycling stability of amorphous silicon was attributed to the structural integrity and efficient binding of silicon atoms to the current collector [24]. *a-Si* can also be obtained by thermal cracking of silane gas (SiH_4) using a low pressure chemical vapor deposition (LPCVD) reactor in the temperature range of 485°C to 500°C [5, 158]. These were mainly utilized in developing 3-D heterostructures, nanowires, nanotubes and core-shell structures, and will be discussed in the subsequent sections. In spite of achieving and displaying better electrochemical performance compared to bulk crystalline silicon, *a-Si* films generated by PVD methods such as evaporation and sputtering are usually expensive and are characterized by low yields, thus preventing them from being implemented for large scale production.

1.2.13.5 Nanoscale silicon architectures

Over the past several years, much interest was shown on developing novel silicon architectures, wherein the morphology of the material was engineered to result in desired improved and sustained electrochemical performance. In these architectures, the structure played a critical role in alleviating the stresses that develop during the volume expansion process, thus preventing or delaying the onset of crack formation, that eventually leads to pulverization and capacity fade as outlined above. These architectures are either single phase, containing only silicon such as nanowires, nanotubes, porous silicon, or multicomponent heterostructures such as core-shells and bio-inspired structures. The silicon comprised in these structures is either in the nanocrystalline or amorphous state. Among the many architectures reported in the literature, few relevant and representative examples have been selected which are discussed briefly in the following sections:

1.2.13.6 Silicon Nanowires

The use of silicon nanowires as Li-ion anodes was first reported by Chan *et al*, which demonstrated very high gravimetric capacities and good cyclability [2]. Since then, immense interest was generated to explore one dimensional structures offering strain relaxation, as a viable solution to address the mechanical failure problem in silicon anodes. The Si-nanowires are typically grown by a vapor-liquid-solid (VLS) mechanism by decomposing SiH_4 on stainless steel substrates which were used directly without using any conductive or binder additives (shown in **Figure 22**). A low first cycle irreversible loss of 27% and reversible capacities >3000 mAh/g were obtained for 10 cycles. In the case of these nanowires, the volume expansion resulted in an increase in the length and diameter; the stresses generated as a result were facile

and less damaging, leading to superior cycling stability. Additionally, the good adherence of nanowires to the current collector contributed to good electronic transport, resulting in good rate characteristics. The first cycle irreversible loss for these nanowires (27%) was still high compared to the graphite based anodes and may be due to possible SEI layer formation [2]. This irreversible loss could be lowered by coating the nanowire surface with carbon [159, 160] or copper [160], which decreased the electrolyte decomposition improving charge transfer kinetics. The long term stability, loading and sustained coulombic efficiency are still nevertheless issues that need to be addressed.

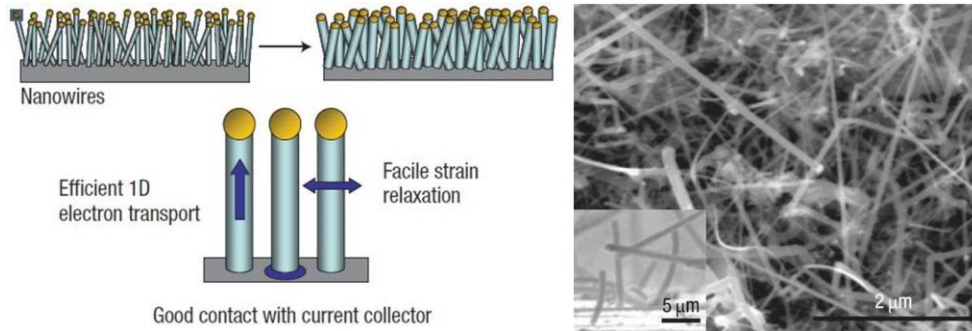


Figure 22: Schematic of SiNWs grown directly on current collector donot pulverize due to facile strain relaxation and SEM image of SiNWs [2]

1.2.13.7 Silicon Heterostructures

Silicon heterostructures are multi-component systems containing amorphous or crystalline silicon along with other electrochemically active/inactive phase(s). These heterostructures are usually designed using a bottom up approach, resulting in a morphology that mitigates the stresses developed as a result of the lithium induced volume expansion known in silicon. Compared to pure silicon containing nanostructures, heterostructures that are electronically conductive offer added advantages in terms of faster charger transfer kinetics, lower impedance and good rate capability.

Carbon nanotubes (CNTs) have attracted immense attention over the past decades due to their extraordinary mechanical and electrical properties [26, 27, 161], thus exhibiting a potential to serve as an excellent secondary inactive matrix or support for silicon. Wang *et al* first demonstrated the use of CNT/Si heterostructures developed by a simple 2-step CVD approach for use as high capacity Li-ion anodes [5]. In this study, long vertically aligned multiwall carbon nanotubes (MWCNTs) were first grown on quartz substrates, and then silicon was coated onto them as droplets by decomposing silane (SiH_4) (shown in **Figure 23**). A low first cycle

irreversible (FIR) loss of 20% and reversible capacities >2050 mAh/g (at 100 mA/g, 25 cycles) were obtained using these structures. An amorphous carbon coating applied to the system by other groups further improved the cyclability and coulombic efficiency of the CNT/Si heterostructures [162].

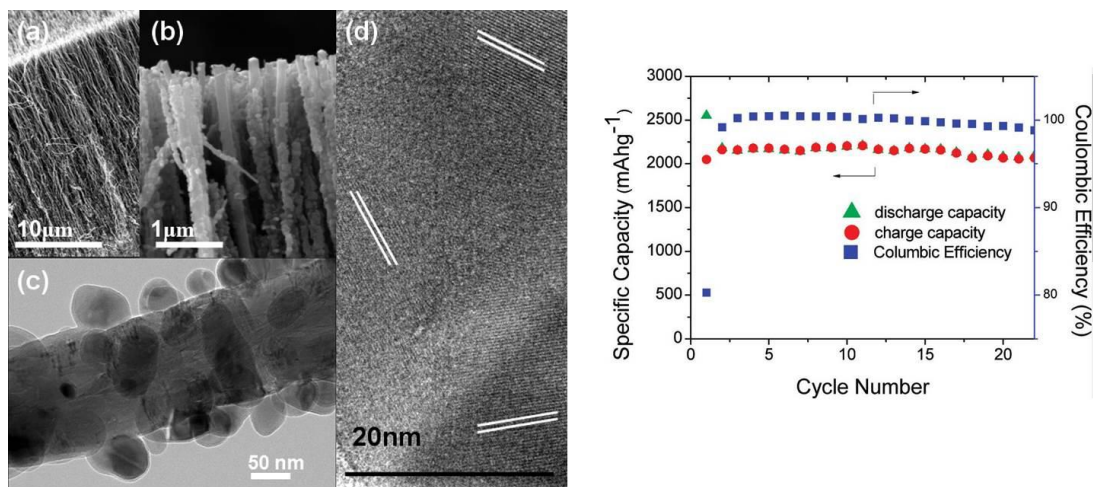


Figure 23: Left- SEM & HRTEM images of vertically aligned carbon nanotubes (VACNTs) coated with silicon droplets; Right-Capacity plot of the heterostructures cycled at 100 mA/g between voltage range-0.02 to 1.2 V vs. Li⁺/Li [5]

In another study, silicon was coated as droplets on annealed carbon black particles and was later coated with carbon using CVD [163]. This resulted in a hierarchical bottom up assembly of rigid spheres with open interconnected channels, delivering capacities close to 2000 mAh/g (at C/20 rate) for 100 cycles. The strong interface between C and Si in these heterostructures is believed to be critical in holding the silicon droplets together, despite the strain mismatch occurring due to the colossal volume changes [5]. However, this interface may not be strong enough to maintain the heterostructure without pulverization at very high current rates. To address this problem, Krishnan *et al* developed a strain-graded structure containing carbon, aluminum and silicon that exhibited excellent rate characteristics [164]. In this study,

carbon nanorods were first deposited on stainless steel substrates using oblique angle sputter deposition (OAD) technique. Following this, a thin layer of aluminum was deposited on these nanorods and finally, silicon was coated to form a tri-material composite, resulting in a nanoscoop like structure. Using these strain-engineered structures, a reversible capacity of 412 mAh/g was achieved at very high current rates of 51.2 A/g for over 100 cycles. The introduction of aluminum as an intermediate layer enabled the gradual transition of strain from carbon to silicon, resulting in the minimization of strain mismatch at the interfaces. In another study, $TiSi_2$ nanonets were used as a strong and conductive core, decorated with CVD derived silicon droplets [165]. These $TiSi_2/Si$ heterostructures when cycled at a high current density of 8.4 A/g and, when cycled in the voltage window 0.15 V to 3 V vs. Li^+/Li , displayed capacities >1000 mAh/g and a low capacity fade of 0.1% between 20th and 100 cycles. Decreasing the lithiation cut-off voltage further to 0.03 V however adversely affected the cyclability. This is because, at lower voltages, lithiation of the $TiSi_2$ core was initiated, resulting in a stress related pulverization of the heterostructure. Another similar heterostructure, $TiC/C/Si$ was also studied, wherein, the TiC/C served as a mechanically robust and electronically conducting core resulting in reversible capacities of ~3000 mAh/g (cycled at 0.84 A/g) with a 92% capacity retention at the end of 100 cycles [166].

More recently, nature inspired egg-yolk shell [167] and pomegranate based structures were also developed that exhibited high capacities and capacity retention for more than 1000 cycles. In the egg-yolk shell structures, commercial silicon nanoparticles were sealed inside a thin, conformal, self-supporting amorphous carbon shell with a well-designed void space that allowed silicon to expand freely without breaking the outer shell. Reversible capacities of ~2800 mAh/g (at C/10 rate) were obtained using these egg-yolk shell structures for over 1000 cycles

with a capacity retention of 74% and a coulombic efficiency of 99.84% [167]. Using this approach, in another study, the carbon encapsulated silicon shells were further self-assembled in a hierarchical arrangement to form a pomegranate type structure, which resulted in a capacity retention of 97% after 1000 cycles. The accommodation of volume expansion of silicon into the void spaces and stabilization of SEI layer formation were believed to be the main reasons for the superior cycling stability of the egg-yolk and pomegranate structures.

1.2.13.8 Silicon Nanotubes

Among strain engineered structures consisting of pure silicon, silicon nanotubes (Si-NTs) have attracted immense interest as Li-ion anodes, owing to their good cyclability and long cycle life. The nanotubes are tubular structures or hollow cylinders of silicon, which are typically made by using a sacrificial one-dimensional template. In addition to the facile strain relaxation exhibited by one-dimensional structure such as silicon nanowires, nanotubes have large amount of free volume that allows the silicon to expand freely without cracking and pulverization. Park *et al* reported the first use of silicon nanotubes as Li-ion anodes [12]. These nanotubes were synthesized first by impregnating alumina membranes with silicon naphthalide. This was followed by their reductive decomposition to form silicon and finally, the alumina membranes were etched to form hollow silicon nanotubes. These nanotubes exhibited a reversible capacity of 3247 mAh/g (at 0.2C rate), a first cycle irreversible loss of 11%, good rate characteristics with capacities approaching 2800 mAh/g at high current rates of 5C (15 A/g) and good cyclability. A thin amorphous carbon layer that was formed on the silicon nanotube surface during the reductive decomposition process was believed to prevent the electrolyte decomposition and promote the formation of a stable SEI layer [12]. A recent report from the same research group

showed double-walled silicon nanotubes consisting of a hollow inner silicon tube and an outer oxide layer (SiO_x) to have extraordinary cycling stability for over 6000 cycles [30] (**Figure 24**). The outer (SiO_x) layer served as a rigid mechanical clamping layer that allowed the silicon to expand inwards, thus preventing contact with electrolyte.

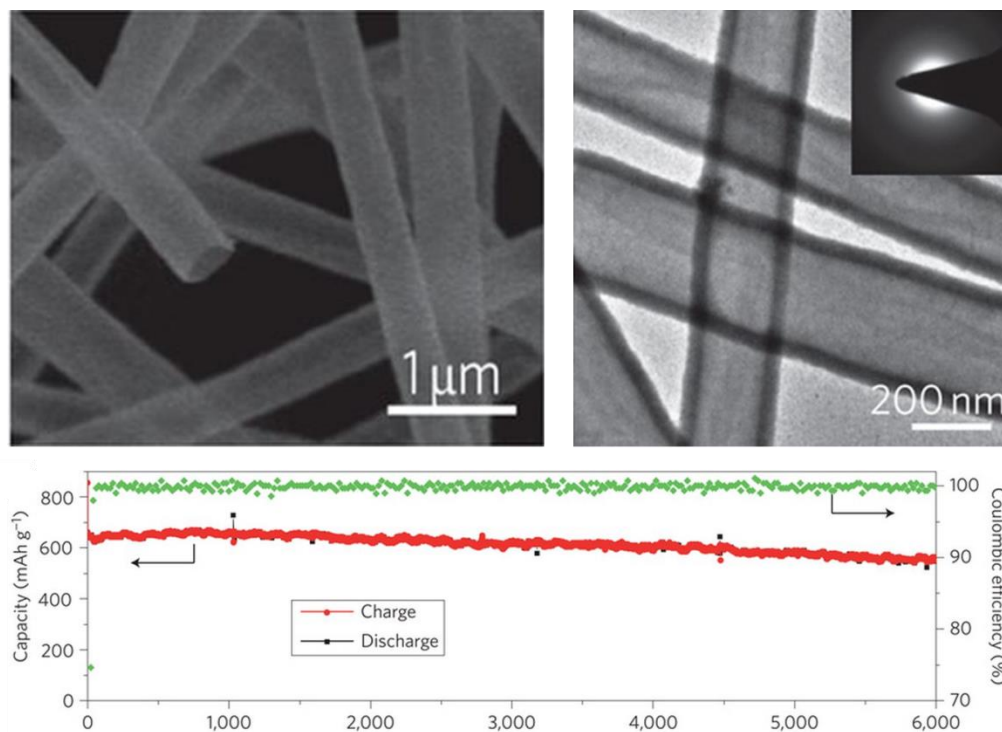


Figure 24: SEM & HRTEM (top) images of the double walled SiNTs; long term stability plot of these nanotubes cycled at 12C rate [30]

In another study, arrays of sealed silicon nanotubes were grown using a sacrificial ZnO nanorod template on current collector by CVD [29]. These free standing aligned sealed silicon nanotube arrays were directly tested without the use of any binders and exhibited good cycling and rate characteristics. The first cycle irreversible loss was observed to be in the range 10-13% and retained 80% of capacity after 50 cycles.

From the above reported studies it can be gleaned that while silicon nanotubes seem an attractive choice, they however suffer from two major disadvantages. The methods employed to synthesize these nanotubes result in low yields of the Si nanotubes. Moreover, they further require use of expensive reagents, and non-recyclable template precursors, which increased the overall production costs rendering the approach questionable in terms of actual implementation for practical applications. Additionally, the low loadings achieved from these approaches ($<1 \text{ mg/cm}^2$) resulting in an overall low areal capacity ($<1 \text{ mAh/cm}^2$) compounded with the low yields is another major drawback. A high areal capacity in the range $2\text{-}3 \text{ mAh/cm}^2$ is typically desired to match the capacity of cathodes in an assembled full cell. Thus, while developing materials for anodes in a Li-ion battery, it is very important that, in addition to obtaining low first cycle irreversible (FIR) loss, good cyclability and rate capability; emphasis is placed on obtaining high loading/areal capacities and developing a synthesis approach that is facile.

1.2.14 Impact of Synthesis Methods

Apart from the material and its electrochemical properties, other factors that play an important role when selecting materials for anode or cathode are cost of the raw materials or precursors, the synthesis technique, recycling costs, and the environmental effects of the by-products generated during the production. From a commercialization standpoint, often, significant emphasis is placed on the synthesis technique for generating materials involved in the battery production as it predominantly affects other factors such as cost, raw materials and environmental effects. Outlined below is a brief description of the procedure and principle of the various synthesis

methods that were employed in this dissertation study to generate different nanocrystalline and amorphous silicon nanostructures.

1.2.14.1 High Energy Mechanical Milling

High energy mechanical milling (HEMM) is a powder processing technique that uses mechanical energy to generate both equilibrium and metastable phases of materials. This technique has been widely used for carrying out several processes such as solid state reactions (also known as mechanochemical reactions), particle size reduction, mixing of materials, and amorphization i.e. introduction of disorder into the structure. Due to the lower costs and faster reaction times associated with this synthesis technique, HEMM has become attractive for large-scale production and processing of variety of powders.

In HEMM, the starting materials are added to the milling vial along with grinding media (usually hardened steel balls) and sealed in an ambient or protective atmosphere. The vial is then subjected to milling action for a desired amount of time. During this process, the powder particles are caught in between the balls or between the ball and the vial, and undergo various stresses due to the absorption of mechanical energy arising from the milling action. The stresses comprising of compression, shear (attrition), impact (stroke) and impact (collision) often result in continuous flattening, cold welding, fracture and rewelding of the particles. The fracturing of particles may occur through two processes: (a) the continual action of mechanical stresses resulting in plastic deformation and work hardening of the particles, eventually leading to fracture due to a fatigue assisted failure mechanism; and/or (b) by fracturing due to the formation of brittle/fragile structures. Furthermore, the secondary particles obtained from fracturing undergo rewelding to form larger particles. Due to the absence of a strong force to form

agglomerates, steady state equilibrium is eventually reached between fragmentation and agglomeration, resulting in a decreased average particle size. The milling reaction is also significantly affected by other process variables such as ball to powder ratio, milling speed, milling time, extent of filling the vial, milling atmosphere, etc. Controlling one or more of these process variables can result in a desired alloying reaction, particle size and morphology.

HEMM offers several advantages over conventional processing techniques. It is an inexpensive and rapid process capable of generating large yields of the final material and is easily amenable to large scale production. It can also be used to synthesize alloys comprising of immiscible elements. This is because HEMM is a completely solid state processing technique and therefore not limited by the phase diagram. However, one of the major drawbacks of using HEMM is that, longer milling times can result in the contamination of the final product with materials present in the milling media or vial, thereby affecting the purity and properties of the final product.

1.2.14.2 Electrodeposition

Electrodeposition or electroplating is a simple technique that has been widely used over several decades to form metal or alloy coatings for protective, decorative and other surface specific functional applications. The deposition is usually carried out in an electrolytic cell by passing an electric current or applying a voltage to the substrate. The electrolytic cell consists of three main components: working electrode, where the deposition occurs; counter electrode, which serves as an inert or sacrificial electrode; and an electrolyte, which serves as the medium for ionic conduction. A third electrode, namely the reference electrode whose potential is fixed is often times connected to the electrolytic cell. This is used to accurately measure the voltage of the

working electrode. Two main methods, namely, potentiostatic and galvanostatic methods are employed for deposition purposes. In the potentiostatic mode, the working electrode which serves as the surface for deposition to occur, is held at a constant voltage; whereas, in galvanostatic mode, a constant current density is applied to this electrode for the deposition to occur. In both cases, electrons are being supplied to the working electrode and the positive ions in the electrolyte accept the electrons resulting in the deposition of a metallic or alloy coating on the surface of the working electrode. Deposition variables such as electrolyte composition, applied voltage, current density and time of deposition can all be varied to generate different coating morphologies such as thin/thick films, nanoparticles, nanowires, nanotubes islands and other core-shell structures, the quantity and nature of the deposit dictated by the well-known Faraday's laws and electrochemical principles. Faraday's law, developed for the electroplating systems states that the amount of the material/coating deposited on the electrode is directly proportional to the amount of electricity (measured in Coloumbs, C) consumed. Due to the efficacy of the process, electroplating can serve as an inexpensive and rapid process to develop thin film coatings on metal substrates on a large scale.

A majority of the electrodeposition processes employed in the plating industry use aqueous based electrolytes, where water is used as the main solvent to dissolve the ionic species. They suffer from several drawbacks such as liberation of unwanted hydrogen gas due to electrolysis, narrow electrochemical window governed by the electrochemical stability of water, higher vapor pressure causing rapid evaporation combined with poor thermal stability. These problems can be overcome by using non-aqueous electrolytes such as molten salts, ionic liquids and organic solvent based electrolytes. Molten salts contain two or more salts melted together at high temperatures along with the electro-active species to form the electrolyte and are known to

exhibit good thermal stabilities and high ionic conductivities. Typical molten salts used for plating experiments are composed of *KCl-NaCl*, *LiCl-KCl* eutectic systems that operate in a temperature range of 400°C to 800°C. Ionic liquids are another class of molten salt electrolytes, but have low melting points and hence, are usually liquid at room temperatures. These are usually made of quaternary ammonium salts such as tetraalkylammonium $[R_4N]^+$, or cyclic cyclic amines: aromatic (pyridinium, imidazolium) and saturated (piperidinium, pyrrolidinium) ones. In the case of organic solvent based electrolytes, the electroactive species is dissolved in an appropriate organic solvent with sufficient dielectric strength. Propylene carbonate (PC), acetonitrile, tetrahydrofuran (THF), N, N dimethylformamide (DMF) and dimethyl sulfoxide (DMSO) are a few examples. The ionic conductivity of these organic solvents is however very low and hence a supporting electrolyte is often added to improve their conductivity.

1.2.14.3 Chemical Vapor Deposition

Chemical vapor deposition (CVD) is an attractive technique to generate uniform and high quality thin films or particle coatings of various materials on a substrate, and is widely used in the semiconductor industry. In a typical CVD process, one or more volatile precursors are introduced into a reactor, where they allowed to react and/or decompose on the substrate to form the desired material. The reactions inside a CVD reactor are governed by thermodynamics, which determines the driving force of the reaction; and by kinetics, which defines the transport phenomenon (or rate-control mechanism). CVD technique can be used to obtain a more uniform coating on the substrate in comparison to PVD methods such as DC/RF sputtering or e-Beam evaporation, as they suffer from a non-conformal coverage due to the shadow effect. Process parameters influencing the CVD process include substrate temperature, flow rate of the carrier

gases, reactor pressure, etc. which can be controlled to obtain several morphologies such as thin films, particles, one dimensional nanowires/nanofibers and other architectures.

The superior mechanical and electrical properties of carbon nanotubes [26, 27, 161], have enabled them to be used in various applications such as catalyst supports [168-170], energy storage devices [4, 5, 171-174], sensors [175-177] etc. Amongst the well-known methods such as arc discharge and laser ablation developed so far for synthesizing CNTs [178], CVD offers a simple and economical way of producing CNTs at relatively lower temperatures and ambient pressures. Additionally, CVD is known to give higher yields and purity when compare to producing CNTs by other methods. Carbon nanotubes can be synthesized in multiple forms and architectures such as powder, thin or thick films, coils, straight or entangled and vertically aligned structures; and CVD offers better control during the growth process to produce these architectures making it a highly versatile technique, especially for CNT production. For example, in Li-ion batteries, CNT/Si heterostructures developed by liquid or gas injected CVD method exhibited high discharge capacities and good rate capabilities [4, 5, 174]. The CVD process also enabled the CNTs to assume an architecture that is dense, long and vertically aligned, and thus played a critical role contributing to the improved electrochemical performance of the CNT/Si hybrid heterostructures.

2.0 OBJECTIVES

2.1 LIMITATION OF CURRENT SILICON BASED ANODES

As described in the earlier sections, though silicon has a very high theoretical capacity of 4200 mAh/g, it suffers from the colossal volume changes that occur in the crystalline bulk silicon during alloying/de-alloying (charge/discharge) processes resulting in the pulverization of the material. This is followed by loss inter-particle electrical contact with the current collector. This severely affects the electrochemical performance such as:

- Large first cycle irreversible loss (>80%) due to loss of active material as a result of pulverization
- Large capacity fade (>5% loss/cycle) due to further continued pulverization of the active material, rendering impractical to be used for long cycle life
- Continual formation of the solid electrolyte interphase (SEI) layer on the newly formed surfaces of the secondary pulverized particles which results in the consumption of extra lithium, resulting in poor coulombic efficiency and capacity fade

As a result of the above mentioned drawbacks, the specific capacity of the bulk crystalline silicon based anodes reduces to less than 100 mAh/g in 20 cycles, preventing the implementation of Si as a replacement to graphite for the next generation of high energy density anodes.

2.2 HYPOTHESIS AND APPROACH

The large first cycle irreversible loss and rapid capacity fade can be minimized by preventing the material pulverization during repeated cycling. The mechanical stresses resulting from the large volumetric changes during the alloying and de-alloying reactions can be greatly minimized by controlling the microstructure, morphology, and particle size combined with use of active/inactive matrices etc. The hypothesis for the approaches that were implemented in this dissertation are discussed in the following:

- **Crystallite size reduction:** Decreasing the particle or crystallite size to less than 100 to 200 nm alleviates the mechanical stresses responsible for propagation of microcracks leading to fracture of material. Smaller particle size materials undergo superplastic deformation, thereby delaying the advent of fracture. Additionally, decreasing the particle size results in short Li^+ ion diffusion distances, improving the rate characteristics of the battery.
- **Use of amorphous phase:** Amorphous silicon has a completely disordered structure containing defects and large amount of free volume. The volume expansion of silicon occurs in an isotropic fashion compared to that of crystalline silicon, resulting in a homogenous distribution of mechanical stresses.
- **Use of appropriate support matrix:** Development and use of a strong, mechanically robust and electronically conducting matrix to accommodate the mechanical strain

developed in silicon will help alleviate the capacity fade contributing to improved charge transfer kinetics.

- Develop strain engineered morphology composed that is able to withstand the strain without fracture upon repeated cycling.

The overall objectives of this dissertation are to develop cost effective strategies to synthesize silicon based nanostructures such that they deliver:

- High specific capacity greater (>1000 mAh/g)
- Low first cycle irreversible loss (FIR) ($<15\%$)
- Good capacity retention, cyclability and rate capability
- High coulombic efficiency ($>99\%$)
- Obtain a fundamental scientific understanding of the ensuing electrochemical and material related phenomena at the structural, microstructural and compositional end

Accordingly, this dissertation is aimed at achieving the above mentioned objectives by synthesizing nanocrystalline and amorphous structures of silicon using cost effective methods.

The specific research goals are thus outlined below:

1. Research goal 1: To generate high surface area silicon nanoparticles by high energy mechanical milling (HEMM) and study its potential for use as Li-ion anodes

A simple and facile approach utilizing inexpensive precursors via a mechanochemical reduction approach will be explored to generate silicon nanoparticles. An acid etching process will be used to generate the desired nanocrystalline silicon exhibiting with very high specific

surface area (SSA), small particle size and high porosity. The obtained silicon nanoparticles will be mixed with binder and conductive additives and tested for their electrochemical response using conventional slurry based electrodes.

2. Research goal 2: To generate and study amorphous silicon by electrodeposition of halide salts of Si from organic solvents

Electrochemical reduction of SiCl_4 from an organic solvent will be conducted to obtain thin films of amorphous silicon (*a*-Si). These films will directly be deposited on copper foil and will be directly assembled in the battery serving as a binder-less approach capable of producing thin films of amorphous silicon and easily scaled up to produce *a*-Si potentially at large industrial scales.

3. Research goal 3: To synthesize and investigate CNT-Si heterostructures by chemical vapor deposition (CVD)

Vertically aligned carbon nanotubes (VACNTs) will be grown on quartz substrates from a liquid based carbon precursor and a floating iron based catalyst. Silicon will be deposited on these CNTs by thermal cracking of silane (SiH_4) gas. The deposition parameters will be selected to obtain two different sets of morphologies of silicon (nanoscale droplets and thin films) on the CNTs. The CNT-Si heterostructures will be removed from the quartz substrate and mixed with conductive additives and binders to prepare conventional slurry based electrodes.

4. **Research goal 4: To identify and conduct a fundamental study of a scalable synthesis approach for the generation of hollow of Silicon Nanotubes as high capacity Li-ion anodes**

To obtain large quantities of silicon nanotubes, high aspect ratio nanowires of *MgO* will be synthesized by a simple hydrothermal route which will be used as a template to uniformly coat amorphous silicon on the surface of the nanowires. The *MgO* nanowires will then be removed by leaching in a mineral acid to obtain copious amounts of silicon nanotubes (SiNTs) that can potentially be extended for large scale production. A fundamental understanding of the synthesis parameters and their influence on the structure and microstructure of hollow (h-SiNTs) and their corresponding contribution to the electrochemical response will be systematically studied.

Characterization of the synthesized Si based nanocomposites

- X-Ray diffraction and Raman spectroscopy will be used to investigate the presence and nature of various phases present and also study the structure of silicon obtained by the various synthesis techniques discussed earlier.
- High resolution scanning electron microscopy (HRSEM) and transmission electron microscopy (HRTEM) will be used to study the morphology of the interface structure of the nanocomposites developed.
- The electrochemical characteristics of the nanocomposites will be investigated in detail and the structure-property correlation relating the morphology and microstructure of the nanocomposites; the interface between the electrochemically active and the electrolyte interphase and their electrochemical performance will be established using a variety of

galvanostatic , potentiostatic and impedance techniques with the ultimate goal being to develop strategies for optimizing the synthesis parameters to develop nanoscale structures and architectures that will exhibit the desired optimal performance characteristics of high capacity, reduced FIR and good capacity retention at low and high current rates.

3.0 EXPERIMENTAL TECHNIQUES

The experimental methods for the earlier mentioned research goals outlined for this study are divided into two sections. The first section contains the different synthesis methods that are employed to generate various nanostructured and amorphous composites of silicon. In the second section, detailed characterization methods that were used to analyze the final product for their structure, morphology and electrochemical properties are discussed in detail.

3.1 SYNTHESIS OF NANOCRYSTALLINE AND AMORPHOUS SILICON STRUCTURES

3.1.1 High Energy Mechanical Milling (HEMM)

HEMM was used to perform solid state reaction between two materials at room temperature. The high energy generated by the impact action of the milling media can be used to initiate a chemical reaction, alloying of materials and the resultant pulverization of the material to reduce the particle size. Milling parameters such as charge to ball ratio and milling time are important as they determine the rate at which the energy is absorbed by the reactants to induce a chemical reaction. Optimization of the parameters results in maximum fragmentation and attrition with

minimum coalescence. Longer milling times may result in the accumulation of contaminants formed by the abrasion of the milling media and the vial. Good attrition results in the formation of nanoparticles which further lead to effective diffusion of chemical species for the reaction to occur. In this dissertation, HEMM was employed to generate silicon nanoparticles via a mechanochemical reduction reaction between Mg_2Si and SiO . The reactants (referred to as charge) are added to a stainless steel milling vial (**Figure 25**) along with milling media composed of hardened stainless steel balls. The vial is then batched to a SPEX CertiPrep mill capable of shaking the vial in a continuous asymmetric back and forth continuous motion at ~1080 cycles per minute (60 Hz model). After the reaction, the vial was removed and the contents of the product were scrapped off using a spatula and used for further characterization.



Figure 25: High energy mechanical mill from SPEX CertiPrep.

3.1.2 Electrodeposition

Electrodeposition can be carried out either in a two or three electrode system. In the present case, since both galvanostatic and potential sweep methods are used which require the monitoring of voltage of the working electrode, a reference electrode was also employed to constitute a three electrode system. Typically, the active material is coated only on one side of the current collector. In the case of electrodeposition, the coating is formed on all the surfaces where the electrode is in contact with the electrolyte. Hence, a custom made cylindrical electrochemical cell was designed wherein only side of the copper foil is in contact with the electrolyte (**Figure 26**). The cylindrical cell is made out of glass (ID=1 inch) with both ends threaded and closed using two polypropylene caps. The bottom cap contains a removable stainless steel base (316 L), a Teflon guide and copper foil (Insullectro), acting as working electrode; all of them screwed together to the cylindrical cell using a silicon o-ring. The diameter of the Teflon guide determines the area of the working electrode that is exposed to the electrolyte. A thin strip of copper foil was attached to the stainless steel base using an insulation tape for electrical conductivity. The top cap houses platinum foil and platinum wire acquired from Alfa Aesar, serving as the counter and reference electrodes, respectively. These electrodes are attached through a glass capillary that extends out of the electrochemical cell through a Plexi® glass top that is hot-glued to the polypropylene cap.

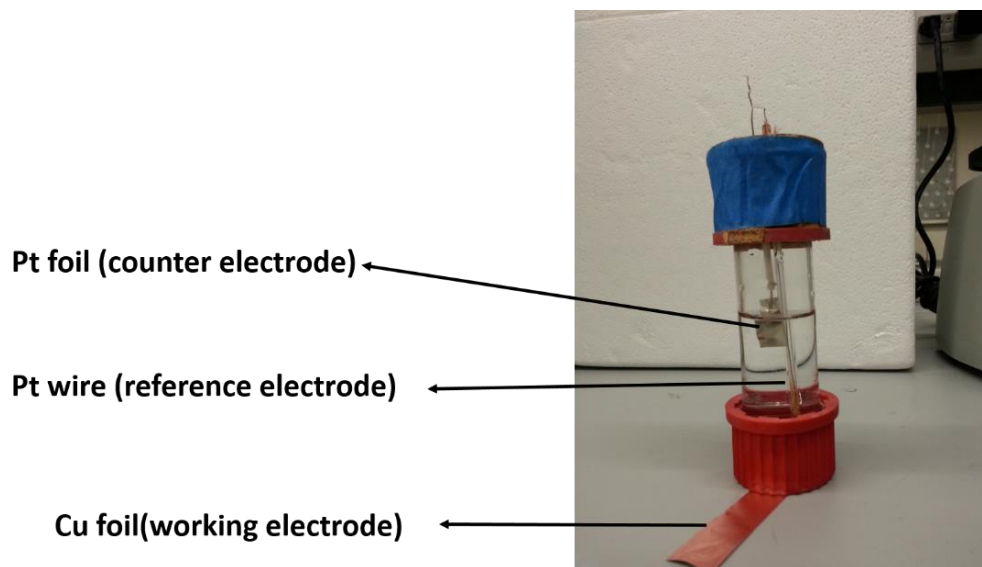


Figure 26: Electrochemical cell used for electrodeposition of silicon from organic solvents

The electrolyte used for the electrodeposition of silicon is non-aqueous based which contains air and moisture sensitive silicon salts. Therefore, the electrolyte was added to the electrochemical cell in an oxygen and moisture free glove box and sealed thoroughly using a PTFE gasket before it was exposed to the atmosphere for deposition experiments. After the coating was obtained, the cell was again transferred to the glove box (Labconco), opened and the electrodes were washed and stored in moisture free anhydrous acetone solvent before being tested for their electrochemical performance.

3.1.3 Chemical Vapor Deposition

Chemical Vapor Deposition (CVD) technique was used in this study for the growth of vertically aligned carbon nanotubes (VACNTs) and for silicon deposition.

The carbon nanotubes were grown using a floating catalyst method wherein the carbon source and the catalyst (*Fe* particles) are introduced into the reactor in vapor phase for subsequent decomposition of the hydrocarbons on the catalyst particles. Ultra high purity (UHP) argon and hydrogen were used as the carrier gases to carry the carbon-catalyst in to the CVD reactor and their flow rates were individually controlled using a Mass Flow Controller (MFC, MKS Instruments). The carbon-catalyst solution is injected using a syringe pump into a cylindrical stainless steel gas bubbler held at 200°C. The carbon-catalyst solution instantly vaporizes and the Ar/H₂ gas mixture carries these vapors into the CVD reactor. The reactor is made of 2 zones: preheater and reaction zone. The temperature in the preheater zone is 200°C and in this region effective mixing of the vapors takes place before entering the reactor zone. The center of the reactor zone is held at 770°C at which the carbon precursor (m-xylene) decomposes to form carbon and hydrogen in the gas phase. Simultaneously, the Ferrocene is reduced by hydrogen in this region to form iron nanoparticles on the quartz substrate. The *Fe* nanoparticles act as catalyst sites onto which the carbon obtained from the decomposition of m-xylene grow in a one dimensional fashion. Multiple catalyst sites are generated on the entire surface of the quartz slide onto which the carbon nanotubes grow in a 1D fashion resulting in a vertically aligned carbon nanotubes (VACNTs), resembling a dense forest like structure. The gases exiting the CVD reactor are bubbled through silicone oil inside a fume hood.

The silicon deposition was performed in a low pressure chemical vapor deposition (LPCVD) system by applying vacuum through the end of the CVD reactor tube. *SiH₄* gas was

used as the silicon source. Because of its high toxicity and reactivity, silane gas was delivered into the CVD reactor from an electronically controlled gas safety cabinet (Applied Energy Systems Inc, Malvern, PA) The stainless steel piping carrying the silane gas and the reactor tube were purged multiple times using UHP argon gas to remove any trace amount of air or moisture. Only UHP argon gas was used as the carrier gas and the Ar/SiH_4 gas mixture was directly fed into the reactor held at 500°C.

3.1.4 Hydrothermal Synthesis

Hydrothermal synthesis method is attractive for growing crystals and nanostructures by employing high temperature and high pressure conditions in a closed reactor. In this study, this technique was used to synthesize scalable quantities of the sacrificial template consisting of magnesium oxide nanorods which was further used to generate hollow silicon nanotubes (h-SiNTs). The temperature of the reaction and solvent used are very important as they determine the hydrothermal conditions (reaction temperature and pressure) that enable the feasibility of the intended reaction with a desirable microstructure. For making the MgO nanorod template, water was used as the solvent to dissolve the magnesium precursor and urea, which acts as a fuel and reducing agent. This solution is added to a reactor, known as the autoclave (**Figure 27**) (Parr Instrument Company, 125 mL) and is placed inside a box furnace. This method is advantageous because it requires lower reaction temperatures (<200°C), shorter reaction times (15-60 minutes) and involves simple equipment to produce large yields (1g of product per 120 ml autoclave capacity) of the product. After the reaction, the autoclave was allowed to cool down and the resulting products are collected on 0.5 μm PTFE membranes and thoroughly washed with DI water, isopropanol and air dried at 100°C.



Figure 27: Autoclave used for hydrothermal reactions

3.2 CHARACTERIZATION OF THE GENERATED SILICON NANOCOMPOSITES

3.2.1 X-ray Diffraction Analysis

The compositional and phase analysis of all the silicon based composites was studied using X-ray diffraction unit from Philips X'Pert Pro system equipped with a copper anode ($\lambda=0.15406$ nm) and operated at 45 kV-40 mA. All powder based samples were well packed in an aluminum sample holder with a stainless steel backing plate. It is important to ensure the X-rays are focused only on the sample and not on the sample holder to avoid any unwanted background

peaks. A Gonio axis scan was employed between the 2θ angles of 11° and 90° with a step size of 0.033° and step time of 50 s. The obtained X-ray scans were analyzed using X'Pert HighScore Plus software. For calculating the crystallite size, a pseudo Voigt function was used to calculate the Lorentzian and Gaussian contribution for the XRD peaks obtained. The effective crystallite size was determined from the Debye Scherrer formula by considering the integral breadth of the Lorentzian contribution using single line approximation after eliminating the instrumental broadening and lattice strain contribution.

For thin film electrodes, glancing angle X-ray diffraction (GAXRD) were performed using a Philips PW3710 based X'Pert diffractometer equipped with a copper anode in parallel beam geometry. In this case, the scans were recorded between 2θ angles of 10° and 67° with a step size of 0.02° and a step time of 0.1 s.

3.2.2 Scanning Electron Microscopy (SEM)

Morphological studies along with elemental compositional analysis were performed using a Philips XL 30 scanning electron microscope (SEM) equipped with an energy dispersive x-ray spectroscopy (EDAX) analyzer. The electron beam voltage was varied between 10 kV to 20 kV for obtaining optimal magnification and resolution. The sample preparation comprises spreading of the powder over an adhesive carbon tape placed on top of a metallic stub. A thin layer of palladium was coated on the powder sample by DC sputtering to prevent charging during the SEM operation.

In the case of imaging *MgO* nanorods and hollow silicon nanotubes (h-SiNTs), the nanostructures were first dispersed in isopropanol and then drop casted over glass slides ($1\text{ cm} \times$

1 cm). The coated glass slide was then placed over the carbon tape and an additional copper strip was attached connecting the glass slide and SEM stub.

3.2.3 Raman Spectroscopy

Raman spectroscopy was used to study the structural characteristics of the silicon composites generated by the various synthesis methods described. A Renishaw in via raman microscope was employed using a 633 nm red laser to study the material vibrational characteristics. The instrument was always calibrated using pure crystalline Si before obtaining any spectra. The sample to be analyzed was spread over a clean glass slide and the region of interest was focused and brought to the center using an optical microscope.

3.2.4 Transmission Electron Microscopy (TEM)

Transmission electron microscopy (TEM) was performed using a JEOL JEM 2000FX TEM (operated at 200 kV) to study additional morphological characteristics such as particle size, shape and distribution. The sample to be analyzed was first dispersed in methanol and sonicated for several hours to form a uniform dispersion. A simple hand held nebulizer was used to spray the methanol solution on to copper grids. The grids were first left to dry in air for one hour and then at 60°C for 2 h to ensure complete evaporation of the solvent.

3.2.5 Electrochemical Characterization

3.2.5.1 Preparation of electrode

All powder based silicon nanocomposites derived from the various synthesis techniques were coated on to the current collector using a typical slurry casting method. The silicon containing electrochemically active material was mixed with conductive additives, binder and solvent to form viscous slurry. Super-P from Timcal was the conductive additive used for all slurry coated electrodes. The binders used in this study are polyvinylidene fluoride (PVDF, Sigma Aldrich), sodium carboxymethyl cellulose (NaCMC, Fisher Scientific) and sodium alginate (NaAlg, MP Biomedicals). The binder was first dissolved in an appropriate solvent (DI water for NaCMC and NaAlg; N-methyl pyrrolidone, NMP for PVDF) and to this binder solution, active material and Super-P was added. For low density material such as in the case of CNT/Si and h-SiNTs, a 50 wt% of the active material along with 40 wt% of binder and 10 wt% of Super-P was used for casting the electrodes. For relatively dense materials such as silicon nanoparticles generated by HEMM, 80 wt% of active material was used along with 10 wt% each of binder and Super-P. Thorough mixing is needed as it is important that all the electrochemically active silicon particles that comprise the active component of the electrode are electronically connected to the current collector. The slurries are usually mixed overnight on a magnetic stirrer. The viscosity of the slurry was adjusted either by adding addition of the solvent used to make the binder solution or by placing it in vacuum for few minutes. The slurries with right viscosity were coated onto copper foils using the Doctor Blade method on an automatic film applicator (AFA III, MTI Corp). The coated foils were first dried in air and then placed in vacuum at 100 C overnight to completely remove the solvent. Electrodes were cut into circular discs using a Precision Die Cutter (MSK-T-06, MTI Corp) with a diameter of 9-11 mm.

3.2.5.2 Assembly of prototype battery

A prototype battery in a coin cell configuration (CR 2016 or CR 2025, Hohsen Corp and MTI Corp) was used to test the electrodes as shown in **Figure 28**. It is a two electrode system wherein the active material coated on copper foil acts as the working electrode and a lithium foil served as the counter as well as reference electrode. A thin polypropylene sheet (MTI Corp) cut in to circular disc was used as the separator between the working and counter electrodes. A stainless steel spring was also used which improved the contact of the current collectors with the base and cap components. The electrode assembly is done in an argon glove box with oxygen and moisture levels maintained less than 0.1 ppm.

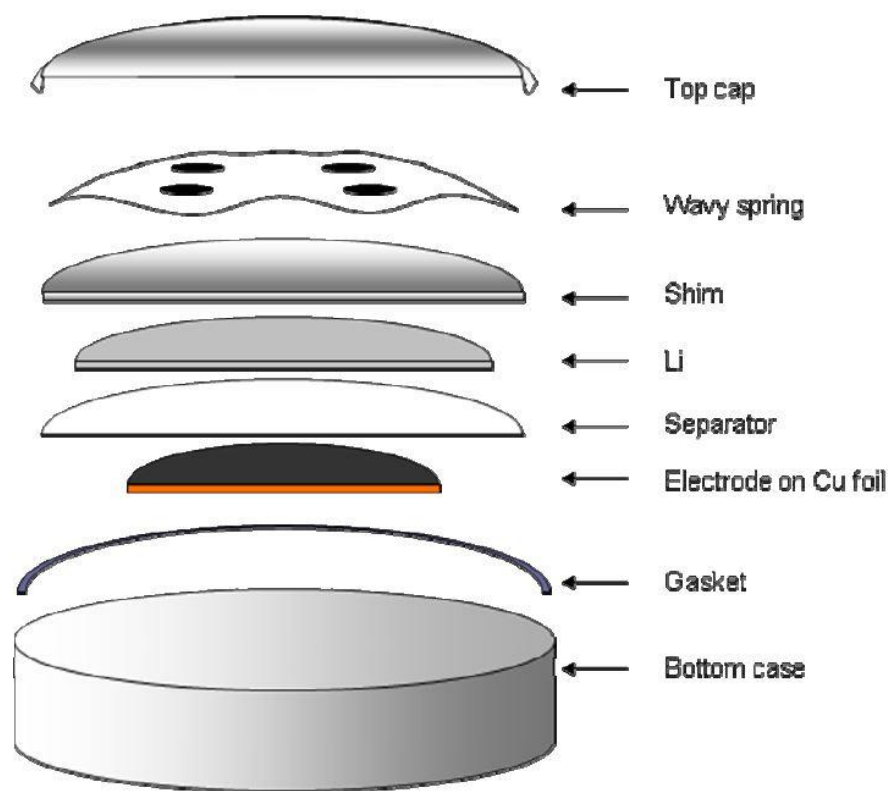


Figure 28: Schematic of the components of a prototype coin cell configuration

3.2.5.3 Electrochemical testing

All electrochemical testing of the electrodes was performed using an Arbin potentiostat (BT 2000). The charge-discharge tests were typically performed in galvanostatic mode, i.e. by applying a constant current density between a set voltage range. The current densities varied from 100 mA/g to 15 A/g, usually depends upon the type of the active material being tested. The electrodes were cycled between the voltages 0.005 to 1.2 V vs. Li^+/Li . A typical testing program contains a rest period before any current was applied, wherein the cell is aged for several hours to allow the voltage to stabilize. Different current densities can be applied to evaluate the performance of the material at different C-rates. C-rate is defined as the rate at which the cell can

be charged or discharged in a given cycle. Higher C- rates correspond to higher applied current densities resulting in short discharge and charge time periods. The data obtained from the galvanostatic testing can be used to plot specific capacity, voltage and differential capacity. Voltage vs. Capacity and differential capacity plots (dQ/dV vs. Voltage) are used to understand the several reactions that occur as a result of lithiation and de-lithiation phenomenon during the discharge and charge processes, respectively as explained in the earlier chapters. The cyclability and capacity retention (cycle life) of the battery can be estimated using capacity vs. cycle number plots.

4.0 SILICON NANOPARTICLE ANODE GENERATED BY HIGH ENERGY MECHANICAL MILLING (HEMM)

4.1 INTRODUCTION

As explained in the background section, nanosized silicon is expected to exhibit improved electrochemical performance compared to bulk crystalline silicon due to the alleviation of mechanical stresses preventing particle fracture and enhanced Li^+ ion diffusion resulting in better rate capability. Several mechanistic models supported by experimental results have been developed that support this hypothesis [15, 131]. For example, silicon nanoparticles obtained by the decomposition of SiH_4 showed a first discharge capacity of 2775 mAh/g followed by a first cycle irreversible loss of 24% [143]. However the capacity dropped to 1729 mAh/g at the end of 10 cycles. Nest like silicon nanoparticles have found to exhibit capacities in the range of 4000 mAh/g with capacity retention of 38% at the end 20 cycles [148]. Cho *et al* showed that commercially available nanosized silicon are usually aggregated with an average particle size of 30 nm and exhibit capacities > 4000 mAh/g for the first cycle with a capacity retention of 5% at the end of 30 cycles [146]. The cyclability and coulombic efficiency can further be improved by preventing the aggregation of Si particles and controlling the particle size [144]. Furthermore, the silicon nanoparticles discussed in the above mentioned methods are typically synthesized by laser or thermal assisted decomposition of gaseous silicon precursors such as SiH_4 . These

methods require sophisticated equipment, expensive precursors and skilled personnel, thereby making it unattractive for commercial large scale production of powders.

Although the vast efficacy and applications of *Si* nanoparticles is well documented, and there are several approaches reported for synthesizing nanostructured silicon, methods for large scale generation of silicon nanoparticles are relatively scarce. Anodic etching of silicon wafers in hydrofluoric acid (*HF*) solutions has been one of the earlier and widely employed methods to produce thin films of porous or nanostructured silicon [179, 180]. However, this method uses a substrate and has the potential to generate only microscopic quantities of the nanoparticles per silicon wafer. Solution based approaches involving the reduction of silicon halides (*SiCl₄*, *RSiCl₃*) using metallic reducing agents, Zintl salts (*ASi*, *A=K, Na, Mg*) and in inverse micelles were also explored to produce silicon nanoparticles along with some functional properties [181-187]. Recent approaches reported for producing silicon nanoparticles include laser pyrolysis [16], laser ablation [17], gas evaporation [18, 19] and high temperature solid state reduction [20]. Though some of these methods claim to be scalable approaches for producing silicon nanoparticles, they require expensive starting materials, complicated equipment and highly skilled labor which ultimately increase the cost of the production process. For high volume applications such as solid state lighting, solar cells and lithium ion batteries, it is imperative that a simple approach for the generation of large quantities of silicon nanoparticles involving lower production and maintenance costs be identified.

High energy mechanical milling (HEMM) is a very inexpensive and a simple technique used to generate scalable quantities of powders in a short amount of time [21]. The milling reaction can also induce a chemical reaction between the different reagents in which case the approach is also called as a ‘mechanochemical reduction’. There are several reports in the

literature on mechanochemical approaches for synthesizing a variety of organic composites, ceramics and metal alloys [188-191]. In the case of silicon as well, there are mechanochemical reactions reported wherein silicon dioxide and silicon monoxide were reduced by elements such as carbon [192], lithium [193] and magnesium [194]. The reducing agents used in these methods are flammable and require controlled atmospheric conditions to avoid any hazardous reactions. In the case where lithium metal is used as a reducing agent, notably there are other limitations such as sticking of metallic lithium on the walls of the milling vial and generation of unwanted lithium orthosilicate (Li_4SiO_4) phase [193]. In another instance, graphite was used to reduce SiO_2 to produce ultrafine silicon nanoparticles by ball milling but this process requires extended reaction time lasting 7-10 days of continuous milling to obtain the final product [192]. Additionally, the use of graphite along with silicon subjected to extended periods of milling results in the formation of silicon carbide (SiC) as a by-product, which is difficult to separate from the $Si-SiC$ composite [195]. Also in a recent report, Russo *et al* synthesized silicon nanoparticles by ball milling of silicon membranes obtained by anodic etching of p-doped silicon wafers [196]. However, this approach employs the use of expensive precursor materials (p-doped wafers) and processing (anodic etching) methods. In contrast, the present approach discusses a very simple mechanochemical reduction reaction to generate nanosized silicon in only 5 hours.

In this approach, SiO and magnesium silicide (Mg_2Si) were used as the starting materials in a high energy mechanical mill to generate nano-particles of silicon via the direct mechanochemical reduction process involving the two reactants. The approach apart from being facile and simple, moreover, utilizes precursors that are relatively safe to handle compared to lithium and magnesium. The milled products obtained are subsequently acid washed to obtain

pure and single phase of silicon nanoparticles. These high surface area silicon nanoparticles are then casted into slurries using Super-P and binder to study their electrochemical properties in a half cell configuration.

4.2 EXPERIMENTAL

4.2.1 Materials synthesis

Silicon monoxide (SiO , 325 mesh, Sigma Aldrich) and magnesium silicide (Mg_2Si , Alfa Aesar) were mixed according to the stoichiometric ratio ($SiO: Mg_2Si = 2:1$) and batched along with stainless steel balls in a hardened stainless steel (SS) grinding vial. The charge to ball ratio was maintained at 1:10. A high energy shaker mill (SPEX CertiPrep 8000 M) was utilized which results in subjecting the SS vial and the grinding media in an asymmetric back and forth continuous motion at ~1080 cycles per minute (60 Hz model) to initiate comminution induced diffusion and reaction of the reacting agents. Milling time up to 15 h with 30 minutes of rest time for every one hour of milling was employed to initiate and complete the mechanochemical reduction reaction. The product obtained after milling was collected and stirred continuously in a 50/50 (v/v) mixture of 6M HCl and ethanol to dissolve the magnesium oxide (MgO) resulting from the reaction. After one hour of mixing, the solution containing the powders was centrifuged twice with ethanol and further dispersed and sonicated in 2% HF solution for 30 minutes. This step was necessary to remove any unreacted SiO/SiO_2 present in the product and etch the silicon particle surface by continuous oxidation and dissolution. During this step, a dark foamy

substance was continuously forming which overflowed over the beaker. To avoid this, ethanol was sprinkled intermittently throughout the sonication process to prevent the foam formation. After sonication, the solution was centrifuged 5 times in ethanol and dried overnight in a vacuum oven at 90°C.

4.2.2 Materials characterization

X-ray diffraction measurements of the silicon obtained at various stages were carried out using a Philips X'Pert Pro system using a copper anode, $\lambda=0.15406$ nm. All scans were taken between the 2θ angles 11° and 90° with a step size of 0.033° . Raman spectroscopy was performed using a Renishaw in via raman microscope equipped with a 633 nm red diode laser. Three scans were taken and then averaged to minimize the signal to noise ratio. Morphological studies were done using scanning and transmission electron microscopy. For SEM studies, the powder sample was applied onto a conductive adhesive carbon tape. A thin layer of palladium was coated on the material surface using a table top sputter coater to minimize the charging effects caused by the electron beam in the SEM machine. SEM was done using a Philips XL 30 equipped with a field emission gun. An Energy Dispersive X-ray spectroscopy analyzer was connected to the SEM instrument to perform compositional analysis of the sample. For TEM characterization, the samples were dispersed either in ethanol or isopropanol and sonicated for one hour to remove any particle agglomerates. The solution was then sprayed onto holey carbon grids and left to dry at room temperature. The TEM studies were done using JEOL JEM 2000FX machine operated at 200KV. Specific surface area (SSA) measurements were determined from the N_2 adsorption-desorption isotherms obtained using the Brunauer-Emmett-Teller (BET) method performed on a

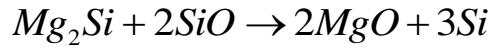
Micromeritics ASAP 2020 instrument. The Barret-Joyner-Halenda (BJH) method was applied to the N_2 adsorption and desorption isotherms to estimate the pore volume and pore size distributions.

4.2.3 Electrochemical characterization

Electrochemical characteristics such as charge-discharge, differential capacity and voltage vs. capacity were determined using an Arbin Instruments' MITS Pro battery cycler. The electrodes containing the active material were tested in a half cell configuration against pure lithium metal. The silicon nanoparticles after acid etching were mixed with polyvinylidene fluoride (PVDF, Aldrich) binder and Super-P (Timcal) conductive additive in 80:10:10 (active material: binder: Super-P, wt%) ratio. N-Methyl-2-pyrrolidone (NMP) was used as the solvent for the binder and the slurry was mixed well on a magnetic stirrer for several hours until a uniform dispersion was obtained. The slurry was then cast on the rough side the copper foil (Insuletro, 18 μ m) using a Mayer rod or by a thin film applicator (MTI, AFA-III). The slurry was left to dry in air for 4-6 hours after which they were transferred to a vacuum drying oven at 100°C and dried overnight. Electrodes of 9 mm or 11 mm diameter disks were cut and served as the working electrode. A 2016 coin cell assembly was utilized for electrochemical testing wherein pure Li foil was used as the counter electrode and a polyethylene based separator (Celgard) was used to prevent the shorting of working and counter electrode. 1M $LiPF_6$ dissolved in ethylene carbonate (EC) and diethylcarbonate (DEC) (EC:DEC=1:2) served as the electrolyte. All electrochemical measurements were cycled between 0.02 V to 1.2 V vs. Li^+/Li .

4.3 RESULTS AND DISCUSSION

The mechanochemical reaction between *SiO* and *Mg₂Si* can thus be understood by the following displacement reaction (Equation 1):



Equation 1

Figure 29 shows the progress of the mechanochemical reaction with the X-ray diffraction patterns showing the complete formation of silicon and magnesium oxide (*MgO*) with increasing milling time. After 30 seconds of milling, the diffraction pattern shows only the presence of *Mg₂Si* indicating that the reduction reaction has not yet commenced with both starting precursors only existing as a physical mixture of the reactants. After 3 hours of milling however, the peaks corresponding to *Mg₂Si* are reduced significantly and replaced correspondingly, with *Si* and *MgO* indicative of the initiation of the mechanochemical reduction reaction following the Equation 1 above. The milling was continued to proceed for a total of 15 hours to ensure the complete reduction of *SiO* with *Mg₂Si*. With increasing milling time as expected, broadening of the silicon peaks is also observed to occur in the XRD pattern which can be attributed to a decrease in the crystallite size and/or strain induced by the continuous pulverization action prevalent in mechanical milling. A pseudo Voigt function was applied to the maximum intensity peak to determine the Gaussian and Lorentzian contribution. An effective crystallite size of 20 nm was determined from the Debye-Scherrer equation obtained from the integral breadth of the Lorentzian contribution determined from the peak profile analysis using the single line approximation method after eliminating the instrumental broadening and lattice strain contribution.

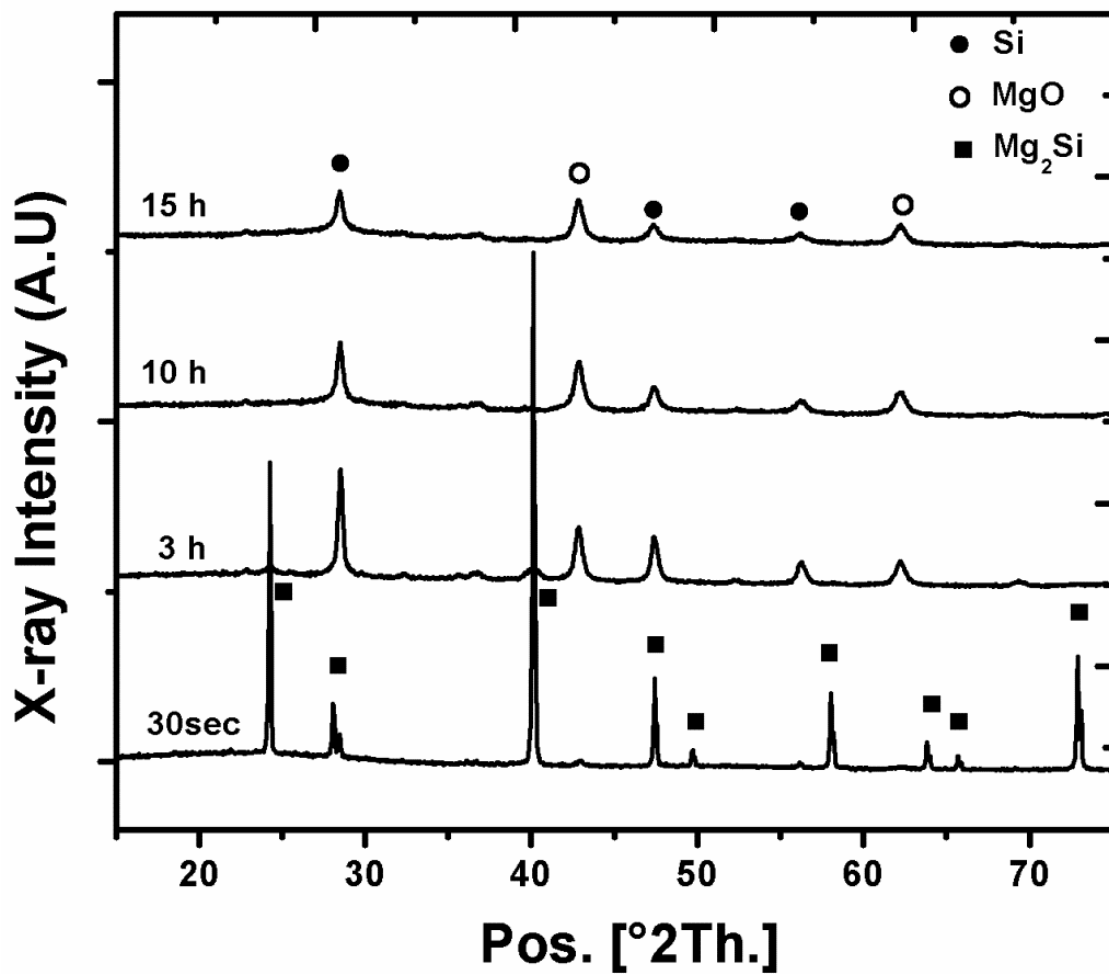
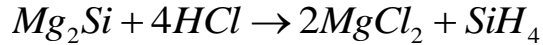
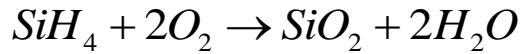


Figure 29: X-ray diffraction patterns of showing the phase evolution with increased milling time and progress of the mechanochemical reaction - $Mg_2Si + SiO$ with different milling times [197].

The product at the end of 15 hours of milling consists of silicon, MgO , unreacted SiO that remains amorphous, and possibly unreacted Mg_2Si . Hence, in order to obtain pure single phase silicon, the final product at the end of the milling step was subjected to two acid wash steps. In the first wash, 6N HCl was used wherein the reaction product, MgO obtained reacts with HCl to form soluble magnesium chloride ($MgCl_2$) which dissolves immediately in water. Unreacted Mg_2Si also reacts with HCl in this step to form silane and $MgCl_2$ according to the Equation 2. Silane, being a pyrophoric and reactive gas oxidizes immediately in the presence of atmospheric air to form silica according to Equation 3.



Equation 2



Equation 3

In the second wash step, the wet product obtained after HCl wash was dispersed in 2% HF solution. The justification behind employing 2% HF acid wash was to fulfill the following three aspects: (1) to dissolve any unreacted SiO present at the end of the milling reaction; (2) dissolve SiO_2 formed as a result of the 1st wash step due to generation of any silane and the consequent oxidation reaction shown above in **Equation 3**, and (3) to etch the silicon particle surface to decrease the particle size while also possibly inducing porosity in the silicon obtained, thus contributing to the high specific surface area. It can be clearly seen from **Figure 30** that following the acid treatment, the peaks corresponding to MgO completely disappear and only Si peaks remain. Also, from the **Figure 31** some amount of peak broadening for Si has been

observed which can be attributed to the decrease in particle size obtained by repeated etching of the silicon surface by *HF*.

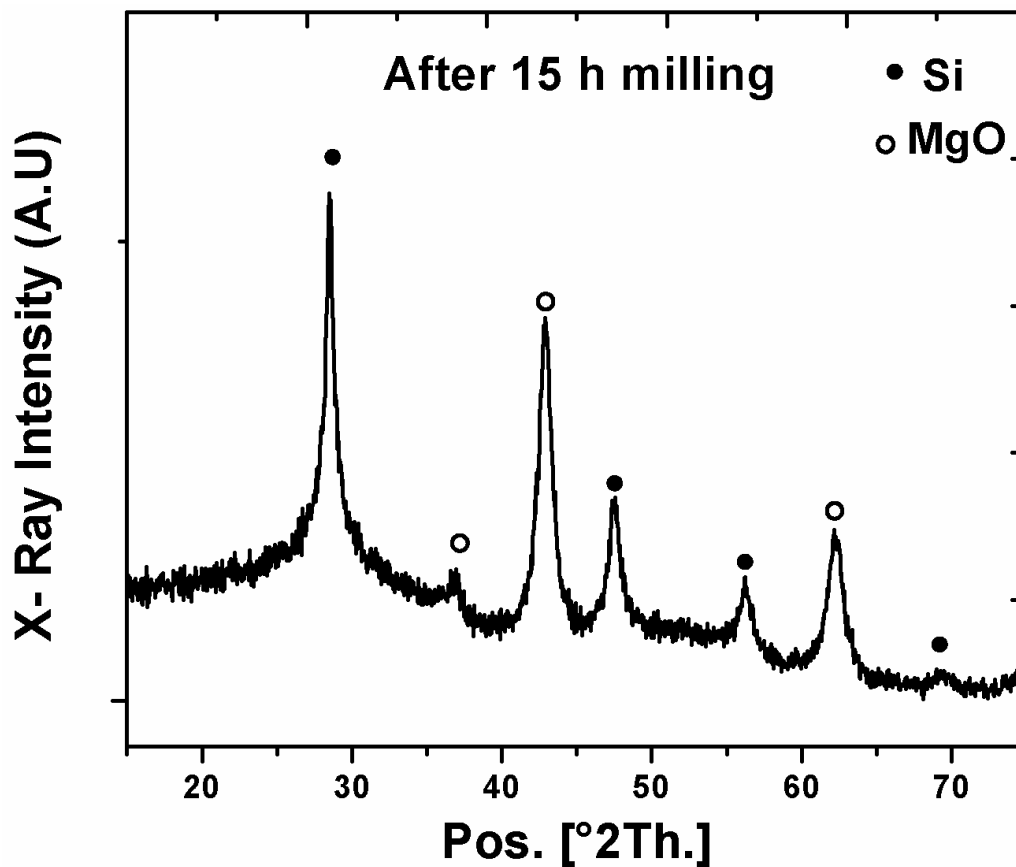


Figure 30: X-ray diffraction patterns of the product derived following mechanochemical reduction [197]

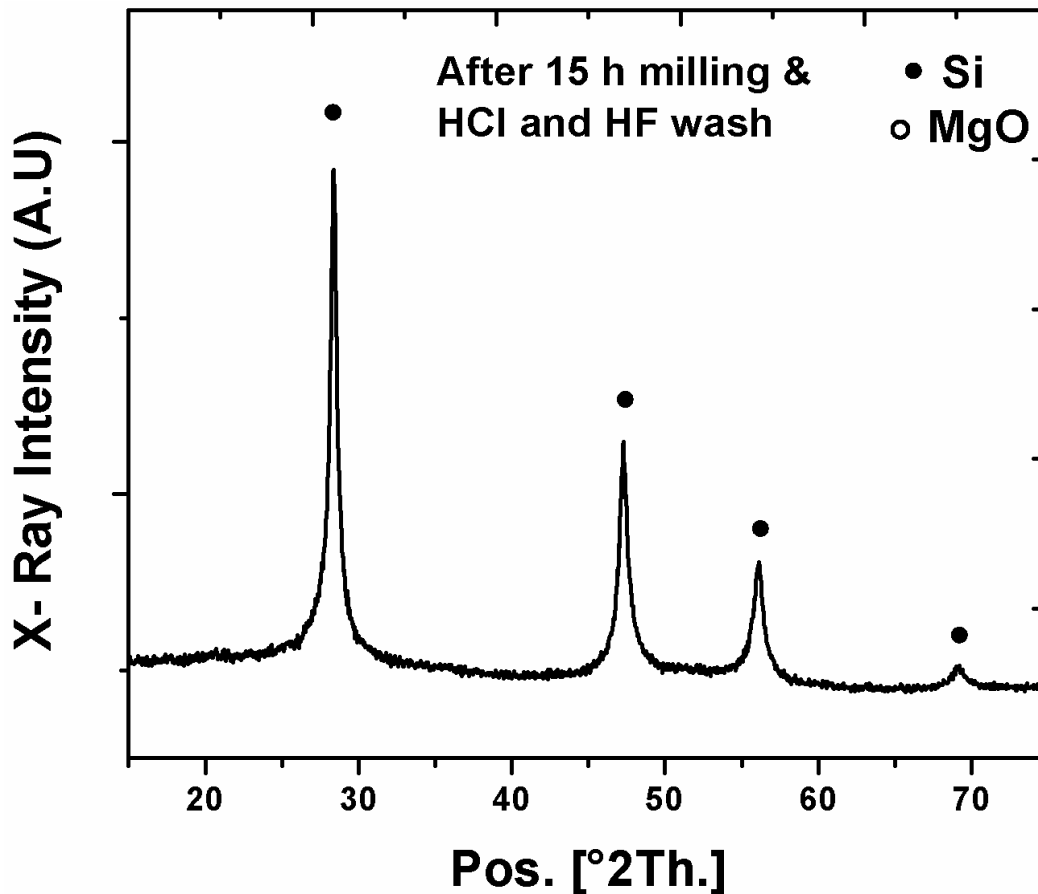


Figure 31: X-ray diffraction patterns of the product derived following mechanochemical reduction followed by HCl and HF wash [197]

It can be observed from **Figure 32** that a sharp peak is seen at 508 cm^{-1} instead of the characteristic 520 cm^{-1} peak observed for bulk crystalline silicon. This peak can thus be attributed to the TO phonon mode of nanocrystalline silicon [198-200]. No peaks corresponding to *MgO* or *SiO* were observed in the spectra, indicating completion of **Equation 1**, and formation of single phase elemental silicon in the nanocrystalline state validated by Raman analysis.

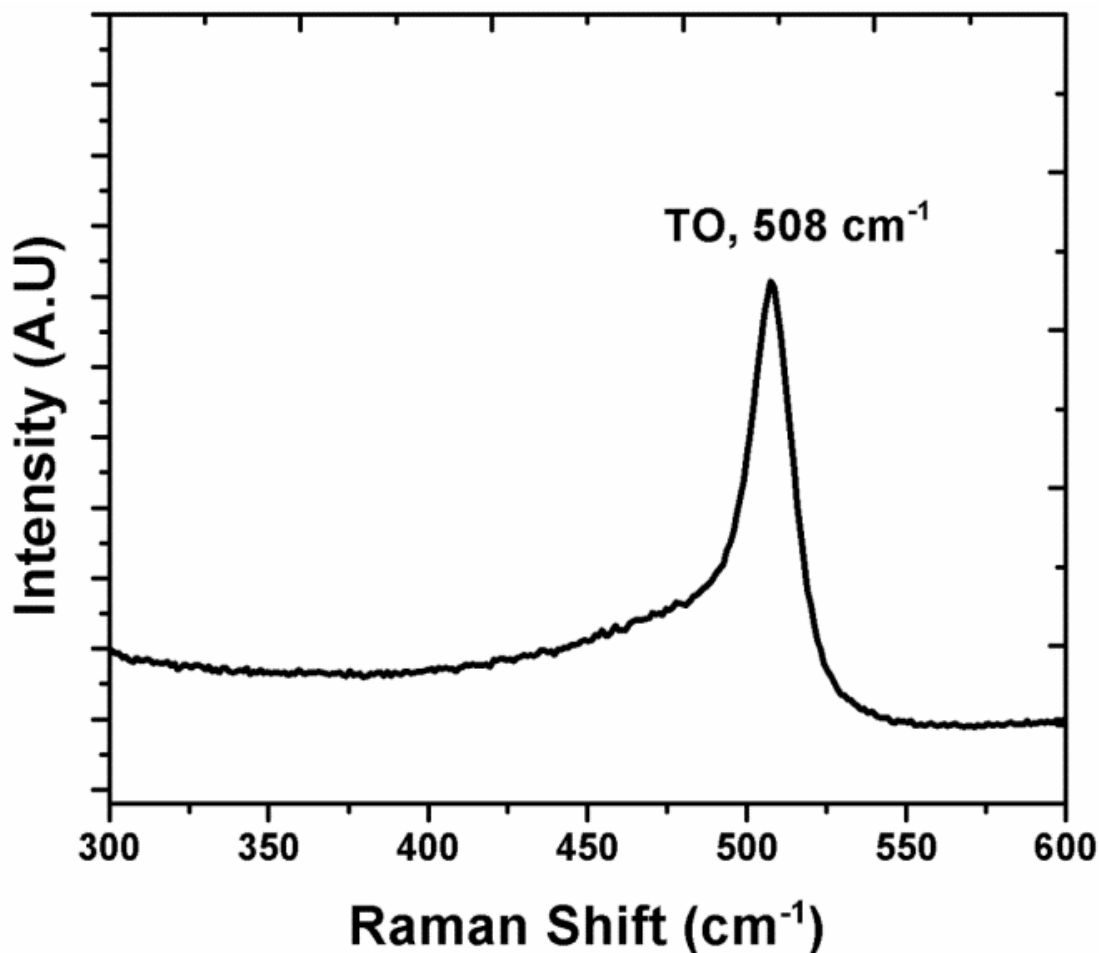


Figure 32: Raman spectra obtained on the sample obtained after 15 hours of milling followed by HCl (6N) and HF (2%) wash [197].

SEM and TEM characterization was performed to analyze the morphology of the synthesized product. From the SEM images, **Figure 33 (a-c)**, particles of different sizes and extent of agglomeration could be observed. The individual particles and the agglomerates range from few hundred nanometers to few microns in diameter. Such morphology is characteristic of mechanochemical and mechanical milling reactions. Significant amount of porosity can be observed in the final product (see **Figure 33 (a-c)**), The wide range in particle size is usually observed in the synthesis of materials involving high energy mechanical milling wherein the

pulverizing media (stainless steel balls) break the original charge into particles of different sizes and shapes [21]. The product obtained at the end of the milling step is accordingly scaled down by the acid etching process giving rise to a non-uniform final product. An aggregate of the few particles agglomerated together is clearly seen in the TEM bright field image (**Figure 33 (d)**).

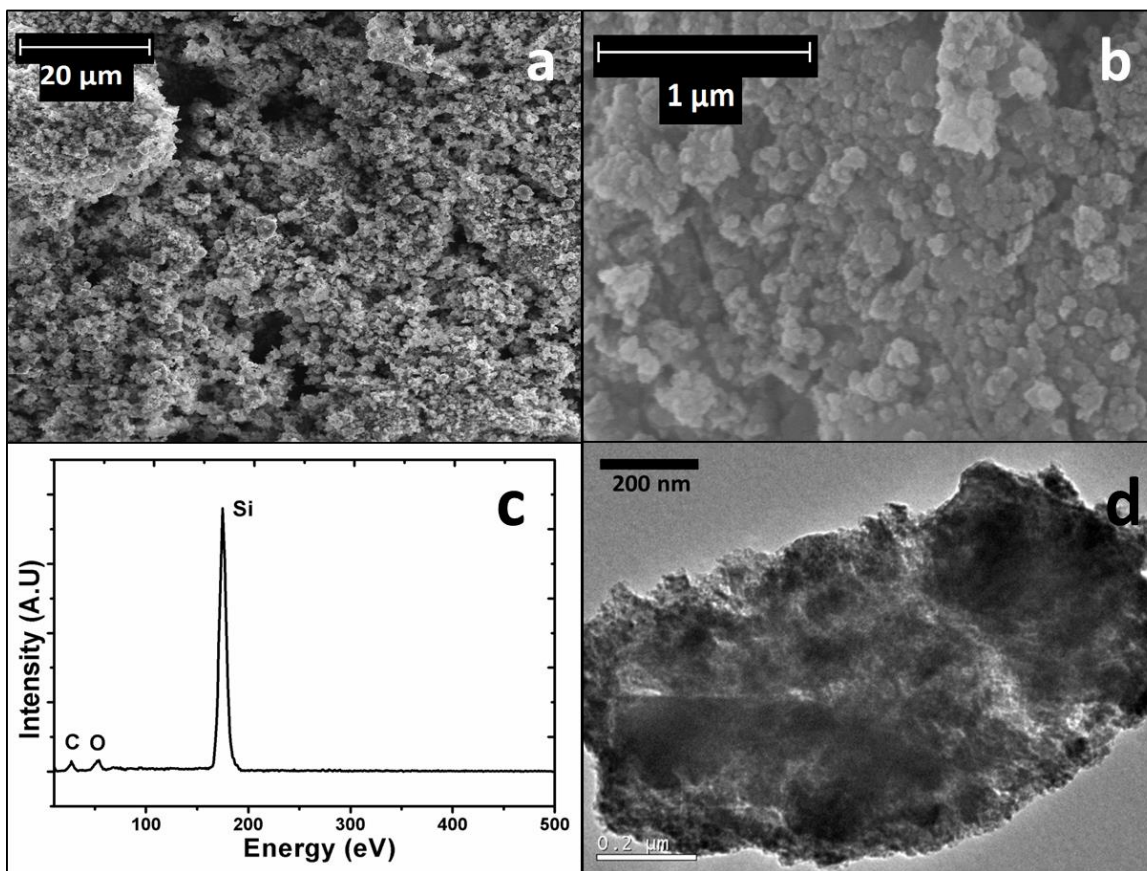


Figure 33: (a) – (c) SEM images obtained on the final product and (d) Bright field TEM image of the agglomerated final product [197].

The particle size reduction can be understood from the schematic in **Figure 34**. The newly formed nanocrystalline silicon at the end of the 15h mechanochemical reduction step is highly reactive and thus quickly absorbs oxygen from the atmosphere to form a thin layer of SiO_2 on its surface. This thin oxide layer then dissolves in the second wash step (2% HF) exposing a new silicon surface. The new silicon surface again develops another oxide layer as a result of the reaction with oxygen dissolved in the acid solution forming a new thin oxide layer. This sequence of continuous formation and dissolution of the oxide layer during the wash step of sonication thereby leads to a decrease in the overall size of the silicon particle. The decrease in

the crystallite size determined from the crystallite size analysis from the broad XRD diffraction patterns and nanoparticles observed from the SEM images and microstructural analysis should result in a very high specific surface area.

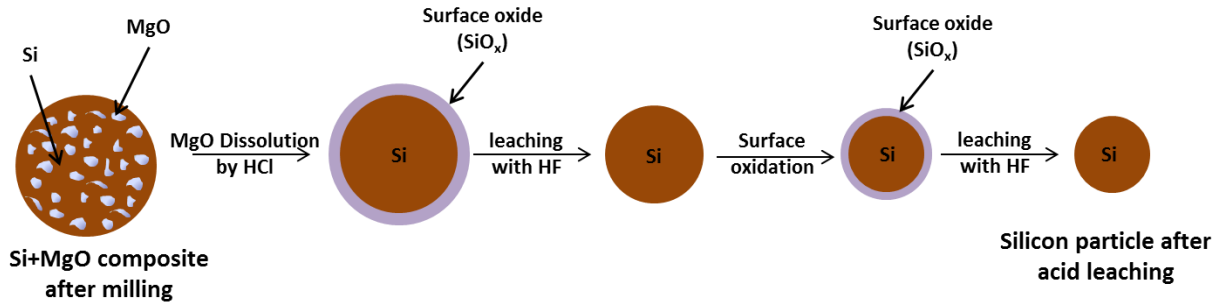


Figure 34: Schematic of silicon particle size reduction obtained by chemical etching induced by the 2% HF acid wash [197].

The expected increase in surface area can be corroborated from BET analysis of the powder after milling and the two acid washes. A sharp increase in surface area from $\sim 6 \text{ m}^2/\text{g}$ for the as-milled product to $\sim 97 \text{ m}^2/\text{g}$ for the product after the 1st wash (6N *HCl*) can be seen in **Figure 35**. At the end of the 2nd wash (2% *HF*), a very high surface area $\sim 190 \text{ m}^2/\text{g}$ is obtained for the final product. This very high surface area is therefore the result of the continuous size reduction of the silicon particle induced by the acid wash particularly, due to the second wash step in the presence of 2% *HF* solution. The SSA value obtained in this work appears to be remarkably high compared to the work reported in the literature to date.

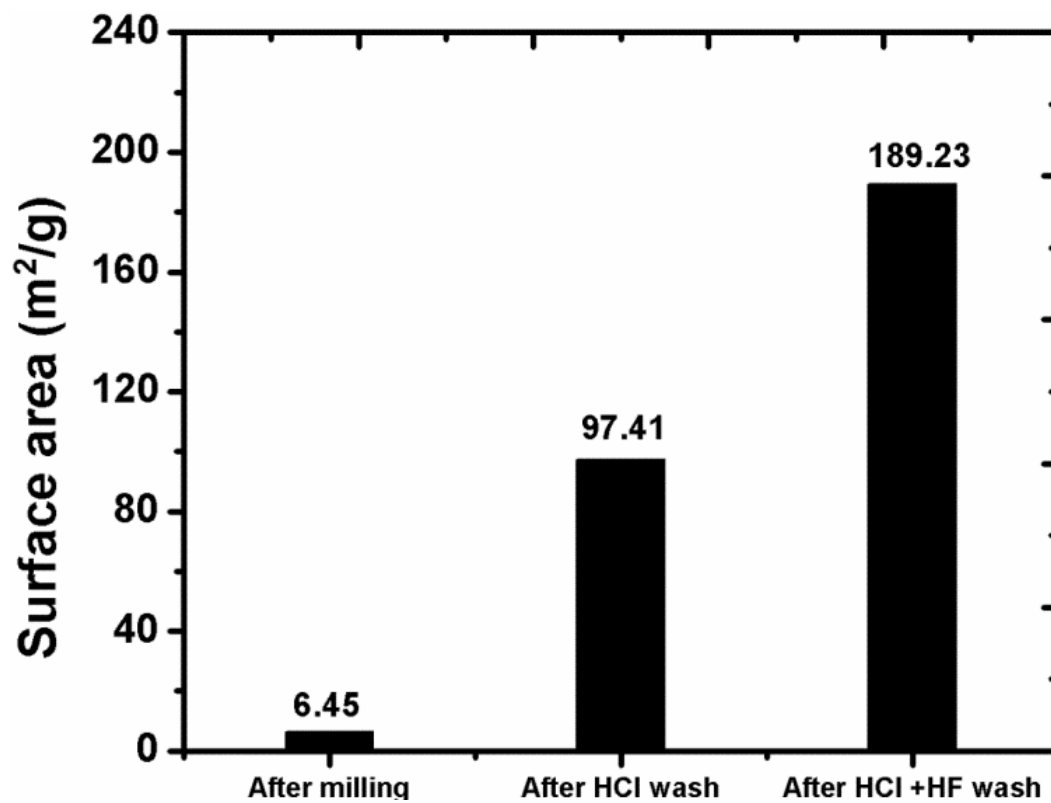


Figure 35: BET surface area (m²/g) of the powder obtained at the end of 15 h of mechanochemical reaction, after HCl (6N) wash and after HF (2%) wash steps [197].

The N₂ adsorption-desorption isotherms shown in **Figure 36(a)** represent a typical type II isotherm and does not exhibit any limiting adsorption even at high relative pressures. From **Figure 36(b)**, the pore sizes of the silicon nanoparticles calculated from the Barret-Joyner-Halenda (BJH) method range from a few angstroms to 100 nm with an average pore width of 12 nm. An average pore volume of 0.71 cm³/g is also estimated from these calculations. Also, majority of the pores can be seen to be in the mesoporous range (between 2 and 50 nm) and some in the macroporous range (>50 nm), thus contributing to the high specific surface area. Due to a wide range of particle sizes generated by the mechanical milling action, a wide pore size distribution is expected following the acid wash treatments. An important characteristic of this approach is that the entire process is scalable and utilizes inexpensive starting materials. Compared to the conventional methods for synthesizing nano silicon such as gas pyrolysis/laser ablation (surface area: 69 m²/g, [43]), this process is capable of being scaled up to generate large quantities of nanosized silicon in a very short time when used in industrial scale mechanical mills.

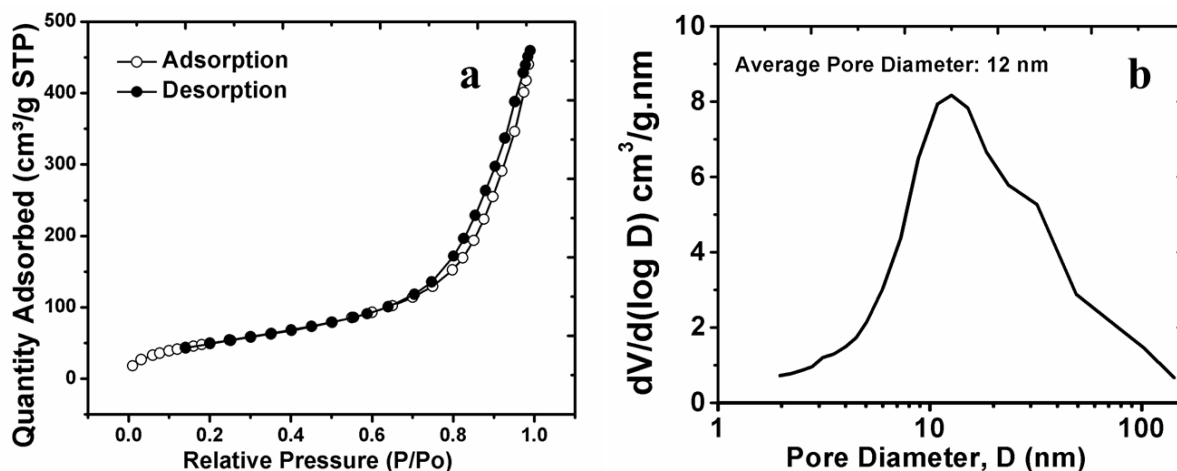


Figure 36: (a) Nitrogen adsorption isotherms and (b) pore diameter distribution obtained by BJH method on the silicon nanoparticles [197].

Electrochemical cycling of the HSA-Si powder exhibited a high first discharge capacity of 2230 mAh/g at a current density of 100 mA/g between the voltage range 0.02 to 1.2 V vs. Li^+/Li . This was followed by expectedly, a large first cycle irreversible loss of 73% resulting in a first charge capacity of only 590 mAh/g (**Figure 37(a)**). This large first cycle irreversible (FIR) loss could be due to many factors such as: (a) presence of surface oxide (SiO_x) that is reduced electrochemically during Li^+ insertion in the first cycle to form Si and Li_2O ; (b) formation of large amount of SEI layer, owing to the high specific surface area of the silicon nanoparticles; and (c) particle fracture. A voltage plateau can be observed indicating the formation of two phase region according to the Gibbs phase rule. The different lithiation reactions can clearly be observed from the differential capacity plots in **Figure 37(b)**. The sharp peak at around 0.08 V indicates the significant lithiation resulting in the formation of Li_xSi phase. During the charge

process, a sharp peak was observed at 0.32 V which is consistent with literature reports for the de-lithiation reaction.

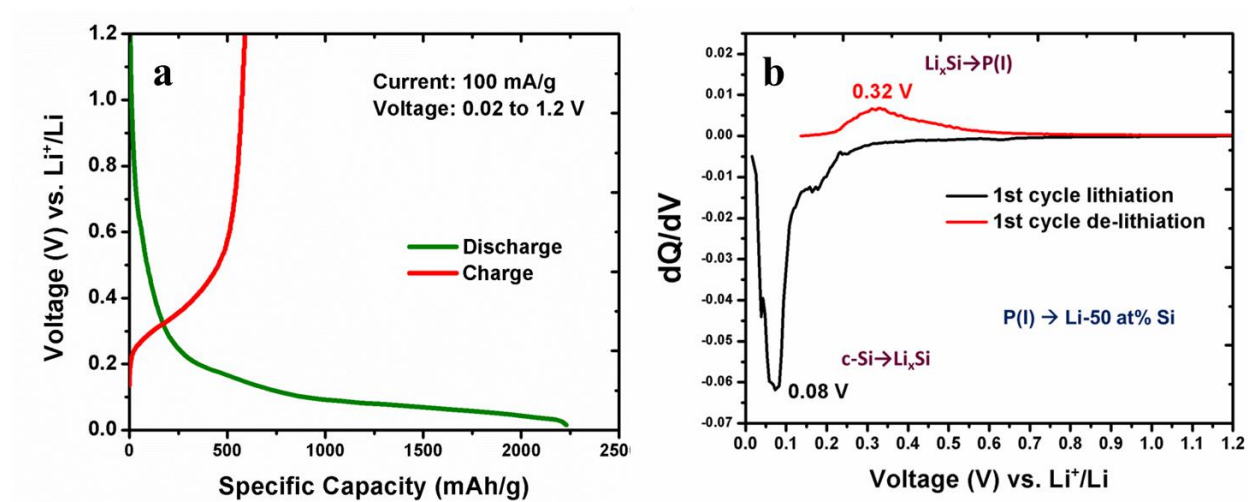


Figure 37: (a) Voltage vs. capacity plot and (b) dQ/dV plot of the high surface area (HSA) silicon particles cycled at 100 mA/g between 0.02 to 1.2 V vs. Li⁺/Li [197]

Figure 38 shows the extended cycling at a current density of 100 mA/g where the specific capacity drops to less than 350 mAh/g at the end of only 8 cycles. This corresponds to a fade rate of 6.66% loss per cycle. Additionally, the coulombic efficiency is only 80% indicating the occurrence of side reactions such as SEI formation and reduction of SiO_x which was left unwashed during the *HF* etching step. The poor cycling response and the large FIR are indeed characteristics of the nanoscale Si alone and the surface impurities as explained above. Despite these characteristics, the approach shows the ability to generate high SSA nanostructured Si in a very economical and scalable form. Improvements in the electrochemical response can be

obtained by conducting additional surface treatments to eliminate the surface oxide thus increasing the capacity stability while also reducing the FIR. These studies are part of the future work.

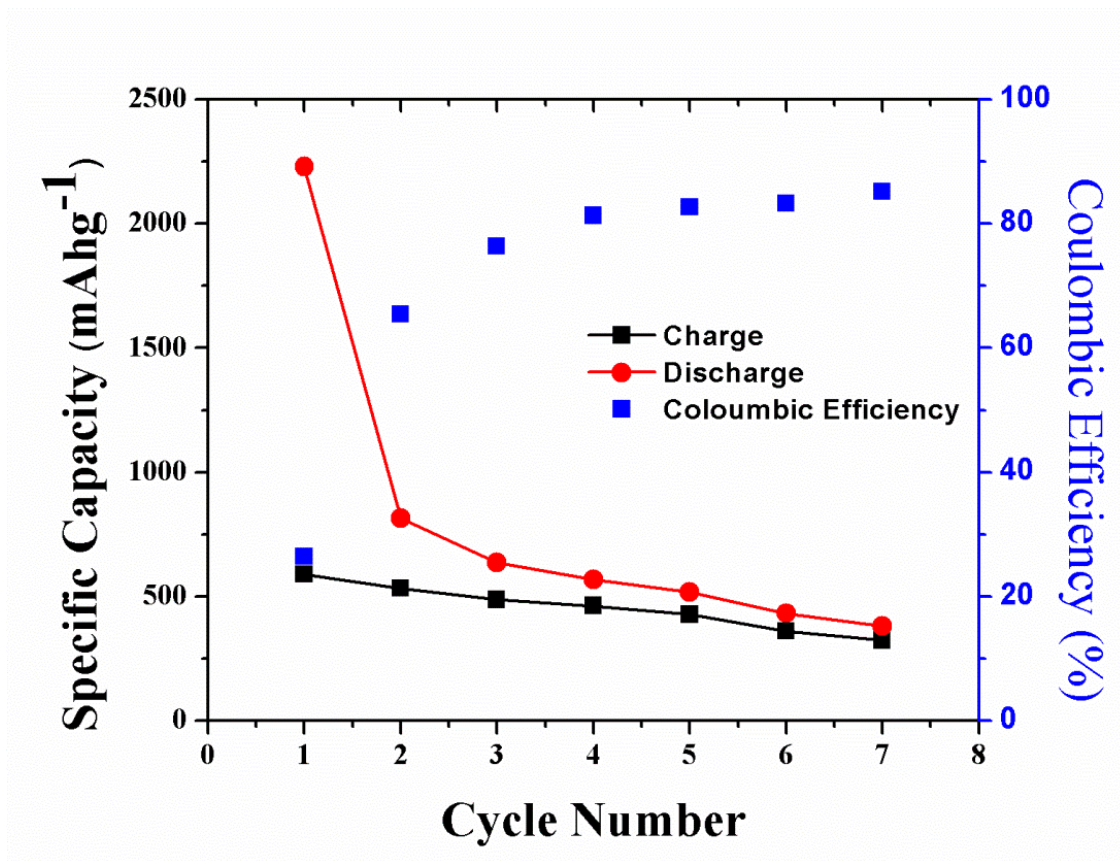


Figure 38: Capacity vs. cycle number plot of the HSA-Si particles cycled at 100 mA/g between 0.02 V to 1.2 V vs.

Li+/Li [197]

4.4 CONCLUSIONS

A simple and facile method involving the use of high energy mechanical milling (HEMM) induced mechanochemical reduction followed by acid etching was used to achieve silicon nanoparticles in a high throughput fashion. Silicon monoxide (SiO) was used as the starting silicon precursor which was reduced completely by magnesium silicide (Mg_2Si) by mechanochemical reaction after only 15 hours of milling reaction. Continuous acid etching of the surface by the formation and dissolution of a thin silicon oxide surface layer by 2% HF resulted in the formation of single phase silicon with reduced crystallite and particle size, and high surface area. SEM and TEM characterization revealed the presence of nanoparticles in the size range 100-200 nm which are coalesced to form agglomerates in the size range 1-2 μm . The broad peaks of silicon observed in the X-ray diffraction pattern and the shift in the TO peak seen in the Raman spectra to 508 cm^{-1} both validate the nanocrystalline nature of the product obtained. BET analysis of the product showed an increase in surface area with subsequent acid washing steps resulting in the attainment of a final surface area $\sim 190\text{ m}^2/\text{g}$ for the final product. BJH calculations of the pore size distribution also indicate an average pore size of $\sim 12\text{ nm}$. These results therefore justify that the present reaction scheme is a very convenient, high throughput scalable approach to generating high specific surface area nanocrystalline Si . These silicon nanoparticles exhibit a first discharge capacity of 2230 mAh/g followed by a large first cycle irreversible loss of 73%, owing to the formation of large SEI layer on the high specific surface area of silicon nanoparticles. The sharp peak at 0.08 V in the dQ/dV plot during the first

discharge cycle shows the typical lithiation of crystalline silicon to form amorphous Li_xSi alloys. A high capacity fade of 6.66% loss per cycle can be observed resulting in the capacity of 350 mAh/g at the end of 8 cycles. Though these results show significantly better cyclability compared to that of bulk crystalline silicon, the electrochemical performance is still not acceptable for them to be used in commercial applications which require lower first cycle irreversible loss, better cyclability and long cycle life. Further modifications to the surface state will be required to improve the electrochemical response and will be part of the future work.

5.0 AMORPHOUS SILICON FILM ANODE BY ELECTRODEPOSITION FROM ORGANIC SOLVENTS

5.1 INTRODUCTION

It is believed that both nanostructured and amorphous forms provide mechanical integrity without pulverization due to the reduced number density of atoms within a nano-sized grain and the ‘free volume’ effects in amorphous silicon which results in better capacity retention and cycle life as explained in the earlier chapters. Furthermore, due to the presence of defects and absence of long range order in amorphous *Si*, the volume expansion upon lithium insertion is distributed homogenously and the net effect of crack formation and propagation is less catastrophic compared to crystalline silicon [13, 14, 156]. Hence, the amount of pulverization of the active material is significantly reduced which gives rise to enhanced capacity retention and cyclability. Amorphous silicon is generally obtained by physical and chemical vapor deposition methods. Physical vapor deposition methods include RF or magnetron sputtering and pulsed laser deposition (PLD) using silicon targets [23, 24, 201, 202]. Chemical vapor deposition methods include thermal, microwave or plasma assisted decomposition of silicon precursors such as SiH_4 [4, 5, 203, 204]. These techniques though universally applied in the electronics industry are however deemed not economically viable for secondary battery energy storage devices.

Secondary batteries are primarily used for energy storage devices as auxiliary attachments to any consumer portable electronic devices including the high end electric or hybrid electric vehicle and are susceptible to very stringent demands of competitive price reduction. Therefore, there is a need to explore alternative economical approaches for the generation of amorphous silicon in bulk as well as thin film forms.

In line with the goal for exploring an economical approach to amorphous *Si* generation, electrodeposition is a simple and inexpensive technique and has been extensively used in industrial applications such as in plating processes to modify the surface properties of metals and alloys to improve their corrosion resistance as well as offer an aesthetic finish. Several attempts have already been made to produce thin films of silicon on metallic substrates by electrodeposition [205-212] wherein, the silicon source is usually one of the silicon based halides: $SiCl_4$, $SiHCl_3$, $SiBr_4$, SiI_4 dissolved in an appropriate solvent. The halide silicon precursors are not stable in air and in aqueous media, and therefore moisture-free organic solvents such as propylene carbonate, acetonitrile and tetrahydrofuran are generally used. Non-aqueous electrolytes usually have poor conductivity and hence, supporting electrolytes, which comprise non-reactive ionic species or salts are usually added to improve their ionic conductivity, decrease cell resistance and maintain uniform current density. Most common supporting electrolytes for electrodeposition of silicon are tetraalkylammonium salts such as tetramethylammonium chloride (TMACL), tetraethylammonium chloride (TEACL), tetrabutylammonium chloride (TBACL), tetrabutylammonium perchlorate (TBACLO) etc.

In this study, a simple electrodeposition method for generating thin amorphous silicon films by electro-reduction of $SiCl_4$ directly on copper substrates is reported. These deposited films are directly used as the anode without the addition of any other other conductive additives, and binders thereby simplifying the approach for lithium ion battery applications.

5.2 EXPERIMENTAL

5.2.1 Amorphous silicon film deposition

All chemicals used for the deposition studies were purchased from Sigma Aldrich (St. Louis, MO). Propylene carbonate (PC, 99.9% anhydrous) and silicon tetrachloride ($SiCl_4$, 99.99%) were used without further purification. PC was selected as the solvent for $SiCl_4$ because of its high dielectric constant ($k' = 64$) and hence presenting a good environment for solubilizing the halide salts of silicon. To improve the ionic conductivity of the electrolyte, tetrabutylammonium chloride (TBACL, >97%), dried overnight at 100°C in vacuum, was added as a supporting electrolyte to the solvent. In a typical deposition, the electrolyte comprised of 0.5M $SiCl_4$ and 0.1M TBACL dissolved in PC. All the deposition based experiments were carried out in a cylindrical three electrode cell made of glass, sealed with teflon gaskets. Copper foil (Insulectro, ~18 μm thick) was used as the working electrode, platinum wire (diameter, $\Phi=0.5$ mm, 99.95%, Alfa Aesar) and platinum foil (0.1 mm thick, 0.5 X 0.5 cm^2 , 99.9%, Aldrich) served as the reference and counter electrodes, respectively. The electrodes were sonicated in ethanol and acetone for 5 minutes and dried in air before use. Voltammetric studies such as linear sweep voltammetry (LSV) and chronopotentiometry were conducted using the EC Epsilon

(Bioanalytical Systems, Inc) potentiostat while the impedance studies were conducted on VersaSTAT 3 (Ametek, Inc). After deposition, the copper foils were thoroughly rinsed in PC and anhydrous acetone separately, to remove any traces of the electrolyte and unwanted impurities. The foils were allowed to dry in an argon filled glove box approximately for 1h before characterizing them further.

5.2.2 Film characterization

Morphological and compositional analyses of the deposited films were conducted using scanning electron microscopy (SEM, Philips XL 30) and energy dispersive X-ray spectroscopy (EDAX, Philips XL 30). Glancing Angle X-Ray Diffraction (GAXRD) was performed using a Philips PW3710 based X'Pert diffractometer equipped with a copper anode in parallel beam geometry. Raman spectroscopy was performed using a Renishaw in-via Raman microscope equipped with a 633 nm red laser to evaluate the vibrational and rotational modes of the deposited films.

5.2.3 Electrochemical characterization

Electrochemical investigations were performed on the electrodeposited copper foil that was cut into circular discs of diameter 11 mm which served as the working electrode. A 2016 coin cell assembly in a half cell configuration was used by employing lithium (*Li*) foil as counter electrode and 1M *LiPF*₆ in ethylene carbonate and di-ethyl carbonate (EC:DEC=1:2 by volume) as the electrolyte. The assembled cells were tested by cycling between 0.02 to 1.2 V vs. *Li*⁺/*Li* employing a constant current density of 400 mA.g⁻¹ with a minute rest between the

charge/discharge cycles. Rate capability tests were performed by cycling the electrodes at C/4, C/2, 1C, 2C and 4C rates. Impedance studies were performed using the VersaSTAT 3 (Ametek, Inc) in the frequency range of 50 KHz to 100 mHz using 10 mV amplitude of an AC stimulus with no applied voltage bias.

5.3 RESULTS AND DISCUSSION

Linear sweep voltammogram (LSV) technique has been used to understand the silicon deposition on copper foil in PC and 0.1M TBACL electrolyte with and without the addition of SiCl₄. The cyclic voltammograms were recorded at a scan rate of 10 mV s⁻¹ (**Figure 39**). The LSV obtained for the solution containing the silicon precursor showed a cathodic peak at -1.6 V suggesting the reduction of SiCl₄. This was validated by the absence of cathodic peak in LSV recorded for solvent and supporting electrolyte without the SiCl₄ precursor (see inset). Galvanostatic reduction was further achieved by applying a current density of -1 mA cm⁻² for 1 hour. The reduction plateau observed around -1.6 V seen in

Figure 40 confirmed the presence of cathodic peak for Si obtained from the voltammetric studies.

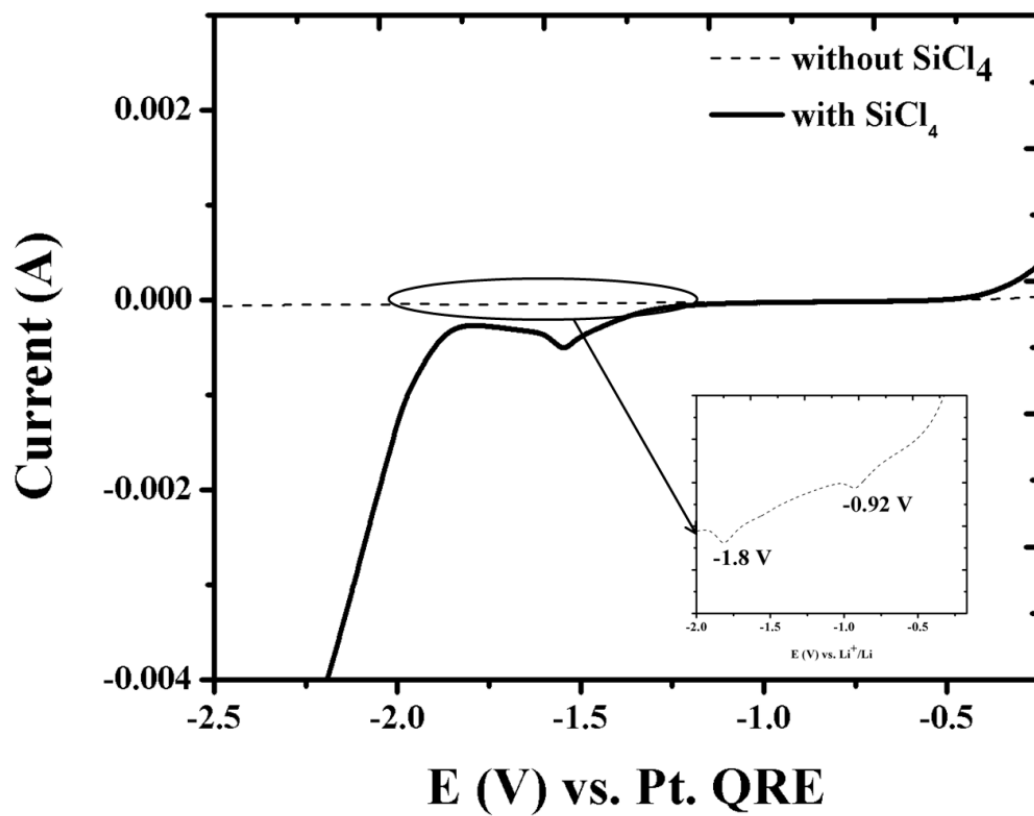


Figure 39: Cyclic voltammogram of 0.5M SiCl₄ in propylene carbonate with 0.1M TBACL as supporting electrolyte (scan rate: 10 mV s⁻¹)

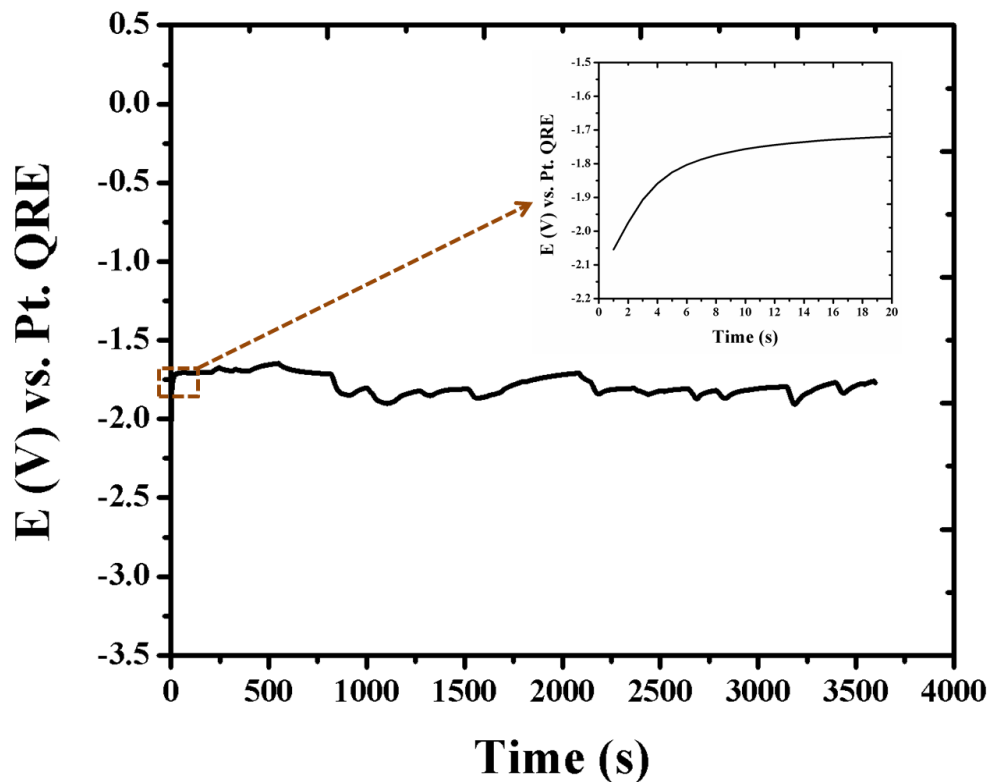


Figure 40: Chronopotentiogram for SiCl_4 electrochemical reduction on copper at -1 mA cm^{-2} for one hour

Raman scattering and GAXRD experiments were performed for the silicon films electrodeposited under galvanostatic conditions. The electrode was rinsed thoroughly in PC and anhydrous acetone for 5 minutes immediately after the deposition for analysis, following which, it was left to dry in the glove box. A uniform yellowish green film was observed on the copper foil which when taken out of the glove box and exposed to the atmosphere for an hour, turned grey due to the rapid oxidation of the silicon to form SiO_2 [207-209]. Therefore, Raman spectroscopy, GAXRD and SEM characterization were performed within 30 minutes of the deposition. GAXRD patterns (**Figure 41**) obtained on the deposited films at incidence angles of 0.1° , 0.5° and 1.0° showed only peaks of copper from the substrate and no peaks were recorded

corresponding to silicon validating the presence of amorphous Si. The intensity of the copper peaks was observed to decrease with decrease in the incidence angle which is due to the presence of an amorphous phase on the surface of the copper foil.

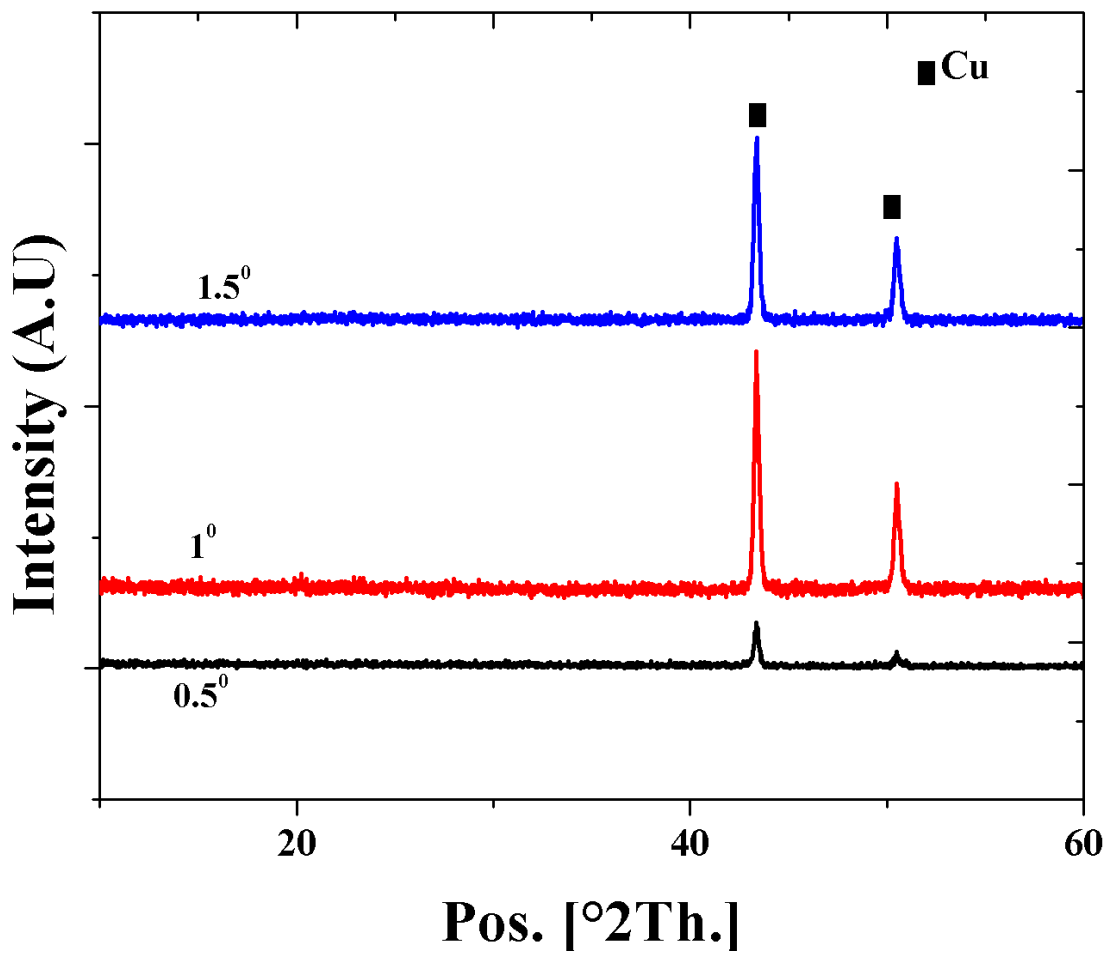


Figure 41: GAXRD plots of electrodeposited silicon at incidence angles of 0.1 $^{\circ}$, 0.5 $^{\circ}$ & 1.5 $^{\circ}$

Raman spectra obtained from the electrodeposited region indicates a broad peak at approximately, 485 cm^{-1} as shown in **Figure 42**. For crystalline silicon, a sharp peak, attributed to the transverse optical (TO) vibrational mode, is reported to appear at 520 cm^{-1} [198, 199]. Since the long range order is lost, the TO peak becomes broad and shifts to lower wavenumbers [199, 200]. For the deposited films, no sharp peak at 520 cm^{-1} was observed, whereas a broad peak with peak position at 485 cm^{-1} was found suggesting that the deposited film is predominantly amorphous which was validated by the GAXRD results. However, the presence of nanocrystalline silicon is also evident from the slight narrowing of the peak centered at 485 cm^{-1} in lieu of 480 cm^{-1} .

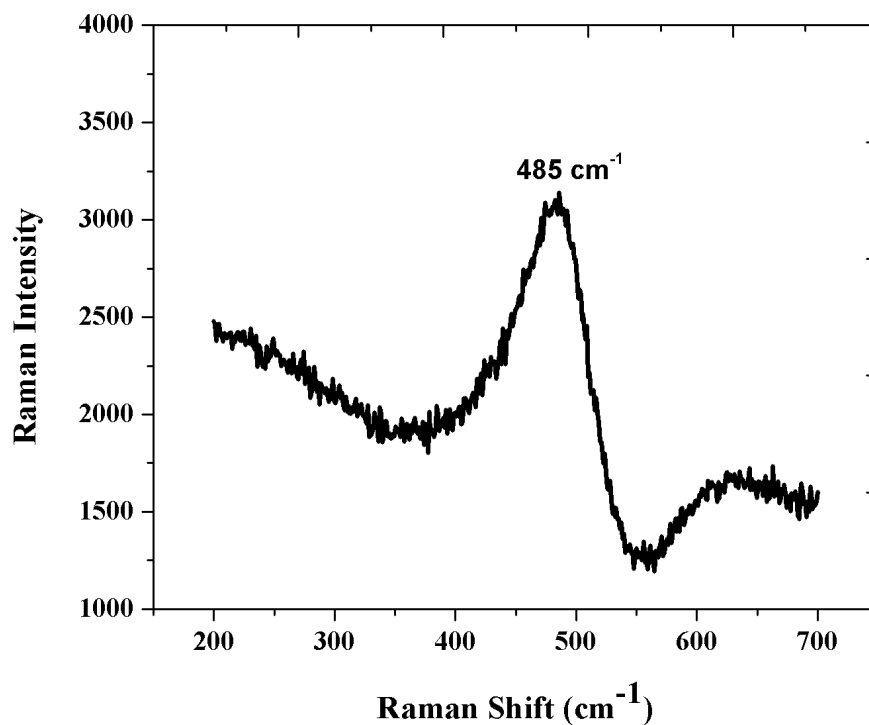


Figure 42: Raman spectra of the electrodeposited silicon using 633 nm red laser

SEM image of the amorphous silicon film electrodeposited on copper foil showed the presence of cracks with *Si* islands ranging from 10-20 μm (**Figure 43a**). This is similar to the morphology obtained by Gobet et al [206] by electrodeposition of silicon halides employing a current density of -1 or -2 mA cm^{-2} . EDAX analysis (**Figure 43b**) indicates the presence of *Si*, *C*, *O* and *Cu*. The presence of oxygen is due to the surface oxidation of the film following exposure to atmospheric air while transferring the sample to the SEM chamber [206, 208, 209]. Small amounts of carbon were also observed which might be due to the presence of residual solvent following washing of the electrode with PC and acetone or due to possible contamination in the chamber which is typically observed in SEM analysis arising from a large usage. The presence of the copper peak can be attributed to the background signal from the substrate onto which *Si* was electrodeposited.

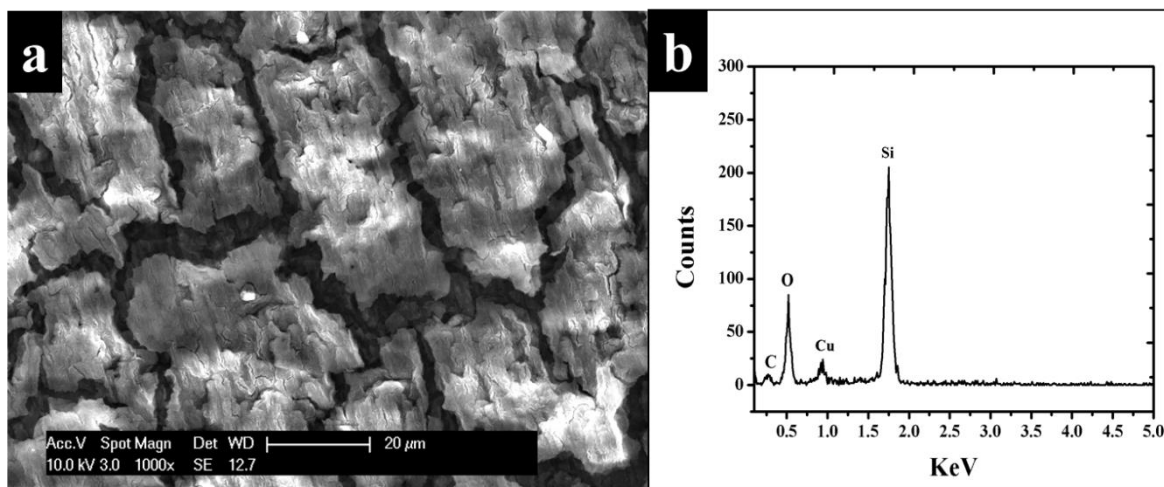


Figure 43: (a) SEM image of the electrodeposited film after 1 hour of galvanostatic reduction at -1mA cm^{-2} & EDAX spectra of the electrodeposited film after 1 hour of galvanostatic reduction at -1mA cm^{-2}

The gravimetric capacity of the deposited silicon films was calculated based on the moles of silicon reduced following Faraday's law. However, the electrochemical reduction of $SiCl_4$ is accompanied by other side reactions such as solvent decomposition and reduction of tetrabutylammonium ion (TBA^+) present in the electrolyte [205, 206, 209]. Hence, an efficiency parameter, η , is introduced into the Faraday's law to calculate the actual number of moles of silicon reduced. Based on previously reported work on electrodeposition of silicon using similar electrolyte and deposition conditions, a 35% ($\eta = 0.35$) efficiency is used in the current work.

Figure 44 shows the charge/discharge profiles for the electrodeposited silicon using a current density of 400 mA g^{-1} cycled between 1.2 to 0.02 V vs. Li^+/Li . Discharge and charge capacities of $\sim 3400 \text{ mAh g}^{-1}$ and $\sim 1150 \text{ mAh g}^{-1}$, respectively were obtained with a first cycle irreversible loss of $\sim 65\%$. The large FIR can be attributed to the formation of the surface oxide indicating need for surface treatments similar to the high SSA Si generated by mechanochemical reduction discussed in the previous chapter. Significant alloying however, can be observed to occur at $\sim 0.2 \text{ V}$ for the first discharge cycle suggesting the lithiation of amorphous silicon and the presence of a two phase region (partially lithiated and unlithiated phase) as reported in the literature [4, 22, 24, 156]. This can be confirmed by the appearance of a large peak close to 0.2 V in the differential capacity plot (**Figure 45**). Other reactions are also observed to occur until a potential of $\sim 0.08 \text{ V}$ (see **Figure 45**), which may be attributed to various intermediate alloying reaction stages of Li_xSi alloys [4, 156]. During the charge cycle, lithium can be extracted from silicon at $\sim 0.3 \text{ V}$ and $\sim 0.45 \text{ V}$ which is commonly observed for delithiation reaction from the amorphous alloys of Li_xSi [4, 7, 22, 24, 213].

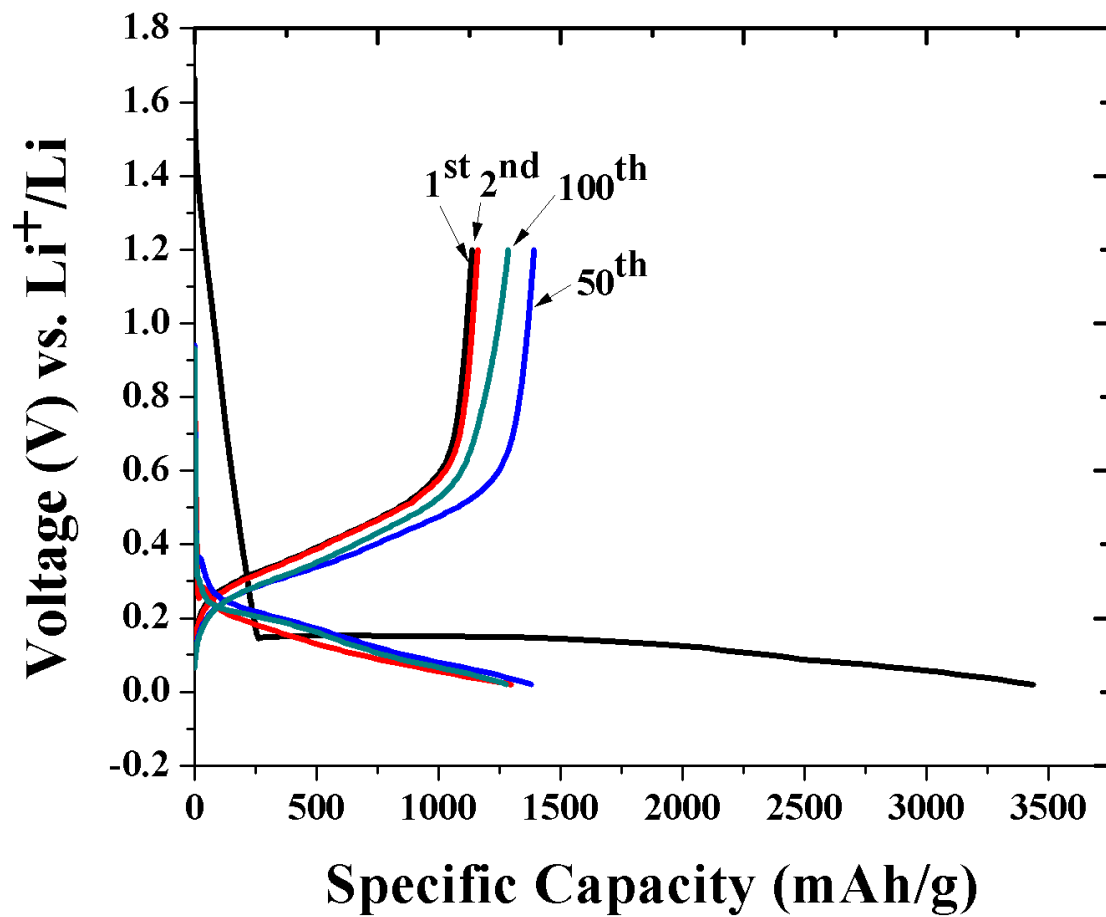


Figure 44: Charge/discharge profile of electrodeposited silicon cycled at 400 mA g⁻¹ for cycles: 1, 2, 50 and 100

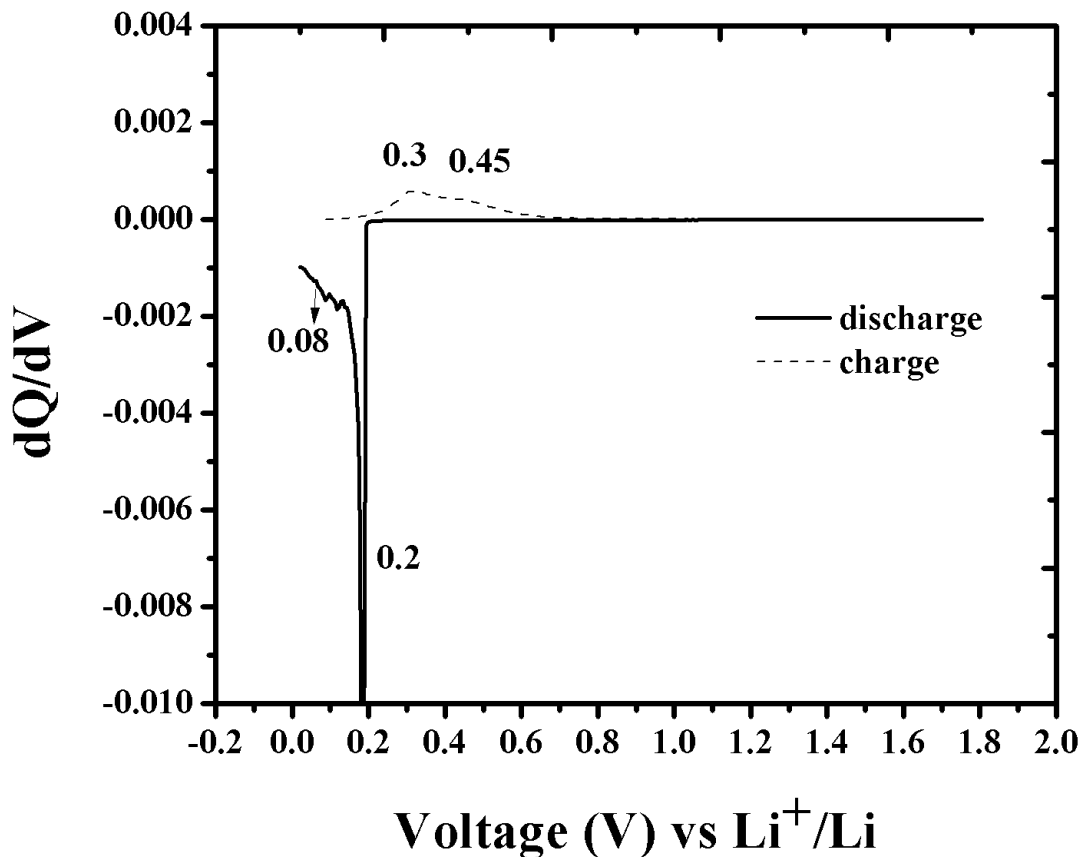


Figure 45: Differential capacity plot vs. voltage for the electrodeposited films at the end of 1st and 2nd cycles

Studies on investigating the electrochemical stability of the deposited films were conducted by electrochemical cycling the films using 400 mA.g^{-1} of current between 1.2 V to 0.02 V vs. Li^+/Li . A reversible capacity of $\sim 1300 \text{ mAh.g}^{-1}$ was obtained for 100 cycles as shown in **Figure 46**. The columbic efficiency varied from 94% to 98% from the 2nd to 5th cycle, after which it further improved and remained close to 99.9% for the rest of the cycles. An impressive fade rate of $\sim 0.016\%$ per cycle was observed which resulted in a capacity of $\sim 1260 \text{ mA.g}^{-1}$ at the end of 100th cycle. Rate capability tests were also conducted on a similar electrode for increasing current densities. **Figure 47** shows the capacity plots for the films cycled at 0.25C, 0.5C, 1C, 2C

and 4C rates. Negligible capacity loss was observed when the rate was increased from 0.25C to 0.5C. However, the capacity decreased progressively with further increase in current density and a capacity of $\sim 520 \text{ mAh.g}^{-1}$ was obtained for 4C rate. The decrease in capacity at higher rates could be attributed to the relatively poor electronic conductivity of amorphous silicon. Nevertheless, no noticeable capacity fade was observed for any given rate/current density.

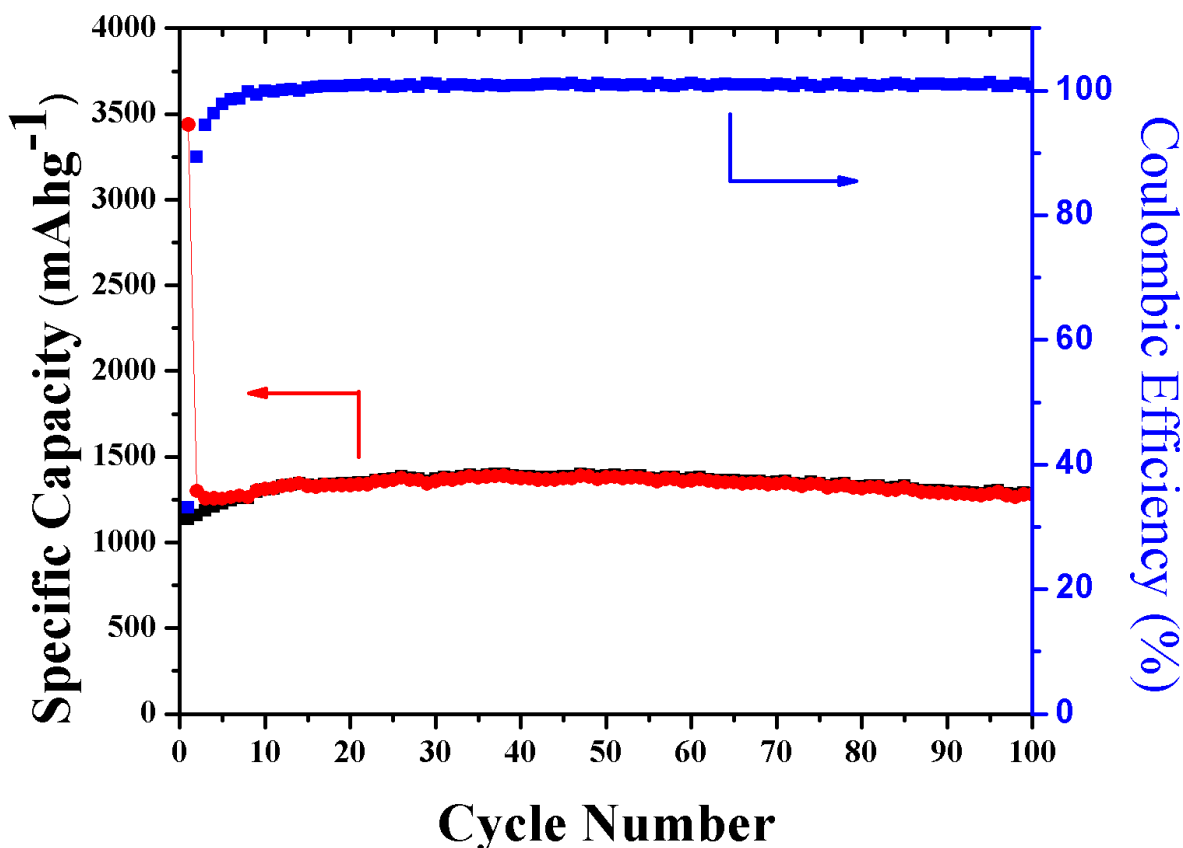


Figure 46: Capacity and coulombic efficiency plots cycled at 400 mA g⁻¹ between 1.2 to 0.02 V for 100 cycles

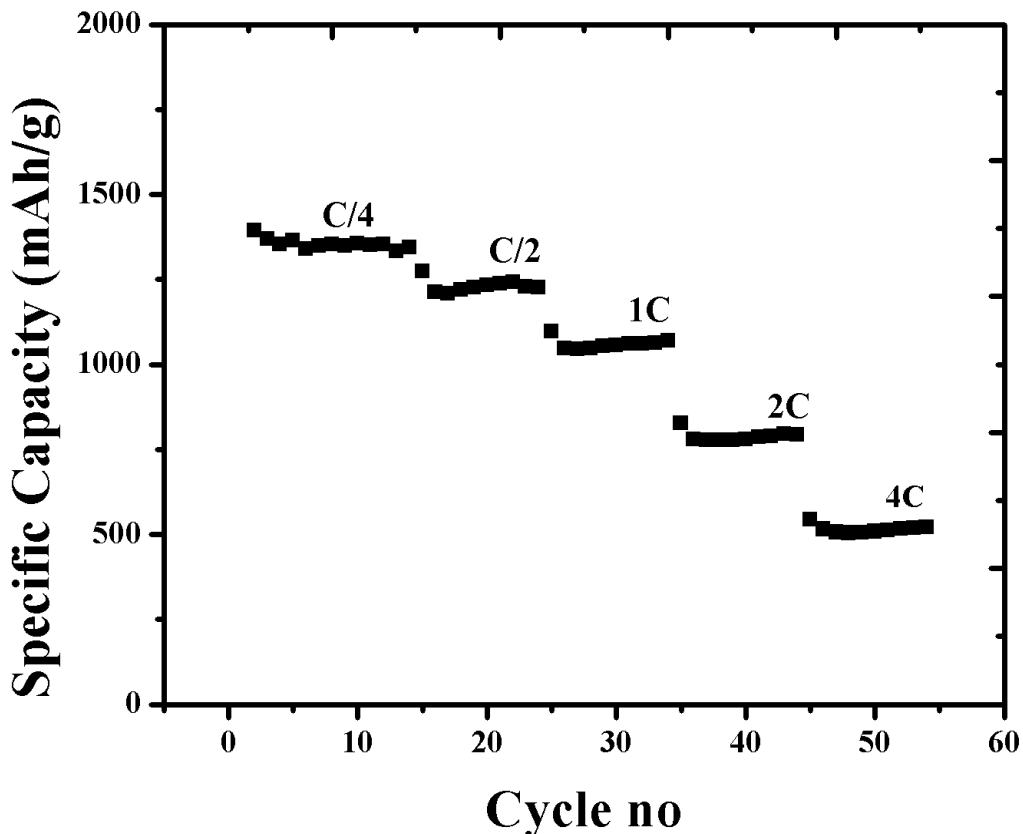


Figure 47: Rate capability tests performed on the deposited films at C/4, C/2, 1C, 2C and 4C rates

In order to understand the effect of cycling on the morphology of the deposited films, the electrodes were analyzed using SEM after cycling. At the end of the 100th cycle, the electrode was transferred to a glove box, where it was carefully opened and rinsed in ethylene carbonate (EC) to dissolve the electrolyte. The electrode was left to dry in the glove box until all the EC evaporated, following which; it was immediately stored in an airtight vial and transferred to the SEM chamber. **Figure 48** shows the morphology of the film at the end of 100th cycle. Consistent with the cycling response, there appeared to be no extension, modification or growth of the crack width or length in comparison to what is already seen in the pristine films as shown in **Figure 43a**. However, in contrast to **Figure 43a**, the film appears to have developed increased porosity upon cycling. Analyses of these regions corresponding to the onset of the pores, appeared as pits

of varying depths. The origin of these pits is intriguing and unclear at present. It is speculated at present that these pits are forming due to the possible erosion of the film upon likely dissolution of silicon in the electrolyte. Further studies are clearly warranted to understand the nature and the cause of the formation of these pits and pores. These studies are currently on-going and part of the future work to be executed. It should be noted however, that apart from the formation of pores, the silicon islands appear to have maintained the morphology and island size even after 100 cycles of charge and discharge, which is well supported from the excellent capacity retention of the film.

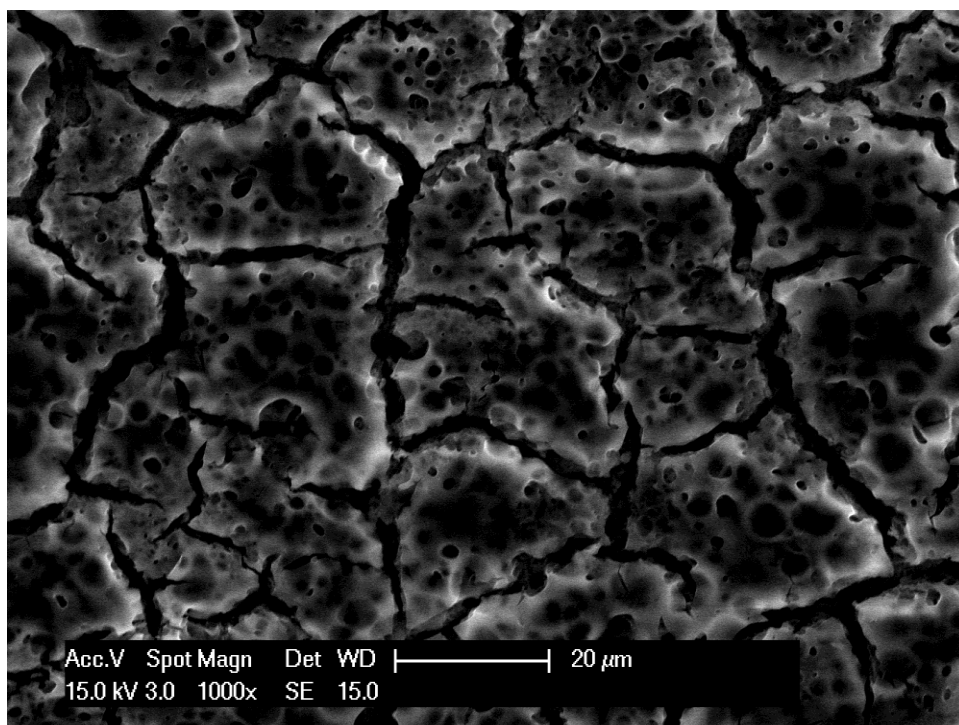


Figure 48: SEM image of the electrodeposited film at the end of the 100th cycle showing the presence of surface pits.

Impedance studies were performed at the end of complete charged state for various cycles and are shown in **Figure 49**. The impedance spectra indicate a suppressed semi-circle and a straight line at approximately 45° to the Z (real) axis. The semi-circle is due to the charge transfer resistance caused by the surface of the deposited film while the straight line corresponds to the diffusion of lithium ions through the film. The spectra collected at the end of various cycles almost coincide with each other with no predominant change in the shape and thereby delineating no significant increase in film resistance for all the cycles. This observation shows that the deposited film is quite stable with no chemical or compositional changes occurring in the films during electrochemical cycling.

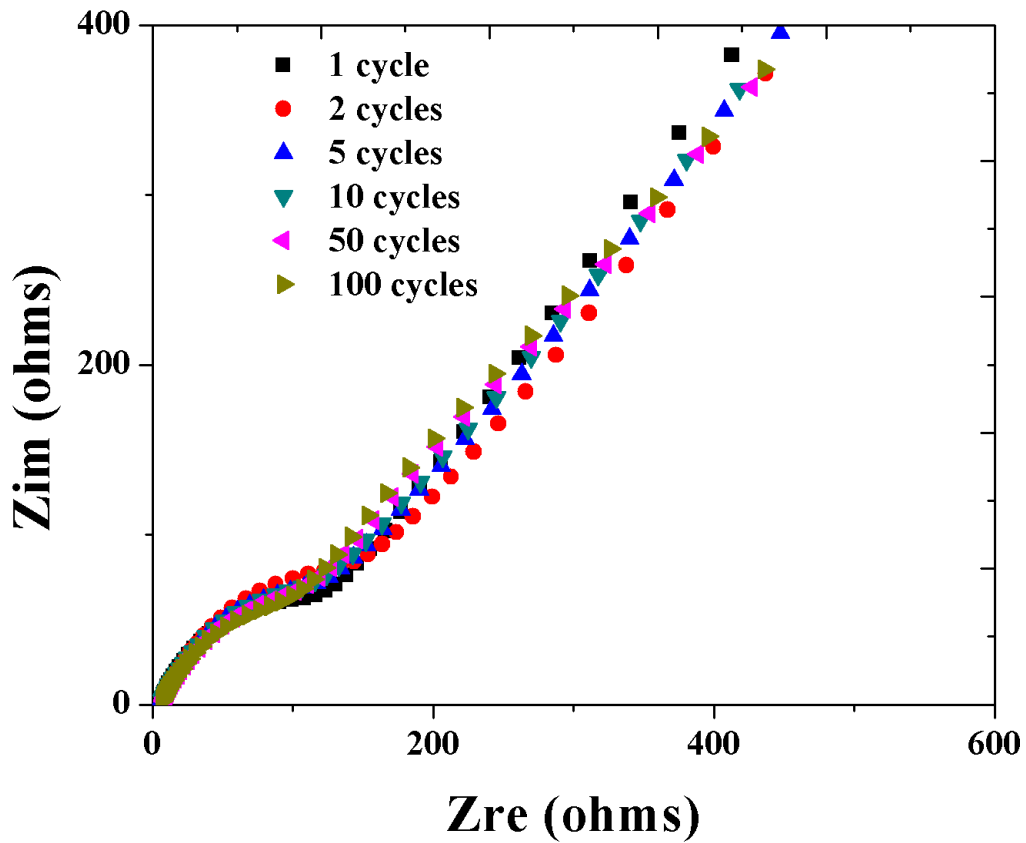


Figure 49: Impedance spectra of the electrodeposited amorphous silicon at the end of charged state for the 1st, 2nd, 5th, 10th, 50th and 100th cycle

5.4 CONCLUSION

Electro-reduction of $SiCl_4$ to silicon has been achieved at a cathodic potential ~ -1.6 V vs. Pt.QRE on copper substrates from a PC based solvent. Galvanostatic reduction at a current density of -1mA cm^{-2} yields a greenish yellow film which is mainly comprised of *Si*, *C* and *O* as indicated by EDAX analysis. Raman spectra obtained from the deposited region showed a broad peak at 485 cm^{-1} indicative of amorphous *Si*. Islands of silicon with mud crack type morphology were observed under the SEM, which, after cycling, showed no further change except the evolution of pits and pores on the islands. The deposited films showed a reversible capacity of $\sim 1300\text{ mAh.g}^{-1}$ when cycled at a current density of 400 mA.g^{-1} between 1.2V to 0.02 V vs. Li^+/Li . Columbic efficiencies exceeding 99.5% and a fade rate of less than 0.016 % per cycle were obtained for up to 100 charge/discharge cycles. These films also showed good rate capability performance conducted at 0.25C, 0.5C, 1C, 2C and 4C rates resulting in a capacity of $\sim 520\text{ mAh.g}^{-1}$ at 4C rate. Impedance studies conducted at the end of 1, 2, 5, 10, 50 and 100 charged cycles showed a consistent invariant charge transfer resistance with cycling, which can be correlated to the excellent long term cyclability obtained for 100 cycles despite the large FIR loss of 65% observed in the first cycle suggesting need for surface treatments which is part of the future work.

6.0 CHEMICAL VAPOR DEPOSITION DERIVED SILICON COATED VERTICALLY ALIGNED CARBON NANOTUBE ANODES

6.1 INTRODUCTION

The excellent cycling stability exhibited by the electrodeposited *a-Si* films discussed in the previous chapter shows the efficacy of the free volume and disordered structure present in amorphous silicon to accommodate the volume expansion during the lithiation and de-lithiation processes. Though, electrodeposition method offers a simple way of preparing the electrodes without the use of binders and conductive additives, it is still not effective to make electrodes with high active material loadings (around 1-2 mg/cm²) that are typically recommended by battery manufacturing companies. The active material loading reported in the previous chapter is in the range of 0.1 to 0.5 mg/cm² and increased loading using higher current densities or longer deposition times cannot be achieved without compromising on mechanical stability of the deposited film. Additionally, the films generated by electrodeposition are extremely sensitive to atmospheric air and are completely oxidized to *SiO*₂ within few minutes of exposure. Hence, it is beneficial to obtain amorphous silicon in bulk powder form that can be cast into slurries with the desired active material loading and also that is relatively stable to atmospheric exposure for easier handling. Chemical vapor deposition (CVD) is a simple and effective way for producing large quantities of amorphous silicon (*a-Si*) by decomposing silicon precursors such as SiH₄ gas

in an inert atmosphere. The CVD derived a-Si is relatively stable to atmospheric exposure, as the silicon surface is often passivated by hydrogen (-H) bonds formed between the dangling Si bonds and hydrogen gas generated by the decomposition of silane.

SiH_4 decomposed in a low pressure CVD reactor results in the deposition of a continuous film of *a-Si* on the walls of the quartz tube of the reactor. This silicon film is difficult to remove from the tube in order to make slurries and cast them on current collectors. Hence, a substrate will be beneficial onto which *a-Si* can be deposited via CVD and the bulk substrate-Si composite can be used to make slurries for electrode fabrication. The substrate selected for this purpose needs to be light weight to minimize reduction in gravimetric capacity due to added substrate weight, electronically conductive to allow effective charge transport between *a-Si* and current collector, high specific surface area for maximizing the number of sites for silicon deposition and mechanically durable to allow for the volume changes occurring in silicon during electrochemical cycling.

One dimensional (1D) structures such as carbon nanotubes (CNTs) are known for their light weight, excellent electronic [161] and mechanical properties [26, 27] which have been exploited by our group in our earlier work [4, 5] wherein nanoscale droplets of defined spacing deposited on vertically aligned CNTs on quartz substrates were generated using CVD on quartz substrates and subsequently stripped to form electrodes by slurry coating on *Cu* foil. Stable capacities in the range of 2050 mAh/g with a low first cycle irreversible loss of ~20% was reported for these CNT/Si heterostructures. The CNT substrates provided good electronic conducting pathway for silicon to the current collector providing good charge and Li-ion transport during cycling. In this work, the deposition condition of silicon in the CVD reactor was

varied to generate two different morphologies (droplet and film) on the CNTs. A comparison of their cyclic performance and other structural and material characteristics is made in this study.

Furthermore, a 'binder-less' electrode was also fabricated from the CNT/Si heterostructures that can be directly assembled in a coin without the use of binders and conductive additives. This was achieved by a novel technique involving a manual scribing action of CNT/Si pellet directly onto copper foil to form the active material coated current collector.

6.2 EXPERIMENTAL

6.2.1 SiCNT nanocomposite preparation

Microscopic quartz slides, 3 in. x 1 in. were employed to grow the heterostructures of vertically aligned carbon nanotubes (CNT) and silicon employing a simple 2 step liquid injection CVD approach. The first step involved the growth of carbon nanotubes using liquid injection technique, wherein, m-xylene acted as the carbon source while ferrocene served as the catalyst. Specifically, 0.1 g of ferrocene, dissolved in 10 ml of m-xylene was loaded onto a syringe pump set to flow at 0.11 ml/min. A stainless steel bubbler maintained at 200°C was used to vaporize the carbon-catalyst solution before it was fed into the reactor using argon and hydrogen as the carrier gases (Ar/H₂=85/15 sccm). The reactor was already purged with argon gas and maintained at 770°C. The carbon-catalyst solution was then injected for 90 minutes following which the hydrogen gas was turned off and the quartz tube was allowed to cool down to room temperature while maintaining the argon gas flow. The second step involved the growth of silicon, wherein, hydrogen was replaced with silane gas (20 sccm) and the growth temperature

was lowered to 500°C. The flow rate of argon was varied from 200 sccm to 600 sccm to control the morphology of silicon during deposition.

6.2.2 Materials and electrochemical characterization

The obtained heterostructures of CNTs and silicon were characterized for structure and phase identification using X-ray diffraction (Philips X'Pert Pro system with a copper anode, $\lambda=0.15406$ nm). Raman studies were performed using a Renishaw inVia Raman microscope equipped with a 633 m red diode laser to investigate the order-disorder characteristics of CNTs, and the crystalline/amorphous structure of *Si*. Morphological assessment of *Si* was performed by scanning electron microscopy (SEM, Philips XL30, 15-20 kV).

For electrochemical characterization, slurry coated electrodes of CNT/*Si* heterstructures were used using the following procedure. 50 wt% of silicon coated CNTs were mixed with 10 wt% Super-P and 40 wt% carboxymethyl cellulose sodium salt (binder) to form the slurry. The heterostructures (droplet and film) prepared by this method are of very low density. Initially, 10-20wt% of the binder was used in making the slurries for preparing the electrodes but the quality of these casted slurries was inconsistent, resulting in a non-uniform coating on the copper foil. From our previous studies, increasing the binder content to 40wt% seemed to have significantly improved the slurry consistency and was amenable for generating uniform coatings on copper foil [5]. The slurry was coated onto copper foils and dried in vacuum at 100°C overnight. The dried copper foils were cut to 11 mm circular discs which served as the working electrode. This electrode was tested in a 2016 half-cell configuration with lithium foil as the counter electrode and 1M *LiPF*₆ dissolved in ethylene carbonate (EC) and diethyl carbonate (DEC) (EC:DEC=1:2)

as the electrolyte. All electrochemical measurements were carried out in an Arbin potentiostat and cycled between 0.02 V to 1.2 V vs. Li^+/Li at a current density of 100 mA/g and a loading of 2-3 mg/cm² for both droplet and thin film morphologies.

6.2.3 Binder-less CNT/Si electrode preparation using scribable technique

To obtain the scribable pellet, 200 mg Si-CNTs were pressed using an isostatic press (Carver Inc, IN) under a load of 5 Tons for 60 seconds into pellet (diameter=13 mm, height= ~2 mm). The obtained pellets were used as pencil lead to scribe on a copper foil (18 μ m thick, Insulectro). For better adhesion, the scribed SiCNTs on copper foil were pressed using a cylindrical roller (MTI Corp, CA). Electrodes of 9 mm diameter were cut using a precision disc cutter (MTI Corp, CA) and which then served as the working electrode for electrochemical characterization. For electrochemical measurements, the SiCNT scribed electrodes were directly assembled in CR 2025 coin cells in an oxygen and moisture free glove box (Innovative Technologies Inc). Pure lithium foil was used as the counter electrode in a half cell configuration and a Celgard 2250 polyethylene was used as the separator (MTI Corp, CA). The electrolyte was composed of 1M $LiPF_6$ salt dissolved in the following solvent composition: ethylene carbonate (EC)/diethyl carbonate (DEC)/fluoroethylene carbonate (FEC)=45/45/10 (BASF, NJ). Following the assembling step, the cells were aged for a minimum of 6 hours before performing electrochemical testing. All charge-discharge tests were studied using Arbin Potentiostat (Arbin Instruments, TX) between 0.01V and 1.0 V vs. Li^+/Li . Gamry 4G 300 potentiostat (Gamry Instruments, Warminster, PA) was used for impedance characterization. Impedance scans were

recorded after the de-lithiation reaction at the end of 1st and 50th cycles, over a frequency range 0.1 Hz to 300 Hz with an AC stimulus of 10 mV bias at open circuit potential.

6.3 RESULTS AND DISCUSSION

The heterostructures of CNT/Si were synthesized by a simple 2-step liquid injection approach in a CVD reactor. In the first step, growth of carbon nanotubes on the quartz slides was achieved by the decomposition of m-xylene used as the carbon source on the iron nanoparticles formed as a result of the decomposition of ferrocene in the hydrogen atmosphere at atmospheric pressure conditions. **Figure 50 (a)-(b)** represents the dense vertically aligned carbon nanotube forests on the quartz surface. The length of the CNTs varied from 100 μm to 250 μm with diameters in the range of 50-60 nm.

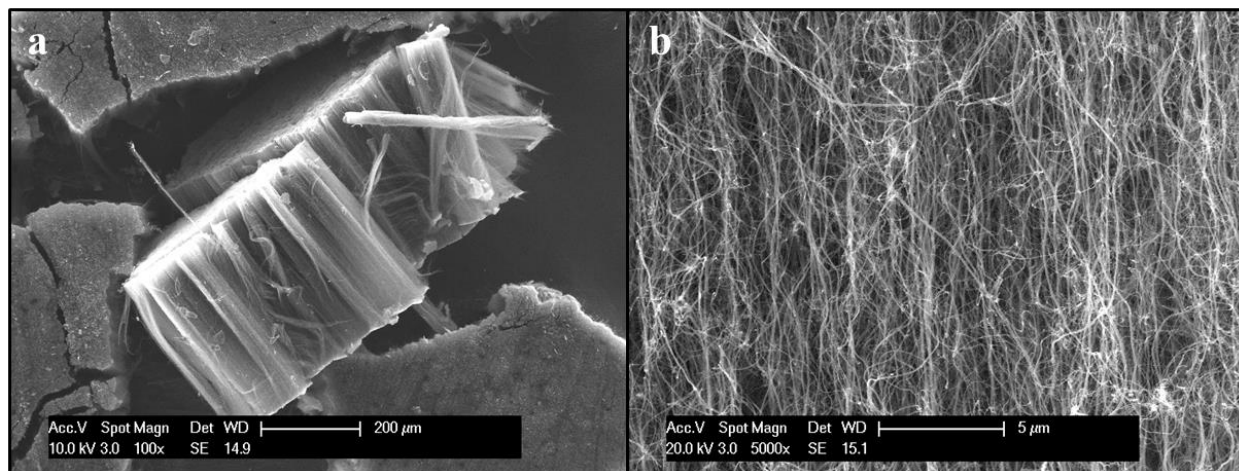


Figure 50: (a) and (b): SEM images of the vertically aligned carbon nanotubes

Silicon deposition on the CNTs was achieved by replacing the hydrogen gas with silane and the reactor was allowed to operate at a low pressure of 5-7 Torr. The growth temperature was maintained at 500°C for 20 minutes. The flow of argon gas was varied to control the partial pressure of the silane gas in the reactor which would result in obtaining various morphologies such as thin films and droplets. **Figure 51 (a)** shows the thin film type morphology which was achieved by using argon flow rate at 200 sccm while the droplet morphology (**Figure 51 (b)**) resulted from a higher flow rate of 600 sccm. Higher silane partial pressure in the former case would facilitate relatively higher nucleation site density of silicon particles on the surface of the CNTs resulting in the formation of films. In both cases (droplet and film), the CNT surface was uniformly coated with silicon and no silicon in loose or agglomerated forms was observed. The morphology and the ordered structure of the CNTs remained unchanged following the deposition of silicon.

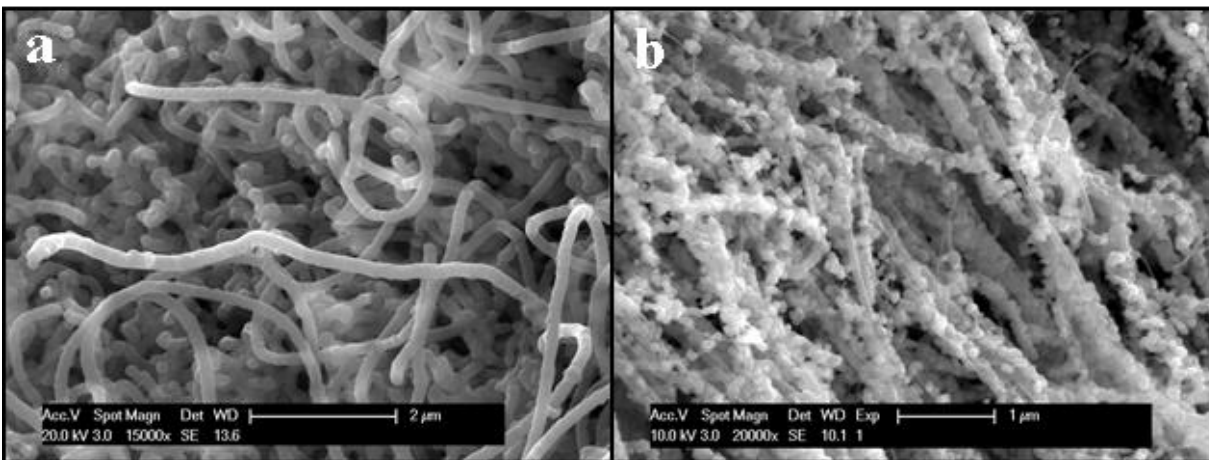


Figure 51: SEM images of Si deposited on CNTs with (a) thin film type and (b) droplet type morphologies

X-ray diffraction patterns of the bare CNTs and CNT/Si heterostructures for both film and droplet type morphology are shown in **Figure 52**. The graphitic structure can be seen from the (002) planes corresponding to the hexagonal arrangement of carbon atoms of the pure CNTs. The peaks corresponding to iron can also be found in the pattern which can be attributed to the iron catalyst particles being retained from the decomposition of ferrocene during the CNT growth. The XRD pattern of the CNT/Si heterostructure for both the morphologies show the presence of silicon in nanocrystalline and amorphous form as seen from the broad peaks of (111) and (220) planes of silicon. According to our earlier reports, based on thermal analysis, it was found that ~5.5 wt% of iron catalyst particles were trapped inside the CNTs [5].

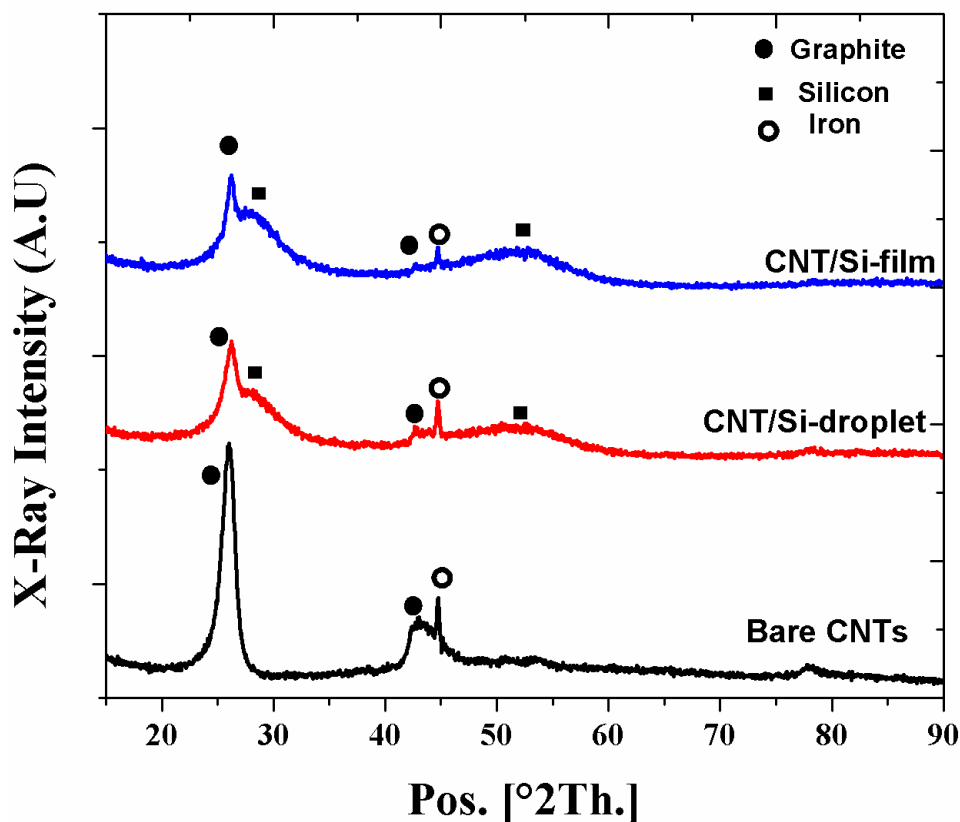


Figure 52: X-ray diffraction pattern of the pure CNTs and CNT/Si heterostructures with both film and droplet type morphologies

The Raman spectra of the CNT/Si composite shows the presence of G (order), D (disorder) and G' (long range order) peaks (**Figure 53(a)**) typically found for CNTs [214, 215]. The I_D/I_G ratio of ~ 0.57 indicates that CNTs grown are pure with fewer number of defects or disordered carbon present and the presence of the sharp G' peak indicates the presence of a good degree of long range order [214]. Crystalline silicon has a sharp peak at 520 cm^{-1} seen in the Raman spectra but as the crystallite size decreases, this peak moves to lower values of Raman shift and with the loss of long range order, a broad peak is observed at 480 cm^{-1} [198, 200, 216]. In the Raman spectra collected on the heterostructures, a sharp peak at 500 cm^{-1} and a broad peak at 480 cm^{-1} were observed (**Figure 53(b)**) which indicates the presence of both nanocrystalline and amorphous phases of silicon deposited on the CNTs on both droplet and thin film morphologies of Si.

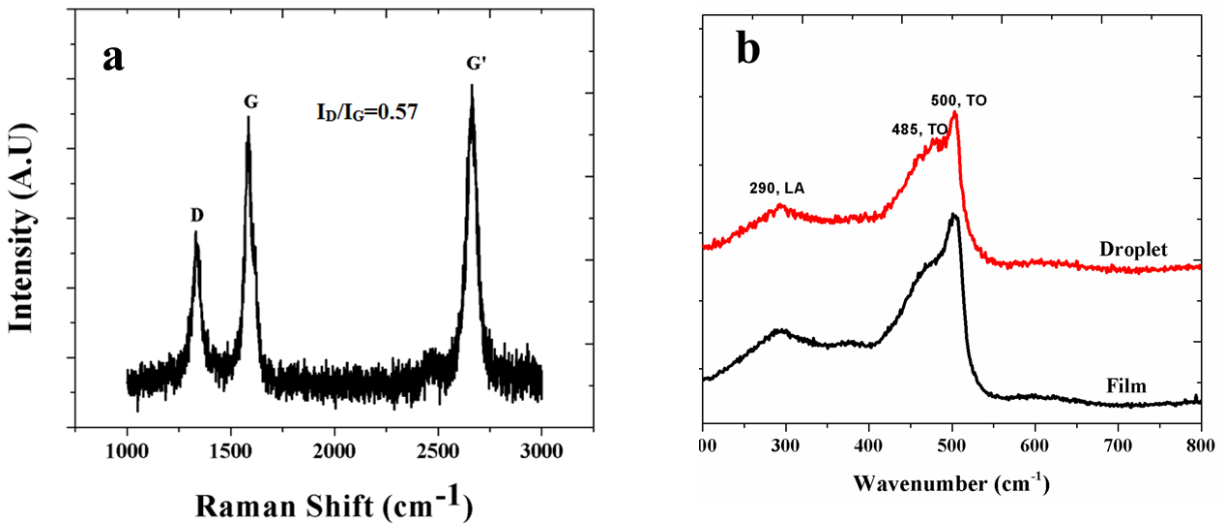


Figure 53: Raman spectra of (a) vertically aligned CNTs and (b) Si with film and droplet morphologies

The reactions of lithium with CNT/Si heterostructure can be understood by the differential capacity plots of the lithiation and delithiation processes occurring during electrochemical cycling. **Figure 54** shows the differential capacity plots at the end of 1st, 2nd and 20th cycle of the heterostructure with the film type morphology. A sharp peak at 0.2 V is observed during the lithiation in the first cycle followed by another peak at 0.08 V [4, 8, 24]. The reaction at 0.2 V is considered to be the lithiation of amorphous silicon and the presence of two phase (partially lithiated and unlithiated) region, consistent with other reports on lithiation of amorphous silicon during the first cycle. The bell shaped peak between 0.12 V and 0.07 V corresponds to the well-known amorphization of crystalline silicon in the composite and further lithiation of the Li_xSi alloys formed from the reaction at 0.2 V [8]. During the delithiation step, two peaks at 0.3 V and 0.45 V were observed which correspond to the phase transition between amorphous Li_xSi alloys and formation of amorphous silicon, respectively [213, 217]. Although, these differential capacity plots were obtained for the thin film type morphology of silicon on CNTs, similar reactions during lithiation and delithiation processes were seen to occur for the droplet morphology which is also reported in the earlier reports from the Kumta group [4, 5]. In the second cycle, the lithiation of amorphous silicon to form the Li_xSi alloys is slightly shifted to higher potential values of ~0.24 V which is consistent with the earlier reports from the Kumta group and other reports in the literature [4, 8]. The lithiation and delithiation curves superimpose very well till the 20th cycle indicating there are no additional reactions occurring while cycling the CNT/Si heterostructures.

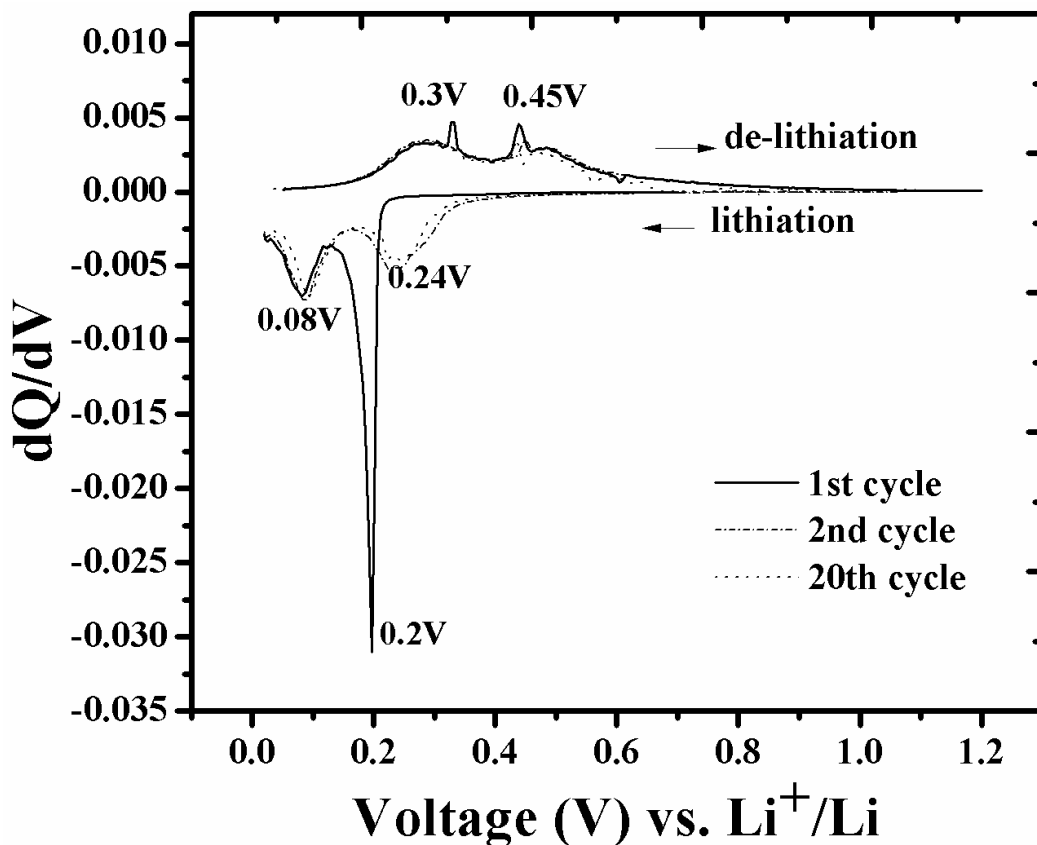


Figure 54: dQ/dV plot of lithiation and delithiation of silicon for 1st, 2nd and 20th cycles

Figure 55 shows the cycling performance of the heterostructures with thin-film and droplet morphologies. The film shows a slightly greater first discharge capacity (3213 mAh/g) when compared to the droplet morphology which is around 2720 mAh/g. The capacities reported here are calculated based on the whole mass of the CNT/Si heterostructure. The silicon (droplet/film) formed during the chemical vapor deposition step is mostly amorphous with some amount of nanocrystalline silicon also present, which is evident from the Raman spectra and the differential capacity plots. Due to the amorphous nature of silicon, one can expect X-ray diffraction intensity of silicon peaks to be significantly lower than the sharp peaks of CNTs. In addition, the CNTs account to very small weight percent of the total CNT/Si composite where

most of the mass is contributed by silicon, resulting in a high first discharge capacity of the heterostructure. Additionally, electrodes of pure CNT have been cycled which give a capacity of only ~150 mAh/g when cycled at similar current density used in this research. This difference can be attributed to the higher Si content in the film morphology resulting from the higher silane partial pressure in the reactor tube. Despite the droplet morphology showing a lower capacity, it exhibited higher stability with a fade rate of 0.25% per cycle when compared to a film that showed a fade rate of 1.61% per cycle. The availability of free space in the droplet-type heterostructure during the lithiation process allowing for expansion could explain the higher stability. Furthermore, the defined spacing of the droplets also allow for the droplets to migrate under the high stress and strain conditions prevalent during cycling thus allowing the heterostructure system to be more compliant exhibiting the higher observed stability. Additionally, the Si droplets are tethered to the underlying CNTs by a thin amorphous carbon layer [5] which provides the added stability to the droplet morphology. Such a compliant situation however is not afforded by the thin film morphology despite the available free volume of the amorphous component of Si. The continuous film coverage of Si on CNT is more likely to undergo fragmentation under the higher stress conditions due to the larger mass of Si deposited on the CNT structure. As a result, the film morphology undergoes rapid capacity fade since the fragmented silicon regions are unlikely to be tethered as the droplets deposited on CNT.

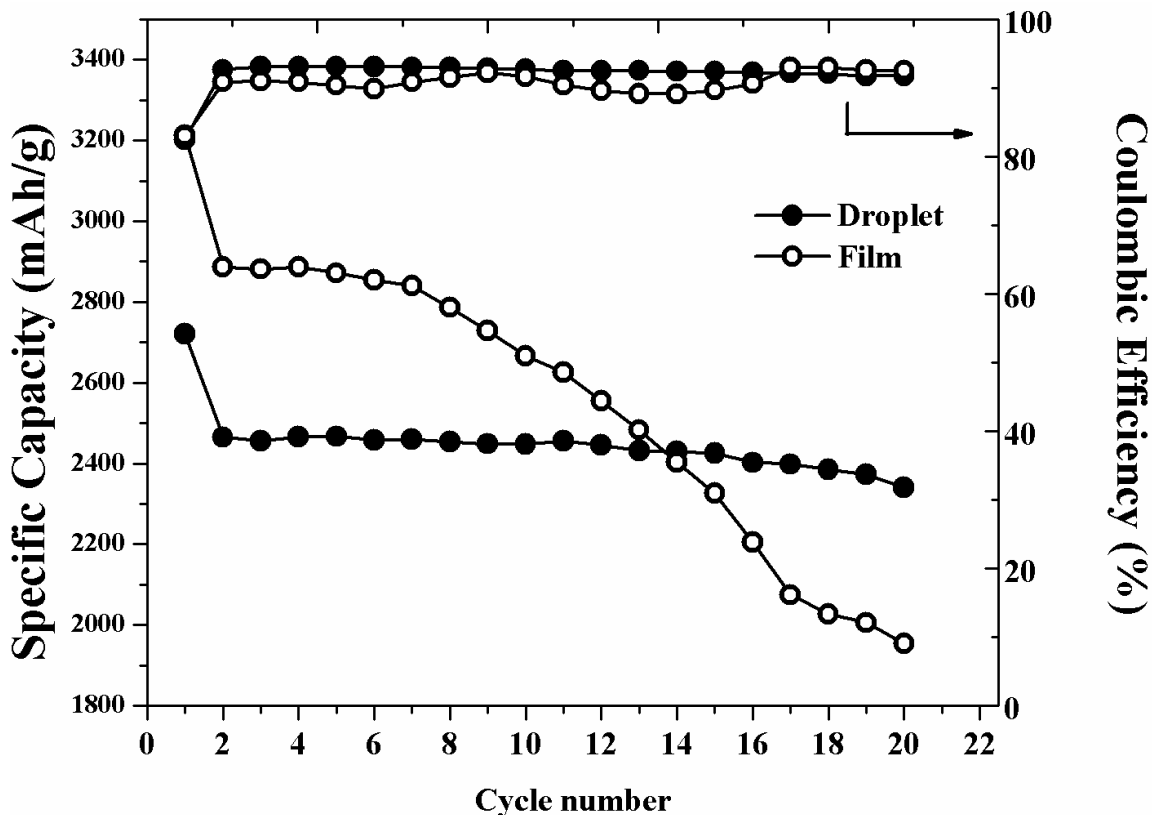


Figure 55: Cycling performance and coulombic efficiencies of CNT/Si heterostructure for thin film (open circle) and droplet (filled circle) morphologies

Figure 56 shows the voltage-capacity plots for both the film and droplet type morphologies which exhibit a low irreversible discharge capacity loss of $\sim 10\%$ and this was still comparable to what is generally observed for graphite based anodes. The results clearly show the influence of the droplet and thin film morphology of Si on the electrochemical capacity as well as the capacity retention. It should also be noted that the loading of the heterostructures is in the range of $\sim 2\text{-}3 \text{ mg/cm}^2$ in both cases demonstrating that the CNT-Si heterostructures comprising the Si droplets potentially is a viable system to replace the graphite anode.

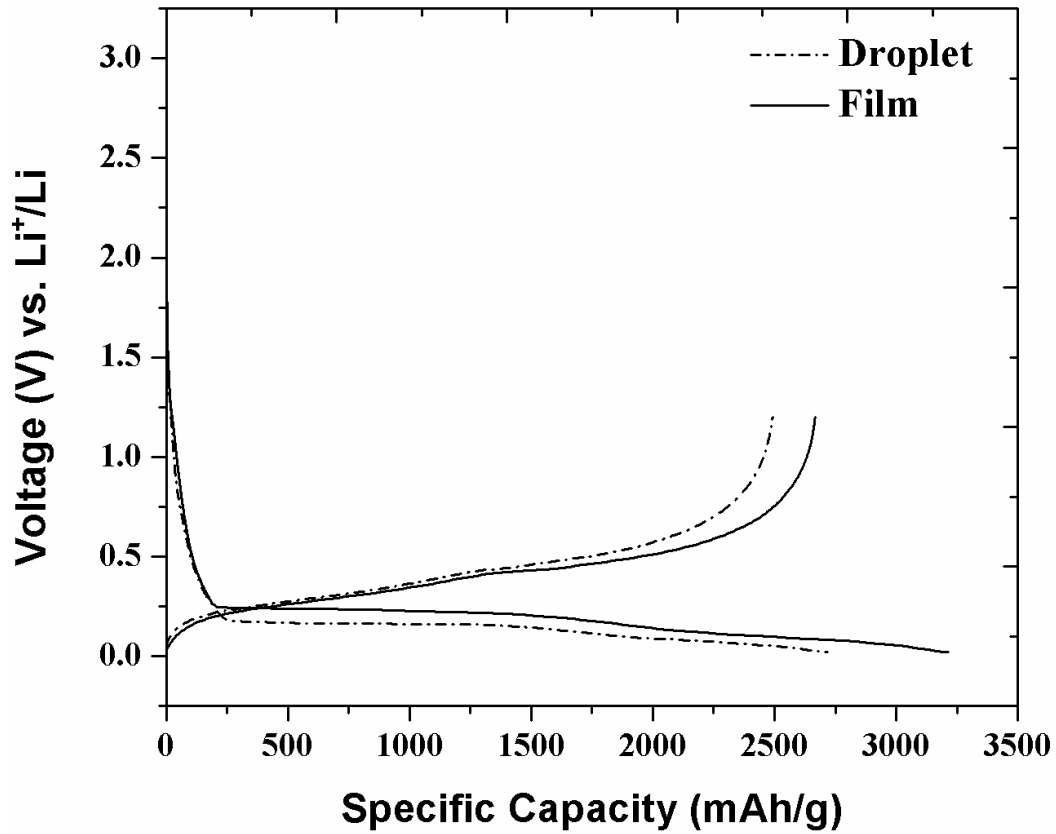


Figure 56: Voltage vs Capacity plots of CNT/Si heterostructure for thin film (solid line) and droplet (dash-dot line) morphologies

6.4 BINDER-LESS, SCRIBABLE CNT/SI HETEROSTRUCTURE ANODES

Figure 57 shows the various steps involved in the fabrication of the scribed electrodes containing multiwall carbon nanotubes coated with silicon at different stages. Long vertically aligned multiwall carbon nanotubes (VACNTs) were first grown using a simple liquid injection approach similar to earlier published work from the Kumta group wherein ferrocene and m-xylene were used as the catalyst and carbon source for the growth of the carbon nanotubes, respectively [4, 5, 28]. The obtained SiCNT heterostructures were compacted using an isostatic press into a pellet (diameter=13 mm, height= ~2 mm) which was then used to manually scribe the SiCNT on a copper foil employing a conventional writing action. A uniform dark coverage of the SiCNT composite film was obtained within few strokes of the scribing action. A mechanical roller was then used to further press the coated electrodes to enhance adhesion of the scribed particles onto the copper electrode.

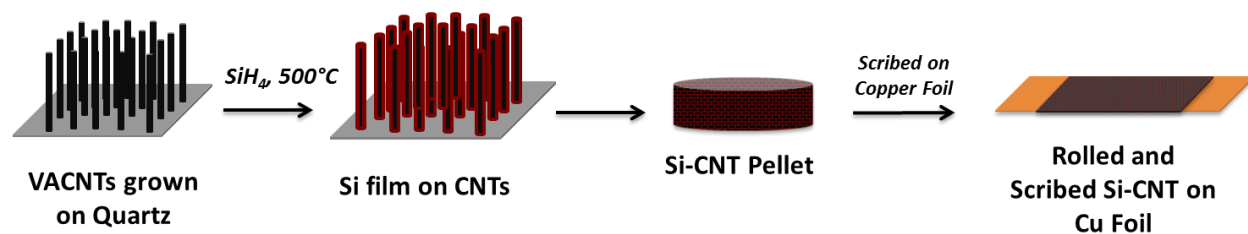


Figure 57: Schematic showing the fabrication of scribed SiCNT electrode on copper foil

Figure 58 shows the SEM images of the SiCNT heterostructures at various stages of the synthesis and electrode preparation. From **Figure 58a**, the carbon nanotubes obtained on quartz appear to be dense, vertically aligned with lengths varying from 200 μm - 300 μm and diameters in the range 25-35 nm[28]. Upon silane decomposition, the silicon is coated as uniform thin layer on the CNTs as observed from the SEM image in **Figure 58b**. **Figure 58 c & d** show the SEM images of the SiCNTs in the pellet and on the copper foil obtained after the scribing action, respectively. **Figure 58e** shows the high resolution image of the Si-CNTs which indicates the uniform coating of silicon in the range of 25-30 nm around the CNTs. Some amount of shortening of the overall length of the heterostructures can be noticed which may be due to the application of the large load during the compaction process leading to fracture of the CNTs. However, silicon coating on the CNTs remained intact even after being compacted by the isostatic press and scribed on a copper foil. It may be reasoned by the fact that the vertically aligned carbon nanotubes are held together by strong van der Waals forces as this principle is used to generate CNT yarns by dry spinning methods[218]. In the present case, the scribing action of the SiCNT pellet on the copper foil enables the individual silicon coated carbon nanotubes to glide over each other and adhere physically to the surface of the copper foil[219].

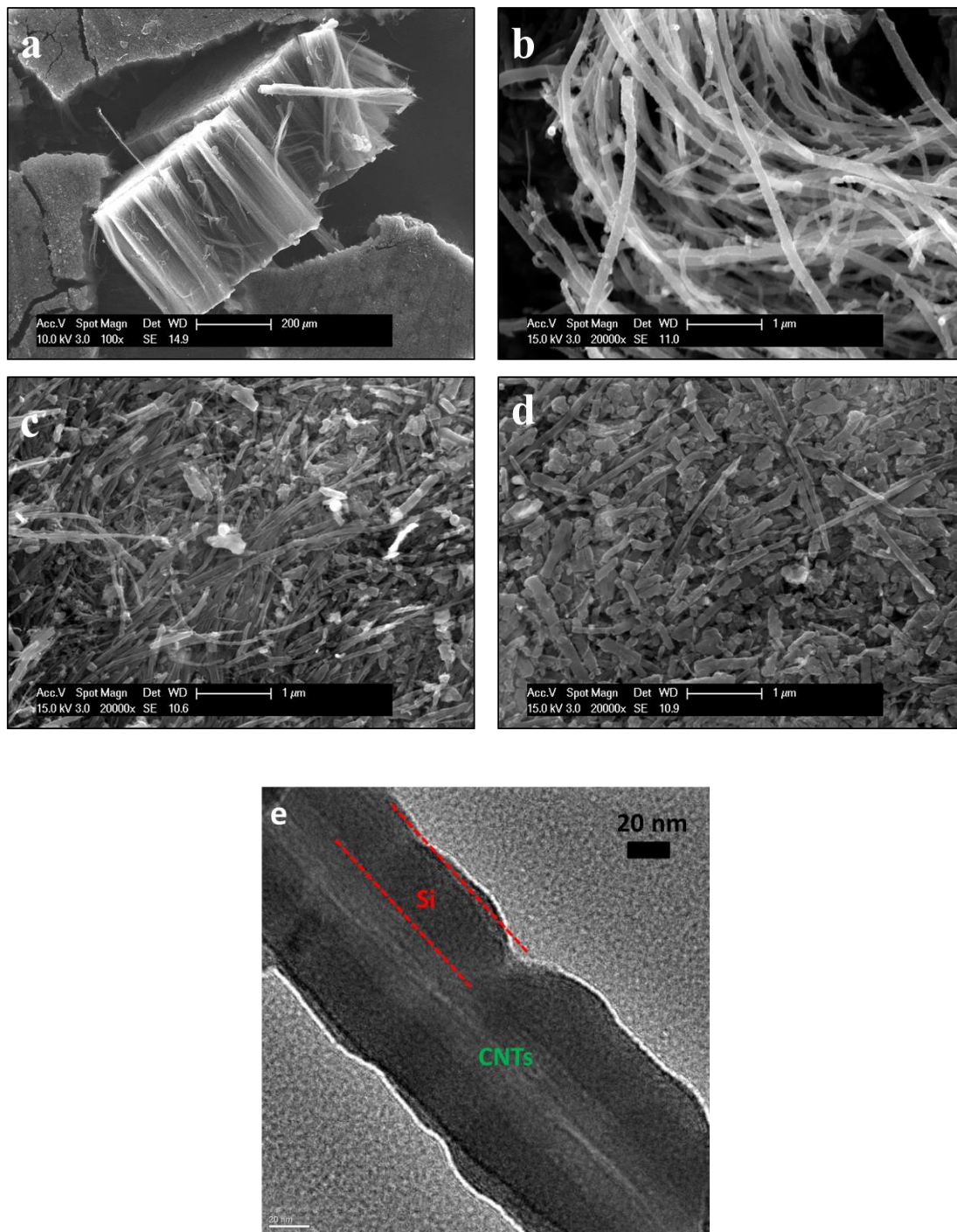


Figure 58: SEM images of (a) vertically aligned carbon nanotubes grown on quartz (VACNTs), (b) VACNTs coated with silicon (SiCNT), (c) SiCNTs after being pelletized by isostatic pressing, (d) SiCNTs after being scribed and rolled and (e) HRTEM image of the silicon coated CNTs

As mentioned earlier, in addition to the electrochemically active material that is present in a typical lithium-ion battery electrode, electrochemically inactive components such as conductive additive and binder that add to the undesirable additional weight and volume to the electrode are present as well. Conductive additives provide the inter-particle electronic conductivity and the binder aid in holding all the components (active and inactive) to the current collector. The scribed electrode containing SiCNTs already contain electronically conductive MWCNTs at the inner core which display a strong adherence to the current collector, thereby eliminating the need to use any conductive additives and binders. These scribed electrodes can be directly assembled in a coin cell (CR 2025) configuration for studying their electrochemical properties. **Figure 59** shows the voltage vs. capacity plot of the scribed SiCNTs for the 1st, 2nd and 50th cycles obtained at a current density of 300 mA/g between the voltage range 0.01V to 1.0 V vs. Li^+/Li in a half cell configuration. Lithiation during the first cycle resulted in a very high discharge capacity of 3112 mAh/g. During the subsequent de-lithiation, a charge capacity of 2523 mAh/g was obtained resulting in a first cycle irreversible (FIR) loss of only 19% which is comparable to the commercially available graphite based anodes. The large capacity of 3112 mAh/g obtained can be realized by assuming all of the Si deposited on the 200-300 μm aligned CNT of diameter 25-35 nm that is scribed onto the Cu foil is electrochemically active. A very high first discharge capacity as mentioned above suggests that the Si-CNT nanocomposite is mainly composed of silicon, owing to the low density of the underlying MWCNTs. Thermogravimetric (TGA) analysis (**Figure 60**) performed on the SiCNT composite indicated the amount of silicon to be close to 90 wt% in the SiCNT composite, which corresponds to a theoretical capacity of 3780 mAh/g. The different lithiation and de-lithiation reactions that

during the charge-discharge processes are usually observed as voltage plateaus in the voltage vs. capacity plots.

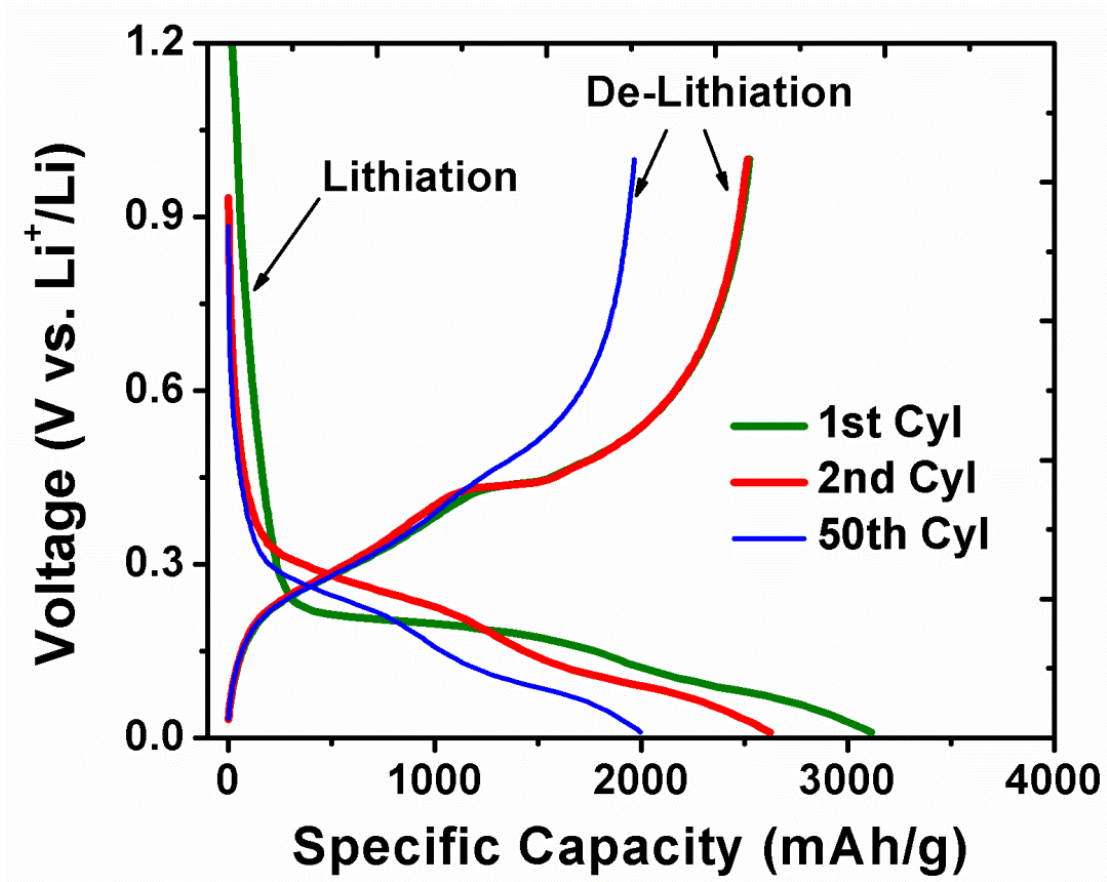


Figure 59: Voltage vs. capacity plot of the scribed CNT/Si composite on copper foil cycled at 300 mA/g between 0.01 to 1 V vs. Li^+/Li

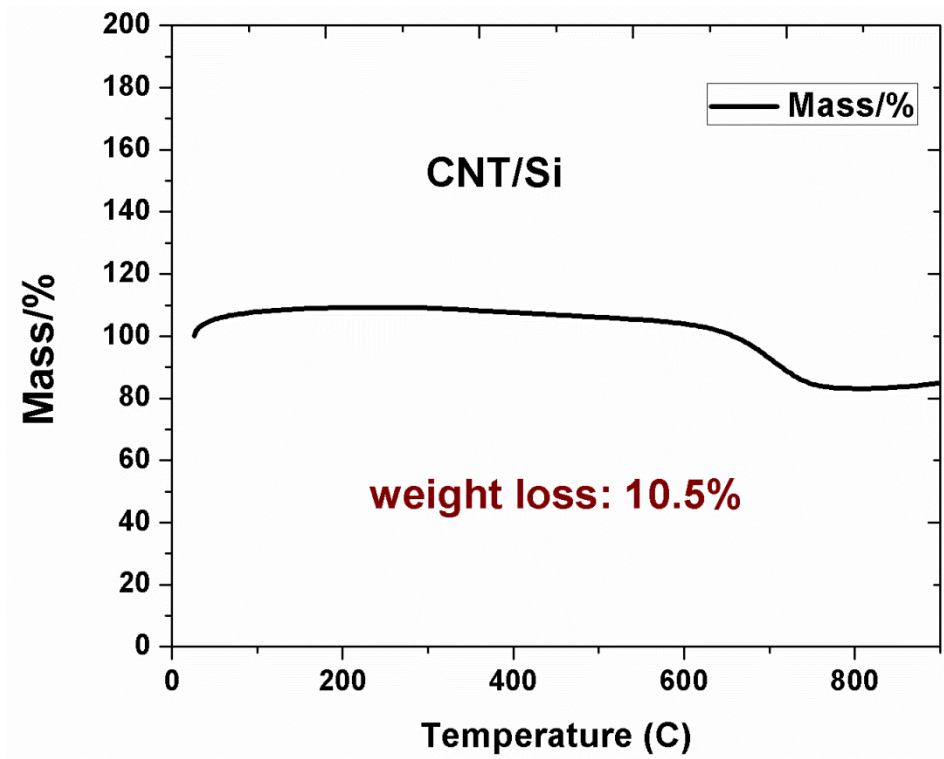


Figure 60: TGA plot of CNT/Si heterostructures performed in air from 25°C to 1000°C at a heating rate of 10°C/min

However, the differential capacity plots represent a better representation of the reaction as indicated by peaks instead of plateaus. As shown in **Figure 61**, during the 1st cycle lithiation, a huge peak at 0.2 V was observed followed by a bell shaped curve at 0.09 V. The peak at 0.2 V corresponds to the voltage plateau in **Figure 59** which indicates the presence of a two phase region governed by Gibbs phase rule. These phases correspond to the unlithiated amorphous silicon (*a-Si*) and partially lithiated silicon phases (Li_xSi) that co-exist until the voltage reaches 0.1 V where complete lithiation of the parent amorphous silicon phase to form the amorphous Li_xSi phase takes place [4, 8, 24, 28]. Below 0.1 V, further lithiation of Li_xSi phase continue to occur along with lithiation of any crystalline silicon present and is represented by the bell curve

centered at 0.09 V. During the de-lithiation step, two major peaks are observed at 0.28 V and 0.43 V which represent the de-lithiation reactions between the lithiated amorphous silicon phases [8, 24]. In the 2nd cycle, the first lithiation reaction now appears to occur at a slightly higher voltage at around 0.24 V and is consistent with other published reports using amorphous silicon [24, 28, 158]. The differential capacity curves for the de-lithiation reactions for 1st and 2nd cycles overlap well indicating the absence of any other additional reactions.

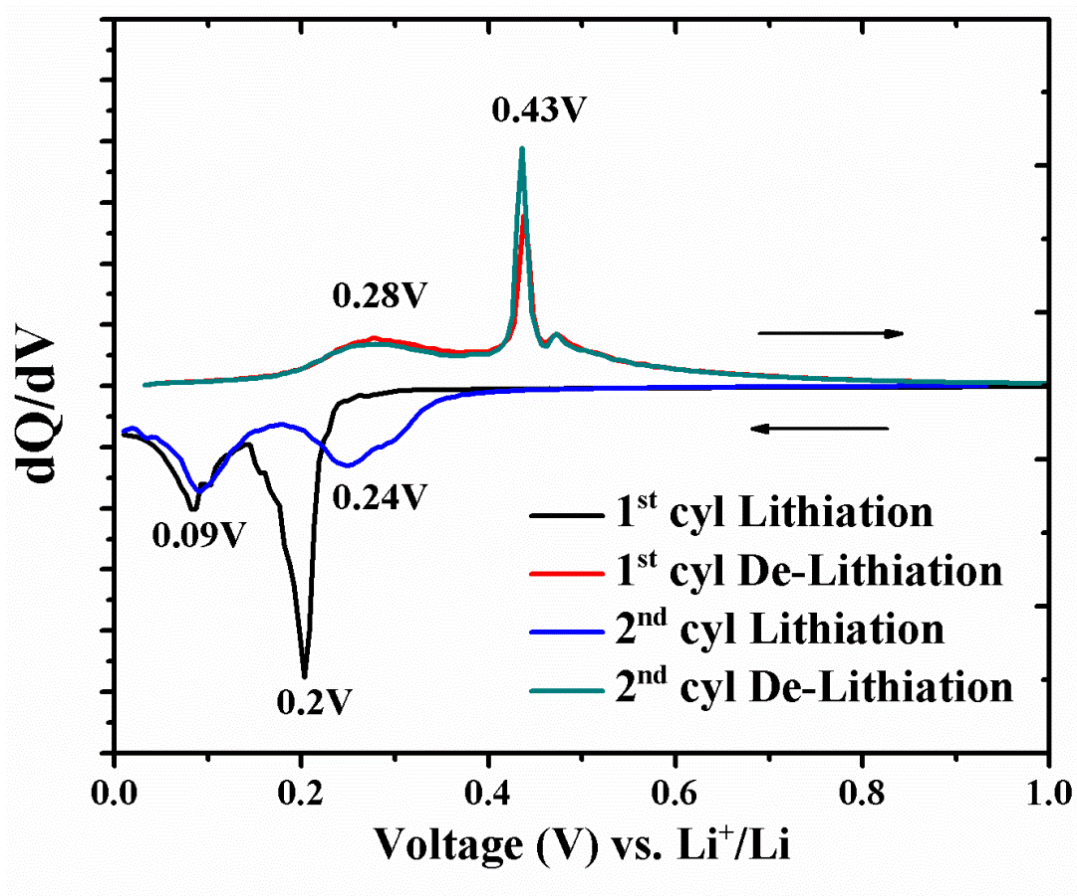


Figure 61: dQ/dV plot of the scribed CNT/Si electrodes

The long term stability plot or the charge-discharge plot shown in **Figure 62** shows the reversibility of the SiCNT electrode. After the first cycle irreversible loss, the SiCNT electrode

exhibits good cyclability and stability for 50 cycles with very little capacity fade compared to commercial silicon electrodes. At the end of 50 cycles, capacities close to 2000 mAh/g were obtained which represents a capacity retention of 76% (calculated with respect to capacity obtained from 2nd cycle) and a fade rate of 0.48% loss per cycle. The coulombic efficiency calculated at the end of the 2nd cycle was 96% but improved upon repeated cycling and reached a value of 98.5 % at the end of 50 cycles. The low coulombic efficiency in the early stages of cycling may be due to the formation of a stable solid electrolyte interphase (SEI) layer or due to the irreversible intercalation of Li⁺ ions into the defect sites of the multiwall carbon nanotubes.

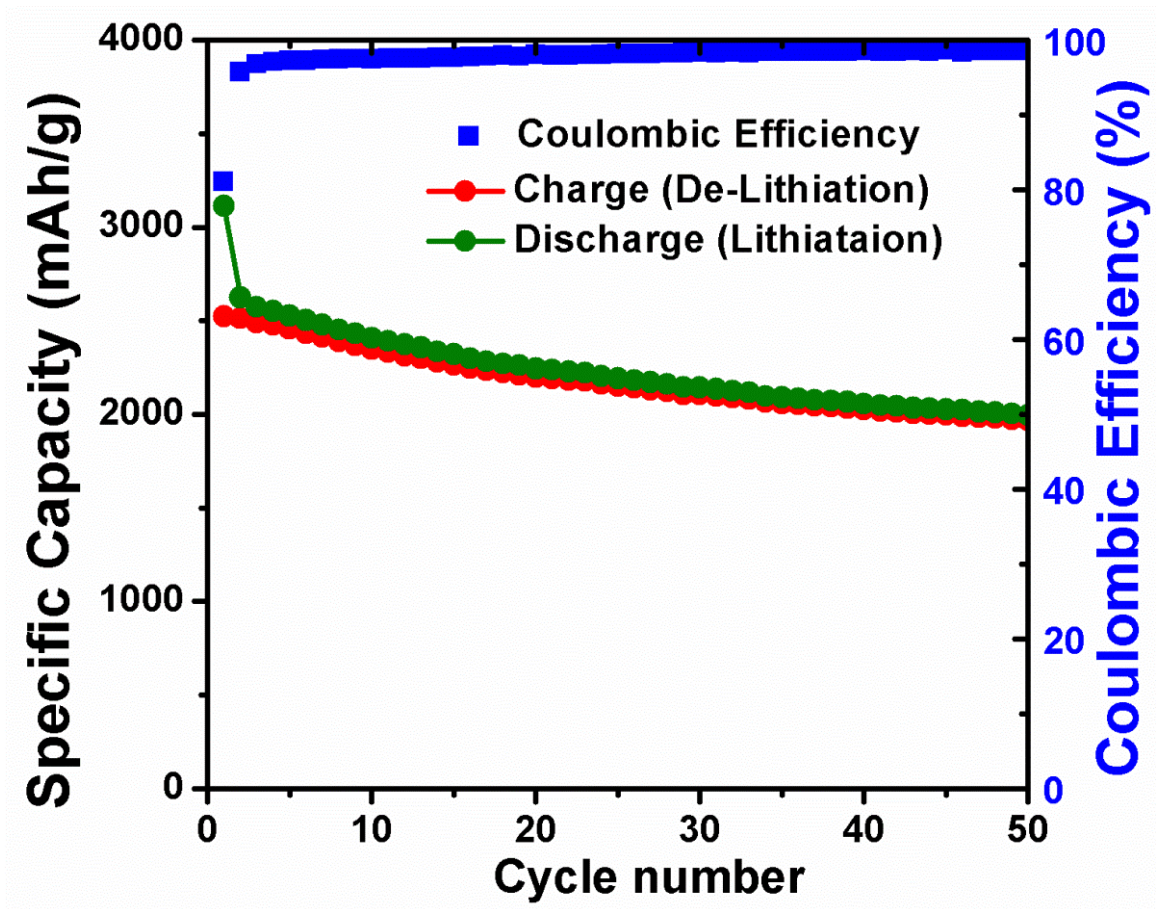


Figure 62: Long term electrochemical cycling plot of the scribed CNT/Si composite on copper foil cycled at 300 mA/g between 0.01 to 1 V vs. Li+/Li

Rate capability is an important characteristic for the battery which relates its performance or the amount of charge stored at various current densities (load) as outlined in the earlier chapters. **Figure 63** shows the rate capability plot performed at currents of 100, 250, 500, 1000 and 2000 mA/g. No significant reduction in capacity can be observed as the current densities were increased from 100 mA/g to 2000 mA/g. Capacities greater than 1500 mAh/g can be obtained even for very high current densities of 2000 mA/g which is nearly 5 fold greater than the capacity obtained using commercial graphite as the anode indicating the promise of the scribing action.

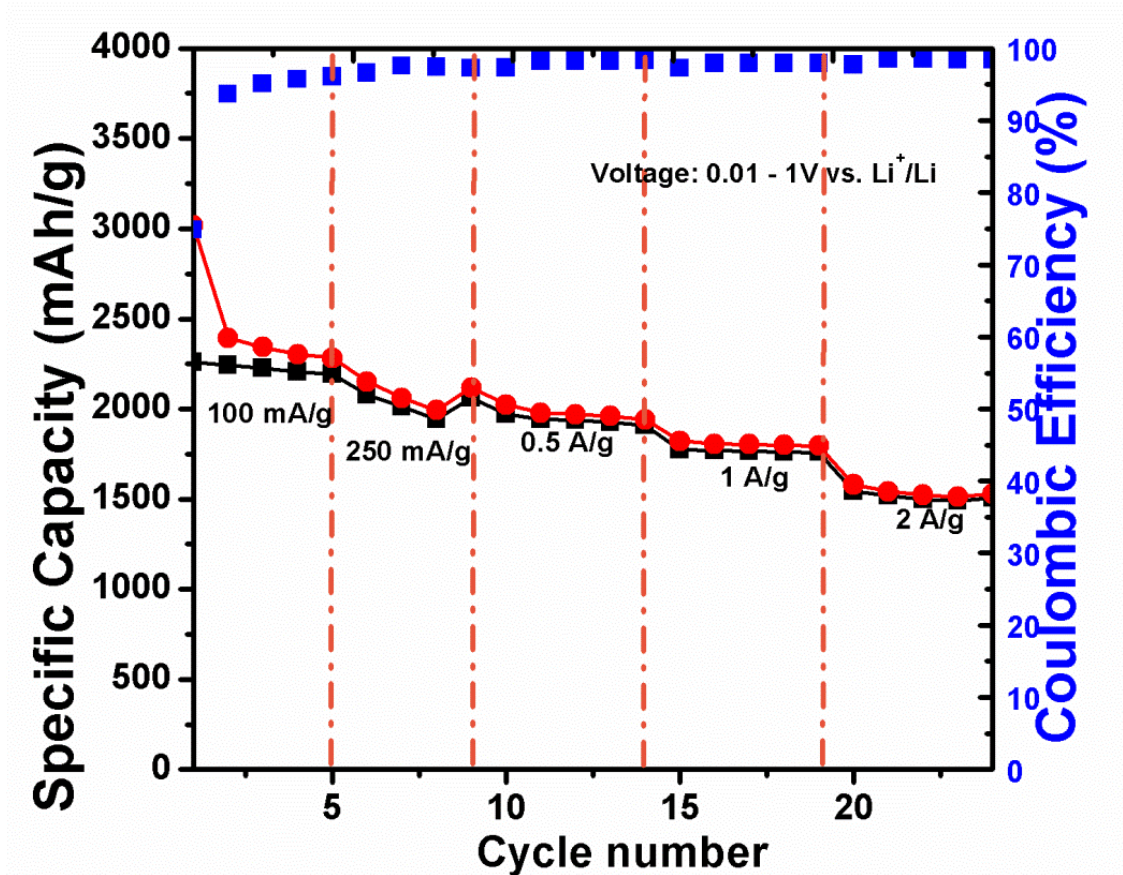


Figure 63: Rate capability plot of the scribed CNT/Si composite on copper foil cycled at 300 mA/g between 0.01 to 1 V vs. Li⁺/Li

Figure 64 shows the Nyquist plots from impedance testing performed on the cells following de-lithiation reactions at the end of 1st and 50 cycles. The plot in general, is characterized by a semi-circular region at higher frequencies and this is associated with charge transfer resistance due to the electron transfer processes involved in the the lithiation and de-lithiation reactions occurring at the interface of SiCNTs and the electrolyte. The linear region at lower frequencies is attributed to diffusion limited processes. The inset in **Figure 64** represents the equivalent circuit that was used to model which best describes the electrode interface of the

tested battery. As shown in the circuit, the physical structure of the electrode interface may be represented using a combination of a resistor and constant phase element (CPE) corresponding to the semi-circle at higher frequencies; and a Warburg element at lower frequencies, respectively. The charge transfer resistance (R_{ct}) generated from modelling the equivalent circuit, does not show a significant change in the electrode impedance following 50 cycles of charge and discharge, thus indicating the possible absence of pulverization of the scribed CNT-Si films that may generate new electrochemically active surfaces or undergo compositional and chemical changes. The scribed SiCNT electrodes thus exhibit high capacity, good electrochemical stability and use a simple scribing action to generate stable electrode coatings without the use of conductive additives and binders. Similar electrode configuration can be designed for the cathode side in the future wherein, thin film coatings of compounds such as $LiCoO_2$, LMn_2O_4 and $LiFePO_4$ could be grown on the CNTs which could eventually be scribed onto aluminium foils, leading to the development of an 'all-scribable' Li-ion battery. These plans are part of the future work which will be executed in the near future.

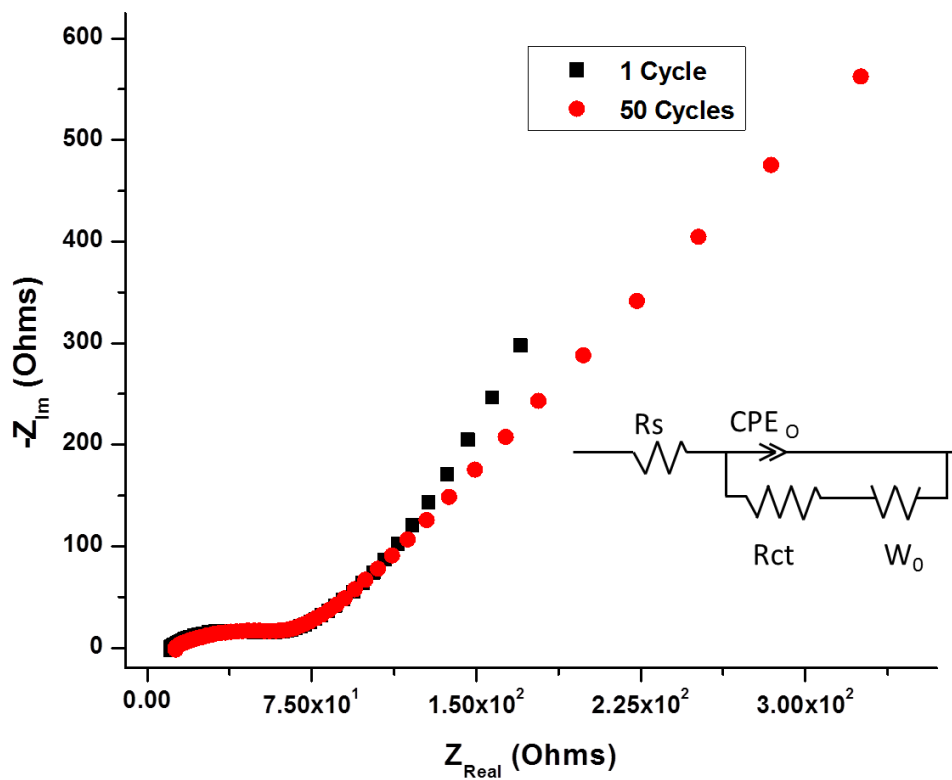


Figure 64: Impedance spectra of the SiCNT scribed electrodes after the de-lithiation step at the end of 1st and 50th cycles

6.5 CONCLUSIONS

Heterostructures of CNT/Si were synthesized on quartz substrates by a simple two step CVD approach. Uniform deposition of silicon in the form of droplets and thin films were obtained on the CNTs by varying the silane partial pressure inside the reactor. The obtained silicon was found to be nanocrystalline from the XRD pattern and some amount of amorphous silicon was also present as evident from the Raman spectra. The differential capacity plot showed significant alloying at 0.2 V and 0.08 V corresponding to the lithiation of amorphous silicon and formation of Li_xSi alloys, respectively consistent with earlier reports. These heterostructures exhibited a high first discharge capacity (2720-3213 mAh/g) followed by a very low irreversible discharge capacity loss of ~10%. The droplet morphology of silicon on CNTs showed better cyclability with a fade of 0.25% per cycle delivering a capacity of in excess of 2300 mAh/g at the end of 20th cycle. The proposed approach shows the feasibility of utilizing CNT/Si based heterostructures prepared by CVD and the ability to alter the thin film deposition parameters to generate systems exhibiting high capacity, low irreversible discharge capacity loss and improved stability as possible next generation lithium ion anodes.

Additionally, a novel scribable technique for achieving electrochemically active SiCNT coatings on copper foil was developed. The SiCNT heterostructures synthesized by a simple two-step chemical vapor deposition technique were compressed into a pellet and used to scribe the active material directly onto a copper foil to form the electrode coating. A very high first discharge capacity of 3112 mAh/g was obtained followed by a low first cycle irreversible loss (19%). The scribed electrodes also exhibited good cyclability with a 76% capacity retention at the end of 50 cycles, corresponding to a fade rate of 0.48% loss per cycle. Impedance studies

performed at the beginning and at the end of the charge-discharge tests do not show any significant increase in the charge transfer resistance correlating well with the good cyclability observed for the scribed SiCNT electrodes.

7.0 HOLLOW SILICON NANOTUBE ANODE PREPARED USING SACRIFICIAL *MgO* NANOROD TEMPLATE

7.1 INTRODUCTION

In the previous chapter, the CNT/Si heterostructures prepared using CVD by the decomposition of carbon and silane precursors exhibit high gravimetric capacities (>2000 mAh/g) and very low irreversible loss ($\sim 10\%$). The capacity retention is superior to the commercially available crystalline silicon and HEMM derived nanosized silicon. However, for practical applications, long cycle life with much lower fade rates ($<0.1\%$ loss per cycle) for several hundreds of cycles is desired. Among the various silicon based nanostructures studies so far, *a-Si* films synthesized by electrodeposition have exhibited very low fade rates ($\sim 0.016\%$ loss per cycle, for 100 cycles). However, they suffer from two major problems which make them unattractive to be used for commercial production. The first major drawback is the large first cycle irreversible loss (65%) due to the presence of the surface oxide layer or possible contaminants that consume *Li* during the first cycle. This extra *Li* is provided by packing additional equimolar quantity of cathode material, which in turn adds to the cost and weight of the battery pack. The second drawback is the inability to use the deposited *a-Si* films to form a slurry and cast onto the copper foil to achieve high active material loading.

Among several nanostructures of silicon i.e, nanowires [2, 156], core-shells heterostructures [4, 5, 28, 220], nanoshells [221], etc, hollow silicon nanotubes [3, 29, 30] have attracted tremendous interest due to their high capacity and excellent cyclability with minimal capacity fade, arising from its unique nanostructure enabled mechanical properties. Silicon nanotubes offers facile strain similar to the one dimensional silicon nanowires and the free volume available due to the hollow tubular configuration allow the silicon to freely expand/contract without fracture. Furthermore, the nanotube configuration exhibits good rate characteristics due to its shorter Li^+ diffusion distances and increased wetting of the electrolyte on the inner and outer portions of the nanotube [3]. Initial studies on silicon nanotubes reported capacities in excess of 3000 mAh.g^{-1} with more than 85% capacity retention [12, 29]. More recently, an SEI controlled double walled silicon nanotubes exhibited excellent capacity retention for 6000 cycles [30].

Apart from the material and electrochemical properties, other factors that play an important role when selecting battery materials from a commercialization standpoint are: cost of the raw materials or precursors, the synthesis technique, recycling costs and environmental effects of the by-products generated from the production process. Despite their excellent electrochemical characteristics, the silicon nanotubes mentioned above are prepared by synthesis techniques that require large volume of expensive inorganic solvents, expensive templates; and further, have lower product yield and the electrochemical tests reported involve reduced loading densities. For example, the first report on using silicon nanotube anode as Li-ion anode required expensive porous alumina membrane templates and glyme based organic solvents. In another study, arrays of sealed hollow silicon nanotubes grown directly on metallic substrates using sacrificial ZnO nanorod templates, exhibited good capacity and cyclability. However, such

substrate growth process is unfavorable from an industrial standpoint wherein slurry casting methods are typically employed to achieve desired loading densities. The double walled hollow silicon nanotube anodes developed by Wu et al, use a relatively inexpensive technique but the low loadings (0.02 to 0.1 mg.cm^{-2}) achieved by this method make them unattractive for practical applications where higher loadings or areal capacities are required.

Therefore, in order to render these silicon nanotubes as an industrially viable anode system that can potentially replace graphite, it is very critical to adopt a synthesis route that utilizes inexpensive precursors, involves unsophisticated equipment and are capable of producing large yield of nanotubes that could eventually be used to make slurries using contemporary battery processing techniques. Upon in-depth observation into the existing methods for making silicon nanotubes, it can be hypothesized that the production of the sacrificial template remains the major bottle-neck to achieving the aforementioned attributes for a better synthesis design. In this study, a novel synthesis approach is proposed wherein, large quantities of *MgO* nanorods were synthesized using a simple hydrothermal technique utilizing inexpensive precursors. These nanorods served as the sacrificial template onto which silicon was deposited as a thin layer by chemical vapor deposition. The core-shell structure thus formed was treated with an acid to leach off the inner core (*MgO* nanorods) to form the hollow silicon nanotubes. Furthermore, a regenerative process was developed using simple precipitation techniques to recover the original precursors which could then be reused to synthesize a subsequent batch of *MgO* nanorod template that can be then used for h-SiNT generation and subsequently continuously re-used thus enabling a continuous closed loop recyclable process. The approach is therefore cost effective while also being efficient in generating h-SiNTs with unique and desirable attributes as described in the following.

7.2 EXPERIMENTAL

7.2.1 Synthesis of MgO nanorods

Magnesium oxide nanorods were synthesized according to a modified published method [222]. Specifically 6.44 g of magnesium acetate tetrahydrate (Aldrich) and 1.2 g of urea was dissolved in 75 ml and 25 ml of DI water, respectively. The urea solution was added drop wise to the acetate solution under vigorous stirring and left for an hour. The solution was then added to a Teflon lined stainless steel autoclave (125 ml total capacity) and heated to 180°C at 5 °C/min for 1h. At the end of the reaction, the vessel was allowed to cool down to room temperature before it was opened. A white precipitate was observed which was washed thrice thoroughly with DI water and isopropanol to remove any unwanted dissolved products and collected on a 0.5 µm PTFE membrane using vacuum filtration. The wet cake at the end of filtration was dried overnight in a 60°C oven to evaporate the solvent. A final calcination step was employed in pure oxygen gas by first heating from room temperature to 310°C at a heating rate of 3°C/min for 7 hours and then to 500°C at 1°C/min for 1hour, resulting in a *MgO* nanorod cake.

7.2.2 Synthesis of h-SiNTs

The dried *MgO* nanorod cake after vacuum drying was coated with a uniform amorphous *Si* coating utilizing a low pressure chemical vapor deposition system (LPCVD). 2% silane (SiH_4) diluted in argon gas was decomposed at 500°C for 10 minutes. The core-shell *Si/MgO* cake was then dispersed in 6N *HCl* solution and homogenized in a bath sonicator for 2 hours to dissolve the underlying *MgO* nanorods. After the dissolution, the hollow silicon tubes (h-SiNTs) were thoroughly washed with DI water and isopropanol and were collected on 0.5 μm PTFE membrane filters using vacuum filtration. Finally, the solvent from the wet h-SiNT cake was removed by heating to 100°C overnight in a drying oven. The h-SiNTs obtained were then ready for use.

7.2.3 MgO template regeneration

The supernatant left after washing the *Si/MgO* core-shell structure comprises mainly of $MgCl_2$ dissolved in water and excess *HCl*. *NaOH* was added to precipitate $Mg(OH)_2$ and the excess *HCl* would react with *NaOH* to form *NaCl* which further dissolves in water. The white suspension was centrifuged and filtered over 0.5 μm PTFE membrane to obtain a white solid. To this white ($Mg(OH)_2$) solid, stoichiometric amount of acetic acid was added, stirred for 2 hours and the concentration adjusted to 86 mg.ml⁻¹. 75 ml of this regenerated magnesium acetate solution was then used to prepare the second generation of *MgO* nanorod template.

7.2.4 Materials Characterization

For phase analysis, X-ray diffraction studies were performed using Philips X'Pert Pro system with $Cu K\alpha$, $\lambda = 0.15406$ nm radiation. Raman spectroscopy was performed using a 633 nm red diode laser using a Renishaw in via microscope. Morphological studies were performed using a Philips XL30 (10-20 KV operating voltage) scanning electron microscope (SEM) equipped with an energy dispersive X-Ray spectroscopy (EDAX) analyzer. High resolution transmission electron microscopy (HRTEM) studies were done using JEOL JEM-2100F microscope.

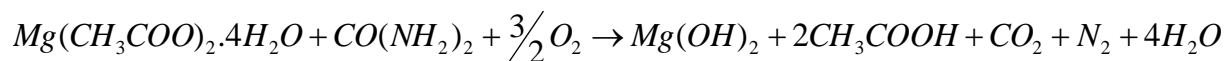
7.2.5 Electrochemical testing

The h-SiNTs were prepared by mixing 50 wt% of active material (h-SiNTs) with 40 wt% binder (sodium alginate, MP Biomedicals) and 10 wt% Super-P (MTI Corp) in DI water for at least 8 hours to ensure formation of a good dispersion. The slurries were degassed for few minutes before being casted on copper foils which were later dried in air for 1 hour and then in vacuum at 100°C overnight. An electrode loading in the range 0.6 – 1 mg/cm² was achieved on the cut copper foils. CR 2025 coin cells (MTI Corp) were used where *Li* metal and Celgard 2250 served as cathode separator, respectively. The electrolyte used in all the studies was 1M *LiPF*₆ in ethylene carbonate/diethyl carbonate/fluoroethylene carbonate (45:45:10, BASF). Electrochemical testing was conducted within the voltage range 0.01 - 1 V vs. *Li*⁺/*Li* in a galvanostatic current mode. Impedance studies of the electrodes were performed using a Gamry potentiostat in the frequency range 0.1 Hz to 300,000 Hz with 10 mV amplitude and no applied potential bias.

7.3 RESULTS AND DISCUSSION

7.3.1 Silicon nanotube synthesis

Hydrothermal synthesis technique offers a simple and commercially viable method, as it is capable of generating large amounts of the product in a short amount of time and uses inexpensive and unsophisticated equipment. The effect of high pressure conditions, which is usually generated inside the autoclave reactor lead to better kinetics and faster diffusion of chemical species. This mechanism enables the chemical reactions to occur at relatively lower temperatures in the hydrothermal reactor compared to synthesizing via a solid state reaction or heating in an open system. In this work, hydrated magnesium acetate ($Mg(CH_3COO)_2 \cdot 4H_2O$) was used as the precursor for MgO and urea served as the combustion agent for the decomposition of magnesium acetate according to **Reaction 1**.



(Reaction-1)

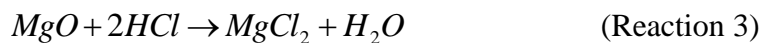
The final product collected over the PTFE membrane at the end of the washing step was in the form of a white, fibrous thick cake that was calcined in the presence of oxygen gas for several hours to convert the magnesium hydroxide to magnesium oxide (MgO) according to

Reaction 2. A multi-stage and slow heating rate is important in order to preserve the morphology of the *MgO* nanorods. Heating rapidly, may cause fracture of the rods due to rapid evaporation of moisture and other volatile substances that are present inside the pores of the nanorods.



The yield of the *MgO* cake obtained at the end of the calcination step was found to be approximately 1g, which corresponds to nearly a conversion rate of 85% from magnesium acetate to magnesium oxide. The *MgO* cake obtained after the calcination step is shown in **Figure 65a**. Even after the calcination step, the cake structure was still maintained and could be held using tweezers and transported to the CVD reactor for subsequent silicon deposition. This is very advantageous from a practical standpoint; as it is easier to employ the template in the form of a solid cake instead of a loose powder for easy insertion and removal from the CVD reactor. The silicon deposition was performed using a method similar to previously reported approaches from the Kumta group for generating CNT/Si heterostructures [4, 5, 223]. The deposition was carried out at 500°C in a low pressure CVD reactor using 2% silane (diluted in UHP argon gas). The *MgO* cake was placed at the center on a quartz slide. The silicon deposition was carried out for 10 minutes to form a uniform thin layer of silicon coating on the surface of the *MgO* nanowires. After the deposition, the reactor tube was allowed to cool to room temperature under the flow of argon gas before it was opened to avoid any oxidation of the nanotubes.

The obtained *Si/MgO* core-shell structure was treated with hydrochloric acid (*HCl*) to dissolve the core or the nanorod template to generate the hollow nanotubes of silicon. The dissolution of *MgO* template in *HCl* occurs according to the following reaction (**Reaction 3**):



After a series of washing steps using DI water and isopropyl alcohol (IPA) to remove the dissolved $MgCl_2$ or any other unwanted impurities, the final product containing the hollow silicon nanotubes (h-SiNTs) are collected on top of the PTFE membranes. After drying, the h-SiNTs can be collected in the form of a cake (shown in **Figure 65b**) which can be easily dispersed in aqueous or non-aqueous solvents using ultra sonication for generating the slurries for electrode fabrication. In this case, nearly 0.5 g of h-SiNTs (using ~1g of MgO nanorods) are obtained from a short 15 minute CVD deposition of silicon in the reactor. The yield of the MgO nanorods can easily be scaled up to several kilograms by employing larger autoclave vessels, capable of holding several hundred gallons of the initial precursors. Also, a similar scale up method for silicon deposition can be envisioned by using large Si-CVD reactors that are typically used in photovoltaic industry and can accommodate bulk quantities of MgO nanorod cakes (weighing several kilograms) as templates for subsequent *a-Si* deposition. Thus, upon removing the template by dissolving in acid and washing with water, several kilograms of h-SiNTs can be obtained from a single batch of the sacrificial nanorod template.

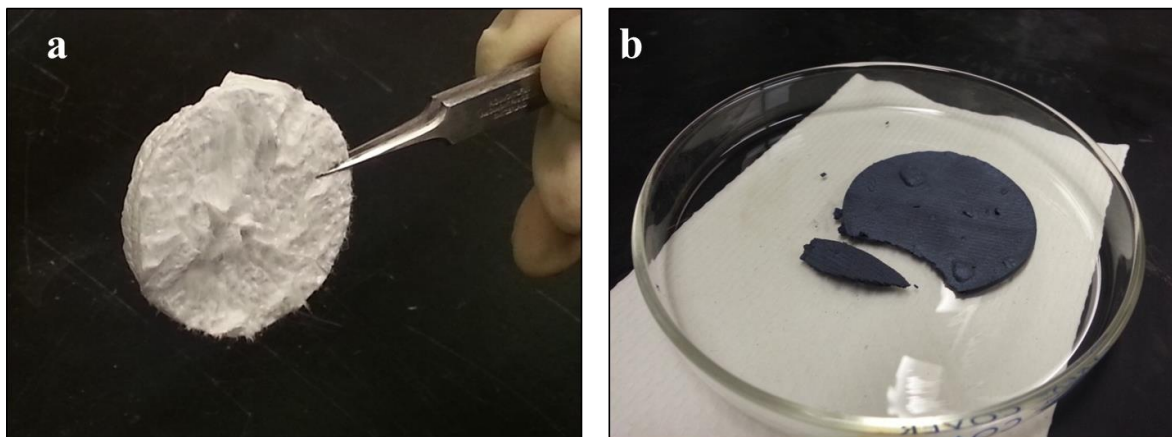


Figure 65: (a) MgO nanorod cake obtained after calcining Mg(OH)₂ and (b) Hollow silicon nanotube (h-SiNT) cake obtained after leaching the MgO nanorod template using HCl

7.3.2 Materials characterization

Phase analysis and crystal structure of the composites comprising the sacrificial *MgO* nanorod template; core-shell structure containing the *MgO* nanorods and silicon coating; and silicon obtained after template dissolution can be performed using X-ray diffraction analysis. **Figure 66a** shows the X-ray diffraction patterns of the nanocomposites generated during the various stages of the synthesis process. It can be observed that the X-ray pattern for the sacrificial template is only composed of peaks corresponding to that of *MgO*, indicating the complete conversion of magnesium acetate to oxide during the hydrothermal and calcination processes. After the silicon deposition, two broad peaks at 2θ angles of 28° and 55° are observed in the diffraction pattern, indicating the presence of an amorphous phase. The location of these broad peaks correspond to the first and second short range order for amorphous silicon and is consistent with previous reports from the Kumta group related to amorphous silicon obtained on multiwall carbon nanotubes grown using similar conditions [28].

After the acid etching process, the X-ray diffraction pattern do not contain any crystalline peaks that correspond to the template, MgO or that of $MgCl_2$ which is formed during the etching process, thereby indicating the complete dissolution and thorough washing of the sacrificial template. The presence of amorphous silicon was further confirmed by Raman spectra obtained on the final cake obtained after acid etching process. Previous studies indicate that the presence of a sharp peak at 520 cm^{-1} in the Raman spectra corresponds to the transverse optical (TO) phonon mode characteristic of crystalline silicon [198-200]. As the crystallite size or the long range order decreases for silicon, the peak expectedly becomes broader and shifts to lower wavenumber values. The Raman spectra (**Figure 66b**) of the final obtained cake show the presence of broad peak at 480 cm^{-1} which is corresponds to that of amorphous silicon and is consistent with the previous reports obtained [22, 25, 28, 197].

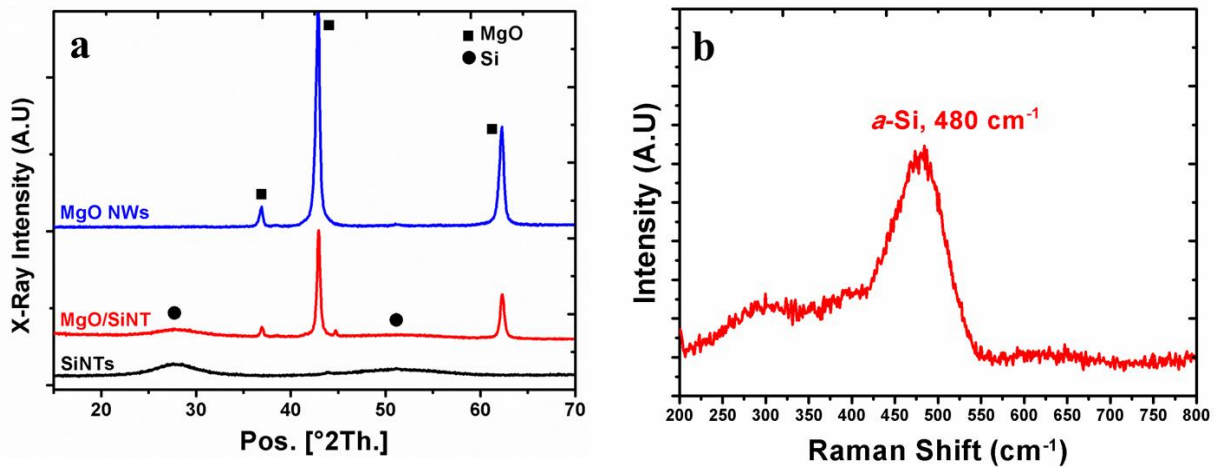


Figure 66: (a) XRD patterns of calcined MgO, core-shell MgO/Si and h-SiNTs formed after leaching MgO nanorods and (b) Raman spectra obtained on the h-SiNTs after leaching MgO nanorods

The morphology of the nanostructures (*MgO* nanorods, silicon coated *MgO* nanorods and h-SiNTs) formed at different stages were analyzed by scanning electron microscopy (SEM) and are shown in **Figure 67**. These images indicate that the final product contains only one dimensional structure or presence of nanorods. The nanorods appear to have varying lengths ranging from few microns to a maximum of 200 μm . The diameters varied from 0.5 μm to 1 μm . This large variation in the dimensions of the nanorods can be attributed to the extremely dynamic and harsh conditions present in the autoclave during the hydrothermal synthesis reaction, resulting in the rapid nucleation and growth of the nanorods that could also simultaneously lead to fracture of the nanorods causing the large variation in geometry and length. The morphology of the nanorods template is very important because the silicon deposited in the next step would assume this template morphology to form the hollow nanotubes. Despite the huge variation in the dimensions of the *MgO* nanorods template, no other morphologies such as particles or aggregates are found. Additionally, from the **Figure 67(a)**, it can be observed that the surface of *MgO* is very smooth. These attractive features of the nanorods template produced in this step, thus enable the formation of smooth hollow nanotubes of silicon.

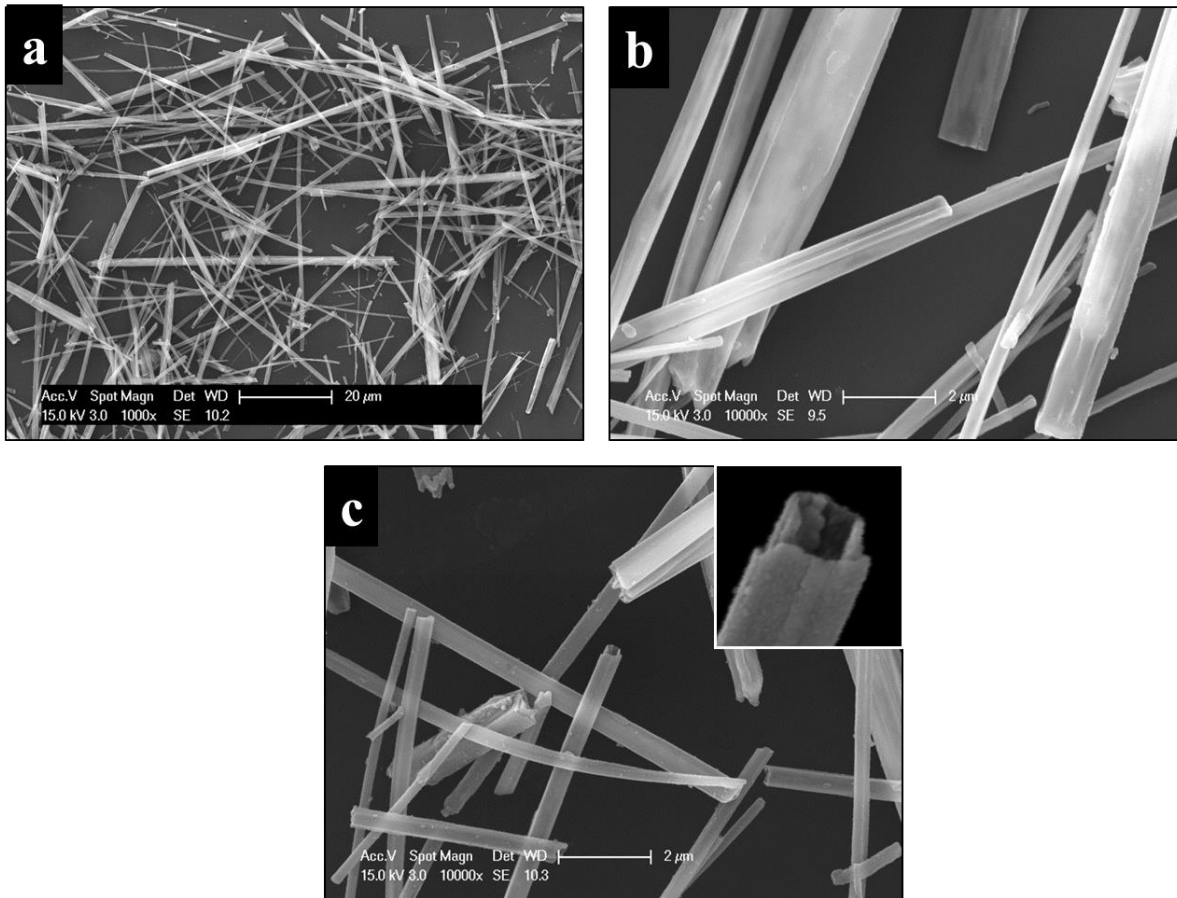


Figure 67: SEM images of (a) MgO nanorods obtained after calcination at 500C, taken 1000X (b) silicon coated MgO nanorods taken at 10,000X and (c) hollow silicon nanotubes at 10,000X (h-SiNTs) after etching MgO template using HCl (inset shows open end of the nanotube taken at 80,000X)

In the next step, the thermal cracking of silane (SiH_4) resulted in a thin uniform coating of silicon on the MgO nanorod template. This result in a core-shell structure, with the inner core being MgO and the outer shell made of silicon. Also, as observed in **Figure 67(b)**, the deposition of silicon does not lead to the formation of any particles or aggregates that may decrease the total yield of nanotubes in the final product. From the **Figure 67(b)**, an average increase in the thickness (50-100 nm) of the nanorods can also be observed.

The etching of the MgO nanorod template from the MgO/Si core-shell structure results in the formation of the hollow nanotubes of silicon as shown in **Figure 67(c)**. During this etching step, the chloride ions (Cl^-) from the acid bath diffuse through the silicon coating and react with MgO to form $MgCl_2$, which is water soluble. After the dissolution of MgO , the silicon coating is well preserved and results in the formation of hollow nanotubes of silicon. The open ends of these tubes can clearly be observed in **Figure 67(c)**.

Figure 68 shows the HRTEM images of the nanotubes, wherein, the open ends of the tubes can clearly be observed in **Figure 68(a)**. From these images, the silicon wall thickness of 60 to 80 nm can be estimated. Furthermore, from the high magnification image (**Figure 68(b)**) and the diffuse hollow ring in the selected area diffraction pattern (SAED) (**Figure 68(c)**) obtained from the h-SiNT surface indicate that the silicon formed is amorphous and is consistent with the Raman data.

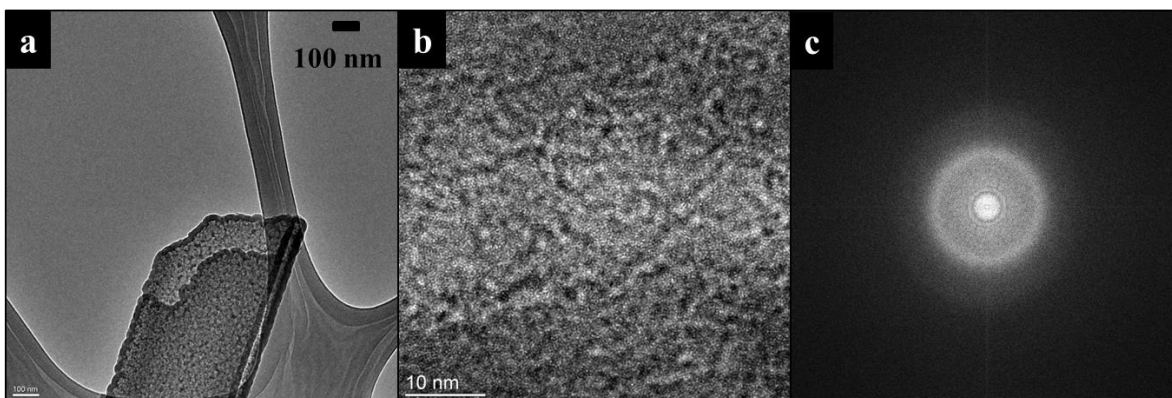


Figure 68: (a) HRTEM image of an open ended h-SiNT; (b) High magnification of h-SiNT showing amorphous structure and (c) SAED pattern of h-SiNTs

7.3.3 Electrochemical characterization

The electrochemical properties of the h-SiNTs were investigated on the electrodes obtained using a slurry casting method on the copper current collectors. Due to the hollow tubular configuration of the h-SiNTs with small wall thickness (60-80 nm), they exhibit very low tap density and hence a large amount of binder (40 wt%) was employed for achieving a good dispersion of h-SiNTs to generate a slurry. **Figure 69** shows a typical voltage vs. specific capacity plot of the h-SiNTs cycled at a medium current density of 300 mA/g. The h-SiNTs exhibited a high first discharge capacity of 2615 mAh/g followed by an irreversible loss of 25%, giving rise to a charge capacity of 1970 mAh/g. The first cycle irreversible loss obtained in the case of h-SiNTs is significantly higher compared to the CNT/Si heterostructures (10%) reported in the earlier chapter. In the case of small wall thickness, the nanotube configuration offers larger exposed specific surface area of the silicon to the electrolyte, thereby contributing to larger SEI formation and hence the huge (25%) first cycle irreversible loss. Voltage plateaus can be observed in these

plots during the discharge and charge process, which are representative of the two phase regions formed by several Li_xSi alloy phases. However, a better representation of these phases as a result of various alloying reactions can be identified from the differential capacity plots shown in **Figure 70**. During the discharge or lithiation process in the first cycle, a small peak around 0.18 V followed by a large peak at 0.1 V is observed. The first peak corresponds to the voltage plateau due to the presence of two phase region between the $a-Si$ and partially lithiated Li_xSi alloy [4, 8, 22, 28]. Further lithiation of this Li_xSi alloy occurs at lower voltages (~ 0.1 V), resulting in a completely amorphous Li_xSi alloy. During the charging or delithiation process, two peaks at 0.28 V and 0.44 V are observed which correspond to the delithiation reactions, eventually leading to the formation of $a-Si$. However, in the second cycle, the lithiation of $a-Si$ occurs at relatively higher potentials (~ 0.24 V) and is consistent with previous reports relating to lithiation of $a-Si$. The delithiation reactions for the second cycle occur at similar voltages, thereby indicating good reversibility and absence of any other reactions.

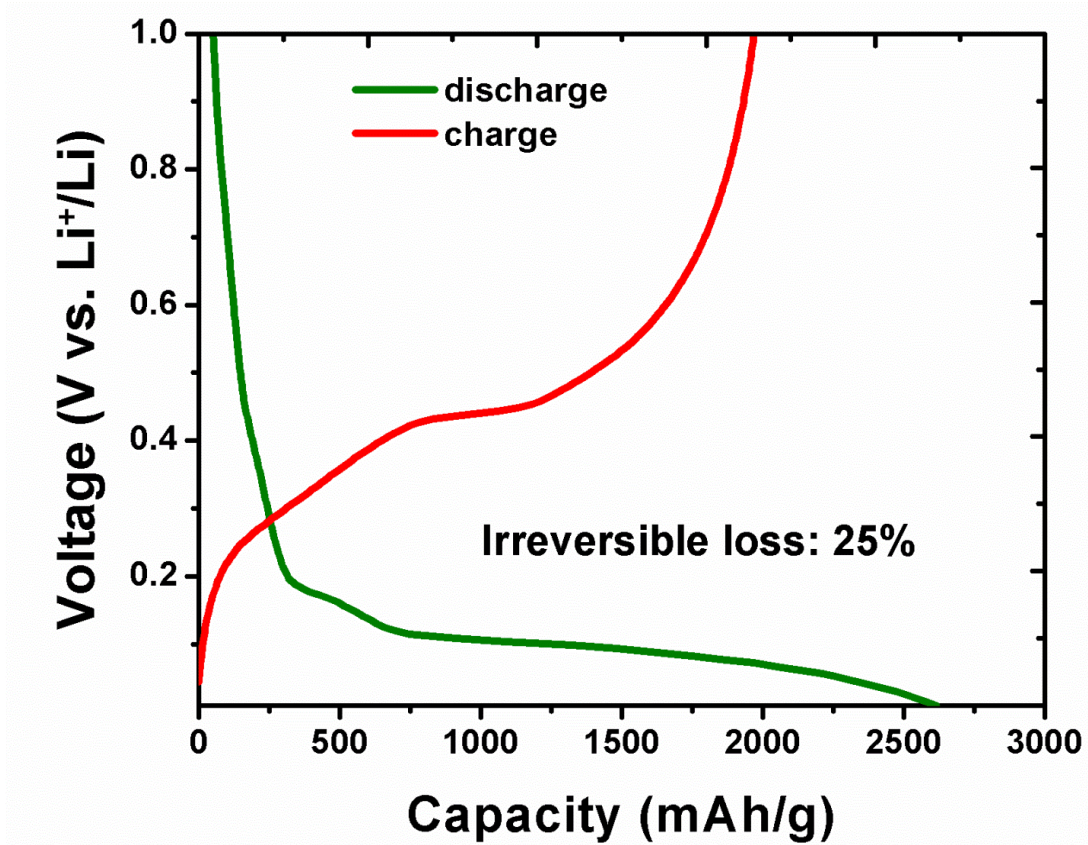


Figure 69: Voltage vs. specific capacity plot of h-SiNTs cycled at 300 mA/g between the voltage ranges: 0.01 to 1

V vs. Li⁺/Li

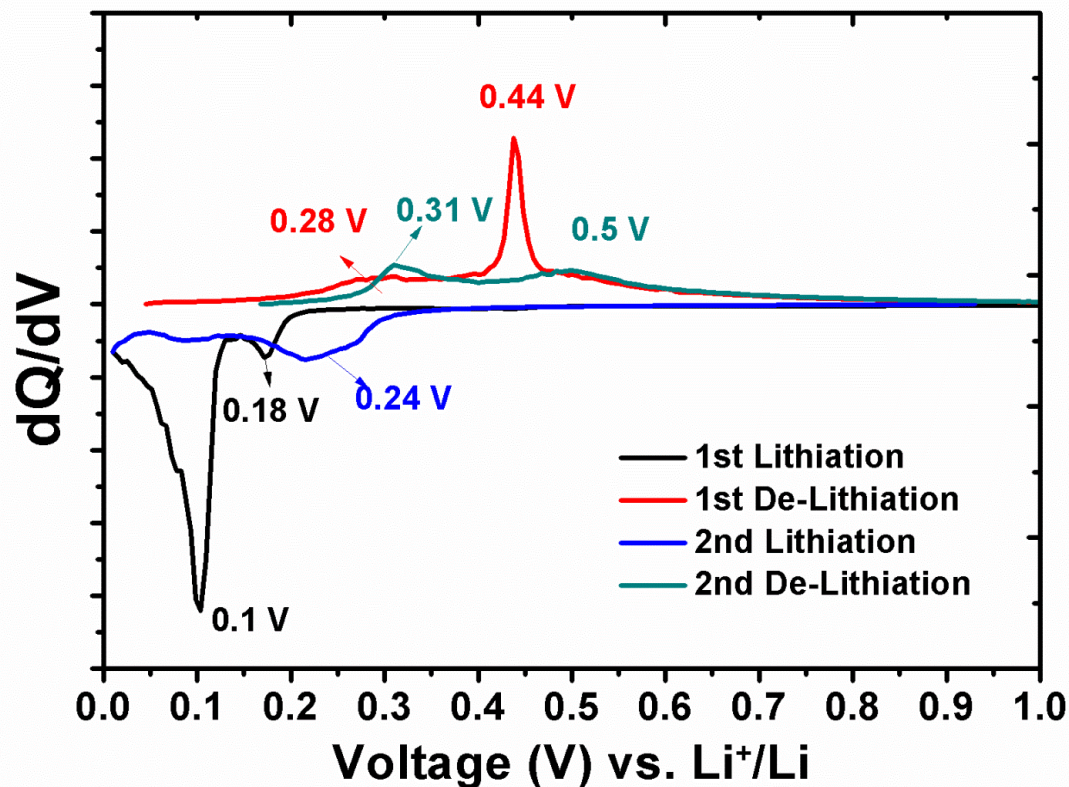


Figure 70: Differential capacity plot of h-SiNTs cycled at 300 mA/g between the voltage range: 0.01 to 1 V vs.

Li⁺/Li

Figure 71 shows the long term cycling of the h-SiNTs cycled at 2A/g between the voltage range 0.01 to 1 V vs. Li^+/Li . In this case, the first cycle was run at 300 mA/g to allow the formation of stable solid electrolyte interphase (SEI) on the nanotube surface. When the current was switched to 2A/g, the capacity dropped to 1551 mAh/g. A slight increase in the specific capacity up to 1738 mAh/g was observed for the first few cycles and this can be attributed to the progressive wetting of the h-SiNTs by the electrolyte especially when high current densities are used. The h-SiNTs exhibited excellent cyclability, resulting in a high capacity of 1132 mAh/g at the end of 400 cycles. This corresponds to very high capacity retention of 73% and an extremely

low fade rate of 0.067% loss per cycle (for 400 cycles). The coulombic efficiency for the first 10 cycles was close to 98.5% but improved with cycling and remained close to 99.9% after 300 cycles. A corresponding voltage versus capacity plot of the long term cyclability plot is illustrated in **Figure 72**. It is observed from this plot that after the 1st cycle, the shape of the discharge/lithiation and the charge/de-lithiation curve did not change, indicating good reversibility of the alloying reactions.

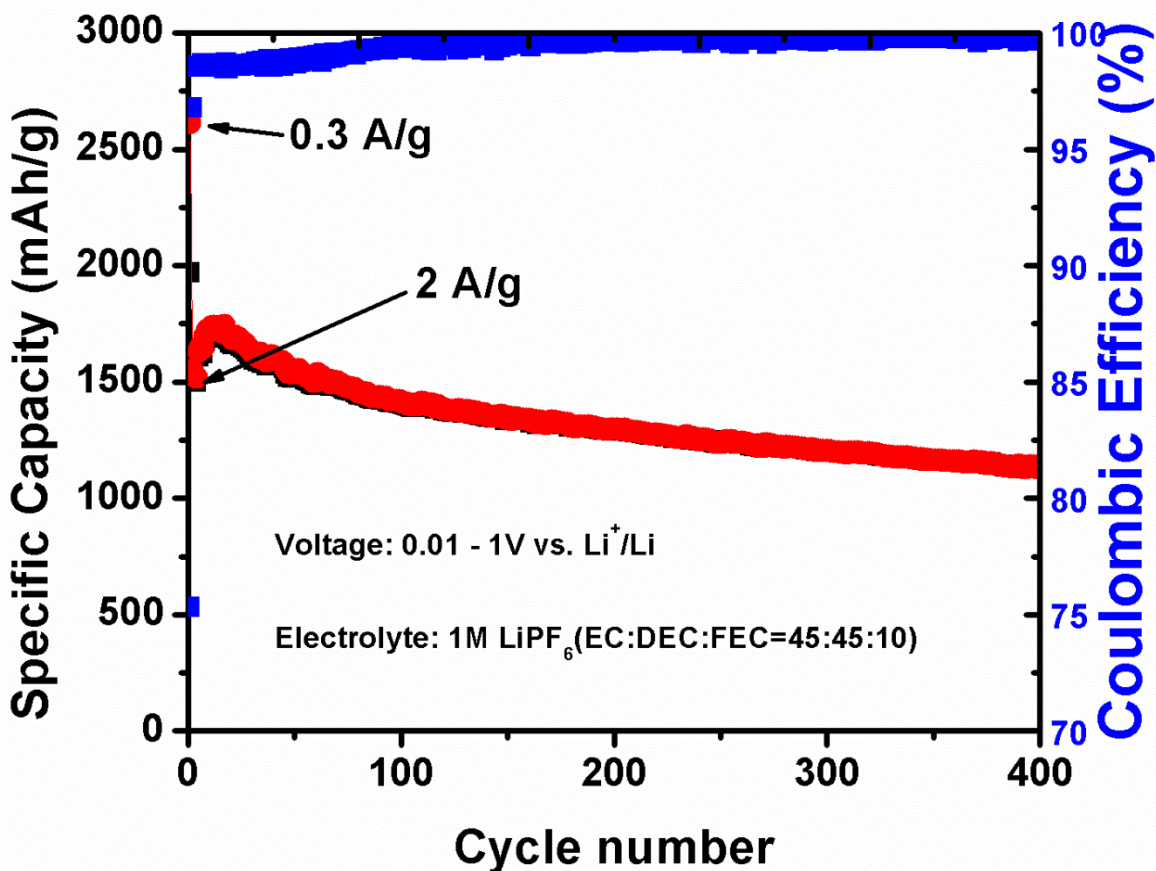


Figure 71: Long term cycling plot of h-SiNTs cycled at 300 mA/g for 1st cycle and 2A/g for the rest of the cycles between the voltage range: 0.01 to 1 V vs. Li+/Li

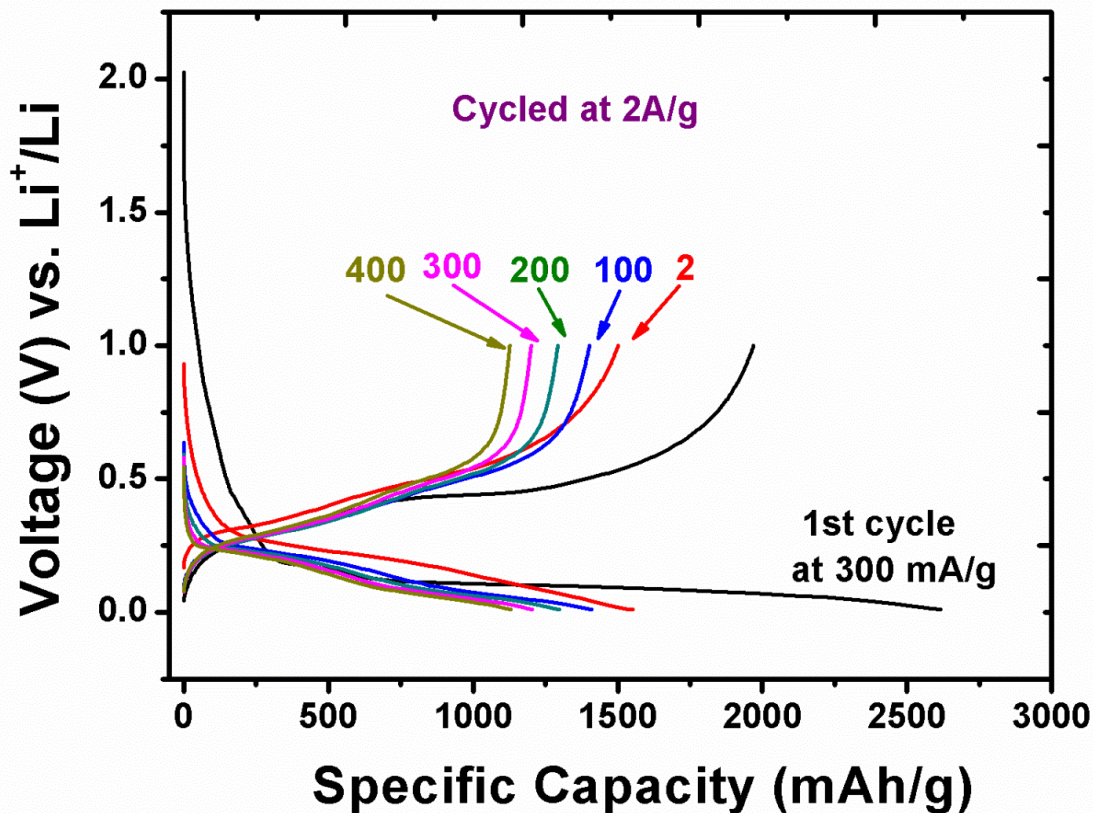


Figure 72: Voltage vs capacity plots of h-SiNTs cycled at 300 mA/g for 1st cycle and 2A/g for the rest of the cycles between the voltage range: 0.01 to 1 V vs. Li+/Li

Figure 73 shows the rate characteristics of h-SiNTs cycled at different current densities (0.5 A/g, 1 A/g, 2 A/g and 4 A/g). At relatively low current densities and reversible capacities of approximately, 2200 mAh/g were obtained. However, by increasing the current density to 1 A/g, the capacity dropped to only 2000 mAh/g. Furthermore, capacities ~1700 mAh/g were obtained for a current density of 2 A/g and finally, even at high current densities of 4 A/g, very high specific capacities of 1300 mAh/g were achieved. Similar or even higher capacities were

regained when the current densities were lowered. This increased capacity, as discussed earlier, may be due to the progressive wetting of the active material.

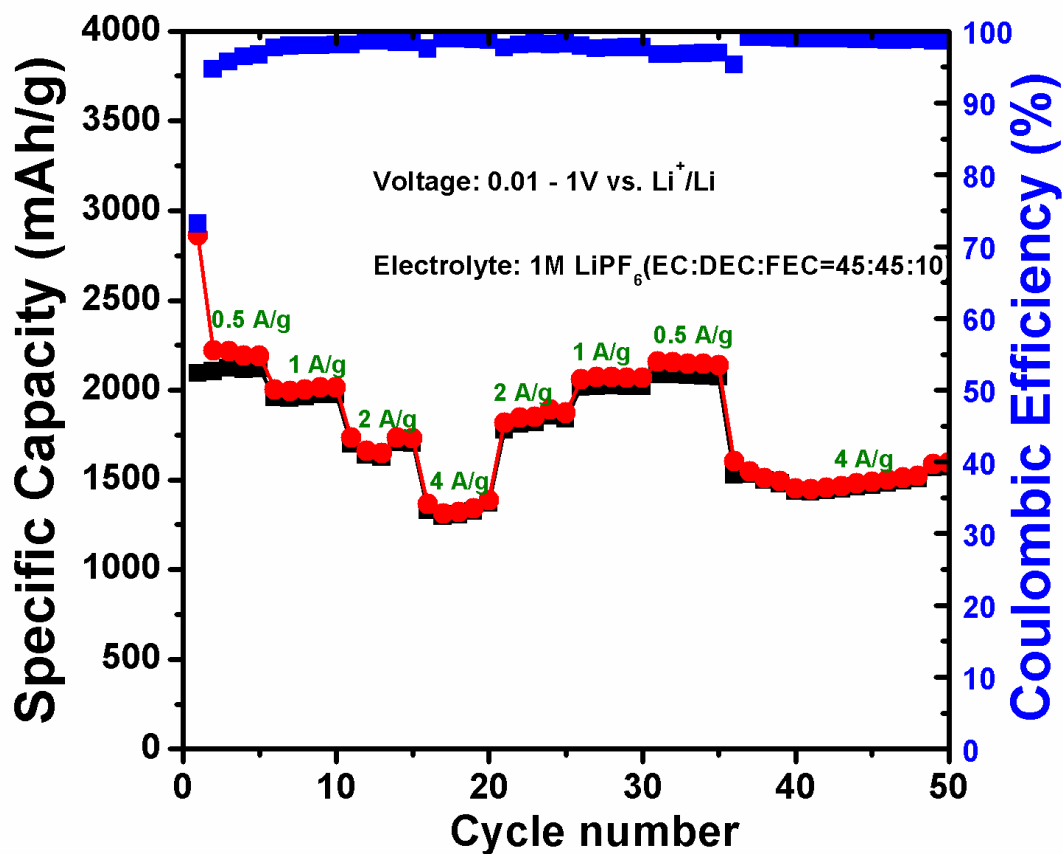


Figure 73: Rate characteristics of h-SiNTs cycled at 0.5 A/g, 1 A/g, 2 A/g, 4 A/g between the voltage range: 0.01 to 1 V vs. Li⁺/Li

Because of the hollow tubular configuration of h-SiNTs, they can expand freely inwards as well as outwards during the volume expansion when lithiated. This phenomenon can be compared to that of silicon nanowires wherein, the facile strain upon lithiation resulted in increase of length and diameter of the nanowires without causing any pulverization. In a similar manner, the h-SiNTs are expected to undergo volume changes that result in very minimal stresses and do not result in the fracture of the nanotubes. To validate this, SEM analysis was performed on the as cast composite electrode on copper current collector containing h-SiNTs, binder (sodium alginate) and Super-P; analyzed again after lithiation and de-lithiation processes. These SEM images obtained at different magnifications are shown in **Figure 74**.

The as-cast electrodes at a magnification of 5000X clearly show the h-SiNTs along with other electrochemically inactive species (binder and Super-P). The open ends of the hollow tubes are also visible at 10,000X. However, after lithiation, there appears to be an average increase in the diameter of the nanotubes. This increase could be due to the volume expansion as a result of lithiation and/or due to the formation of SEI layer on the nanotube surface. After the de-lithiation step, a slight decrease in the diameter can be noticed, due to possible volume contraction upon de-alloying of *Li* from *Si*. Also, from the SEM images at 1000X magnification, no fracturing of the nanotubes was observed either after the lithiation or de-lithiation processes, indicating no loss of active material at the end of first cycle. Therefore, the origin of the large first cycle irreversible loss can be attributed only to the SEI layer formation on the nanotube surface. Furthermore, the low magnification images from all the samples appear to be similar, indicating the preservation of the mechanical integrity of the composite electrode upon electrochemical cycling.

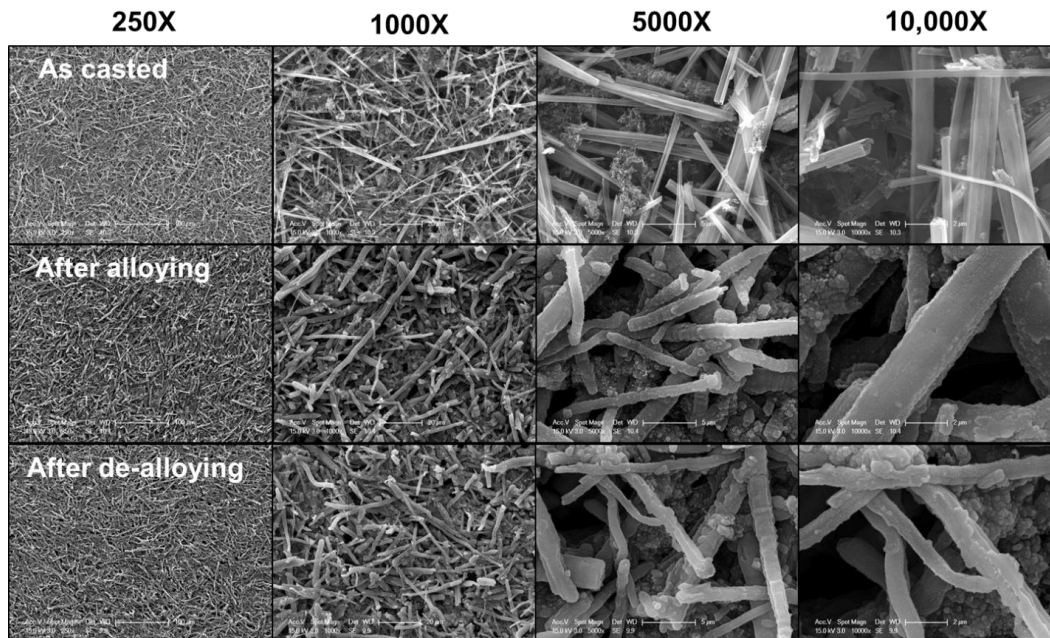


Figure 74: SEM images of as cast (top row), after lithiation (middle row) and after de-lithiation (bottom row) of h-SiNT electrodes along with binder and Super-P at different magnifications

In this study, it is hypothesized that the excellent cyclability or capacity retention of the h-SiNTs is due to their strain engineered structure, wherein, the repeated volume changes does not adversely affect the overall structure of the material. To validate this hypothesis, the electrode was analyzed using SEM before cycling and after it was subjected to a repeated long term cycling at a current density of 2 A/g between the voltage range 0.01 to 1 V vs. Li^+/Li . **Figure 75** shows the SEM images of the electrode before (left) and after 500 cycles (right) of charge and discharge. As described earlier, the as-cast electrode shows that the h-SiNTs are dispersed uniformly along with binder (sodium alginate) and Super-P. Despite using a low weight fraction of active material (50 wt%) and a large amount of binder (40 wt%), the h-SiNTs do not appear to be enveloped inside the binder-SuperP matrix. This is due to the fact that the hollow tubular configuration of the h-SiNTs gives rise to a very low packing density material

and higher volume fraction compared to its inactive counterparts (binder and Super-P). Even after 500 cycles of repeated charge and discharge, the one dimensional nature of the nanotubes still appears to be preserved. However, an average increase in the diameter of the nanotubes can clearly be noted, due to possible formation of SEI layer. Furthermore, a scenario could be envisioned wherein if the nanotubes were to fracture due to repeated cycling, the resulting broken tubes would lead to loss of inter-particle contact (or loss of active material) and formation of new surfaces that could lead to additional SEI formation (or *Li* consumption). Both these phenomena would however result in a rapid capacity fade or poor cyclability, a scenario that is not representative of the h-SiNTs developed in this study. Therefore, it can be deduced that the preservation of the nanotube morphology after repeated cycling mainly resulted in the low capacity fade or long cycle life. However, there is still some capacity loss at the end of 400 cycles. This decrease in capacity of the h-SiNTs after extended cycling could be due to the particle (nanotubes in this case) isolation or detachment from the electrochemically inactive matrix (binder and Super-P) due to constant expansion and contraction of the nanotubes.

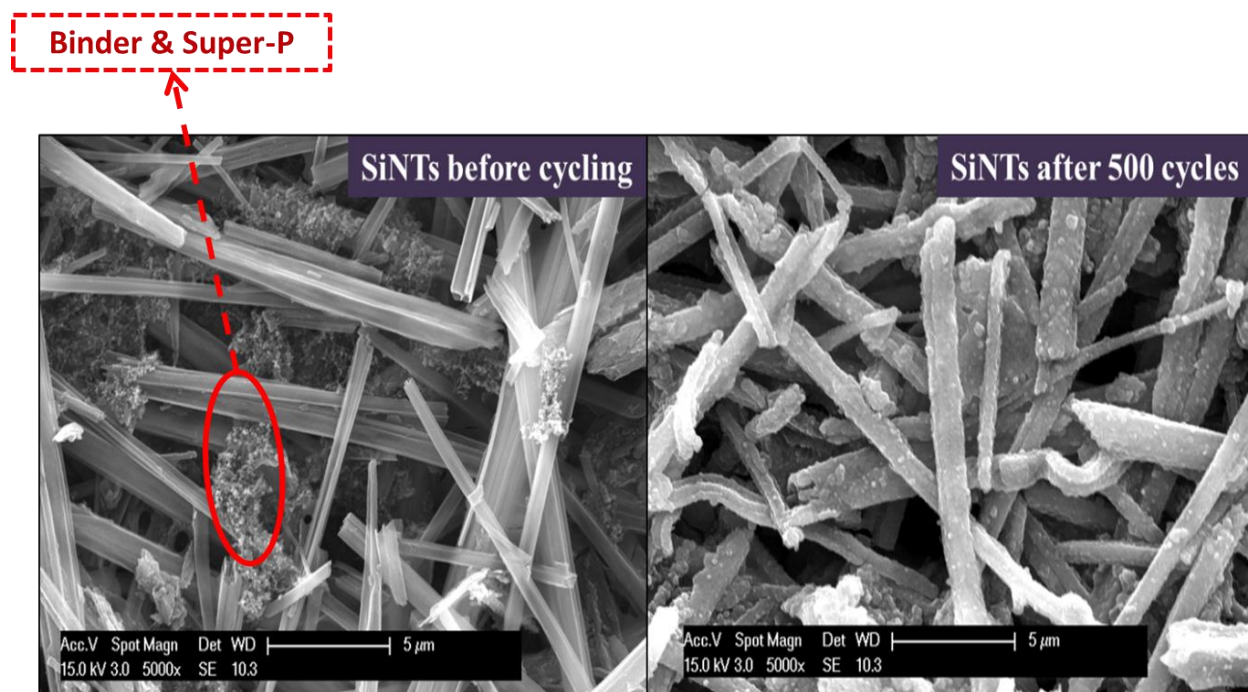


Figure 75: SEM images of h-SiNT electrodes along with binder and Super-P (a) before cycling and (b) after 500 charge-discharge cycles, cycled at 2 A/g between the voltage range 0.01 to 1 V vs. Li+/Li

As described in the previous chapters, impedance characterization of the electrodes at different stages of cycle life provides important information on the changes in charge transfer kinetics due to repeated lithiation and de-lithiation processes. Similarly, in the case of h-SiNTs, impedance spectra was collected at the end of de-lithiation step after 1st, 100th, 200th, 300th and 400th cycle and the resulting Nyquist plots are shown in **Figure 76**. In these plots, a semi-circular region can be observed at high frequencies which is indicative of the charge-transfer processes as a result of alloying reaction of Li^+ species with Si . Following this, a linear region can be observed at lower frequencies, commonly referred to as Warburg tail, and this typically represents the diffusion phenomenon of Li^+ species from the electrolyte to the electrode-

electrolyte interface. The various phenomena present in the current electrochemical cell such as resistance associated with the charge transfer reaction occurring at the electrode-electrolyte interface and SEI layer; the capacitance effect due to the adsorption of ions at various interfaces; and the diffusion phenomenon can be represented by a corresponding equivalent circuit containing elements such as resistors, capacitors, Warburg and constant phase elements (*CPEs*), etc.,

Figure 77 illustrates the equivalent circuit developed using the Zview modeling software, which contains a series resistor element R_s , mainly represents the solution resistance, two other resistors R_i and R_o connected in parallel with two constant phase elements, CPE_i and CPE_o , respectively. The subscripts '*i*' and '*o*' correspond to inner and outer molecular layers of the Si nanotubes, respectively. The electron or charge transfer reaction during the lithiation/de-lithiation process can occur on the surfaces of the inner h-SiNTs and the outer SEI layer, giving rise to the presence of two resistors in the equivalent circuit. Accordingly, two electrical double layers can be imagined to be formed by the adsorption of ions and solvent molecules; the corresponding *CPEs* are represented by CPE_i and CPE_o . The total charge-transfer resistance is thus mainly associated with the kinetics of the lithiation/de-lithiation reaction occurring at the h-SiNT and the SEI layer. In the event of active material fracture due to volume changes during cycling, new active surfaces are formed and in the subsequent cycle, an additional SEI layer is formed on these new surfaces, increasing the overall charge-transfer resistance. **Figure 76** shows that the semicircular region of the Nyquist plots obtained at different stages of the cycle life are superimposable, indicating that there is no significant change in the charge-transfer resistance upon repeated cycling. This clearly explains that no new active surfaces are formed during repeated charge/discharge processes and further validates the observation from post

cycled SEM images of h-SiNTs (**Figure 75**), that the nanotubes did not fracture even at the end of 500 cycles. **Table 7** shows the values of the circuit elements obtained after modeling the equivalent circuit using a complex non-linear least square (CNLS) method. A small rise in the charge transfer resistance can be observed with cycle number and this increase may be attributed to the increase in the thickness of SEI layer over the course of 400 cycles of charge and discharge.

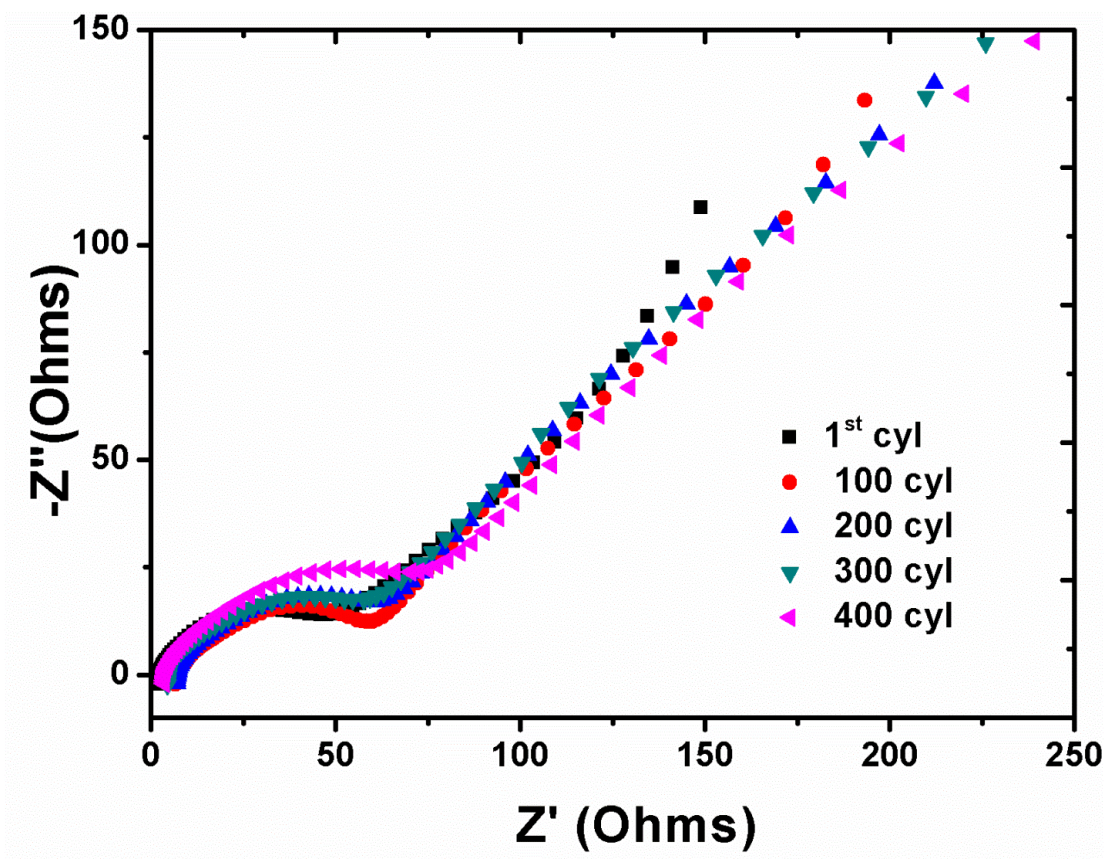
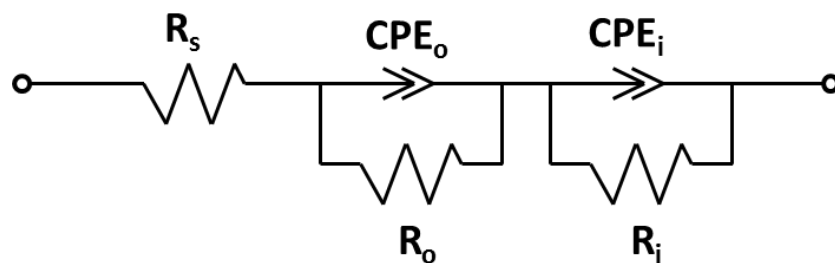


Figure 76: Impedance spectra of the h-SiNTs obtained at the end of de-lithiation step after 1st, 100th 200th, 300th and 400th cycles. Current density applied: 2A/g, Voltage: 0.01 to 1 V vs. Li+/Li



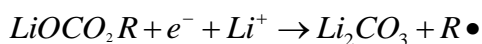
Equivalent circuit model

Figure 77: Equivalent circuit for the interpretation of h-SiNTs (R_s : solution resistance; R_o and R_i : charge transfer resistance of inner and outer molecular layers; CPE_i and CPE_o : constant phase elements of the inner and outer molecular layers)

Table 7: Values of the circuit elements obtained after modeling the equivalent circuit using a complex non-linear least square (CNLS) method for EIS spectra obtained at the end of de-lithiation step after 1st, 100th, 200th, 300th and 400 cycles

Cycles	R_s (ohms)	$CPE_o(T)$ (Farads)	$CPE_o(P)$ (Farads)	R_o (ohms)	$CPE_i(T)$ (Farads)	$CPE_i(P)$ (Farads)	R_i (ohms)
1	1.92	0.000116	0.69325	42.41	0.005359	0.54646	240.9
100	7.22	0.00017	0.60614	58.74	0.003086	0.76668	186.8
200	6.557	0.000119	0.63465	55.27	0.002731	0.6196	541.5
300	4.108	8.58E-05	0.66452	49.24	0.002696	0.5637	715.2
400	3.108	7.61E-05	0.67065	64.4	0.002173	0.57166	805.8

One of the main contributions of the first cycle irreversible loss is the irreversible consumption of lithium to form the solid electrolyte interphase (SEI) layer that is usually formed on the surface of the electrode. This layer is mainly composed of alkyl lithium carbonates ($LiOCO_2R$), lithium carbonate (Li_2CO_3) and other polymers such as polycarbonate, polyethylene oxide (CH_2CH_2O)_n etc., **Figure 78** shows the FTIR spectra obtained on the h-SiNTs obtained at different stages of cycling. The peaks obtained in the absorption spectra were matched with the previously reported literature values that correspond to the various vibration and stretching modes of the SEI layer components [224-226]. It can be observed that the SEI layer formed after the first cycle contain alkyl lithium carbonates ($LiOCO_2R$), lithium carbonate (Li_2CO_3) and polyethylene oxide (CH_2CH_2O)_n. But as the cycling progressed, a significant increase in the intensity of the peaks corresponding to Li_2CO_3 are observed compared to $LiOCO_2R$ and (CH_2CH_2O)_n. This is due to further reduction of the already formed alkyl carbonates $LiOCO_2R$ during subsequent cycling to form Li_2CO_3 according to the reaction below.



The formation of Li_2CO_3 also consumes Li that is irreversible and may be attributed to the loss in capacity over several hundreds of cycles. Also no additional peaks are observed in the spectra, indicating that no additional parasitic reactions are occurring during the extended cycling process.

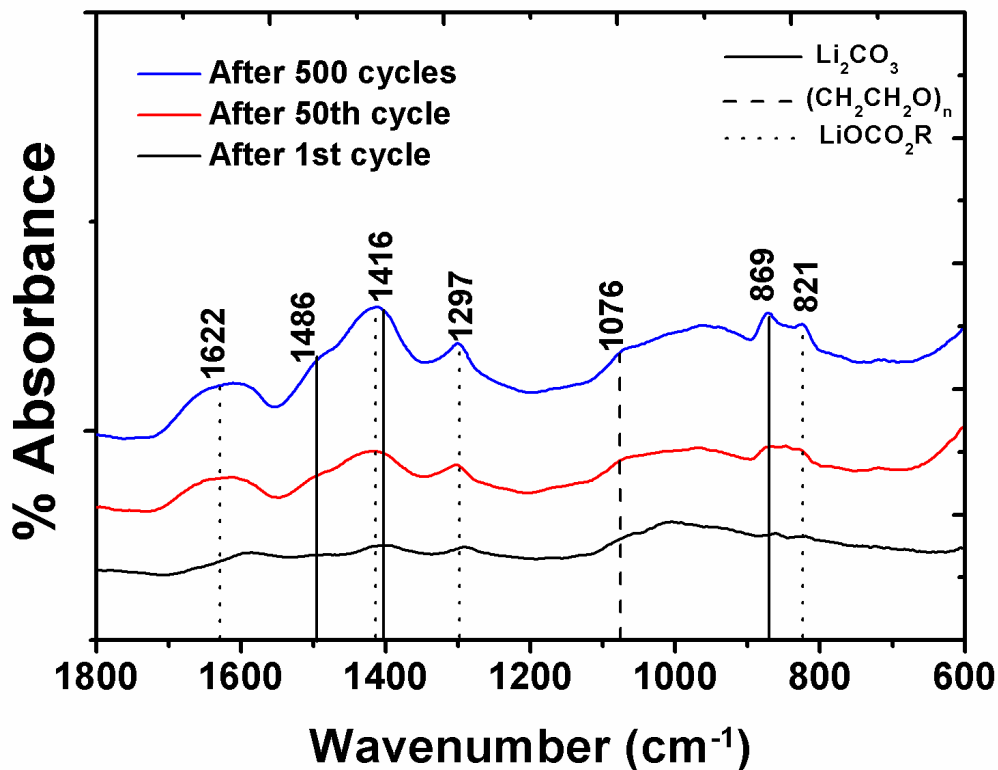


Figure 78: FTIR spectra obtained on the cycled h-SiNTs at different stages (1st, 50th and 500 cycles). The electrodes were cycled at 2A/g between the voltage range 0.01 to 1 V vs. Li+/Li . Spectra were obtained at the end of the de-lithiation step

Additives are often added to the electrolyte to add certain specific functionalities such as forming a good quality SEI layer [227], improving the stability of LiPF₆ salt [228-230], inhibiting Al corrosion on the cathode side [231], improving the wettability of the separator [229], retarding flammability [232, 233] etc. Among them, the formation of SEI layer on electrode surface during the first and subsequent cycles plays an important role in the first cycle irreversible loss and subsequent capacity fade, respectively. Therefore, formation of a good quality SEI layer is necessary for a better battery performance and long cycle life. A good quality SEI layer is one when once formed, is stable and covers uniformly over the electrode surface, and prevents further electrolyte decomposition. In this study, the h-SiNTs were tested using two

commercially obtained electrolytes; one containing 3% vinylene carbonate (VC) as additive and the other containing 10% fluoro ethylene carbonate (FEC). **Figure 79** shows the discharge capacity plots of h-SiNTs using the above mentioned additives. It can be observed that there is no significant difference in the first discharge capacity (2424 mAh/g using VC and 2615 mAh/g using FEC) and first cycle irreversible loss (24% using VC and 25% using FEC). However, h-SiNTs cycled using FEC additive exhibited better cyclability compared to the ones where VC was added. In the case of VC, the specific capacity decreased rapidly during the first 100 cycles, resulting in a capacity of 748 mAh/g at the end of 400 cycles, corresponding to a capacity retention of only 51 % (fade rate: 0.122% loss per cycle). On the other hand, h-SiNTs cycled using FEC additive exhibited a capacity of 1132 mAh/g at the end of 400 cycles resulting in a higher capacity retention of 73% (fade rate: 0.067% loss per cycle). Though VC and FEC are reported to improve cyclability in negative electrode for lithium-ion batteries, electrolytes containing more than 2% VC (by weight) have been shown to have greater charge transfer resistance compared to electrolytes containing FEC [234]. A poor and non-uniform coating of SEI layer could result in the larger charge transfer resistance in the case of VC based electrolytes. This results in relatively sluggish kinetics when operated at high current densities such as 2A/g, leading to lower specific capacities or poorer cyclability.

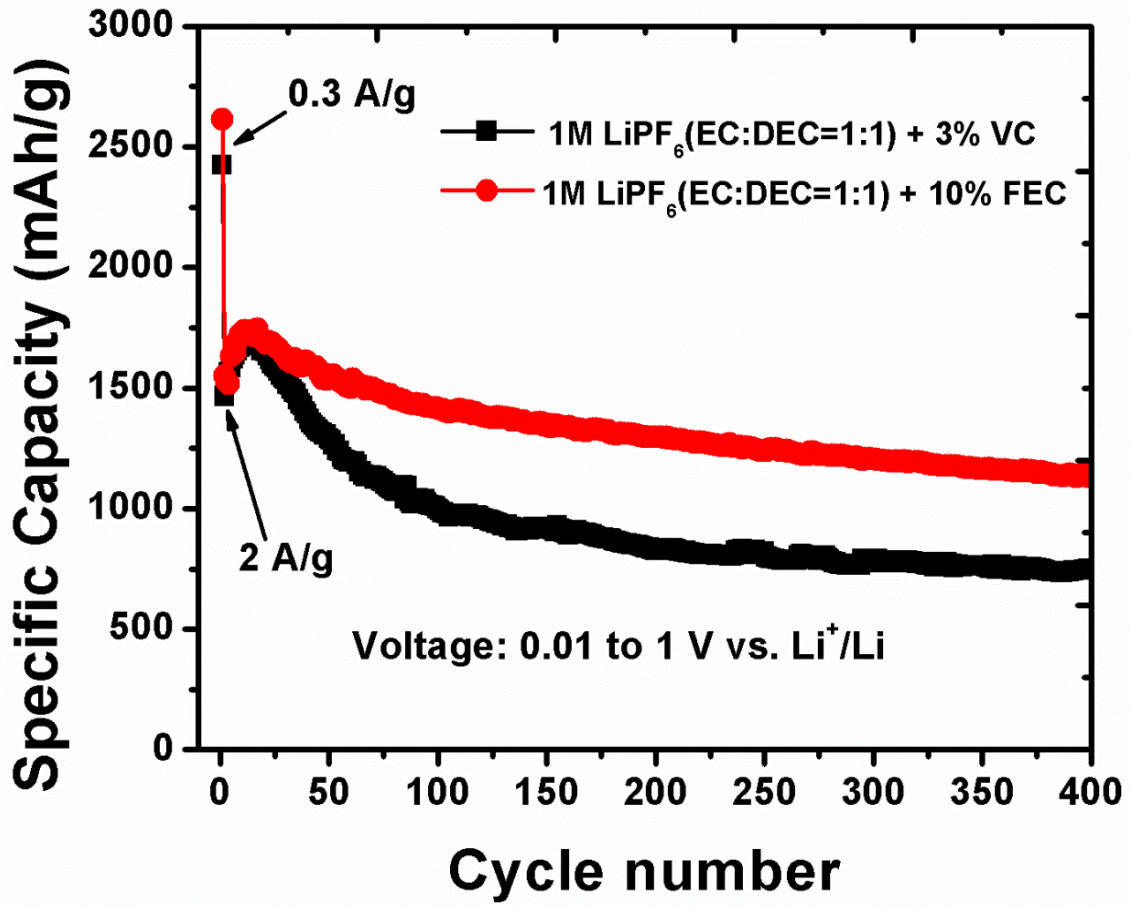
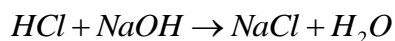
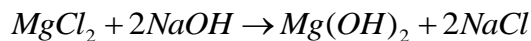


Figure 79: Discharge capacities of h-SiNTs using VC and FEC as additives to the LiPF₆ electrolyte cycled at 300 mA/g for 1st cycle and 5A/g for the rest of the cycles between the voltage range: 0.01 to 1 V vs. Li⁺/Li

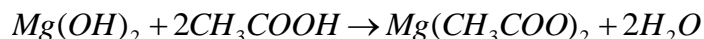
7.3.4 Template regeneration

Most of the methods reported in the literature for generating hollow silicon nanotubes use a sacrificial template that cannot be regenerated. Therefore, in order to produce a new batch of silicon nanotubes, the template needs to be re-synthesized using a new set of precursors, which adds to the raw material and processing costs. An attractive feature of this approach for making h-SiNTs is the ability to recycle or regenerate the *MgO* nanorod template which could potentially be used to synthesize a subsequent batch of h-SiNTs. This is very advantageous from commercialization standpoint, since it does not involve continuous utilization of a new set of precursors for producing the template and the h-SiNTs.

In this approach, after the *MgO* nanorod template was dissolved using *HCl*, the filtrate mainly contains *MgCl₂* dissolved in water and excess of *HCl*. To this solution, a stoichiometric amount of sodium hydroxide (*NaOH*) equivalent to the number of moles of *HCl* was added. This results in the precipitation of the soluble *MgCl₂* to form magnesium hydroxide, *Mg(OH)₂* and neutralization of *HCl* according to the following reactions:



The white *Mg(OH)₂* precipitate was separated using vacuum filtration and further treated with acetic acid to form a clear solution. In this step, the hydroxide readily reacts with acetic acid to form magnesium acetate according to the reaction below.



$Mg(ac)_2$ is highly soluble in water and can easily be extracted by heating the solution to 110°C to evaporate the solvent (water). The resulting white solid was thoroughly dried and is composed of single phase hydrated magnesium acetate, $Mg(ac)_2 \cdot 4H_2O$. The regenerated $Mg(ac)_2 \cdot 4H_2O$ can be used along with urea in the autoclave reactor to synthesize a new set of MgO nanorods, which can further be employed to generate h-SiNTs. **Figure 80** shows the X-ray diffraction patterns of $Mg(OH)_2$ and $Mg(ac)_2 \cdot 4H_2O$ obtained after the addition of $NaOH$ and acetic acid during the template recovery process, respectively. The strong low angle reflections (especially at $2\theta=11^\circ$) and other smaller peaks is characteristic of the hygroscopic magnesium acetate structure and is consistent with other literature reports [235]. No other impurities or by-products such as $NaCl$ could be observed in the X-ray pattern, which indicates the efficacy of the approach and washing processes. Apart from the quality of the product, it is also important to have a good yield of the products obtained at different stages of the template regeneration process. **Table 8** shows the efficiency of the several reaction steps involved in the synthesis of h-SiNTs and regeneration of the starting precursor, in terms of percentage of the product obtained relative to the theoretical amount assuming the complete conversion of the chemical reaction. It can also be observed from the **Table 8** that during the first step, nearly 15 % of the precursors were left unreacted. However, the subsequent reactions which involves the template leaching and recovery steps are very efficient, with a conversion rate above 98%.

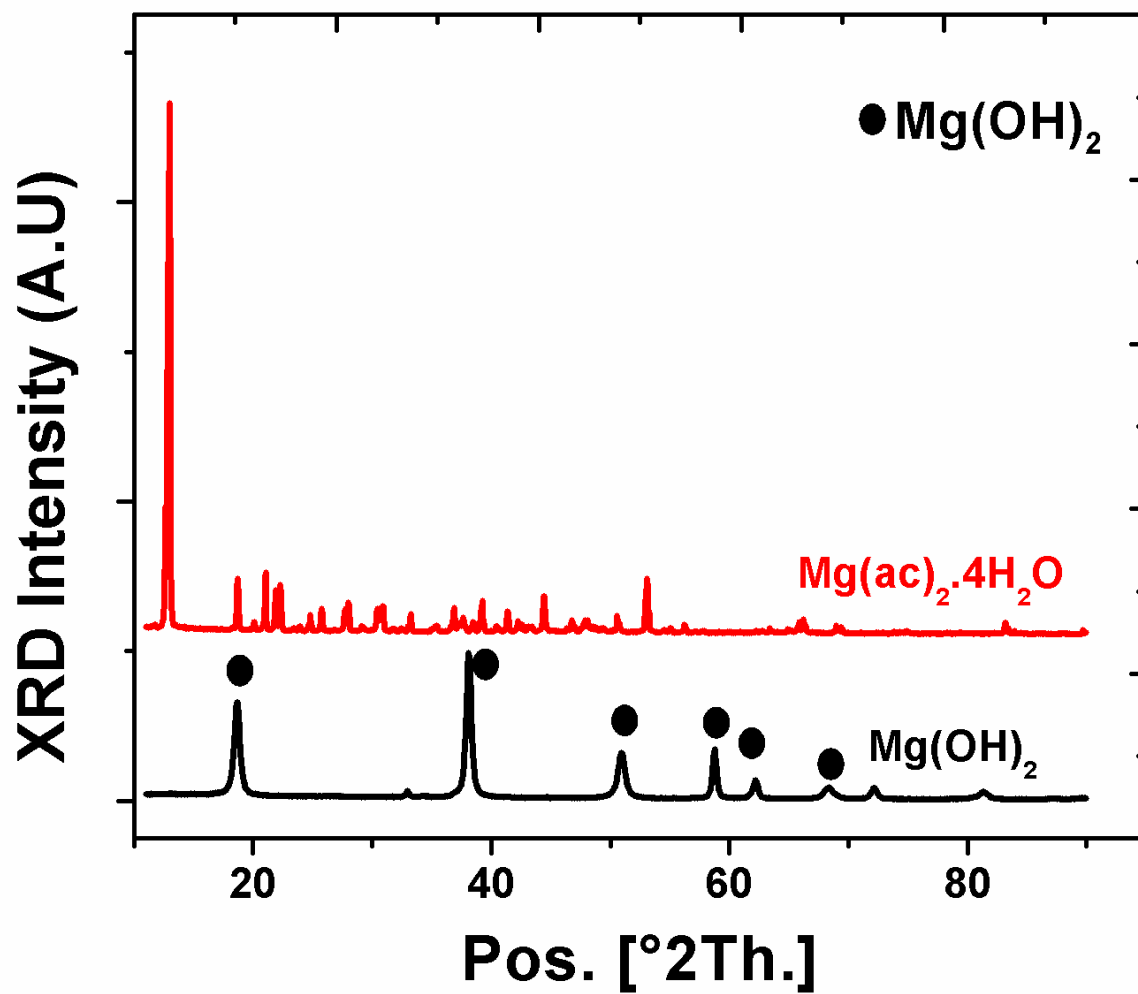


Figure 80: XRD pattern of $\text{Mg}(\text{OH})_2$ and Magnesium acetate obtained during the template regeneration process.

NaOH reacted with the MgCl_2 formed during the etching reaction to precipitate out $\text{Mg}(\text{OH})_2$ that is further reacted with acetic acid to form magnesium acetate

Table 8: Percentage of conversion of various reactions during the MgO nanorod template synthesis and regeneration processes

Reaction	Percentage conversion (%)
<i>Mg(ac)₂.4H₂O to Mg(OH)₂</i>	84.5
<i>Mg(OH)₂ to MgO</i>	100
<i>MgO to MgCl₂</i>	98
<i>MgCl₂ to Mg(OH)₂</i>	99
<i>Mg(OH)₂ to Mg(ac)₂.4H₂O</i>	98

7.4 CONCLUSION

In summary, a facile and inexpensive approach for producing scalable quantities of hollow silicon nanotubes (h-SiNTs) (nearly 0.5 g of final product using only 15 minutes of silicon deposition) was developed. A sacrificial MgO nanorod template was first synthesized in an autoclave reactor by hydrothermal synthesis, onto which amorphous silicon was deposited as a thin layer by CVD to form a core-shell structure. The MgO core was leached off by acid etching to generate hollow nanotubes of silicon (h-SiNTs). These h-SiNTs exhibited high specific capacities, excellent cycling stability and good rate capability. A first discharge capacity of 2615 mAh/g and a charge capacity of 1970 mAh/g was obtained at 300 mA/g current density corresponding to a first cycle irreversible loss of 25%. The h-SiNTs exhibited high capacity retention of 73% at the end of 400 cycles corresponding a very low fade rate of only 0.067% loss per cycle. The excellent cyclability demonstrated by the h-SiNTs was validated by post cycling SEM images of the cycled electrodes wherein, it was observed that the hollow tube structure was still preserved, despite the volume expansion of silicon during 400 cycles of charge and discharge. Additionally, a closed loop process using simple precipitation techniques was developed to regenerate the starting precursor, $Mg(ac)_2 \cdot 4H_2O$ with high purity demonstrating the cost effectiveness, efficacy, and recyclable nature of this simple h-SiNT generation process.

8.0 SUMMARY

In this dissertation, four different structures (nanocrystalline and amorphous) of silicon have been developed and studied, and their findings are summarized here:

Silicon nanoparticle anode generated by high energy mechanical milling (HEMM)

1. Silicon nanoparticles were synthesized by the reduction of SiO with Mg_2Si via a mechanochemical reaction followed by acid etching using hydrofluoric acid.
2. Primary particles in the size range of few tens of nanometers to 100 nm were found along with agglomerates of size 1-2 μm were formed at the end of the reaction.
3. XRD and Raman spectra indicate that the silicon obtained is a pure single phase nanocrystalline silicon with some surface oxide present.
4. These particles exhibited very high specific surface area (SSA) of 190 m^2/g with an average pore size of 12 nm.
5. The electrochemical characteristics show a first discharge capacity of 2230 mAh/g followed by a huge first cycle irreversible loss of 73%.
6. A high capacity fade of 6.66 % loss per cycle (for 8 cycles) was estimated resulting in a capacity of only 350 mAh/g at the end of 8 cycles. The electrochemical performance of these high specific surface area silicon

nanoparticles is marginally superior to that of bulk crystalline silicon suggesting the need for surface modifications which will be conducted as part of the future studies.

Amorphous silicon film anode by electrodeposition from organic solvents

1. Thin films of amorphous silicon were directly deposited on copper current collector via electro-reduction of $SiCl_4$ from a non-aqueous electrolyte.
2. Raman and glancing angle X-ray results indicate that the obtained film is amorphous and composed of silicon along with a surface oxide (SiO_x) layer.
3. Upon cycling, these films exhibited a very high first discharge capacity of ~ 3400 mAh/g) and charge capacity of 1150 mAh/g, corresponding to a large first cycle irreversible loss (65%).
4. After the first cycle, the *a-Si* films exhibit excellent cycling stability with reversible capacities in the range 1300 mAh/g and a fade rate of only 0.016% loss per cycle (for 100 cycles)
5. Post cycling SEM analysis indicate that upon repeated cycling (100 cycles), no significant change in the film morphology or the silicon island size can be noticed, resulting in good cycling stability.

CVD derived silicon coated vertically aligned carbon nanotube anodes

1. Heterostructures of silicon coated on vertically aligned carbon nanotubes were generated by decomposing m-xylene and silane (SiH_4) precursors on quartz substrates in a CVD reactor.

2. Two types of silicon morphologies (droplets and films) were obtained on the CNTs by controlling the deposition conditions inside the CVD reactor.
3. These heterostructures exhibited first discharge capacities in excess of 2700 mAh/g and charge capacities (2465 mAh/g) corresponding to a very low irreversible discharge capacity loss of ~10%.
4. The droplet morphology of silicon on CNTs showed better cyclability with a fade of 0.25% per cycle compared to that of the films, which showed 1.61% loss per cycle.
5. A scribeable technique was developed wherein, the CNT/Si heterostructures were pressed into a pellet and scribed onto copper foil to form a 'binder-less' electrode.
6. The scribed electrodes exhibited first discharge capacity of 3112 mAh/g and a charge capacity of 2523 mAh/g corresponding to a first cycle irreversible loss of 19%.
7. Additionally the scribed electrodes also showed good cyclability with capacity retention of 76% at the end of 50 cycles corresponding to a fade rate of 0.48% loss per cycle.

Hollow Silicon Nanotubes generated by a sacrificial *MgO* nanorod template

1. A cost effective and scalable approach to synthesizing hollow silicon nanotubes (h-SiNTs) was developed using a hydrothermal derived *MgO* nanorod sacrificial template.
2. The obtained h-SiNTs were amorphous and contained open ends with an average silicon wall thickness in the range 60-80 nm.

3. The h-SiNTs exhibited a high specific discharge capacity of 2615 mAh/g and a charge capacity of 1970 mAh/g at a current density of 300 mA/g corresponding to a first cycle irreversible loss of 25%.
4. The h-SiNTs exhibited excellent cycling stability showing reversible capacities in the range of ~1000mAh/g for several hundreds of cycles.
5. At 2 A/g, the h-SiNTs retained a capacity of 73% (specific capacity of 1132 mAh/g) even after 400 cycles, corresponding to a very low fade rate of 0.067% loss per cycle.
6. Post cycling of the h-SiNTs does not show any pulverization of the hollow silicon nanotubes; the one dimensional nature of the nanotubes still remained intact after several charge-discharge cycles.
7. h-SiNTs also show excellent rate capability, delivering a specific capacity of 1500 mAh/g at 4A/g current density.
8. Finally, a regenerative process was developed wherein, the *MgO* nanorod template was recovered by using simple precipitation techniques, thereby, further improving the efficacy of the approach.

APPENDIX A

PERMISSIONS

This dissertation has text, figures and tables reprinted / reproduced with permission from several publishing companies and societies. All the journal papers listed here have been published in print and electronic form, wherein I (Rigved Epur) am a co-author.

The six journal papers listed below have been used in **Section 4.0**, **Section 5.0** and **Section 6.0**:

1. R. Epur, M. K. Datta, P. N. Kumta, Nanoscale engineered electrochemically active silicon-CNT heterostructures-novel anodes for Li-ion application. *Electrochimica Acta* 85, 680 (Dec, 2012).
2. R. Epur, L. Minardi, M. K. Datta, S. J. Chung, P. N. Kumta, A simple facile approach to large scale synthesis of high specific surface area silicon nanoparticles. *Journal of Solid State Chemistry* 208, 93 (2013).
3. R. Epur, M. Ramanathan, F. R. Beck, A. Manivannan, P. N. Kumta, Electrodeposition of amorphous silicon anode for lithium ion batteries. *Materials Science and Engineering B-Advanced Functional Solid-State Materials* 177, 1151 (Aug, 2012).

BIBLIOGRAPHY

- [1] M. Winter, R.J. Brodd, *Chem. Rev.*, 104 (2004) 4245-4269.
- [2] C.K. Chan, H.L. Peng, G. Liu, K. McIlwrath, X.F. Zhang, R.A. Huggins, Y. Cui, *Nat. Nanotechnol.*, 3 (2008) 31-35.
- [3] M.-H. Park, M.G. Kim, J. Joo, K. Kim, J. Kim, S. Ahn, Y. Cui, J. Cho, *Nano Letters*, 9 (2009) 3844-3847.
- [4] W. Wang, R. Epur, P.N. Kumta, *Electrochem. Commun.*, 13 (2011) 429-432.
- [5] W. Wang, P.N. Kumta, *Acs Nano*, 4 (2010) 2233-2241.
- [6] U. Kasavajjula, C. Wang, A.J. Appleby, *Journal of Power Sources*, 163 (2007) 1003-1039.
- [7] L.F. Cui, L.B. Hu, J.W. Choi, Y. Cui, *Acs Nano*, 4 (2010) 3671-3678.
- [8] L.-F. Cui, R. Ruffo, C.K. Chan, H. Peng, Y. Cui, *Nano Letters*, 9 (2008) 491-495.
- [9] I. Kim, G.E. Blomgren, P.N. Kumta, *Electrochem. Solid State Lett.*, 6 (2003) A157-A161.
- [10] I. Kim, P.N. Kumta, G.E. Blomgren, *Electrochem. Solid State Lett.*, 3 (2000) 493-496.
- [11] I.S. Kim, G.E. Blomgren, P.N. Kumta, *Journal of Power Sources*, 130 (2004) 275-280.
- [12] M.H. Park, M.G. Kim, J. Joo, K. Kim, J. Kim, S. Ahn, Y. Cui, J. Cho, *Nano Letters*, 9 (2009) 3844-3847.
- [13] J.W. Kim, Y.E. Sung, S.M. Oh, *Electrochemical and solid-state letters*, 7 (2004) A306-A309.
- [14] S. Ohara, J.J. Suzuki, K. Sekine, T. Takamura, *Electrochemistry*, 71 (2003) 1126-1128.
- [15] X.H. Liu, L. Zhong, S. Huang, S.X. Mao, T. Zhu, J.Y. Huang, *Acs Nano*, 6 (2012) 1522-1531.
- [16] X.G. Li, Y.Q. He, M.T. Swihart, *Langmuir*, 20 (2004) 4720-4727.

- [17] K. Hata, S. Yoshida, M. Fujita, S. Yasuda, T. Makimura, K. Murakami, H. Shigekawa, *Journal of Physical Chemistry B*, 105 (2001) 10842-10846.
- [18] H. Morisaki, H. Hashimoto, F.W. Ping, H. Nozawa, H. Ono, *Journal of Applied Physics*, 74 (1993) 2977-2979.
- [19] R. Okada, S. Iijima, *Applied Physics Letters*, 58 (1991) 1662-1663.
- [20] C.W. Won, H.H. Nersisyan, C.Y. Shin, J.H. Lee, *Microporous and Mesoporous Materials*, 126 (2009) 166-170.
- [21] C. Suryanarayana, *Progress in Materials Science*, 46 (2001) 1-184.
- [22] M.K. Datta, J. Maranchi, S.J. Chung, R. Epur, K. Kadakia, P. Jampani, P.N. Kumta, *Electrochimica Acta*, 56 (2011) 4717-4723.
- [23] J.P. Maranchi, A.F. Hepp, A.G. Evans, N.T. Nuhfer, P.N. Kumta, *Journal of The Electrochemical Society*, 153 (2006) A1246-A1253.
- [24] J.P. Maranchi, A.F. Hepp, P.N. Kumta, *Electrochem. Solid State Lett.*, 6 (2003) A198-A201.
- [25] R. Epur, M. Ramanathan, F.R. Beck, A. Manivannan, P.N. Kumta, *Materials Science and Engineering B-Advanced Functional Solid-State Materials*, 177 (2012) 1151-1156.
- [26] V. Meunier, J. Kephart, C. Roland, J. Bernholc, *Physical Review Letters*, 88 (2002).
- [27] M.F. Yu, B.S. Files, S. Arepalli, R.S. Ruoff, *Physical Review Letters*, 84 (2000) 5552-5555.
- [28] R. Epur, M.K. Datta, P.N. Kumta, *Electrochimica Acta*, 85 (2012) 680-684.
- [29] T. Song, J.L. Xia, J.H. Lee, D.H. Lee, M.S. Kwon, J.M. Choi, J. Wu, S.K. Doo, H. Chang, W. Il Park, D.S. Zang, H. Kim, Y.G. Huang, K.C. Hwang, J.A. Rogers, U. Paik, *Nano Letters*, 10 (2010) 1710-1716.
- [30] H. Wu, G. Chan, J.W. Choi, I. Ryu, Y. Yao, M.T. McDowell, S.W. Lee, A. Jackson, Y. Yang, L.B. Hu, Y. Cui, *Nat. Nanotechnol.*, 7 (2012) 309-314.
- [31] M.S. Whittingham, *Science*, 192 (1976) 1126-1127.
- [32] M. Yoshio, R.J. Brodd, A. Kozawa, *Lithium-Ion Batteries: Science and Technologies*, Springer, 2010.
- [33] D. Aurbach, E. Zinigrad, H. Teller, P. Dan, *Journal of The Electrochemical Society*, 147 (2000) 1274-1279.
- [34] P. Dan, E. Mengeritsky, D. Aurbach, I. Weissman, E. Zinigrad, *Journal of Power Sources*, 68 (1997) 443-447.

- [35] R.R. Agarwal, *Journal of Power Sources*, 25 (1989) 151-158.
- [36] K. Mizushima, P.C. Jones, P.J. Wiseman, J.B. Goodenough, *Materials Research Bulletin*, 15 (1980) 783-789.
- [37] G.-A.P. Nazri, Gianfranco, *Lithium Batteries: Science and Technology*, 2004.
- [38] J.M. Tarascon, M. Armand, *Nature*, 414 (2001) 359-367.
- [39] M.S. Whittingham, *Materials Research Bulletin*, 13 (1978) 959-965.
- [40] D.W. Murphy, F.A. Trumbore, *Journal of The Electrochemical Society*, 123 (1976) 960-964.
- [41] F.A. Trumbore, *Journal of Power Sources*, 26 (1989) 65-75.
- [42] D.E. Fenton, J.M. Parker, P.V. Wright, *Polymer*, 14 (1973) 589-589.
- [43] G. Oradd, L. Edman, A. Ferry, *Solid State Ionics*, 152 (2002) 131-136.
- [44] L.O. Hagman, Kierkega.P, *Acta Chemica Scandinavica*, 22 (1968) 1822-&.
- [45] H. Aono, E. Sugimoto, Y. Sadaoka, N. Imanaka, G.-y. Adachi, *Solid State Ionics*, 47 (1991) 257-264.
- [46] S.E. Sloop, J.K. Pugh, S. Wang, J.B. Kerr, K. Kinoshita, *Electrochemical and Solid State Letters*, 4 (2001) A42-A44.
- [47] L. Vogdanis, B. Martens, H. Uchtmann, F. Hensel, W. Heitz, *Makromolekulare Chemie-Macromolecular Chemistry and Physics*, 191 (1990) 465-472.
- [48] J.R. Dahn, U. Vonsacken, M.W. Juzkow, H. Aljanaby, *Journal of The Electrochemical Society*, 138 (1991) 2207-2211.
- [49] M. Broussely, F. Perton, J. Labat, R.J. Staniewicz, A. Romero, *Journal of Power Sources*, 43 (1993) 209-216.
- [50] A. Rougier, P. Gravereau, C. Delmas, *Journal of The Electrochemical Society*, 143 (1996) 1168-1175.
- [51] L.-Z. Fan, X.-L. Wang, F. Long, X. Wang, *Solid State Ionics*, 179 (2008) 1772-1775.
- [52] T. Itoh, K. Hirai, T. Uno, M. Kubo, *Ionics*, 14 (2008) 1-6.
- [53] H.M.J.C. Pitawala, M.A.K.L. Dissanayake, V.A. Seneviratne, B.E. Mellander, I. Albinson, *J Solid State Electrochem*, 12 (2008) 783-789.
- [54] P. Raghavan, X. Zhao, J.-K. Kim, J. Manuel, G.S. Chauhan, J.-H. Ahn, C. Nah, *Electrochimica Acta*, 54 (2008) 228-234.

- [55] M.M. Thackeray, W.I.F. David, P.G. Bruce, J.B. Goodenough, *Materials Research Bulletin*, 18 (1983) 461-472.
- [56] M.M. Thackeray, P.J. Johnson, L.A. Depicciotto, P.G. Bruce, J.B. Goodenough, *Materials Research Bulletin*, 19 (1984) 179-187.
- [57] G. Amatucci, J.M. Tarascon, *Journal of The Electrochemical Society*, 149 (2002) K31-K46.
- [58] J.R. Dahn, A.K. Sleight, H. Shi, J.N. Reimers, Q. Zhong, B.M. Way, *Electrochimica Acta*, 38 (1993) 1179-1191.
- [59] Gasparou.H, *Carbon*, 5 (1967) 441-&.
- [60] T. Tran, K. Kinoshita, *Journal of Electroanalytical Chemistry*, 386 (1995) 221-224.
- [61] M.M. Thackeray, *Progress in Solid State Chemistry*, 25 (1997) 1-71.
- [62] M. Yoshio, Y. Xia, N. Kumada, S. Ma, *Journal of Power Sources*, 101 (2001) 79-85.
- [63] G.H. Li, H. Ikuta, T. Uchida, M. Wakihara, *Journal of The Electrochemical Society*, 143 (1996) 178-182.
- [64] A.D. Robertson, S.H. Lu, W.F. Averill, W.F. Howard, *Journal of The Electrochemical Society*, 144 (1997) 3500-3505.
- [65] J.M. Tarascon, E. Wang, F.K. Shokoohi, W.R. McKinnon, S. Colson, *Journal of The Electrochemical Society*, 138 (1991) 2859-2864.
- [66] S. Xun, X. Song, M.E. Grass, D.K. Roseguo, Z. Liu, V.S. Battaglia, G. Liu, *Electrochem. Solid State Lett.*, 14 (2011) A61-A63.
- [67] Y.S. Hu, R. Demir-Cakan, M.M. Titirici, J.O. Muller, R. Schlogl, M. Antonietti, J. Maier, *Angew. Chem.-Int. Edit.*, 47 (2008) 1645-1649.
- [68] S.P.V. Nadimpalli, V.A. Sethuraman, S. Dalavi, B. Lucht, M.J. Chon, V.B. Shenoy, P.R. Guduru, *Journal of Power Sources*, 215 (2012) 145-151.
- [69] W.-J. Zhang, *Journal of Power Sources*, 196 (2011) 13-24.
- [70] Y.-C. Yen, S.-C. Chao, H.-C. Wu, N.-L. Wu, *Journal of The Electrochemical Society*, 156 (2009) A95-A102.
- [71] M. Winter, J.O. Besenhard, M.E. Spahr, P. Novak, *Advanced Materials*, 10 (1998) 725-763.
- [72] N.S. Choi, K.H. Yew, K.Y. Lee, M. Sung, H. Kim, S.S. Kim, *Journal of Power Sources*, 161 (2006) 1254-1259.
- [73] S. Dalavi, P. Guduru, B.L. Lucht, *Journal of The Electrochemical Society*, 159 (2012) A642-A646.

- [74] H. Li, X. Huang, L. Chen, Z. Wu, Y. Liang, *Electrochemical and Solid-state letters*, 2 (1999) 547-549.
- [75] Z.P. Guo, J.Z. Wang, H.K. Liu, S.X. Dou, *Journal of Power Sources*, 146 (2005) 448-451.
- [76] A.K. Padhi, K.S. Nanjundaswamy, J.B. Goodenough, *Journal of The Electrochemical Society*, 144 (1997) 1188-1194.
- [77] M.S. Whittingham, *Chem. Rev.*, 104 (2004) 4271-4301.
- [78] D. Morgan, A. Van der Ven, G. Ceder, *Electrochem. Solid State Lett.*, 7 (2004) A30-A32.
- [79] A. Funabiki, M. Inaba, Z. Ogumi, *Journal of Power Sources*, 68 (1997) 227-231.
- [80] X.Y. Song, K. Kinoshita, T.D. Tran, *Journal of The Electrochemical Society*, 143 (1996) L120-L123.
- [81] S.Y. Chung, J.T. Bloking, Y.M. Chiang, *Nature Materials*, 1 (2002) 123-128.
- [82] R. Fong, U. von Sacken, J.R. Dahn, *Journal of The Electrochemical Society*, 137 (1990) 2009-2013.
- [83] J.R. Dahn, *Physical Review B*, 44 (1991) 9170-9177.
- [84] Z.H. Chen, J.R. Dahn, *Journal of The Electrochemical Society*, 149 (2002) A1184-A1189.
- [85] J.O. Besenhard, H.P. Fritz, *Journal of Electroanalytical Chemistry and Interfacial Electrochemistry*, 53 (1974) 329-333.
- [86] M. Winter, P. Novák, A. Monnier, *Journal of The Electrochemical Society*, 145 (1998) 428-436.
- [87] P.P. Prosini, D. Zane, M. Pasquali, *Electrochimica Acta*, 46 (2001) 3517-3523.
- [88] B. Kang, G. Ceder, *Nature*, 458 (2009) 190-193.
- [89] K. Xu, *Chem. Rev.*, 104 (2004) 4303-4417.
- [90] R.A. Huggins, *Advanced Batteries : Materials Science Aspects*, Springer, 2009.
- [91] N.P. Yao, L.A. Heredy, R.C. Saunders, *Journal of The Electrochemical Society*, 118 (1971) 1039-&.
- [92] F.J. Martino, D.R. Vissers, F.C. Mrazek, H. Shimotake, *Journal of The Electrochemical Society*, 124 (1977) C274-C274.
- [93] M.S. Foster, Croutham.Ce, S.E. Wood, *Journal of Physical Chemistry*, 70 (1966) 3042-&.
- [94] C.J. Wen, R.A. Huggins, *Journal of Solid State Chemistry*, 35 (1980) 376-384.

- [95] C.J. Wen, R.A. Huggins, *Journal of The Electrochemical Society*, 128 (1981) 1181-1187.
- [96] C.S. Tedmon, W.C. Hagel, *Journal of The Electrochemical Society*, 115 (1968) 151-&.
- [97] H. Gleiter, *Progress in Materials Science*, 33 (1989) 223-315.
- [98] C.E. Johnson, M.S. Foster, *Journal of The Electrochemical Society*, 116 (1969) 1612-&.
- [99] J.W. Jiang, H. Fortier, J.N. Reimers, J.R. Dahn, *Journal of The Electrochemical Society*, 151 (2004) A609-A613.
- [100] W. Weppner, R.A. Huggins, *Journal of The Electrochemical Society*, 124 (1977) 1569-1578.
- [101] W. Weppner, R.A. Huggins, *Journal of Solid State Chemistry*, 22 (1977) 297-308.
- [102] K. Xu, *Chem. Rev.*, 104 (2004) 4303-4418.
- [103] S.C. Lai, *Journal of The Electrochemical Society*, 123 (1976) 1196-1197.
- [104] R.A. Sharma, R.N. Seefurth, *Journal of The Electrochemical Society*, 123 (1976) 1763-1768.
- [105] C.J. Wen, R.A. Huggins, *Journal of Solid State Chemistry*, 37 (1981) 271-278.
- [106] M. Winter, J.O. Besenhard, *Electrochimica Acta*, 45 (1999) 31-50.
- [107] J. Yang, M. Winter, J.O. Besenhard, *Solid State Ionics*, 90 (1996) 281-287.
- [108] J.O. Besenhard, J. Yang, M. Winter, *Journal of Power Sources*, 68 (1997) 87-90.
- [109] Y. Matsuda, H. Nakashima, M. Morita, Y. Takasu, *Journal of The Electrochemical Society*, 128 (1981) 2552-2556.
- [110] O. Mao, R.L. Turner, I.A. Courtney, B.D. Fredericksen, M.I. Buckett, L.J. Krause, J.R. Dahn, *Electrochem. Solid State Lett.*, 2 (1999) 3-5.
- [111] O. Mao, J.R. Dahn, *Journal of The Electrochemical Society*, 146 (1999) 414-422.
- [112] O. Mao, R.A. Dunlap, I.A. Courtney, J.R. Dahn, *Journal of The Electrochemical Society*, 145 (1998) 4195-4202.
- [113] O. Mao, R.A. Dunlap, J.R. Dahn, *Journal of The Electrochemical Society*, 146 (1999) 405-413.
- [114] O. Mao, J.R. Dahn, *Journal of The Electrochemical Society*, 146 (1999) 423-427.
- [115] B.A. Boukamp, G.C. Lesh, R.A. Huggins, *Journal of The Electrochemical Society*, 128 (1981) 725-729.

- [116] D. Aurbach, K. Gamolsky, B. Markovsky, Y. Gofer, M. Schmidt, U. Heider, *Electrochimica Acta*, 47 (2002) 1423-1439.
- [117] J. Li, J.R. Dahn, *Journal of The Electrochemical Society*, 154 (2007) A156-A161.
- [118] J.H. Ryu, J.W. Kim, Y.E. Sung, S.M. Oh, *Electrochemical and Solid State Letters*, 7 (2004) A306-A309.
- [119] L.Y. Beaulieu, K.W. Eberman, R.L. Turner, L.J. Krause, J.R. Dahn, *Electrochemical and Solid State Letters*, 4 (2001) A137-A140.
- [120] A. Ulus, Y. Rosenberg, L. Burstein, E. Peled, *Journal of The Electrochemical Society*, 149 (2002) A635-A643.
- [121] G. Atthipalli, R. Epur, P.N. Kumta, B.L. Allen, Y. Tang, A. Star, J.L. Gray, *Thin Solid Films*, 519 (2011) 5371-5375.
- [122] G. Atthipalli, R. Epur, P.N. Kumta, M.J. Yang, J.K. Lee, J.L. Gray, *Journal of Physical Chemistry C*, 115 (2011) 3534-3538.
- [123] V.A. Pedrosa, R. Epur, J. Benton, R.A. Overfelt, A.L. Simonian, *Sensors and Actuators B-Chemical*, 140 (2009) 92-97.
- [124] P.H. Jampani, K. Kadakia, D.H. Hong, R. Epur, J.A. Poston, A. Manivannan, P.N. Kumta, *Journal of The Electrochemical Society*, 160 (2013) A1118-A1127.
- [125] R.H. Telling, M.I. Heggie, *Philosophical Magazine Letters*, 83 (2003) 411-421.
- [126] B.E. Warren, *The Journal of Chemical Physics*, 2 (1934) 551-555.
- [127] J.O. Besenhard, H.P. Fritz, *Angewandte Chemie International Edition in English*, 22 (1983) 950-975.
- [128] R. Kanno, Y. Kawamoto, Y. Takeda, S. Ohashi, N. Imanishi, O. Yamamoto, *Journal of The Electrochemical Society*, 139 (1992) 3397-3404.
- [129] R. Fong, U. Vonsacken, J.R. Dahn, *Journal of The Electrochemical Society*, 137 (1990) 2009-2013.
- [130] Y. Idota, in: USPTO (Ed.), 1995.
- [131] R.A. Huggins, W.D. Nix, *Ionics*, 6 (2000) 57-63.
- [132] M.J. Mayo, *Nanostructured Materials*, 9 (1997) 717-726.
- [133] M.B. Yoshio, Ralph. J; Kozawa Akiya, *Lithium-Ion Batteries: Science and Technologies*, Springer, 2009.

- [134] C. van der Marel, G.J.B. Vinke, W. van der Lugt, *Solid State Communications*, 54 (1985) 917-919.
- [135] H. Okamoto, *J. Phase Equilib. Diffus.*, 30 (2009) 118-119.
- [136] H. Kim, M. Seo, M.-H. Park, J. Cho, *Angewandte Chemie International Edition*, 49 (2010) 2146-2149.
- [137] S.P.V. Nadimpalli, V.A. Sethuraman, S. Dalavi, B. Lucht, M.J. Chon, V.B. Shenoy, P.R. Guduru, *Journal of Power Sources*, 215 (2012) 145-151.
- [138] S. Xun, X. Song, L. Wang, M.E. Grass, Z. Liu, V.S. Battaglia, G. Liu, *Journal of the Electrochemical Society*, 158 (2011) A1260-A1266.
- [139] L.B. Chen, K. Wang, X.H. Xie, J.Y. Xie, *Journal of Power Sources*, 174 (2007) 538-543.
- [140] J. Yang, M. Winter, J.O. Besenhard, *Solid State Ionics*, 90 (1996) 281-287.
- [141] J. Yang, Y. Takeda, N. Imanishi, T. Ichikawa, O. Yamamoto, *Solid State Ionics*, 135 (2000) 175-180.
- [142] Q. Fan, P.J. Chupas, M.S. Whittingham, *Electrochem. Solid State Lett.*, 10 (2007) A274-A278.
- [143] A.M. Wilson, J.N. Reimers, E.W. Fuller, J.R. Dahn, *Solid State Ionics*, 74 (1994) 249-254.
- [144] Y. Nagao, H. Sakaguchi, H. Honda, T. Fukunaga, T. Esaka, *Journal of The Electrochemical Society*, 151 (2004) A1572-A1575.
- [145] H. Li, X.J. Huang, L.Q. Chen, G.W. Zhou, Z. Zhang, D.P. Yu, Y.J. Mo, N. Pei, *Solid State Ionics*, 135 (2000) 181-191.
- [146] J. Yang, Y. Takeda, N. Imanishi, C. Capiglia, J.Y. Xie, O. Yamamoto, *Solid State Ionics*, 152 (2002) 125-129.
- [147] M.K. Datta, P.N. Kumta, *Journal of Power Sources*, 158 (2006) 557-563.
- [148] J.S. Xue, K. Myrtle, J.R. Dahn, *Journal of The Electrochemical Society*, 142 (1995) 2927-2935.
- [149] A.M. Wilson, G. Zank, K. Eguchi, W. Xing, J.R. Dahn, *Journal of Power Sources*, 68 (1997) 195-200.
- [150] W. Xing, A.M. Wilson, G. Zank, J.R. Dahn, *Solid State Ionics*, 93 (1997) 239-244.
- [151] D. Larcher, C. Mudalige, A.E. George, V. Porter, M. Gharghouri, J.R. Dahn, *Solid State Ionics*, 122 (1999) 71-83.

- [152] S.E. Hayes, H. Eckert, W.R. Even, R. Guidotti, *Journal of The Electrochemical Society*, 146 (1999) 2435-2442.
- [153] M. Holzapfel, H. Buqa, F. Krumeich, P. Novák, F.-M. Petrat, C. Veit, *Electrochemical and Solid-state letters*, 8 (2005) A516-A520.
- [154] B.A. Boukamp, G.C. Lesh, R.A. Huggins, *Journal of The Electrochemical Society*, 128 (1981) 725-729.
- [155] W. Wang, M.K. Datta, P.N. Kumta, *J. Mater. Chem.*, 17 (2007) 3229-3237.
- [156] L.F. Cui, R. Ruffo, C.K. Chan, H.L. Peng, Y. Cui, *Nano Letters*, 9 (2009) 491-495.
- [157] J. Graetz, C.C. Ahn, R. Yazami, B. Fultz, *Electrochemical and Solid State Letters*, 6 (2003) A194-A197.
- [158] W. Wang, P.N. Kumta, *Journal of Power Sources*, 172 (2007) 650-658.
- [159] R. Huang, X. Fan, W.C. Shen, J. Zhu, *Appl. Phys. Lett.*, 95 (2009).
- [160] H.X. Chen, Y. Xiao, L. Wang, Y. Yang, *Journal of Power Sources*, 196 (2011) 6657-6662.
- [161] A. Thess, R. Lee, P. Nikolaev, H.J. Dai, P. Petit, J. Robert, C.H. Xu, Y.H. Lee, S.G. Kim, A.G. Rinzler, D.T. Colbert, G.E. Scuseria, D. Tomanek, J.E. Fischer, R.E. Smalley, *Science*, 273 (1996) 483-487.
- [162] K. Evanoff, J. Khan, A.A. Balandin, A. Magasinski, W.J. Ready, T.F. Fuller, G. Yushin, *Advanced Materials*, 24 (2012) 533-+.
- [163] A. Magasinski, P. Dixon, B. Hertzberg, A. Kvit, J. Ayala, G. Yushin, *Nature Materials*, 9 (2010) 353-358.
- [164] R. Krishnan, T.M. Lu, N. Koratkar, *Nano Letters*, 11 (2011) 377-384.
- [165] S. Zhou, X.H. Liu, D.W. Wang, *Nano Letters*, 10 (2010) 860-863.
- [166] Y. Yao, K.F. Huo, L.B. Hu, N.A. Liu, J.J. Ha, M.T. McDowell, P.K. Chu, Y. Cui, *Acs Nano*, 5 (2011) 8346-8351.
- [167] N. Liu, H. Wu, M.T. McDowell, Y. Yao, C. Wang, Y. Cui, *Nano Letters*, 12 (2012) 3315-3321.
- [168] W.Z. Li, C.H. Liang, W.J. Zhou, J.S. Qiu, Z.H. Zhou, G.Q. Sun, Q. Xin, *Journal of Physical Chemistry B*, 107 (2003) 6292-6299.
- [169] P. Serp, M. Corrias, P. Kalck, *Applied Catalysis a-General*, 253 (2003) 337-358.
- [170] G.G. Wildgoose, C.E. Banks, R.G. Compton, *Small*, 2 (2006) 182-193.

- [171] C.S. Du, N. Pan, *Nanotechnology*, 17 (2006) 5314-5318.
- [172] V.V.N. Obreja, *Physica E-Low-Dimensional Systems & Nanostructures*, 40 (2008) 2596-2605.
- [173] G.X. Wang, B.L. Zhang, Z.L. Yu, M.Z. Qu, *Solid State Ionics*, 176 (2005) 1169-1174.
- [174] K. Evanoff, J. Khan, A.A. Balandin, A. Magasinski, W.J. Ready, T.F. Fuller, G. Yushin, *Advanced Materials*, 24 (2012) 533-537.
- [175] K. Besteman, J.O. Lee, F.G.M. Wiertz, H.A. Heering, C. Dekker, *Nano Letters*, 3 (2003) 727-730.
- [176] J. Kong, M.G. Chapline, H.J. Dai, *Advanced Materials*, 13 (2001) 1384-1386.
- [177] J. Wang, *Electroanalysis*, 17 (2005) 7-14.
- [178] M. Kumar, Y. Ando, *Journal of nanoscience and nanotechnology*, 10 (2010) 3739-3758.
- [179] S. Shih, K.H. Jung, D.L. Kwong, M. Kovar, J.M. White, *Applied Physics Letters*, 62 (1993) 1780-1782.
- [180] R.L. Smith, S.D. Collins, *Journal of Applied Physics*, 71 (1992) R1-R22.
- [181] J.R. Heath, *Science*, 258 (1992) 1131-1133.
- [182] N. Arul Dhas, C.P. Raj, A. Gedanken, *Chemistry of Materials*, 10 (1998) 3278-3281.
- [183] C.-S. Yang, R.A. Bley, S.M. Kauzlarich, H.W.H. Lee, G.R. Delgado, *Journal of the American Chemical Society*, 121 (1999) 5191-5195.
- [184] D. Mayeri, B.L. Phillips, M.P. Augustine, S.M. Kauzlarich, *Chemistry of Materials*, 13 (2001) 765-770.
- [185] R.A. Bley, S.M. Kauzlarich, *Journal of the American Chemical Society*, 118 (1996) 12461-12462.
- [186] J.P. Wilcoxon, G.A. Samara, P.N. Provencio, *Physical Review B*, 60 (1999) 2704-2714.
- [187] R.D. Tilley, J.H. Warner, K. Yamamoto, I. Matsui, H. Fujimori, *Chemical Communications*, 0 (2005) 1833-1835.
- [188] I.J. Lin, S. Nadiv, *Materials Science and Engineering*, 39 (1979) 193-209.
- [189] V. Šepelák, *Annales de Chimie Science des Matériaux*, 27 (2002) 61-76.
- [190] N.Z. Lyakhov, T.F. Grigorieva, A.P. Barinova, I.A. Vorsina, *Russ. Chem. Rev.*, 79 (2010) 189-203.

- [191] A.F. Fuentes, L. Takacs, J. Mater. Sci., 48 (2013) 598-611.
- [192] C. Lam, Y.F. Zhang, Y.H. Tang, C.S. Lee, I. Bello, S.T. Lee, Journal of Crystal Growth, 220 (2000) 466-470.
- [193] X.L. Yang, Z.Y. Wen, L. Zhang, M. You, Journal of Alloys and Compounds, 464 (2008) 265-269.
- [194] W.C. Zhou, S. Upreti, M.S. Whittingham, Electrochemistry Communications, 13 (2011) 1102-1104.
- [195] I.-s. Kim, G.E. Blomgren, P.N. Kumta, Journal of Power Sources, 130 (2004) 275-280.
- [196] L. Russo, F. Colangelo, R. Cioffi, I. Rea, L. De Stefano, Materials, 4 (2011) 1023-1033.
- [197] R. Epur, L. Minardi, M.K. Datta, S.J. Chung, P.N. Kumta, Journal of Solid State Chemistry, 208 (2013) 93-98.
- [198] J.H. Parker, Jr., D.W. Feldman, M. Ashkin, Physical Review, 155 (1967) 712.
- [199] C. Smit, R. van Swaaij, H. Donker, A. Petit, W.M.M. Kessels, M.C.M. van de Sanden, Journal of Applied Physics, 94 (2003) 3582-3588.
- [200] R.L.C. Vink, G.T. Barkema, W.F. van der Weg, Physical Review B, 63 (2001) 115210.
- [201] J.M. Lackner, W. Waldhauser, R. Ebner, W. Lenz, C. Suess, G. Jakopic, G. Leising, H. Hutter, Surface and Coatings Technology, 163-164 (2003) 300-305.
- [202] S. Yasuda, T. Chikyow, S. Inoue, N. Matsuki, K. Miyazaki, S. Nishio, M. Kakihana, H. Koinuma, Applied Physics A: Materials Science & Processing, 69 (1999) S925-S927.
- [203] M. Janai, D.D. Allred, D.C. Booth, B.O. Seraphin, Solar Energy Materials, 1 (1979) 11-27.
- [204] C. Sutichai, Materials Science and Engineering: B, 137 (2007) 205-209.
- [205] X. Chen, K. Gerasopoulos, J. Guo, A. Brown, C. Wang, R. Ghodssi, J.N. Culver, Advanced Functional Materials, 21 (2011) 380-387.
- [206] J. Gobet, H. Tannenberger, Journal of The Electrochemical Society, 135 (1988) 109-112.
- [207] T. Munisamy, A.J. Bard, Electrochimica Acta, 55 (2010) 3797-3803.
- [208] J.P. Nicholson, Journal of the Electrochemical Society, 152 (2005) C795.
- [209] Y. Nishimura, Y. Fukunaka, Electrochimica Acta, 53 (2007) 111-116.
- [210] M. Schmuck, A. Balducci, B. Rupp, W. Kern, S. Passerini, M. Winter, J. Solid State Electrochem., 14 (2010) 2203-2207.

- [211] S.Z. El Abedin, N. Borissenko, F. Endres, *Electrochem. Commun.*, 6 (2004) 510-514.
- [212] A.K. Agrawal, A.E. Austin, *Journal of The Electrochemical Society*, 128 (1981) 2292-2296.
- [213] M.K. Datta, P.N. Kumta, *Journal of Power Sources*, 194 (2009) 1043-1052.
- [214] R.A. DiLeo, B.J. Landi, R.P. Raffaele, *Journal of Applied Physics*, 101 (2007).
- [215] M.S. Dresselhaus, G. Dresselhaus, R. Saito, A. Jorio, *Physics Reports*, 409 (2005) 47-99.
- [216] C. Smit, R. van Swaaij, H. Donker, A. Petit, W. Kessels, M. van de Sanden, *Journal of Applied Physics*, - 94 (2003) 3582-3588.
- [217] T.D. Hatchard, J.R. Dahn, *Journal of The Electrochemical Society*, 151 (2004) A838-A842.
- [218] A. Ghemes, Y. Minami, J. Muramatsu, M. Okada, H. Mimura, Y. Inoue, *Carbon*, 50 (2012) 4579-4587.
- [219] K.A. Mirica, J.G. Weis, J.M. Schnorr, B. Esser, T.M. Swager, *Angewandte Chemie International Edition*, 51 (2012) 10740-10745.
- [220] K. Evanoff, J. Benson, M. Schauer, I. Kovalenko, D. Lashmore, W.J. Ready, G. Yushin, *Acs Nano*, 6 (2012) 9837-9845.
- [221] Y. Yao, M.T. McDowell, I. Ryu, H. Wu, N. Liu, L. Hu, W.D. Nix, Y. Cui, *Nano Letters*, 11 (2011) 2949-2954.
- [222] F. Al-Hazmi, F. Alnowaiser, A.A. Al-Ghamdi, M.M. Aly, R.M. Al-Tuwirqi, F. El-Tantawy, *Superlattices and Microstructures*, 52 (2012) 200-209.
- [223] R. Epur, M.K. Datta, P.N. Kumta, *Electrochimica Acta*, 85 (2012) 680-684.
- [224] S. Tsubouchi, Y. Domi, T. Doi, M. Ochida, H. Nakagawa, T. Yamanaka, T. Abe, Z. Ogumi, *Journal of The Electrochemical Society*, 159 (2012) A1786-A1790.
- [225] D. Aurbach, M.D. Levi, E. Levi, A. Schechter, *The Journal of Physical Chemistry B*, 101 (1997) 2195-2206.
- [226] D. Aurbach, Y. Ein-Ely, A. Zaban, *Journal of The Electrochemical Society*, 141 (1994) L1-L3.
- [227] C. Korepp, H.J. Santner, T. Fujii, M. Ue, J.O. Besenhard, K.C. Möller, M. Winter, *Journal of Power Sources*, 158 (2006) 578-582.
- [228] S.S. Zhang, K. Xu, T.R. Jow, *Electrochemical and solid-state letters*, 5 (2002) A206-A208.

- [229] X. Wang, H. Naito, Y. Sone, G. Segami, S. Kuwajima, *Journal of The Electrochemical Society*, 152 (2005) A1996-A2001.
- [230] W. Li, C. Campion, B.L. Lucht, B. Ravdel, J. DiCarlo, K.M. Abraham, *Journal of The Electrochemical Society*, 152 (2005) A1361-A1365.
- [231] L.J. Krause, W. Lamanna, J. Summerfield, M. Engle, G. Korba, R. Loch, R. Atanasoski, *Journal of Power Sources*, 68 (1997) 320-325.
- [232] X. Wang, E. Yasukuwa, S. Kasuya, *Journal of The Electrochemical Society*, 148 (2001) A1058-41065.
- [233] K. Xu, S. Zhang, J.L. Allen, T.R. Jow, *Journal of The Electrochemical Society*, 149 (2002) A1079-A1082.
- [234] D.Y. Wang, N.N. Sinha, J.C. Burns, C.P. Aiken, R. Petibon, J.R. Dahn, *Journal of The Electrochemical Society*, 161 (2014) A467-A472.
- [235] S.-W. Bian, J. Baltrusaitis, P. Galhotra, V.H. Grassian, *J. Mater. Chem.*, 20 (2010) 8705-8710.